STRESS AND FRACTURE ANALYSIS OF RIVETED JOINTS

A THESIS SUBMITTED TO
THE GRADUATE SCHOOL OF NATURAL AND APPLIED SCIENCES
OF
MIDDLE EAST TECHNICAL UNIVERSITY

BY

GALİP KEÇELİOĞLU

IN PARTIAL FULFILLMENT OF THE REQUIREMENTS
FOR
THE DEGREE OF MASTER OF SCIENCE
IN
MECHANICAL ENGINEERING

NOVEMBER 2008

Approval of the thesis:

STRESS AND FRACTURE ANALYSIS OF RIVETED JOINTS

submitted by **GALİP KEÇELİOĞLU** in partial fulfillment of the requirements for the degree of **Master of Science in Mechanical Engineering Department, Middle East Technical University** by,

Prof. Dr. Canan Özgen
Dean, Graduate School of **Natural and Applied Sciences** ____________________

Prof. Dr. Suha Oral
Head of Department, **Mechanical Engineering** ____________________

Assoc. Prof. Dr. Serkan Dağ
Supervisor, **Mechanical Engineering Dept., METU** ____________________

Examining Committee Members

Prof. Dr. Bülent Doyum
Mechanical Engineering Dept., METU ____________________

Assoc. Prof. Dr. Serkan Dağ
Mechanical Engineering Dept., METU ____________________

Prof. Dr. Suat Kadıoğlu
Mechanical Engineering Dept., METU ____________________

Asst. Prof. Dr. Ergin Tönük
Mechanical Engineering Dept., METU ____________________

Asst. Prof. Dr. Mehmet Ali Güler
Mechanical Engineering Dept., TOBB ETU ____________________

Date: November 5, 2008

I hereby declare that all information in this document has been obtained and presented in accordance with academic rules and ethical conduct. I also declare that, as required by these rules and conduct, I have fully cited and referenced all material and results that are not original to this work.

Name, Last Name: Galip Keçelioğlu

Signature:

ABSTRACT

STRESS AND FRACTURE ANALYSIS OF RIVETED JOINTS

Keçelioğlu, Galip
M.S., Department of Mechanical Engineering
Supervisor: Assoc. Prof. Dr. Serkan Dağ

November 2008, 184 pages

The objective of this study is to model and analyze a three dimensional single riveted lap joint (with and without a crack). By using finite element method, stress and fracture analyses are carried out under both the residual stress field and external tensile loading. Using a two step simulation, riveting process and subsequent tensile loading of the lap joint are simulated to determine the residual and overall stress state. Residual stress state due to riveting is obtained by interference and clamping misfit method. By employing different interference and clamping misfit values, the effects of riveting process parameters on stress state are examined. Two cracks namely the semi elliptical surface crack at faying surfaces of plates and the quarter elliptical corner crack at rivet hole are the most widely observed crack types in riveted joints. Fracture analysis of cracked riveted joints is carried out by introducing these two crack types to the outer plate at a plane perpendicular to the loading. The mixed mode stress intensity factors (SIFs) and energy release rates (*G*) around the crack front are obtained by using displacement correlation technique (DCT). Effects riveting process parameters (interference and clamping ratios) and geometrical parameters (crack shape and size) on fracture parameters are studied. The stress intensity factor solutions presented herein could be useful for correlating fatigue crack growth rates,

fracture toughness computation, and multiple site damage (MSD) analysis in aircraft bodies.

Keywords: Riveted Lap Joints, Riveting Process Simulation, Residual Stress, Stress Intensity Factor, Displacement Correlation Technique

ÖZ

PERÇİNLİ BAĞLANTILARIN GERİLİM VE KIRILMA ANALİZİ

Keçelioğlu, Galip
Yüksek Lisans, Makina Mühendisliği Bölümü
Tez Yöneticisi: Doç. Dr. Serkan Dağ

Kasım 2008, 184 Sayfa

Bu çalışmanın amacı tek perçinli bindirme bağlantısının çatlaklı ve çatlaksız olmak üzere üç boyutlu sayısal modellerini oluşturmak ve analiz etmektir. Sonlu elemanlar metodu kullanılarak, artık gerilim ve dış çekme yüklemesi altında perçinli bağlantıda gerilim ve kırılma analizleri gerçekleştirilmiştir. İki aşamalı analiz ile perçinleme işlemi ve ardından dış yükleme benzetimi yapılarak artık gerilim ve dış yükleme altındaki gerilim çözümleri bulunmuştur. Perçinleme işlemi sonucu oluşan artık gerilimler girişim ve kenetleme uygunsuzluğu metoduyla bulunmuştur. Farklı girişim ve kenetleme uygunsuzluk değerleri kullanılarak perçinleme işlemi parametrelerinin gerilim durumu üzerindeki etkileri incelenmiştir. Perçinli bağlantılarda sıkça görülen iki tip çatlak vardır. Bunlar plakaların temas eden yüzeyinde oluşan yarı elips yüzey çatlağı ve perçin deliğinde oluşan çeyrek elips köşe çatlağıdır. Bu iki farklı çatlak, perçinli bağlantıya ait dış plaka üzerine, yükleme yönüne dik olarak yerleştirerek iki farklı model elde edilmiş ve bağlantılara ait kırılma analizi gerçekleştirilmiştir. Yer değiştirme korelasyon tekniği kullanılarak çatlak çevresindeki karışık mod gerilme şiddeti çarpanları ve enerji salınım oranları hesaplanmıştır. Perçinleme işlemi parametreleri ve geometrik parametrelerin (çatlak şekil ve boyutları) gerilme şiddeti çarpanlarına etkileri incelenmiştir. Bu çalışmada bulunan gerilme

şiddeti çarpanları değerleri çatlak ilerlemesi, malzemeye ait kırılma tokluğu hesaplanması ve hava taşıtlarında çoklu konum hasarı analizlerinde kullanılabilir.

Anahtar Kelimeler: Perçinli Bağlantılar, Perçinleme İşlemi Benzetimi, Kalıntı Gerilmeler, Gerilme Şiddeti Çarpanı, Yerdeğiştirme Korelasyon Tekniği

To Great Turkish Leader Mustafa Kemal ATATÜRK with Gratitude

ACKNOWLEDGEMENTS

I would like to thank to my supervisor Assoc. Prof. Dr. Serkan DAĞ, for his guidance, advices and criticism throughout this study. I would also like to thank to Asst. Prof. Dr. Mehmet Ali GÜLER for his valuable suggestions and comments.

I am thankful to my company ASELSAN Inc. for letting and supporting of my thesis.

The cooperation and friendly support of my colleagues in ASELSAN during my thesis study also deserves to be acknowledged.

Thanks to my parents for their unique motivation and encouragement.

Finally, many thanks go to my wife Bilgen BİLGİN KEÇELİOĞLU for her continuous help, motivation, encouragement and understanding during my thesis study.

TABLE OF CONTENTS

LIST OF TABLES

TABLES

LIST OF FIGURES

FIGURES

LIST OF SYMBOLS

a	Crack Depth of Elliptical Crack
c	Half Crack Length of Elliptical Crack
t	Thickness of the Plate
ϕ	Parametric Angle at Crack Front
b	Half Width of the Plate
h	Half Length of the Plate
E	Modulus of Elasticity
ν	Poisson's Ratio
κ	3-4ν
λ	First Lamé Elastic Parameter
μ	Second Lamé Elastic parameter
K_c	Critical Stress Intensity Factor, Fracture Toughness
θ	Angle from the Crack Plane
r	Distance from the Crack Tip
Q	Shape Factor for Elliptical Crack
K	Stress Intensity Factor
K_I	Mode I Stress Intensity Factor
K_{II}	Mode II Stress Intensity Factor
K_{III}	Mode III Stress Intensity Factor
G	Energy release Rate
%L	% Height Interference in Interference Misfit Method
%D	% Radial Interference in Interference Misfit Method
L_r	Rivet Shank Height
L_h	Combined Depth of Two Plates
D_r	Rivet Shank Diameter
D_h	Rivet Hole Diameter

CHAPTER 1

INTRODUCTION

1.1 Motivation

Manufacturing large and complex structures is usually possible only when they are composed of assemblies of smaller parts joined together by variety of joining techniques since most products are impossible to be produced as a single piece. Manufacturing components and then joining them into a single product is easier and less expensive than manufacturing the whole product at once. In order to ensure the manufacturability, and reduce the overall manufacturing cost, certain fastening and joining methods should be utilized.

Mechanical fasteners can be described as devices that mechanically join two or more objects of an assembly with desired permanence, stability, and strength. Mechanical fasteners offer several options for joining and fastening mechanical components together. Mechanical fastening methods can be categorized into two main types: permanent (welding, bonding, riveting, etc.) and detachable joints (bolt, screw, pin etc.). Selection of appropriate method among these alternatives should be based on permanence, cost and strength of the fastener.

Rivets are permanent, non-threaded, one-piece fasteners that join parts together by fitting through a pre-drilled hole and deforming the head by mechanically upsetting from one end. Rivets are the most widely used mechanical fasteners especially in aircraft fuselage structures. Hundreds of thousands of rivets are utilized in the construction and assembly of a large aircraft. Solid rivet with universal head is one of the most widely used rivet type in aircraft fuselage manufacturing and repairing processes (Figure 1.1).

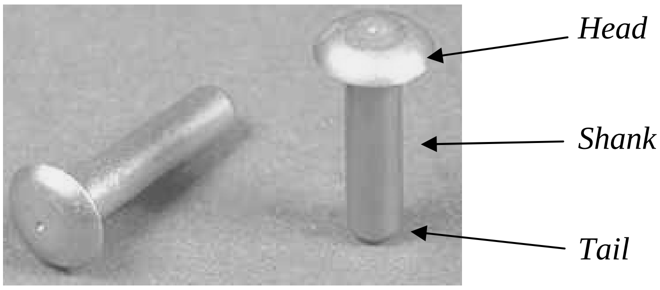

Figure 1.1 Solid rivet having universal head

Aircraft fuselage structures consist of complicated assemblies whose parts are connected to each other by mechanically fastened joints. The fuselage consists of curved skin panels joined by lap joint method. Single shear lap joint with different number of rivets in row and column is a simplification of the complicated lap joint in the real aircraft structure (Figure 1.2). In other words, the lap joint in a real aircraft is a series of single riveted lap joints.

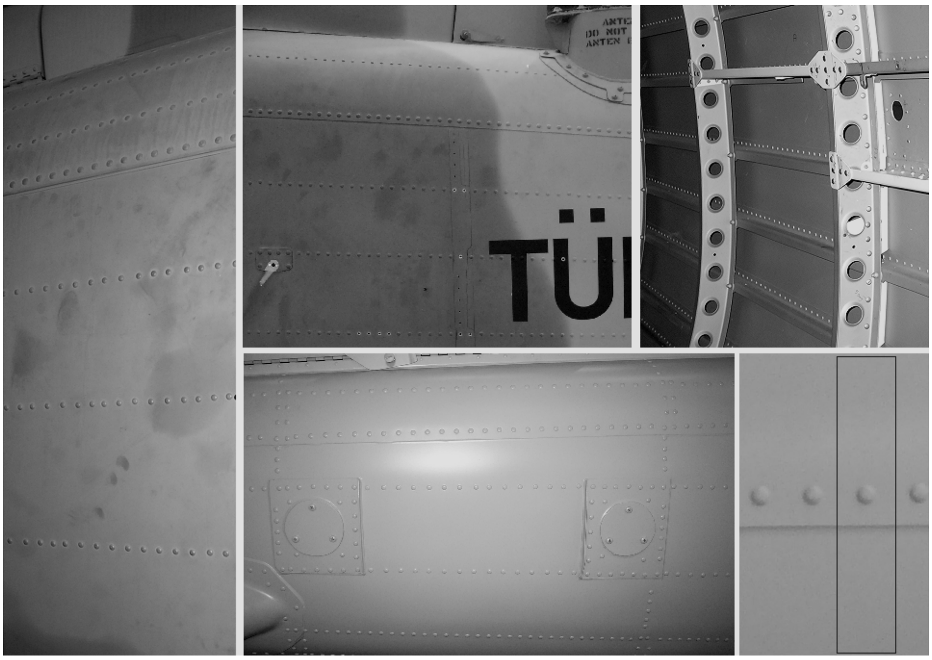

Figure 1.2 Aircraft fuselage structure with riveted joints

In lap joints, by using different number of rivets in column and row, wide variety of configurations can be obtained. One rivet in a row and one rivet in a column, one rivet in a row two rivets in a column, and one rivet in a row three rivets in a column are the most widely used lap joint configurations (Figure 1.3). It is also possible to use more than one rivet in a row to obtain different configurations. In this study, one rivet in a row and one rivet in a column geometric configuration will be examined.

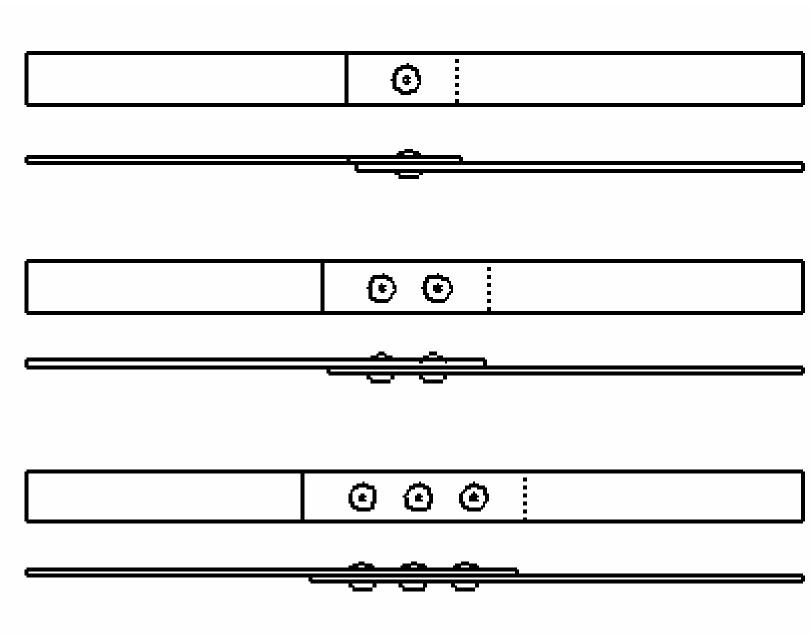

Figure 1.3 Riveted lap joint geometric configurations

Riveted joints are obtained by rivet installation process, also known as riveting process. In a riveting process, the rivet is placed in a pre-drilled hole, and then the tail is upset by a hammer so that rivet shank expands and holds the rivet in place. Rivet types and the equipments for riveting are shown in Figure 1.4.

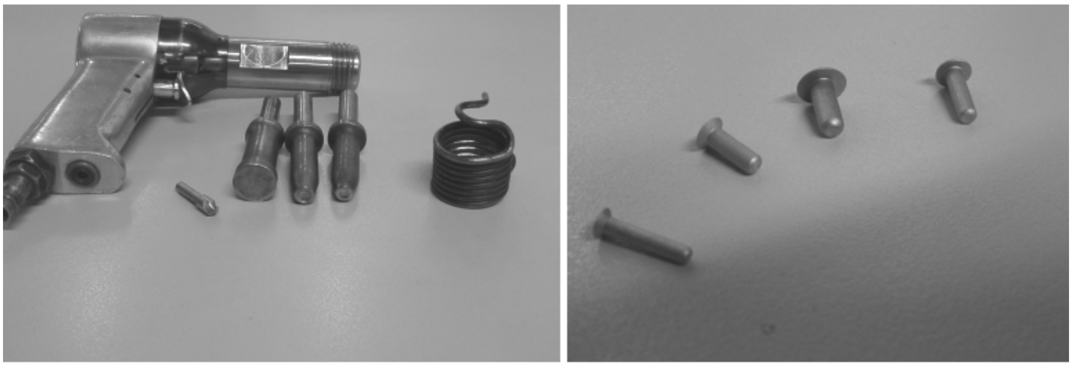

a) **b)**

Figure 1.4 a) A view of the air gun used for deforming the rivet head, **b)** Rivet types [1]

The riveting process introduces a complex residual stress state for the riveted joint (both for the rivet and the plates). Moreover, during the installation process the plates are pressed together by the deformed rivet. This causes surface contact stresses between the joined plates. Contact stress combined with fatigue loading may result in a greater possibility of fretting on the plates around the rivet hole.

The service loading of the riveted joints in aircraft structures is the fatigue type; and it is mainly due to the pressurization and depressurization of the fuselage. During one flight pressurization-depressurization cycle is completed and this is repeated for each flight. Fuselage pressurization is the main fatigue load on riveted lap joints. This pressure introduces lap joints a combination of longitudinal tension, hoop tension and out-of-plane bending among which the longitudinal tension is much more dominant. Therefore the riveted lap joint under tensile loading is analyzed. Figure 1.5 (a) and (b) illustrate the schematics of the riveted lap joints under fuselage pressurization load and equivalent tension load, respectively.

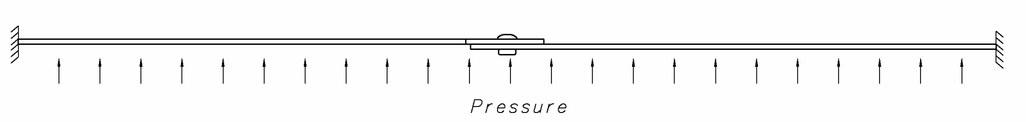

a)

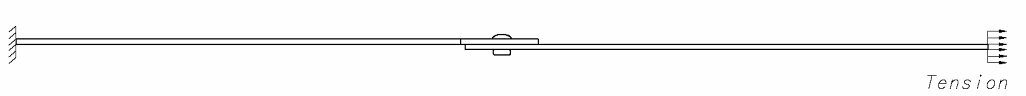

b)

Figure 1.5 Single riveted lap joint under **a)** pressure load **b)** tension load

Riveted lap joints are susceptible to cracks due to fatigue and fretting. There are two major crack types and initiation locations in typically riveted lap joints. First is the semi elliptical surface crack initiated away from the riveted hole. Nucleation of this crack is mostly due to fretting. This type of cracks is generally observed in riveted lap joints with universal head rivet type. Second is the quarter elliptical corner crack initiated at one or both sides of the rivet hole. The main causes of this type of crack are the fatigue and high stress level in riveted joint. It is observed in riveted lap joints with universal and countersunk head rivet types.

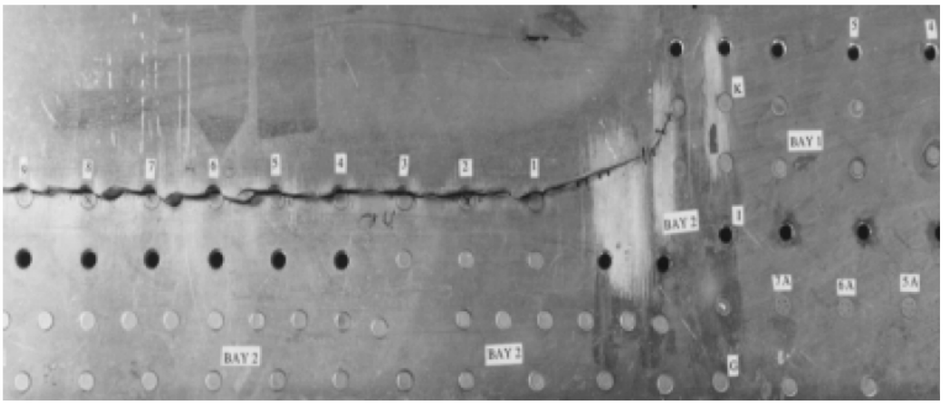

Figure 1.6 A typical lap joint susceptible to MSD (cracks initiate from rivet hole) [2]

Multiple site damage (MSD) sometimes termed widespread fatigue damage (WFD) is also an important phenomena in which small fatigue cracks at different sites in the same structural elements grow and finally link up (join) forming large, more dangerous cracks. Figure 1.6 illustrates a typical lap joint susceptible to MSD. Cracks initiate from the rivet holes, join up and grow.

1.2 Literature Survey

Rivets are highly used in aircraft fuselage manufacturing and repairing processes. Great number of rivets is used for the assembly of aircraft body. For instance, approximately 100,000 solid rivets are utilized for one subassembly of Boeing 747 aircraft [3]. Therefore the integrity of fuselage structures is directly related to the integrity of riveted joints. The reasons why the rivets are preferred over the threaded fasteners are the lower unit cost, short installation time and permanence of rivets after installation.

In the literature, there are numerous studies on this subject. Studies could be categorized as follows:

- Analysis of Rivet Installation Process: Determination of residual stress state introduced by riveting process and effects of riveting process parameters on residual stress state,
- Analysis of Riveted Joints: Fatigue and fretting analysis, stress intensity factor and load transfer analysis of cracked joint, crack growth and multiple site damage (MSD) analysis in riveted joints.

1.2.1. Analysis of Rivet Installation Process

In order to make further fracture, fretting, fatigue, crack growth analyses, the residual stress state of riveted joints should be known as an initial condition. Obtaining the complex residual stress state as a result of rivet installation process is a challenging task. Also the effects of riveting process parameters (rivet squeezing force, clearance between hole and rivet shank, sealant usage, etc.) on fatigue strength of riveted joints have been explored. There are three main approaches to simulate the riveting process.

- Experimental methods
- Finite element methods
- Simplified methods

Each of them is explained in the subsequent sections.

1.2.1.1 Experimental Methods

In order to investigate the riveting process, controlled laboratory experiments can be carried out. By experimental method, realistic models can be obtained to give more accurate results. However experiments are usually difficult to apply. Fitzgerald and Cohen [4] developed a new procedure to measure the residual stresses in and around rivets in clad aluminum plates. For this purpose, X-Ray diffraction method was employed. Residual stress values (radial and tangential components) were obtained on and near the rivet head and tail before and after riveting state. Also in studies [5] and [6], residual stress field created by cold expansion was experimentally obtained by using the X-Ray technique. Cold working of rivet holes is a technique which improves the fatigue life of riveted joints.

Langrand et al. [7] carried out experimental studies to investigate the riveting process and to improve the design of riveted joints. They stated that complex riveted joints are considered as the sum of single riveted joints (simply 2 plates-one rivet joints). Residual stress and strain in rivets and plates were measured by applying a strain gage method. Results of this study showed that the riveting process could be divided into seven main steps. In Figure 1.7, material flow of rivet and plates during rivet installation can be seen clearly. In this study, also the overall behavior and strength of a riveted joint was studied. Basic failure modes of rivets and crack propagation of plates were characterized.

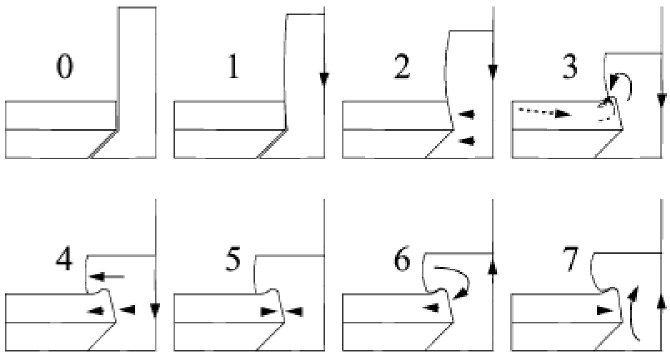

Figure 1.7 Riveting process mechanism (material flow) [7]

Atre and Johnson [8] summarized the fatigue test results for riveted lap joints with critical manufacturing process variables. The influence of under-driven and over-driven rivets, hole quality and sealant effects on the fatigue life of the joint were investigated. Test results showed under-driven lap joints to have the least fatigue strength. They also concluded that fatigue life increased with increasing rivet interference.

1.2.1.2 Finite Element Methods

Besides the experimental methods, finite element methods (FEM) (also known as finite element analysis) are frequently used to investigate the riveting process. By the help of the finite element methods, approximate solutions are obtained by using certain simplifications and idealizations. In order to obtain the residual stress field in a single lap joint structure, Szolwinski and Farris [9] made a simulation of rivet installation process which is quasi-static and squeeze force-controlled. Relationship between riveting process parameters and fatigue behavior of the joints was investigated. The results of the analysis revealed both a strong through-thickness gradient in residual stresses and change in the distribution of residual hoop stress near the rivet/hole interface with squeeze force. Residual hoop stress has a major effect on the propagation of fatigue damage that nucleates at either rivet/hole interface or faying surface.

Ryan and Monaghan [10] had carried out numerical simulation of riveting process for both a fiber metal laminate (FML) and typical aluminum alloy fuselage material (2024-T3), and made comparisons. To obtain a better comprehension of the deformation process due to riveting and the stress state after elastic recovery a number of axisymmetric models were considered. Results of simulations revealed that forming load and rivet material had a significant effect on the initial stress distribution (residual stress state) within the panels. Also it was shown that localized compressive hoop stresses occurred in the panels, which is beneficial to the fatigue life of the joint.

Karasan [11] studied the residual stress state from riveting process. He developed various finite element models in 2-D and 3-D to simulate the installation of the rivet. The effect of clearance between the rivet shank and the hole on the residual stress field was investigated for a universal head rivet.

1.2.1.3 Simplified Methods

In the riveting process, the manufactured head of the rivet is kept fixed and a squeezing force is applied at the other end to form the protruding head. By this the shank of the rivet is expanded laterally to fill the rivet hole, and two plates are pressed together. It reveals that the complex residual stress state consists of two main components: the clamping stress due to the squeezing force and the interference stress due to radial expanding of rivet shank. When the riveting process itself is beyond the scope of a study, residual stress state due to the rivet installation can be obtained by certain simplified methods.

Iyer et al. [12] simulated the riveting process by using interference and clamping misfit methods. Radial stress due to the rivet expansion was simulated by forcing radial conformity between the plate holes and initially oversized rivet shank. In this case, the interference is produced only in the radial direction (shank radial interference). Clamping stresses were generated by forcing the elongation of a rivet whose initial shank height is modeled slightly less than the combined depth of the two plates (shank height interference-clamping). Values of 0, 1, and 2 % shank radial interferences and 0, and 0.5 % shank height interference were used to examine the effect of different riveting processes.

Fung and Smart [13] obtained the residual stress from riveting process by using thermal expansion method. By selecting different coefficients of thermal expansion of the rivet shank, height of the rivet shank was reduced and diameter of the rivet shank was increased. Reducing height of rivet shank corresponds to the clamping force in riveting process. Different coefficients of thermal expansion in the rivet shank were specified to simulate different clamping forces. Four different (0.0, 0.1, 0.2 and 0.5) clamping force ratios (defined as average rivet clamping axial stress to yield stress ratio) were selected. Expanding the rivet shank in the radial direction corresponds to rivet filling in the hole. Similarly different coefficients of thermal expansion were chosen so that different interference fit ratios were obtained. Interference fit ratio was defined as the interfacial pressure divided by the yield stress. For different interference fit ratios (0.00, 0.03, 0.06 and 0.15) were used to examine the effect of different interference level in the rivet hole.

Sometimes the rivet geometry is idealized by beam and spring elements. Bedair and Eastaugh [14] modeled rivets by two separate layers that are linked by beam connectors (Figure 1.8). Rotational spring elements were used to include the rivet heads. Also in reference [15], similar modeling was carried out. Harris et al. [2] modeled riveted connections with rigid links. Fastener elements comprised of linear springs were used to model the mechanical connection between the layers at the rivet locations.

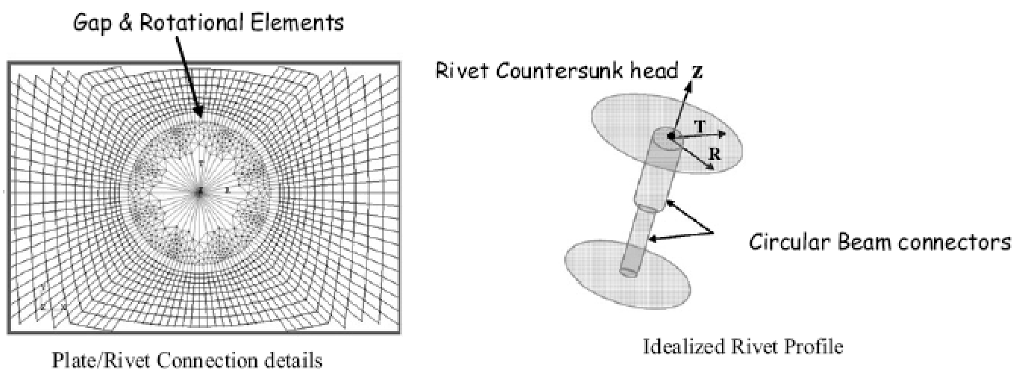

Figure 1.8 Plate/rivet connection and idealized rivet profile [14]

1.2.2. Analysis of Riveted Joints

Analysis of riveted joints includes the following aspects:

- Fatigue and fretting analysis,
- Stress intensity factor and load transfer analysis,
- Crack growth and multiple site damage (MSD) analysis in riveted joints.

1.2.2.1 Fatigue and Fretting Analysis

Due to the service fatigue loading of the joints in aircraft structures, fatigue types of failure are most common failure types in an aircraft fuselage. Therefore there are extensive studies on this subject. Finite element methods are widely utilized to conduct fatigue and fretting analysis. Fung and Smart [26] made a complete three-dimensional finite element model of single riveted lap joints. The total strain range and effective stress were investigated and the fatigue lives of riveted joints are predicted from the plates with open plain holes.

Fretting in riveted joints is a contact damage driven by relative micro-motion and the contact stresses at the contact area of rivet/hole and faying surfaces. It is well known that fretting is the major cause of crack formation in riveted joints in aircraft structures. Riveted joints used in aircraft fuselage structures are susceptible to fretting due to the fatigue service loading and contact stress induced by riveting process itself. Black oxide debris observed on the faying surface around the rivet hole is said to be the evidence of fretting [8]. However there is no direct correlation between crack initiation and fretting. The basic parameters for crack initiation due to fretting in riveted joints are contact pressure, slip amplitude, and cyclic stress at rivet hole and faying surface [12].

Davies et al [30] carried out a survey of fatigue failures in helicopter components. Table 1.1 summarizes the crack initiation sites associated with the aluminum alloy components in helicopter bodies. From this table it can be seen that the majority of the failures are influenced by a stress concentration effect like hole, radii or corner. The main causes of fatigue crack initiation in relation to the failure location are summarized in Table 1.2.

Table 1.1 Main fatigue failure locations in aluminum alloy components of a helicopter [30]

Initiation Site	**Percentage**	
	All	**Fuselage Only**
Hole	34.4	52.9
Surface	30.9	28.1
Radii	19.5	11.6
Corner/Edge	7	6.6
Weld Interface	8.2	-

Table 1.2 Main causes of fatigue initiation in aluminum alloy components of a helicopter [30]

Primary Cause of Initiation	**Number of Failures**				
	Hole	**Radii**	**Surface**	**Corner/Edge**	**Weld**
Fretting/Wear	29	-	19	-	-
No Obvious Cause/ Not Specified	29	19	28	7	4
Manufacture/Assembly (Deburring of Holes, Poor Weld Quality, etc.)	18	16	13	5	15
Corrosion	7	3	7	1	-
Design Issues (Inadequate Stiffness)	5	7	2	1	2
Service (Mechanical Damage)	-	2	7	2	-
Material Defects (Porosity)	-	3	3	2	-

Harish and Farris [16] investigated the crack initiation phenomena due to fretting fatigue. Residual stress, plasticity and contact condition from riveting process were included in the finite element model. In order to predict the fatigue life to crack initiation, multiaxial fatigue model was utilized. Results were also validated by a set of controlled lap joint experiments. Also Szolwinski et al. [18] and Szolwinski and Farris [19] applied conventional multiaxial fatigue theories to fretting. They showed that predictions are in good agreement with the literature.

Iyer et al. [12] modeled a riveted lap joint by using the finite element method to obtain the factors that contribute to fretting fatigue crack initiation in riveted connections. These parameters are distributions of the contact pressure, the slip amplitude at the interface, the coefficient of friction, the tangential shear stress at the interface, the bulk cyclic tensile stress just under the contacting interface and parallel to it, and the number of fretting cycles. They defined two fretting parameters: Fretting wear parameter F_1 is directly related to the depth of the wear scar and F_2 is inversely related to the cyclic life.

1.2.2.2 SIF and Load Transfer Analysis

In order to characterize the stress state of the cracked riveted joints and fatigue life prediction, the stress intensity factors (SIF) solutions should be carried out. In studies on cracks in riveted joints, generally the rivet was assumed to be rigid pin and other plate was not included to eliminate both the residual stress due to rivet installation, out of bending of plates and complex contact condition at the contacting areas of plates. Results of these analyses are the stress intensity factor solutions for cracks emanating from the fastener holes. These results could be used to get a starting insight on cracks in riveted joints. Sometimes the analyses were carried out for riveted joint (two plates and a rivet) by ignoring residual stress state due to the riveting process, frictional contact conditions and plasticity of the plates and rivet. For these analyses generally the crack shapes were simplified as through cracks. Another important parameter in riveted lap joint is the load transfer of joint. Load transfer is the percentage of the applied load which is transferred from one plate to the other by means of the fasteners and friction [17].

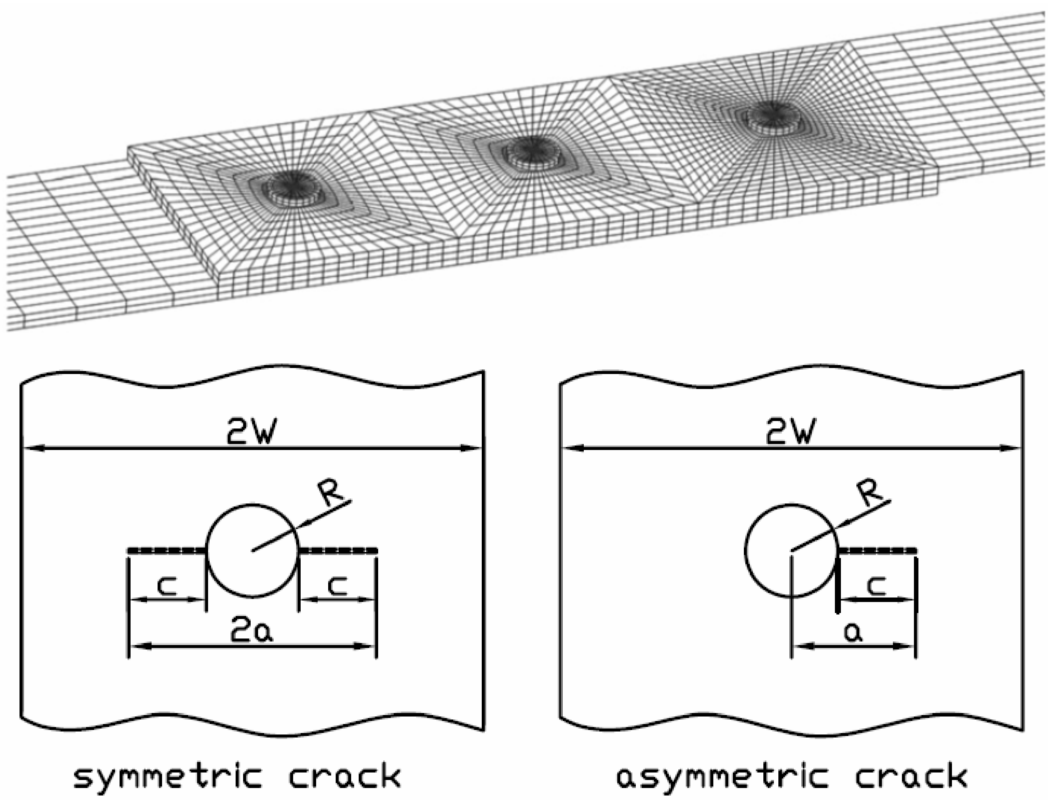

Figure 1.9 Finite element model of riveted joint and crack types analyzed [17]

Moreira et al. [17] carried out three dimensional FEA to analyze cracked riveted lap joints. Load transfer analysis of a single-lap splice with three rivets rows and one rivet column and stress intensity factor determination of cracks at the rivet hole were considered. One asymmetric and two symmetric through cracks emanating from the edge of the hole were modeled (Figure 1.9). The riveted joint was modeled with no interference (perfect fit joint). This means that the residual stress due to riveting process was ignored in this study. It was concluded that mode I SIF is dominant over mode II and mode III. They also concluded that for a given crack length and surface, SIF of the symmetrical crack always higher than that of an asymmetrical crack. On the subject of load transfer behavior, it was found that the first and the last rivets support the majority of the load.

Karasan [11] calculated stress intensity factors (SIF) via displacement correlation technique (DCT) for a through crack far from the rivet hole. Effect of joint clearance on SIF's was studied. Mode I stress intensity factors were calculated under the residual stress field. He concluded that SIF values increased with decreasing clearance. Then, external loading in the form of tensile stress was applied on the edges to calculate mode I SIF values. The geometry of the problem is shown in Figure 1.10.

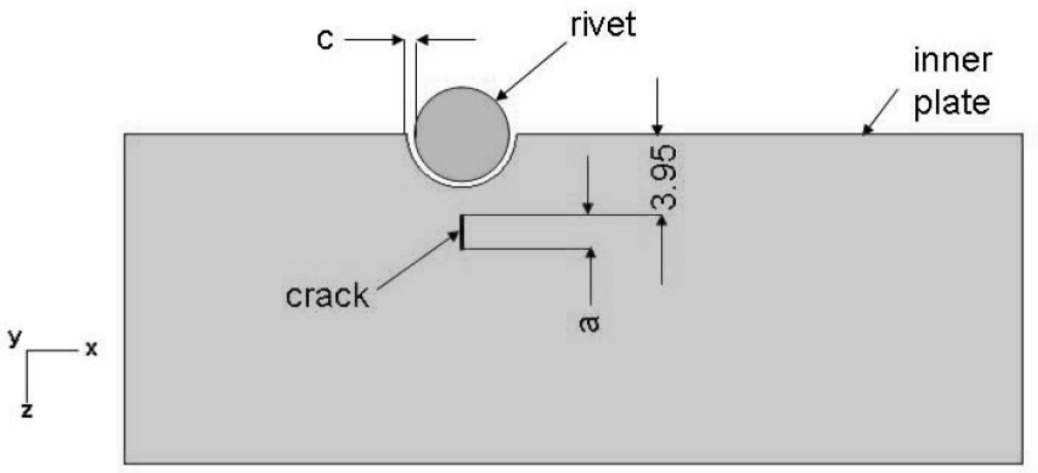

Figure 1.10 Through crack location in riveted joint [11]

Heo and Yang [23] evaluated the mixed-mode stress intensity factors at the surface and deepest points of quarter elliptical corner cracks in mechanical joints (Figure 1.11). They utilized weight function method. The mechanical joint (bolt or rivet), modeled as a pin, was assumed to be rigid without deformation. Then, a tensile external load was applied and the effects of the amount of clearance between the hole and the bolt or rivet on the stress intensity factors were investigated.

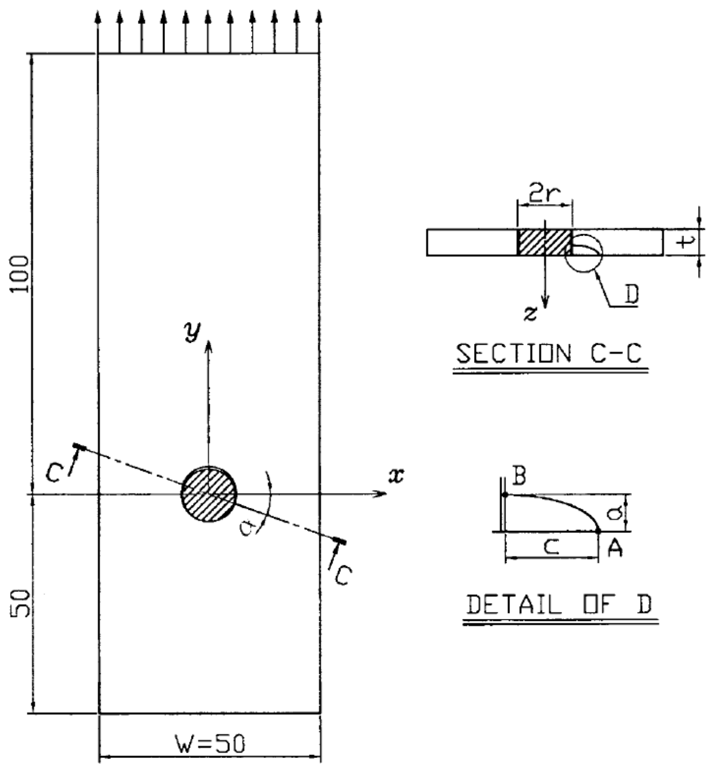

Figure 1.11 Configuration of a quarter elliptical corner crack in mechanical joint [23]

In another study, Lin and Smith [35] evaluated the stress intensity factors for two symmetric quarter elliptical corner cracks subjected to remote tension were evaluated by using both the quarter-point displacement and J-integral methods based on three-dimensional finite element analyses. Fawaz [36] analyzed the stress intensity factor solutions for through cracks with oblique fronts by using the finite-element method and a three-dimensional virtual crack closure technique. Various stress intensity factor solutions for part elliptical through cracks at a central hole under tension, bending and pin loading conditions.

1.2.2.3 Crack Growth and MSD Analysis

Multiple site damage (MSD) sometimes termed widespread fatigue damage (WFD) is an important problem associated with aging aircraft and began to be studied with Aloha accident in 1988 [20]. It is due to fatigue and it affects the service life of an aircraft. In MSD type failure, small fatigue cracks at different sites in the same structural elements grow and finally link up (join) forming large and more dangerous cracks. The crack growth rate is much faster for the case of MSD than the case of an individual crack. In order to investigate the multiple site damage effects Silva et al. [21] conducted experimental fatigue testing and damage characterization of riveted lap joints. Figure 1.12 illustrates the schematic and scanning electron micrographs showing the location of fatigue cracking, crack initiation site (arrows) and fracture morphology of fatigue cracks. Also Figure 1.13 show the schematic and scanning electron micrographs illustrating the sequence of crack propagation in the countersunk sheet.

To predict the onset of widespread fatigue damage in lap joints of fuselage structure Harris et al. [2] have developed a comprehensive analysis methodology based on an extensive experimental database assembled form detailed teardown examinations of fatigue cracks at rivet holes.

Ahmed et al. [22] investigated the MSD crack initiation, growth, and interaction in an initially undamaged curved fuselage panel containing a longitudinal lap joint. They observed that MSD cracks initiated from rivet holes in the lap joint area. Small cracks linked up and crack growth rates increased significantly. They concluded that the condition of the faying surface and the residual stresses from rivet clamping are two factors that affected subsurface crack growth behavior.

Liao et al. [24] predicted the fatigue life of fuselage splices which was measured as the number of cycles to visible cracks. The uncertainties in riveting, manufacturing, and material properties were simulated using a Monte Carlo simulation. In order to obtain the effects of the squeezing force and the coefficient of friction at the contact surfaces, they were taken as random variables. They concluded that the squeezing force has a stronger influence on the life distribution than the coefficient of friction. Also the scatter in the squeezing force and coefficient of friction has a stronger influence on the life distribution than that of material properties

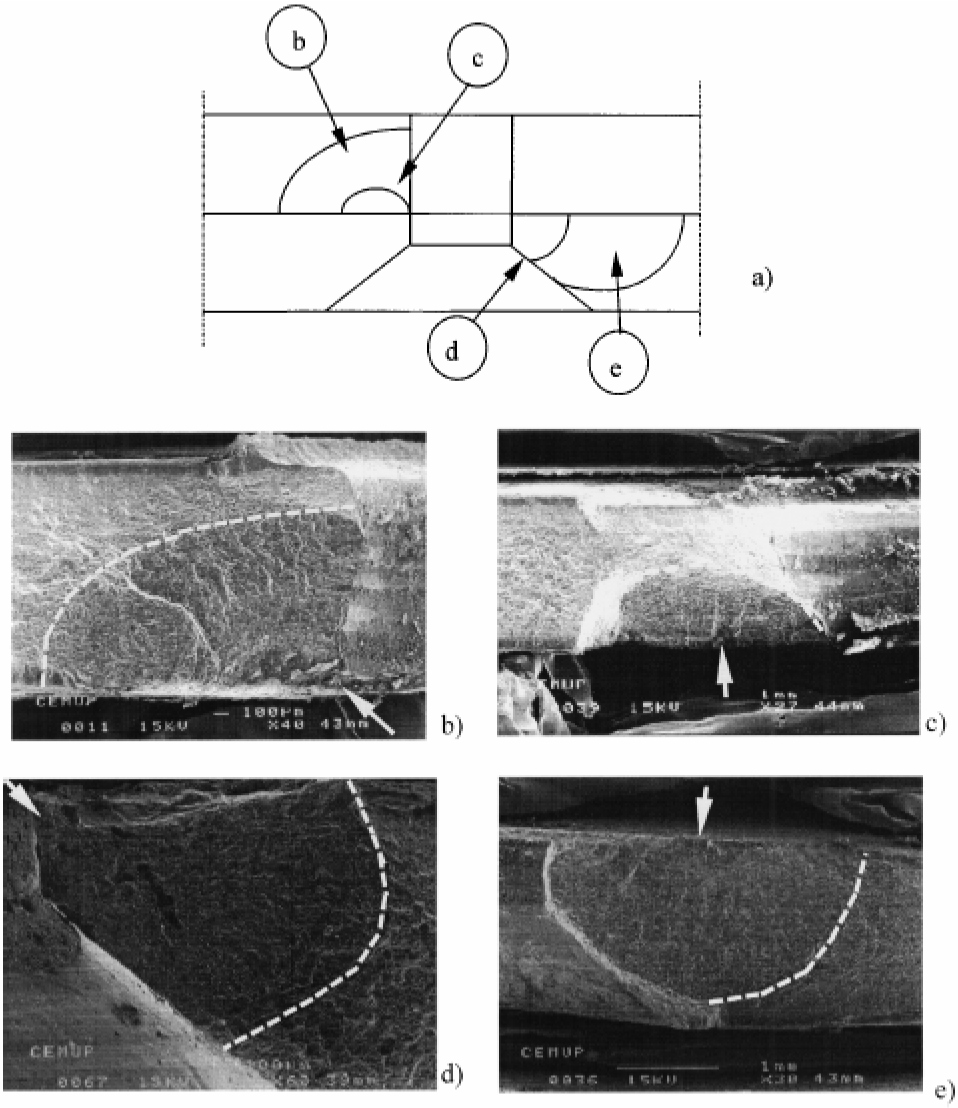

Figure 1.12 Schematic and scanning electron micrographs showing the location of fatigue cracking, crack initiation site (arrows) and fracture morphology of fatigue cracks [21].

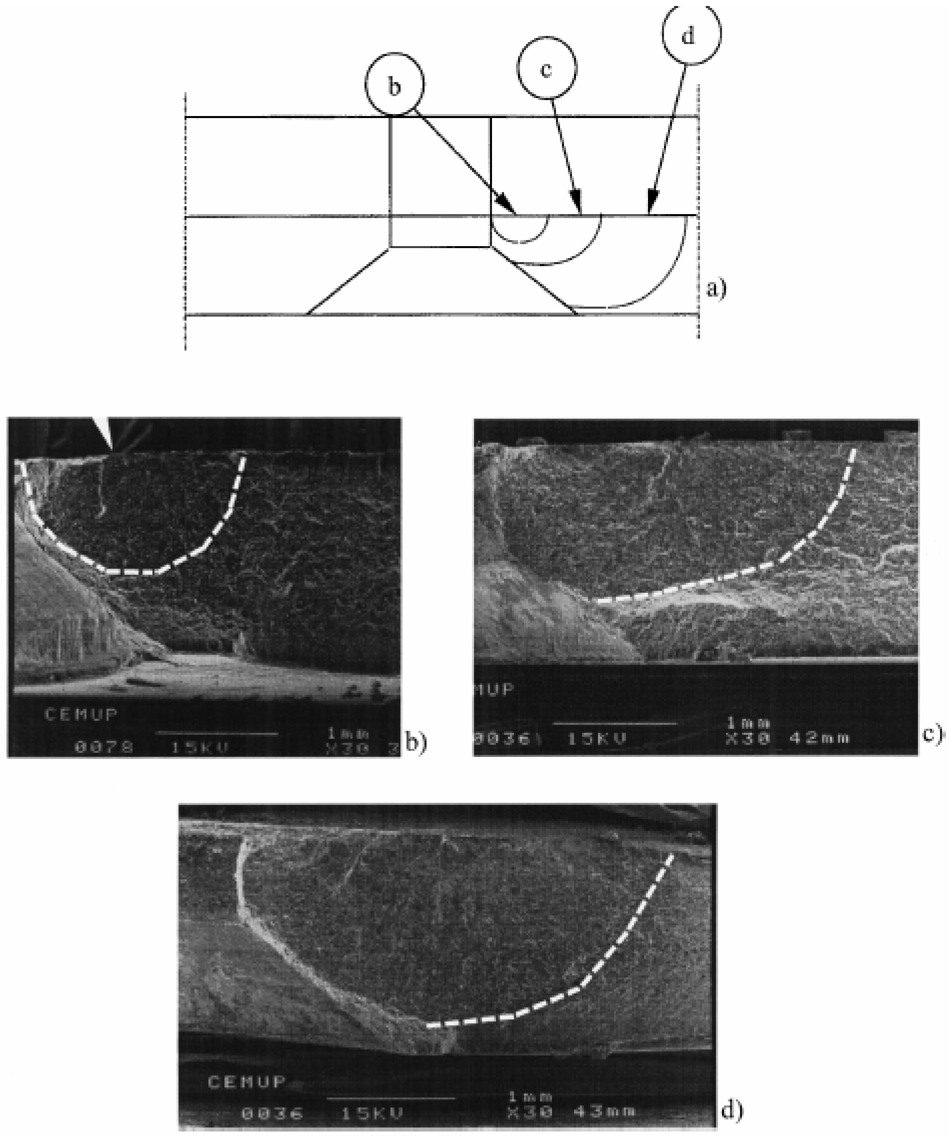

Figure 1.13 Schematic and scanning electron micrographs illustrating the location of fatigue crack initiation (arrows) and sequence of crack propagation in the countersunk sheet. [21].

Apicella et al. [25] carried out numerical analysis to evaluate the residual strength of a cracked lap joint. The author found SIF solutions by using Linear Elastic Fracture Mechanics. Also he investigated the unstable crack growth and crack link-up phenomena. Numerical results were compared with the experimental data to validate the numerical analysis.

Harris et al. [2] carried out crack growth analysis of a riveted joint due to fatigue loading. By using the results of fractographic examination of a rivet hole, they concluded that the main reasons for crack initiation are the local stress level, fretting, and manufacturing faults during rivet installation process. An example of cracks found in the panel of riveted joint is shown in Figure 1.14. A crack initiating due to high local stresses within the rivet hole is shown in Figure 1.14 (a). An example of a crack initiating due to fretting is shown in Figure 1.14 (b).

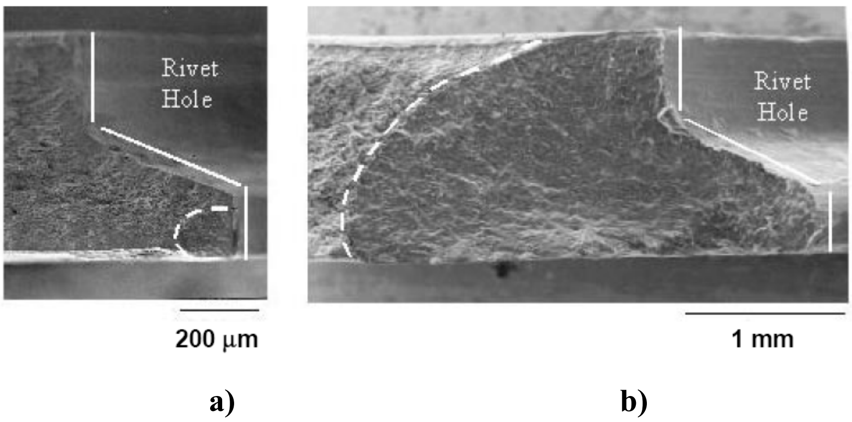

Figure 1.14 Crack initiations due to **a)** high local stress **b)** fretting fatigue (dashed line indicates crack front) [2]

1.3 Aim and Scope of This Study

The main objective of this study is to obtain three-dimensional stress field solutions in the panels of realistic riveted lap joints under both the residual stress field and external tensile loading. Also under the same loading conditions, the stress intensity factor (SIF) solutions have been obtained for semi elliptical surface crack at faying surfaces of plates and quarter elliptical corner crack at rivet hole.

The model considered in this thesis is the riveted lap joint with one rivet in row and one rivet in column geometric configuration which is a simplification of the complex joint in the real aircraft structure. In this type of joint, two plates are joined together by one rivet. The plates are fastened by solid rivet having universal head (Figure 1.15).

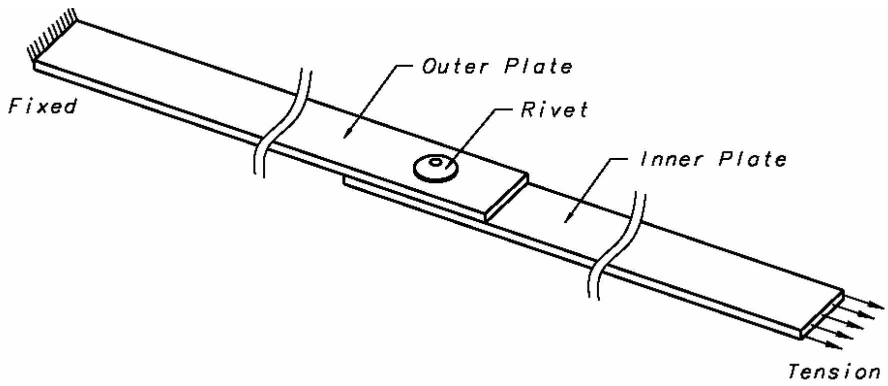

Figure 1.15 Schematic of single riveted lap joint

First of all, three-dimensional finite element models of riveted lap joints have been developed using the commercial finite element program ANSYS [31]. Nonlinearity arising from the interaction between the rivet and plates (contact) is included in the model. Two load steps are applied to the model. First the residual stresses due to the riveting process are obtained and then an external tensile load is applied to the deformed and residual stress loaded riveted joint.

Riveting process is simulated by a simplified method. Residual stress state due to the rivet installation process is obtained by interference and clamping misfit method. Radial stress due to rivet expansion (interference stress) is obtained by forcing radial conformity between the plate holes and initially oversized rivet shank. Clamping stress is generated by forcing the elongation of a rivet whose initial shank height is modeled slightly less than the combined depth of the two plates. Different values of misfit are modeled to capture the effects of riveting process parameters like squeezing force and clearance between hole and rivet shank on the residual stress state.

Before analyzing the cracks in riveted lap joints, a homogeneous plate with semi elliptical surface cracks subjected to uniform tension load is analyzed. By this, validity and accuracy of the computational method used to evaluate SIFs is demonstrated. A three dimensional finite element model containing a semi elliptical surface crack is generated using ANSYS. The crack tip singularity around the crack front is simulated with quarter point three dimensional finite elements. Displacement correlation technique (DCT) is used to extract the mode I stress intensity factors. Parametric modeling is carried out; therefore Ansys Parametric Design Language (APDL) [31] is used throughout the study. Calculated stress intensity factors are compared with those given by Newman and Raju [29] for various crack dimensions under tensile load.

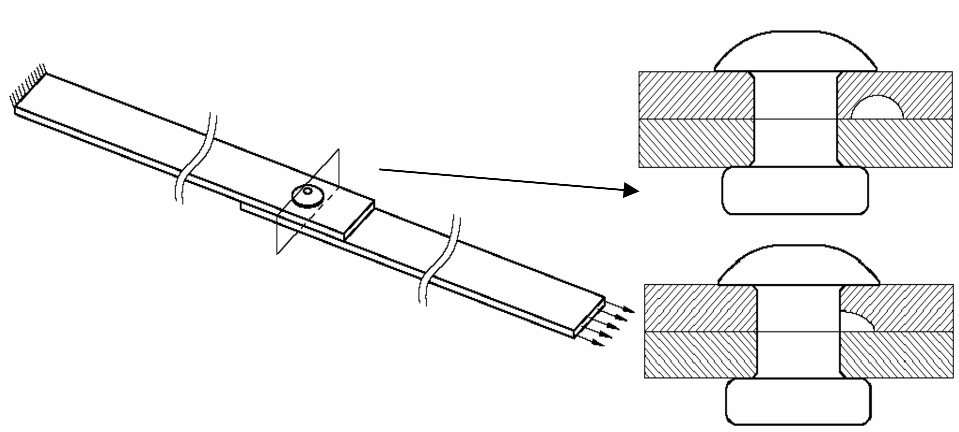

Figure 1.16 Crack locations and crack types analyzed

After developing the capability to carry out fracture mechanics analysis, cracks in riveted lap joints are examined. Semi elliptical surface crack at faying surfaces of plates and quarter elliptical corner crack at rivet hole are introduced (Figure 1.16). Crack planes are perpendicular to the tensile loading. The stress intensity factor (SIF) solutions for these two types of cracks are obtained by using displacement correlation technique (DCT). Effect of residual stress state obtained by using different interference and clamping misfit values and crack geometrical parameters on SIFs are studied.

Although it is well known that majority of the failures of aircraft are due to the cracks originating at and near the rivet hole, there are very few stress intensity factor solutions for these cracks in the literature. Stress intensity factor solutions in the literature have been obtained ignoring residual stress state due to riveting process and for simple thorough crack geometries. This study provides broad stress intensity factor solutions for semi elliptical surface and quarter elliptical corner cracks which are the most common crack types at riveted lap joints taking the residual stress into considerations. Also rivet tilting in the rivet hole and complex contact conditions are involved in the study. The stress intensity factor solutions obtained here could be useful for correlating fatigue crack growth rates. Also they can be used to compute fracture toughness of riveted joints which have surface cracks at the plate and the quarter elliptical cracks at the plate hole. These SIF solutions can also be utilized in multiple site damage (MSD) analysis in aircraft fuselage.

To sum up, this thesis is composed of six chapters. Introductory information, literature survey, and aim and scope of the study are given in the present chapter. Basic knowledge on fracture analysis, stress intensity factors and displacement correlation technique; geometry of the problem, boundary conditions, loading and material model are given in Chapter 2. The stress analysis of riveting process and analysis of riveted joint are presented in Chapter 3. Chapter 4 gives information about stress intensity factors calculations. Stress intensity factor solutions are obtained for cracked riveted lap joints can be found in Chapter 5. Finally, the concluding remarks are given in Chapter 6.

CHAPTER 2

PROBLEM DEFINITION

2.1 Fracture Analysis

The loss of load carrying capacity of a material is defined as mechanical failure. Fracture, thermal shock, wear, yielding, and corrosion are some of the mechanical failure modes. Fracture failure of the material is due to the defects in the form of porosities, cracks or voids in the material. Cracks are observed in many structures for several reasons. Usually cracks are introduced during the manufacturing stage, or later as a result of environmental and loading conditions. The structural integrity of a component is reduced significantly when it contains cracks. In order to analyze the relationship among stresses, cracks, and fracture strength, fracture mechanics is utilized.

Strength of materials approach for designing a component does not anticipate the elevated stress levels due to the existence of cracks. The presence of high stress level could result in catastrophic failure of the structure. The fracture mechanics approach is based on the initial existence of cracks. Crack size is one important variable, and fracture toughness replaces strength of material as a relevant material parameter [31].

Fracture analysis is typically carried out either using the energy criterion or the stress intensity factor criterion. When the energy criterion is used, the energy required for a unit extension of the crack (the energy release rate (G)) characterizes the fracture toughness. When the stress intensity factor criterion is used, the critical value of the amplitude of the stress and deformation fields characterizes the fracture toughness.

The propagation criterion is then given by the stress intensity factor reaching a critical value (K_c) representing the resistance to crack propagation. Therefore, the fracture criterion can be stated as:

$$K = K_c \text{ (at the onset of the fracture)} \tag{2.1}$$

K_c is called the critical stress intensity factor which is also known as the fracture toughness of the material at which the cracks begins to propagate. In other words, a crack propagates only if $K \geq K_c$. Similarly, crack will propagate when a critical energy release rate, G_c, is achieved; that is crack propagate when $G \geq G_c$. G_c is also known as the crack resistance energy.

Another parameter used in fracture mechanics analysis is the *J*-Integral. Stress intensity factors and energy release rates are limited to linear elastic fracture mechanics (LEFM). The *J*-Integral is applicable to both linear elastic and nonlinear elastic-plastic materials [31]. LEFM is valid for linear elastic material. The stress field near the crack tip is calculated using the theory of elasticity. A three-dimensional coordinate system and stress components for the region along the crack front are shown in Figure 2.1.

There are three basic modes of crack tip deformation (Figure 2.2):

- Mode 1: opening or tensile mode (the crack faces are pulled apart)
- Mode 2: sliding or in-plane shear (the crack surfaces slide over each other)
- Mode 3: tearing or anti-plane shear (the crack surfaces move parallel to the leading edge of the crack and relative to each other)

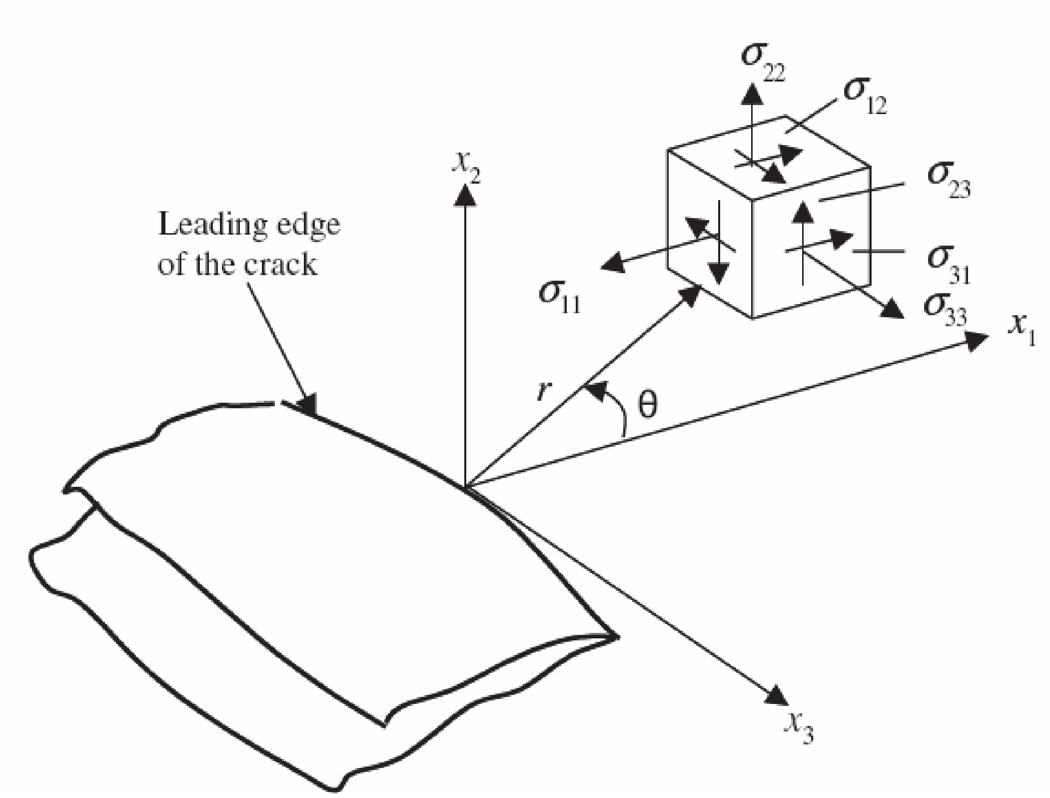

Figure 2.1 Three-dimensional coordinate system for the region along the crack front [32]

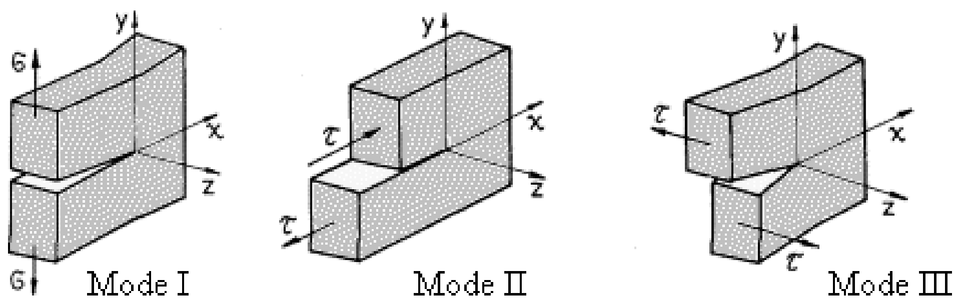

Figure 2.2 Schematic of the fracture modes

In engineering structures, loading is usually combination of two or three of modes which is known as mixed-mode loading.

2.2 Stress Intensity Factors (SIFs)

In the linear elastic fracture mechanics approach, the stress and strain fields near the crack tip are expressed by the help of stress intensity factor (SIF). The SIF is a function of material, loading, crack size, crack shape, and the geometric boundaries of the specimen. The stress intensity factor is defined for the Mode I, II and III loading types (Figure 2.2).

From equilibrium, compatibility and the linear elastic constitutive law, the stresses and displacements close to the crack tip (as shown in Figure 2.1) can be expressed by using stress intensity factors. The following expressions give the stress intensity factors [33].

The stresses in an element located at (r, θ) close to the crack tip (as shown in Figure 2.1) under mode I loading are expressed below.

$$\sigma_{11} = \frac{K_I}{\sqrt{2\pi r}} \cdot \cos\left(\frac{\theta}{2}\right) \cdot \left[1 - \sin\left(\frac{\theta}{2}\right) \cdot \sin\left(\frac{3\theta}{2}\right)\right] \tag{2.2}$$

$$\sigma_{22} = \frac{K_I}{\sqrt{2\pi r}} \cdot \cos\left(\frac{\theta}{2}\right) \cdot \left[1 + \sin\left(\frac{\theta}{2}\right) \cdot \sin\left(\frac{3\theta}{2}\right)\right] \tag{2.3}$$

$$\sigma_{33} = \begin{cases} 0, & \text{for plane stress} \\ \nu(\sigma_{11} + \sigma_{22}), & \text{for plane strain} \end{cases} \tag{2.4}$$

$$\sigma_{12} = \frac{K_I}{\sqrt{2\pi r}} \cdot \cos\left(\frac{\theta}{2}\right) \cdot \sin\left(\frac{\theta}{2}\right) \cdot \cos\left(\frac{3\theta}{2}\right) \tag{2.5}$$

$$\sigma_{23} = 0 \tag{2.6}$$

$$\sigma_{13} = 0 \tag{2.7}$$

The displacement field around the crack tip (Figure 2.1) under mode I loading is expressed as:

$$u_1 = \frac{K_I}{2\mu} \cdot \sqrt{\frac{r}{2\pi}} \cdot \cos\left(\frac{\theta}{2}\right) \cdot \left[\kappa - 1 + 2 \cdot \sin^2\left(\frac{\theta}{2}\right)\right] \tag{2.8}$$

$$u_2 = \frac{K_I}{2\mu} \cdot \sqrt{\frac{r}{2\pi}} \cdot \sin\left(\frac{\theta}{2}\right) \cdot \left[\kappa + 1 - 2 \cdot \cos^2\left(\frac{\theta}{2}\right)\right] \tag{2.9}$$

$$u_3 = 0 \tag{2.10}$$

where κ and μ are expressed as below:

$$\kappa = 3 - 4\nu, \qquad \mu = \frac{E}{2(1+\nu)} \tag{2.11}$$

The stress components under mode II loading are expressed as:

$$\sigma_{11} = -\frac{K_{II}}{\sqrt{2\pi r}} \cdot \sin\left(\frac{\theta}{2}\right) \cdot \left[2 + \cos\left(\frac{\theta}{2}\right) \cdot \cos\left(\frac{3\theta}{2}\right)\right] \tag{2.12}$$

$$\sigma_{22} = \frac{K_{II}}{\sqrt{2\pi r}} \cdot \sin\left(\frac{\theta}{2}\right) \cdot \cos\left(\frac{\theta}{2}\right) \cdot \cos\left(\frac{3\theta}{2}\right) \tag{2.13}$$

$$\sigma_{33} = \begin{cases} 0, & \text{for plane stress} \\ \nu(\sigma_{11} + \sigma_{22}), & \text{for plane strain} \end{cases} \tag{2.14}$$

$$\sigma_{12} = \frac{K_{II}}{\sqrt{2\pi r}} \cdot \cos\left(\frac{\theta}{2}\right) \cdot \left[1 - \sin\left(\frac{\theta}{2}\right) \cdot \sin\left(\frac{3\theta}{2}\right)\right] \tag{2.15}$$

$$\sigma_{23} = 0 \tag{2.16}$$

$$\sigma_{13} = 0 \tag{2.17}$$

The displacement components around the crack tip under mode II loading are expressed as:

$$u_1 = \frac{K_{II}}{2\mu} \cdot \sqrt{\frac{r}{2\pi}} \cdot \sin\left(\frac{\theta}{2}\right) \cdot \left[\kappa + 1 + 2 \cdot \cos^2\left(\frac{\theta}{2}\right)\right] \tag{2.18}$$

$$u_2 = -\frac{K_{II}}{2\mu} \cdot \sqrt{\frac{r}{2\pi}} \cdot \cos\left(\frac{\theta}{2}\right) \cdot \left[\kappa - 1 - 2 \cdot \sin^2\left(\frac{\theta}{2}\right)\right] \tag{2.19}$$

$$u_3 = 0 \tag{2.20}$$

The stress components under mode III loading are expressed as:

$$\sigma_{11} = 0 \tag{2.21}$$

$$\sigma_{22} = 0 \tag{2.22}$$

$$\sigma_{33} = 0 \tag{2.23}$$

$$\sigma_{12} = 0 \tag{2.24}$$

$$\sigma_{23} = \frac{K_{III}}{\sqrt{2\pi r}} \cdot \cos\left(\frac{\theta}{2}\right) \tag{2.25}$$

$$\sigma_{13} = -\frac{K_{III}}{\sqrt{2\pi r}} \cdot \sin\left(\frac{\theta}{2}\right) \tag{2.26}$$

Finally the displacement components around the crack tip under mode III loading are expressed as:

$$u_1 = 0 \tag{2.27}$$

$$u_2 = 0 \tag{2.28}$$

$$u_3 = \frac{K_{III}}{2\mu} \cdot \sqrt{\frac{r}{2\pi}} \cdot \sin\left(\frac{\theta}{2}\right) \tag{2.29}$$

2.3 Energy Release Rate (*G*)

Usually the energy release rate is utilized for fracture criteria under mixed mode loading condition. The energy release rate can be evaluated by using stress intensity factors. The relationship between stress intensity factors and energy release rate is expressed as:

for crack under mode I loading:

$$G_I = \frac{\kappa + 1}{8\mu} \cdot {K_I}^2 \tag{2.30}$$

for crack under mode II loading:

$$G_{II} = \frac{\kappa + 1}{8\mu} \cdot {K_{II}}^2 \tag{2.31}$$

for crack under mode III loading:

$$G_{III} = \frac{1}{2\mu} \cdot {K_{III}}^2 \tag{2.32}$$

where κ and μ are the elastic parameters expressed in equation (2.11). Substituting the values of κ and μ into equations (2.30), (2.31) and (2.32) gives:

$$G_I = \frac{(1-\nu^2)}{E} \cdot K_I{}^2 \tag{2.32}$$

$$G_{II} = \frac{(1-\nu^2)}{E} \cdot K_{II}{}^2 \tag{2.34}$$

$$G_{III} = \frac{(1+\nu)}{E} \cdot K_{III}{}^2 \tag{2.35}$$

The total energy release rate under mixed model loading is the sum of the energy release rates at each loading types. G at mixed mode loading is expressed as:

$$G = G_I + G_{II} + G_{III} = \frac{(1-\nu^2)}{E} \cdot \left[K_I{}^2 + K_{II}{}^2 + \frac{K_{III}{}^2}{1-\nu} \right] \tag{2.36}$$

2.4 Displacement Correlation Technique (DCT)

In three-dimensional crack problems as investigated in this thesis, the geometry and loading is too complex for the SIF to be solved analytically. The SIF is a function of the position along the crack front, crack size and shape, type of loading, and the geometry of the structure. Thus calculation gets further complicated.

Displacement correlation technique (DCT) is one of the most widely used methods to calculate modes I, II and III stress intensity factors for 2D and 3D cracks. In this method, the displacement values for certain nodes near the crack front are obtained by finite element analysis and these displacements values are used in expressions to find SIFs. Nodes used in the DCT for half and full crack models are shown in Figure 2.3.

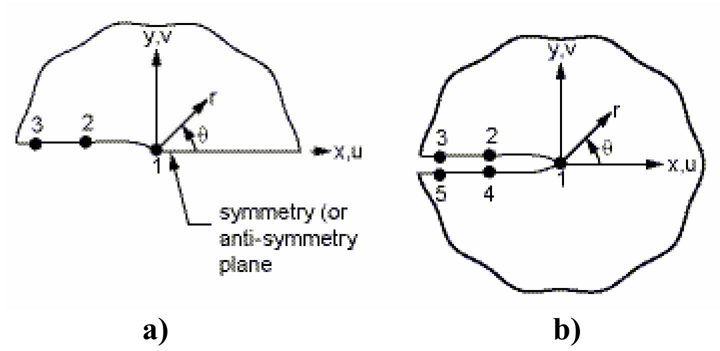

Figure 2.3 Typical crack face nodes used in DCT **a)** half-crack model and **b)** full-crack model [31]

In order to implement DCT for a three dimensional crack, a local coordinate system at the crack front should be defined. Figure 2.4 shows the crack front and the local coordinate system at a point P. The local coordinate system located at point P is composed of the tangential (t), normal (n) and binormal (b) directions and (r, θ) are the polar coordinates in the normal plane (n, b). The parameter s is the arc length of the crack front [33].

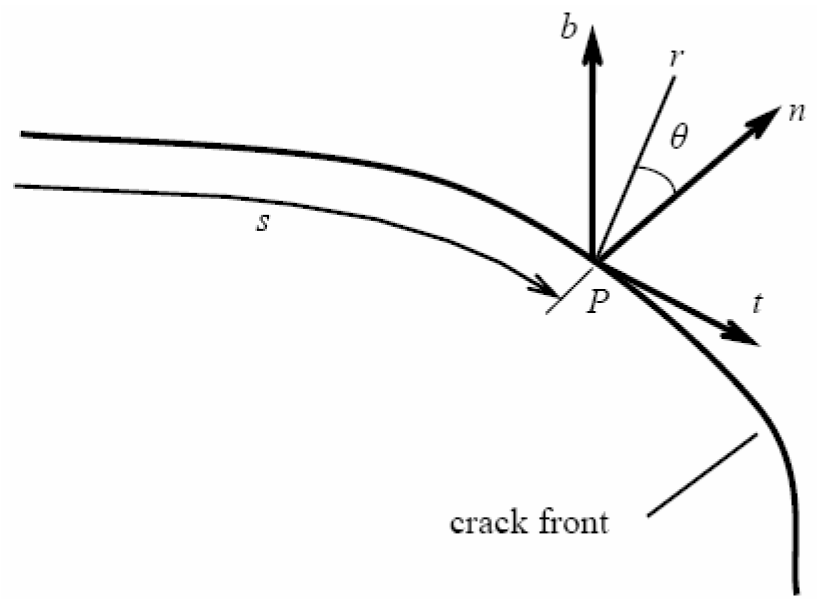

Figure 2.4 Crack front and the local coordinate system at a point *P* [33]

For a non-symmetrical crack (full crack) (Figure 2.5), the mode I, mode II and mode III stress intensity factors obtained using DCT are as follows [33]. SIFs are calculated using five nodes at the crack front.

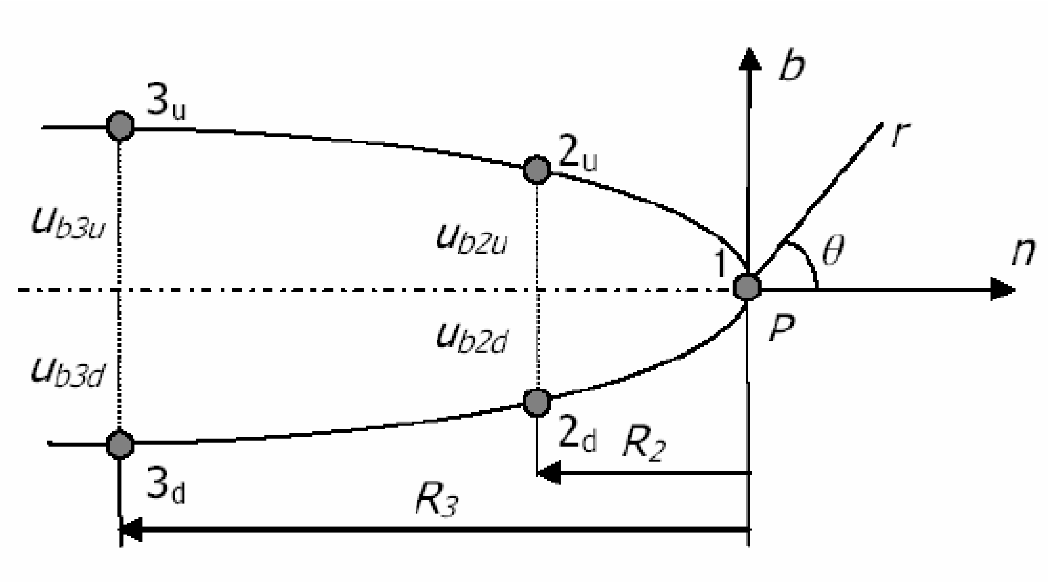

Figure 2.5 Deformed shape of a full crack surface [33]

$$K_I = \frac{\sqrt{2\pi} \times E}{8\left(1-\nu^2\right)} \times \left\{ \frac{R_2^{\frac{3}{2}} \times \left(U_{b2u} - U_{b2d}\right) - R_3^{\frac{3}{2}} \times \left(U_{b3u} - U_{b3d}\right)}{\sqrt{R_2} \times \sqrt{R_3} \times \left(R_3 - R_2\right)} \right\} \tag{2.37}$$

$$K_{II} = \frac{\sqrt{2\pi} \times E}{8\left(1-\nu^2\right)} \times \left\{ \frac{R_3^{\frac{3}{2}} \times \left(U_{n2u} - U_{n2d}\right) - R_2^{\frac{3}{2}} \times \left(U_{n3u} - U_{n3d}\right)}{\sqrt{R_2} \times \sqrt{R_3} \times \left(R_3 - R_2\right)} \right\} \tag{2.38}$$

$$K_{III} = \frac{\sqrt{2\pi} \times E}{8\left(1-\nu^2\right)} \times \left\{ \frac{R_3^{\frac{3}{2}} \times \left(U_{t2u} - U_{n2d}\right) - R_2^{\frac{3}{2}} \times \left(U_{t3u} - U_{t3d}\right)}{\sqrt{R_2} \times \sqrt{R_3} \times \left(R_3 - R_2\right)} \right\} \tag{2.39}$$

2.5 Geometry of the Problem

The structure under investigation is the riveted lap joint with one rivet in row and one rivet in column geometric configuration. The riveted joint consists of two plates fastened by one rivet. The specimen geometry and dimensions are presented in Figure 2.6 and the characteristics of the lap joint are summarized below:

- Specimen type: Lap splice with one rivet row and one rivet column;
- Plate length: 215 mm, 30 mm overlap;
- Plate thickness: 2 mm;
- Plate width: 15 mm (corresponding to an approximate rivet pitch of a fuselage);
- Rivet: MS20470 AD5-7 solid rivet with universal head having *4 mm* nominal diameter [29].

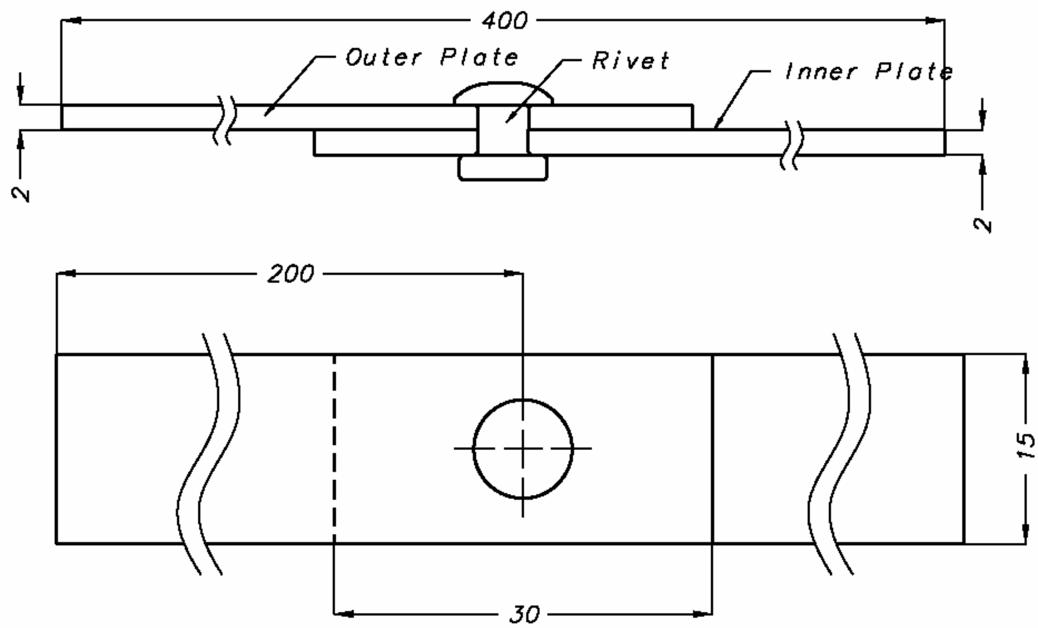

Figure 2.6 Geometry of the riveted lap joint

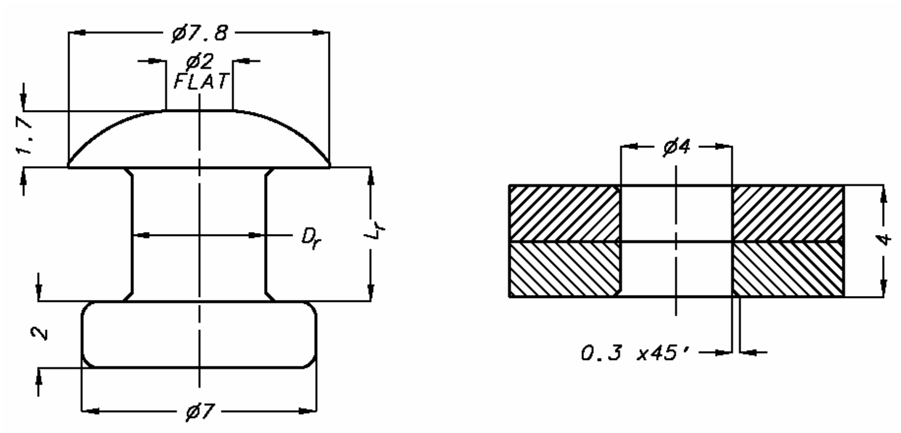

Figure 2.7 Geometries of deformed rivet and rivet hole on the plates

Solid rivet with universal head was employed to form the riveted lap joint. The deformed shapes of the rivet and the hole on the plates are shown in Figure 2.7. Rivet was modeled according the related military standard [29], and deformed head of the rivet is modeled with consistency to the reference [9]. Rivet shank diameter (D_r) and height (L_r) are taken as variables in order to simulate the different radial and height interference stress. *0%* radial and *0%* height interference corresponds to $D_r = 4$ mm and $L_r = 4$ mm, respectively.

For the fracture analysis, two types of cracks are introduced to the riveted lap joints: Quarter elliptical corner crack at rivet hole and semi elliptical surface crack at the faying surface of outer plate. Figure 2.8 illustrates the locations of the cracks at riveted lap joints. The crack plane is perpendicular to the axis of loading and it is shown in Figure 2.8. Locations of the semi elliptical surface crack and the quarter elliptical corner crack are shown in Figure 2.8 (b) and (c), respectively. The schematics of the crack front can be seen at Figure 2.9. The semi elliptical surface crack, which is located at the faying surface of the outer plate, has a length of *2c* and a depth of *a*. The crack is shifted from the center of the rivet hole by an amount of *e* ($e = c + 2.5$). The quarter elliptical corner crack located at the rivet hole edge has a length of *c* and a depth of *a*. For both cracks, a point *P* on the crack front is located by the parametric angle ϕ. Definitions of the locations of point P for both *a/c<1* and *a/c>1* are shown in the figure. In this figure, *t* is the thickness of the outer plate and D_h is the hole diameter.

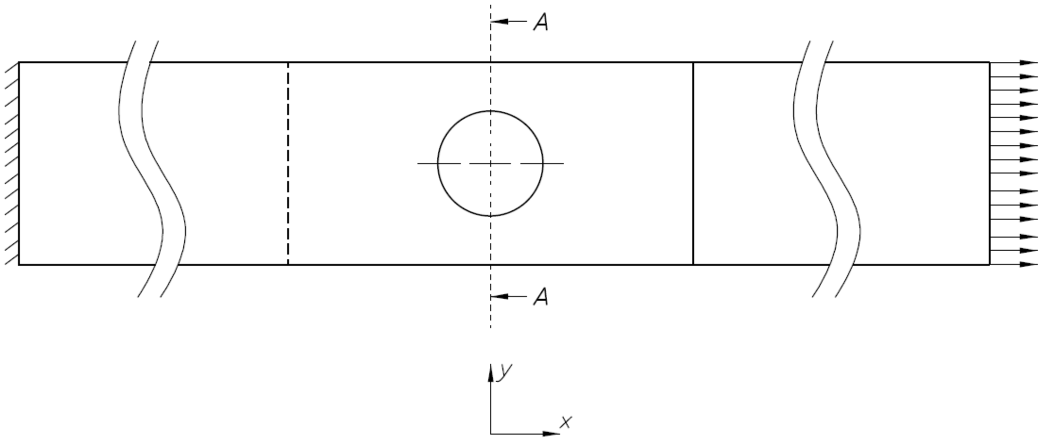

a)

SECTION A-A

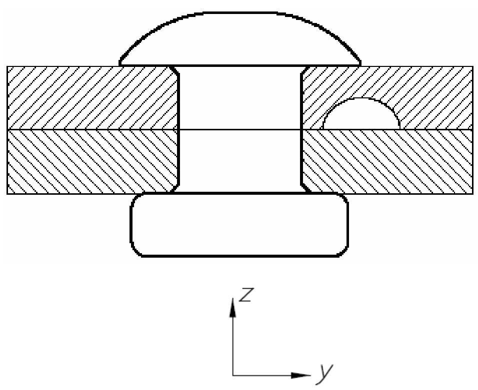

b)

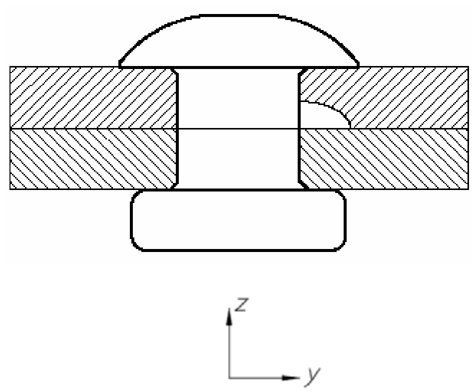

c)

Figure 2.8 Locations of the cracks at riveted lap joints **a)** Crack plane **b)** Semi elliptical surface crack **c)** Quarter elliptical corner crack

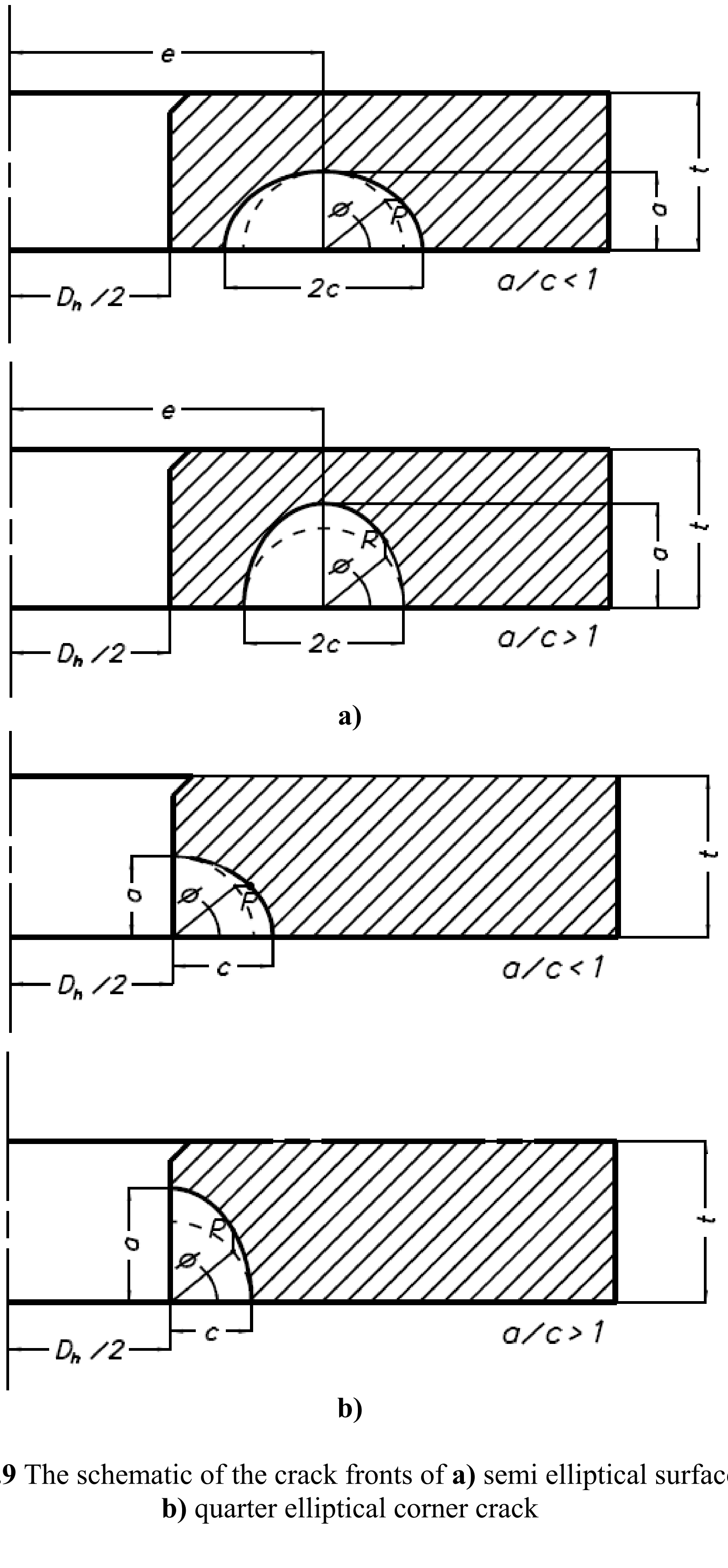

Figure 2.9 The schematic of the crack fronts of **a)** semi elliptical surface crack **b)** quarter elliptical corner crack

2.6 Boundary Conditions

Figure 2.10 demonstrates a typical aircraft skin fastened by rivets. Single shear riveted lap joint is a simplification of the complicated lap joint in the real aircraft structure. As shown in the figure, actual fastened skin consists of series of single riveted lap joints. Therefore it is sufficient to analyze single riveted lap joint with appropriate boundary conditions.

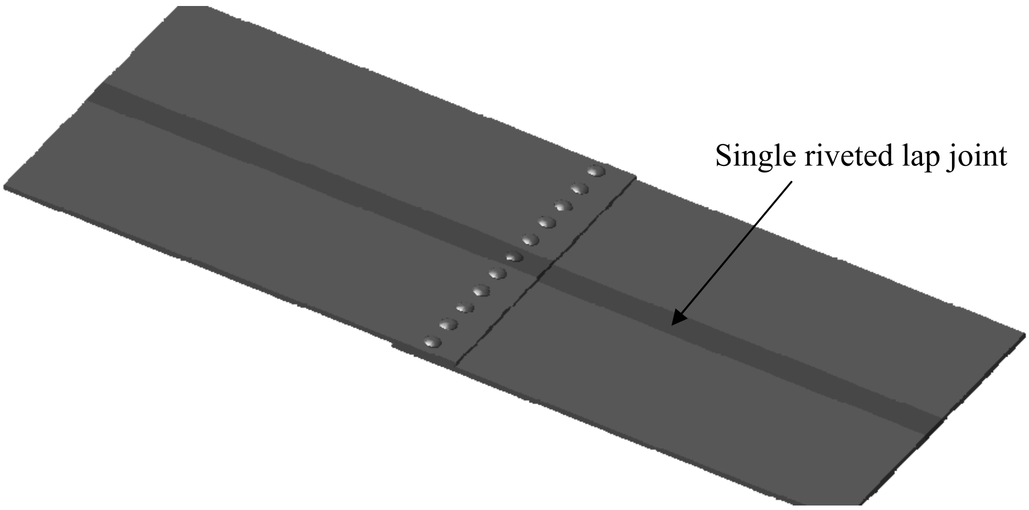

Figure 2.10 Typical aircraft skin fastened by rivets

General sight of the boundary conditions for the lap joint is shown in Figure 2.11. The multi-rivet symmetry condition comes from the fact that single lap joint is a part of the multiple riveted lap joint. There are two load steps applied to the model. First is the riveting simulation. In this load step all boundary conditions are applied except the external loading. In the second load step, an external tensile load of 68.6 MPa is applied to the model at the loading plane. The tensile loading is applied since the riveted joint is in the longitudinal tension resulting from the pressurization of the fuselage. Magnitude of the tensile stress is taken from tests conducted by Hartman to study the fatigue behavior of simple riveted lap joints with straight-shank rivets under laboratory air and room temperature conditions for constant and variable amplitude loading [2].

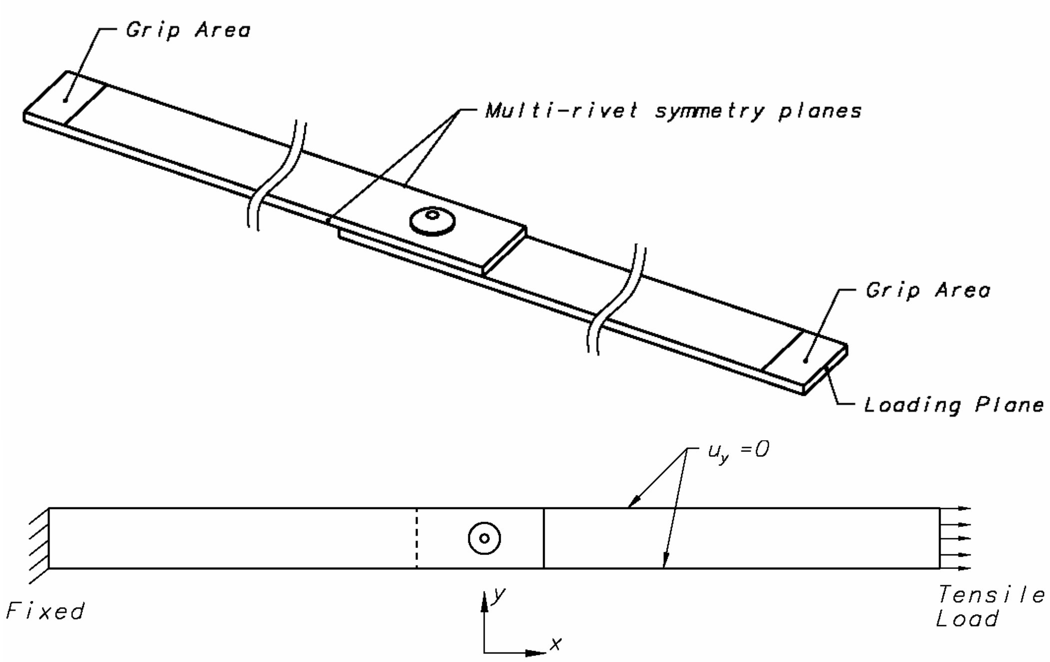

Figure 2.11 General sight of the boundary conditions

2.7 Material

Mechanical properties of the plates and rivet are required for the finite element models. These properties involve the elastic behaviors of the materials of interest (sheet metal plate and rivet). There is little information on the material properties of plate and rivet material in the literature. In the literature, mechanical properties are obtained by applying certain tests like uniaxal tensile, and micro tensile test. Mechanical properties of the specimen under investigation are taken from the literature.

Aluminum alloy 2024-T3 for two plates and 2117-T4 for rivet are used. They are common materials used in aircraft fuselage [1, 7, 8, 9, 11, 17, 21, and 28]. The material properties used for plates and rivet are as tabulated in Table 2.1.

Table 2.1 Material properties used for the analysis [9], [28]

Material		Young's Modulus	Poisson’s ratio
Plates	2024-T3	74 GPa	0.33
Rivets	2117-T4	71.7 GPa	0.33

CHAPTER 3

STRESS ANALYSIS OF RIVETED LAP JOINT

3.1 Introduction

The fatigue life of riveted lap joints depends mainly on the material condition, rivet installation process, and external loading applied on them. Riveting process results in a residual stress state on the riveted joints. Also the external loads give a complex stress state to the joint. Therefore determination of the stress state of the joint is essential. Also it is important to investigate the effects of rivet installation parameters on the stress state of the joint.

In this chapter, three-dimensional stress field solutions are obtained in the outer plate of riveted lap joint with one rivet in row and one rivet in column geometric configuration under both the residual stress field and external tensile loading. Three-dimensional finite element models of riveted lap joints have been developed using a commercial finite element program ANSYS. Nonlinearity arising from the interaction (frictional contact condition) between the rivet and plates was incorporated in the model.

The local stress state in a riveted lap joint is very complex due to the residual stress (clamping stress applied by rivet heads and radial pressure applied by rivet expansion) resulting from rivet installation process, surface shear within the contacting zone due to load transfer through friction, pin loading at hole due to load transfer through rivet shear, secondary bending effects of the joint, and biaxial tension in plates due to the applied tensile load. Accurate determination of the local stress distribution is necessary to analyze fatigue damage in fuselage splices.

In order to capture the effects of rivet installation process variables on the stress state, different interference and clamping misfit values were utilized. The analysis is divided into two stages. First, rivet installation is simulated by interference misfit method. Afterwards, application of an external tensile load to the joint is simulated to obtain the full three-dimensional stress state. After obtaining stress states for both the riveting process and tensile loading, effects of riveting process parameters on the stress components are explored.

The definition of angular locations and depth at which stress components are characterized for the joint model is illustrated in Figure 3.1. Since tangential and radial stresses around the rivet hole will be explored, cylindrical coordinate system as well as Cartesian coordinate system is defined as shown in this figure. (x,y,z) components in Cartesian coordinate system corresponds to the (r,θ,z) components in cylindrical coordinate system. With the help of the Cartesian and cylindrical coordinate systems defined in Figure 3.1, the mathematical expressions of radial, tangential and axial stress components correspond to σ_{rr} , $\sigma_{\theta\theta}$ and σ_{zz} , respectively.

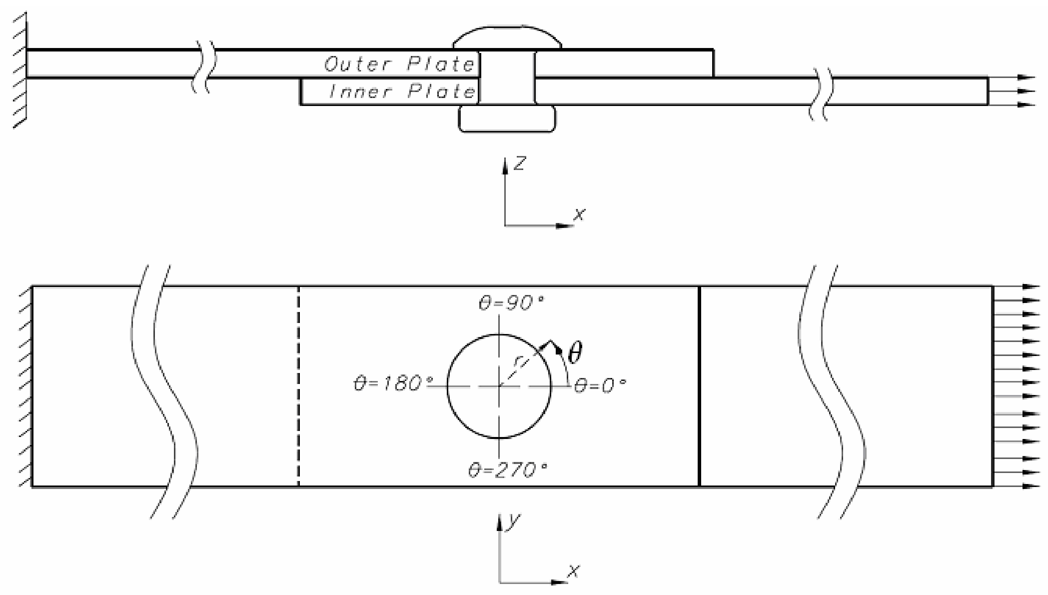

a)

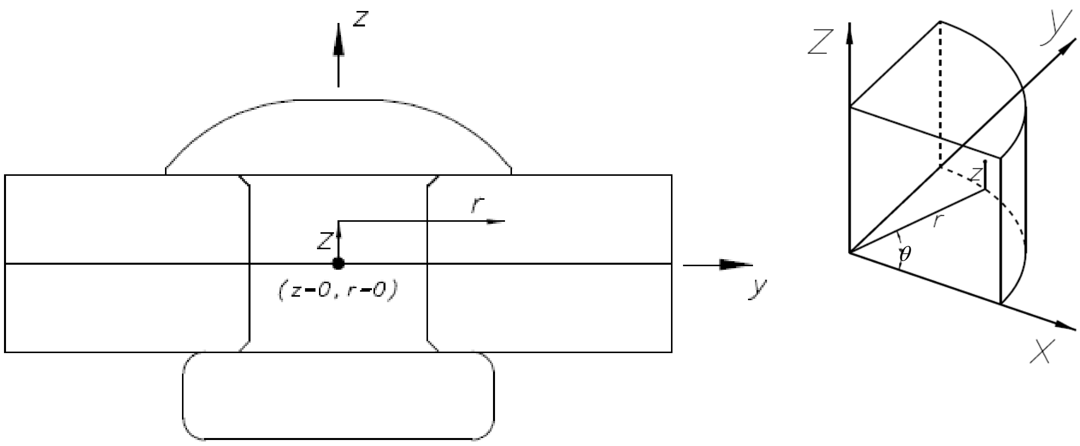

b) **c)**

Figure 3.1 Definition of locations for the joint model **a)** Riveted joint with Cartesian and cylindrical coordinate systems, **b)** Plane perpendicular to the loading, **c)** Cartesian and corresponding cylindrical coordinate systems

3.2 The Finite Element Modeling of Riveted Lap Joint

The finite element method (FEM) sometimes referred to as finite element analysis (FEA) is a powerful numerical technique for finding approximate solutions of complex problems in structural mechanics. Meshing is a vital step of the finite element method. Choosing appropriate element type and size is a trade off between accuracy and time required for the analysis. Therefore element types are selected accordingly and local mesh refinement was applied at locations where they are necessary.

Three dimensional finite element model of the single riveted lap joint is prepared by using ANSYS. The geometry, boundary conditions, and material properties of the model are explained in chapter 2.5, 2.6, and 2.7, respectively.

Three dimensional 20 node structural solid elements (SOLID186) are used for creating the model; and three dimensional 8 node surface-to-surface contact

(CONTA174) and three dimensional target segment (TARGE170) elements are internally generated for modeling the surface-to-surface contact. SOLID186 is a higher order 3-D 20-node solid element that exhibits quadratic displacement behavior. The element is defined by 20 nodes having three degrees of freedom per node: translations in the nodal x, y, and z directions. The element supports plasticity, hyperelasticity, creep, stress stiffening, large deflection, and large strain capabilities. CONTA174 is used to represent contact and sliding between 3-D target surfaces (TARGE170) and a deformable surface. This element is located on the surfaces of 3-D solid elements (here SOLID186) with midside nodes. It has the same geometric characteristics as the solid element face with which it is connected. Contact occurs when the element surface penetrates one of the target segment elements (TARGE170) on a specified target surface. Coulomb and shear stress friction is allowed. TARGE170 is used to represent various 3-D target surfaces for the associated contact elements (CONTA174). The contact elements themselves overlay the solid, shell, or line elements describing the boundary of a deformable body and are potentially in contact with the target surface. This target surface is discretized by a set of target segment elements (TARGE170) and is paired with its associated contact surface via a shared real constant set [31]. Different views of finite element model of riveted joint and mesh densities are illustrated in Figure 3.2.

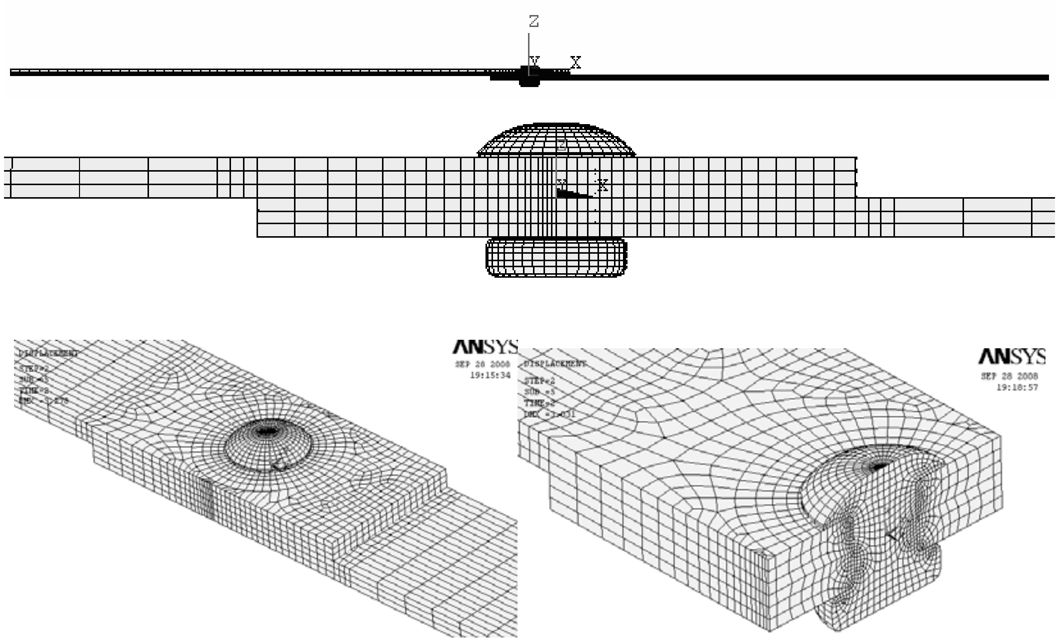

Figure 3.2 Finite element model of riveted lap joint

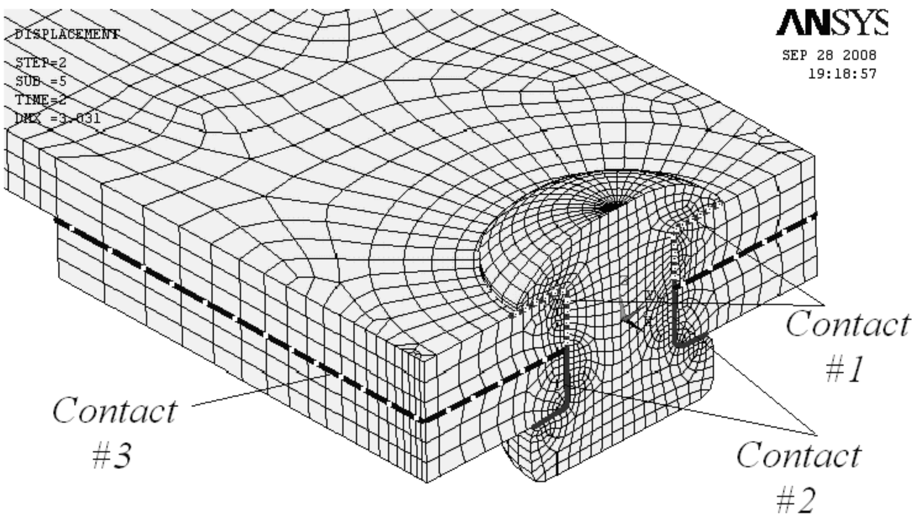

Figure 3.3 Contact surface definitions

Three surface to surface contacts are defined at rivet-upper plate, rivet-lower plate and upper plate-lower plate interactions (Figure 3.3). Coulomb friction model with a coefficient of friction of 0.2 is specified for all surface interactions.

Augmented Lagrange method was selected as the contact algorithm in ANSYS. This method is basically the penalty method with additional penetration control.

The procedure of finite element modeling applied in this study can be summarized as follows: First, key points are created then lines, areas and volumes are generated in the given order. At this point the solid model of the geometry is obtained. Then the meshes are created by appropriate elements; and material properties are introduced to the model. Finally boundary conditions and external loading are applied to the model to find the desired results.

Table 3.1 The finite element models for stress analysis

FE Models	% Shank Radial Interference	% Shank Height Interference (Clamping)
	%D	*%L*
1	0.00	0.00
2	0.00	0.15
3	0.00	0.30
4	0.00	0.50
5	0.15	0.00
6	0.15	0.15
7	0.15	0.30
8	0.15	0.50
9	0.30	0.00
10	0.30	0.15
11	0.30	0.30
12	0.30	0.50
13	0.50	0.00
14	0.50	0.15
15	0.50	0.30
16	0.50	0.50

Sixteen different finite element models were prepared to examine the effect of interference and clamping which are two important rivet installation parameters. Table 3.1 shows the finite element models and corresponding percent shank radial and height interference values. Definitions of the radial and height interference are given in part 3.3.

Actual riveting process (Figure 3.4.a) results in large-scale plastic material flow, especially for the rivet. The formation of the protruding end of the rivet due to the squeezing force and expansion of the rivet shank in the rivet hole with a clearance are two causes of high plastic deformation. However, in case of the rivet simulation by the interference misfit method (Figure 3.4.b), protruding end of the rivet is already modeled. The only source for deformation of rivet and plates is the radial and height interference (diametric and height misfit between the rivet shank and the rivet hole) in this method. Therefore it is advantageous to check the plastic deformation situation of the riveted joint for this simplified method. Because plastic deformation in other words plasticity introduces nonlinearity and nonlinear analysis is known to be time consuming. Therefore it is beneficial to eliminate unneeded nonlinearities in finite element method whenever it is possible. First, riveting simulation and stress analysis under external loading are carried out with plastic material models for both the rivet and the plates. Results of these analysis showed that there was no plastic deformation on both the rivet and the plates during riveting simulation. Upon applying external tensile load, local plastic deformation was observed on small region on the rivet and the plates especially near the rivet hole face. However in order to utilize linear elastic fracture mechanics approach for calculation of the fracture parameters, materials should undergo only elastic deformation. Therefore local plastic deformation is ignored and elastic material model is utilized for all the analysis.

3.3 Simulation and Residual Stress Analysis of Riveting Process

As previously stated, the finite element analysis of the riveted joint was divided into two separate stages. The first stage is the simulation of the rivet installation process to introduce residual stresses to the lap joint. Actual rivet installation is a forming process which generates radial interference and vertical clamping concurrently. It is not the aim of this study to simulate the installation process itself but rather investigate the effects of interference and clamping on residual stress as separate rivet installation parameters.

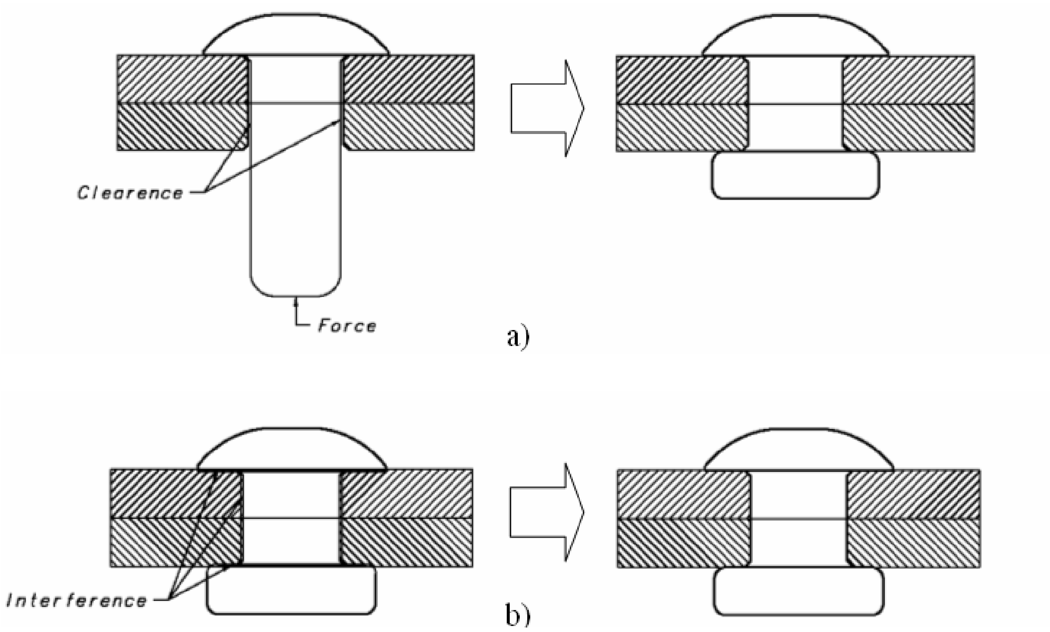

Figure 3.4 Representation of riveting process: **a)** Actual riveting process, **b)** Riveting simulation by interference misfit method

In actual riveting process, a rivet is installed in a pre-drilled hole and an axial compressive force is applied to the end of the rivet to obtain the final deformed shape (Figure 3.4.a). By this operation complex state of residual stresses develops in the rivet and surrounding plate material. Radial expansion of the rivet results in radial stress and clamping effect of two heads of the rivet on the two plates results in axial stress. The deformation of the rivet is constrained by the rivet hole. Then it is possible to obtain these radial and axial stresses by diametric and height misfit between rivet shank and rivet hole, respectively. Thus, riveting process is simulated by interference misfit method (Figure 3.4.b).

In interference misfit method, radial stress due to rivet expansion in rivet installation process is obtained by forcing radial conformity between the plate holes and initially oversized modeled rivet shank. Axial stress due to clamping effect of two rivet heads on the plates in rivet installation process is generated by forcing the elongation of a rivet whose initial shank height is modeled slightly less than the combined depth of the two plates. In other words, rivet diameter (D_r) is modeled larger than the hole diameter (D_h) and rivet shank height (L_r) is modeled smaller than the combined depth of the two plates (L_h) to obtain residual stress state (Figure 3.5). The radial and height interference misfit values are calculated by equations (3.1) and (3.2), respectively. Sixteen different models (Table 3.1) are created by employing different misfit values for both radial and height interference to capture the effects of riveting process parameters like squeezing force and clearance between hole and rivet shank on the residual stress state.

$$\%D = \frac{|D_h - D_r|}{D_h} \cdot 100 \tag{3.1}$$

$$\%L = \frac{|L_h - L_r|}{L_h} \cdot 100 \tag{3.2}$$

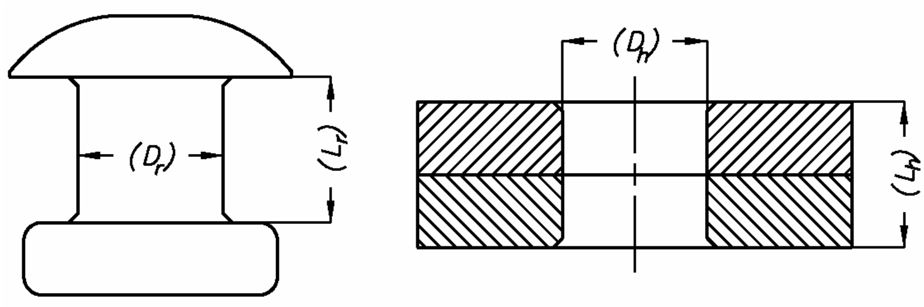

$D_r \geq D_h$ and $L_r \leq L_h$

Figure 3.5 Schematic of interference misfit method

3.4 Stress Analysis of the Riveted Joint

In the second stage of the finite element analysis, an external tensile load is applied on the lap joint model. From the final time step of the rivet installation step phase, a tensile load was applied to the free end of the lap joint as shown in Figure 3.6. The obtained stress state in this stage contains both effect of the residual stress due to the riveting simulation and stress due to the external tension load. A tensile load of 68.6 MPa was simulated and quasi-static assumptions were applied.

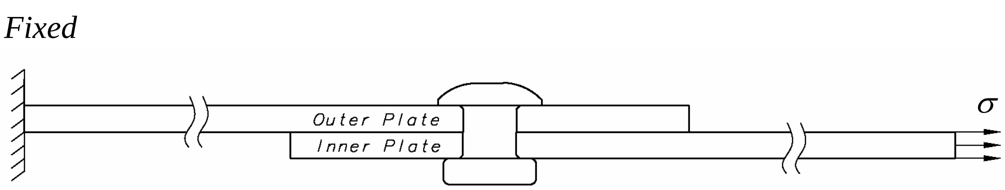

Figure 3.6 Tensile loading on riveted lap joint

3.5 Model Validation

In order to validate the riveting simulation, generally the final diameter and the height of the rivet driven head obtained by the numerical simulation are compared with those found by experimentally. In this study riveting simulation is carried out by a simplified method in which rivet driven head is already modeled. Therefore it is not possible apply this validation method. Instead, for the validation of the present three dimensional models, riveting process and external loading of the riveted lap joint were carried out by using different mesh densities. A convergence check study was carried out by altering the overall mesh density of the numerical model. Results of the models with different mesh densities were compared and checked to determine whether the results are convergent.

For the convergence check study, the model was meshed using coarse, medium, fine and very fine mesh densities. Close up views of these mesh densities are shown in Figure 3.7. The number of elements and corresponding CPU times for the analysis (for hp xw4200 workstation) are tabulated in Table 3.2. As shown in the table, analysis time is very dependent on the number of elements and it dramatically increases with increasing the number of elements.

In a convergence check study, generally a chosen stress value at a specified point is compared for different mesh densities. Then stress values versus number of elements graph is plotted to see whether the value is converging a single value or not. One step forward, stress values are compared along a path, not a point, in this study. By this, more accurate analysis could be carried out since the point result may be misleading.

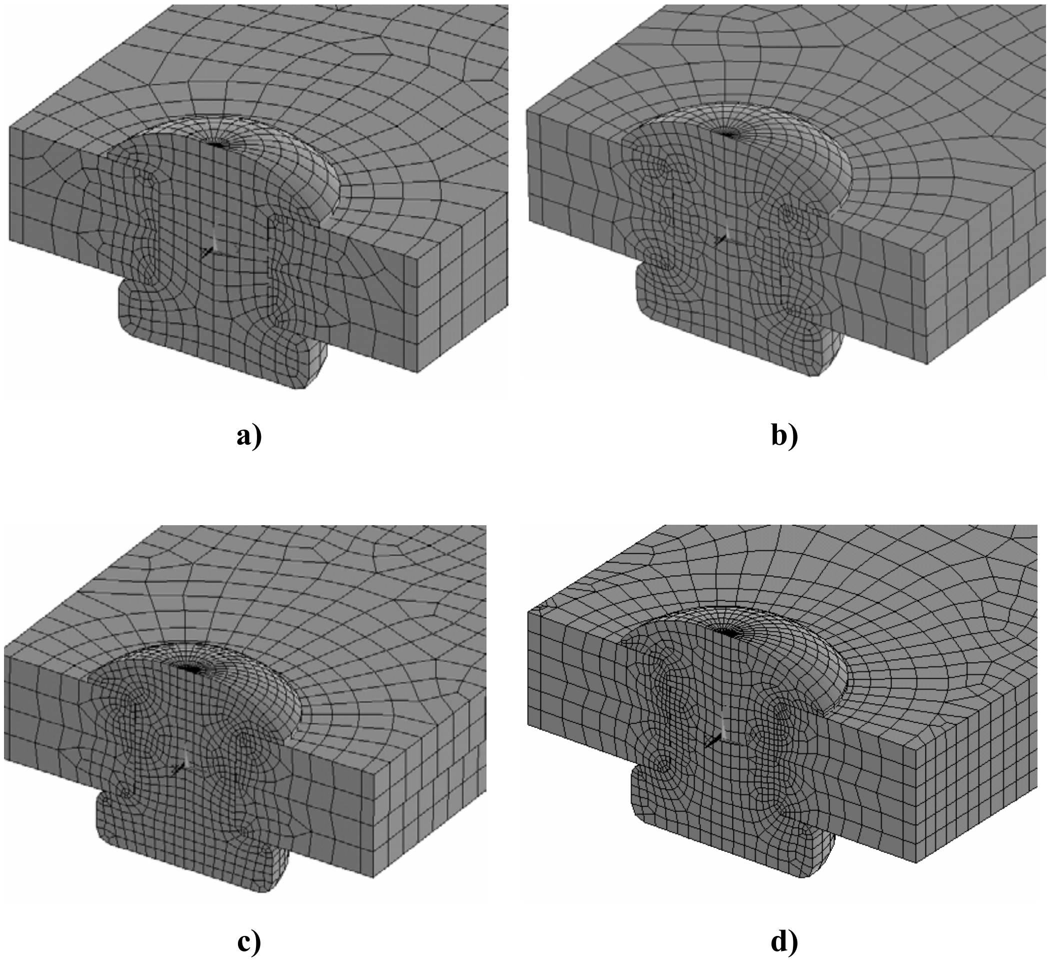

Figure 3.7 Close up views of different mesh densities **a)** coarse mesh **b)** medium mesh **c)** fine mesh **d)** very fine mesh

Table 3.2 The number of elements and CPU times for the analysis for different mesh densities

Mesh densities	Number of elements	CPU time for the analysis
Coarse mesh	12920	2241.4
Medium mesh	17558	4971.6
Fine mesh	24747	17783.3
Very fine mesh	31702	52120.0

For the model validation analysis, the last case in Table 3.1 (*%D=0.50, %L=0.50)* is selected. This is the model in which the rivet and the plates undergo the highest degree of deformation during the riveting simulation among the others. Equivalent stress values along two circular paths around the rivet hole (r=2.5; z=1 and r=2.6; z=0) are compared for four different mesh densities. All comparisons were carried out for both riveting simulation and external loading conditions. Figures 3.8-3.11 show the results.

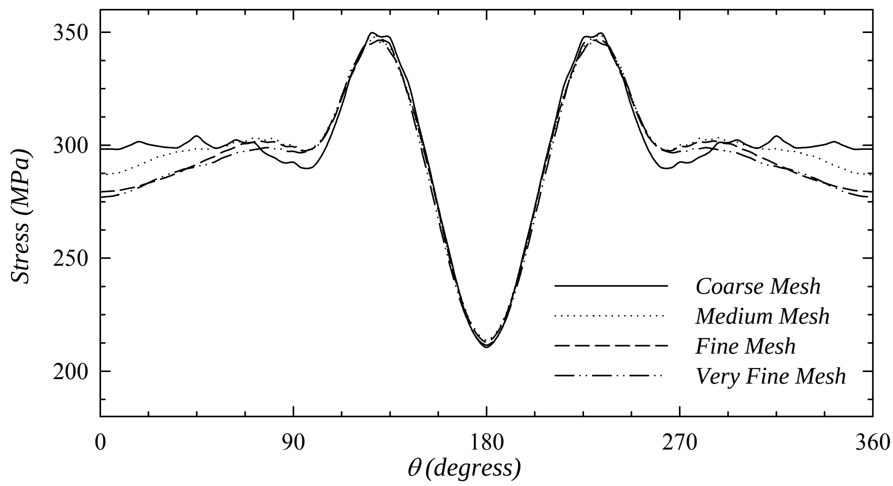

Figure 3.8 Equivalent stress under tensile loading along circular path r=2.6 z=0

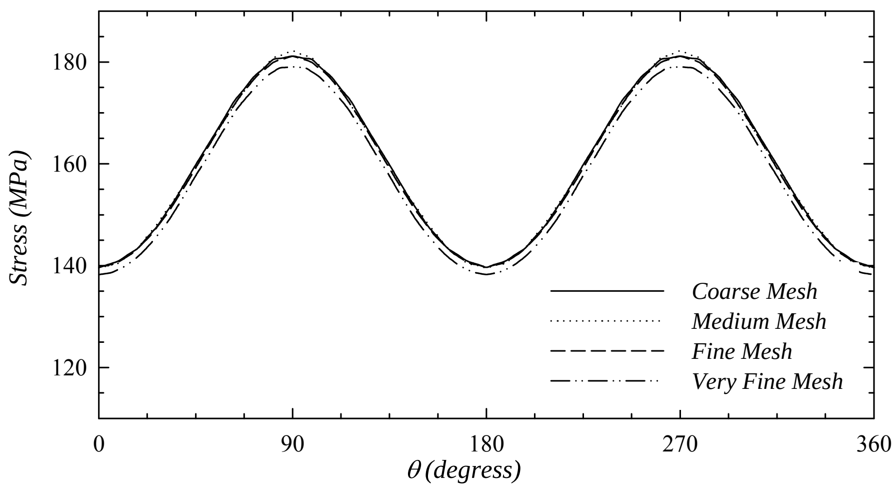

Figure 3.9 Equivalent stress under riveting loading along circular path r=2.6 z=0

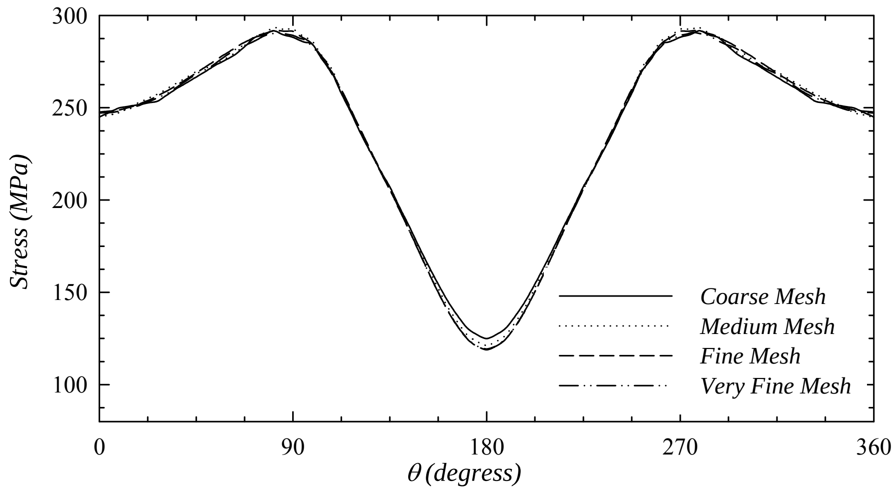

Figure 3.10 Equivalent stress under tensile loading along circular path *r*= 2.5 z=1

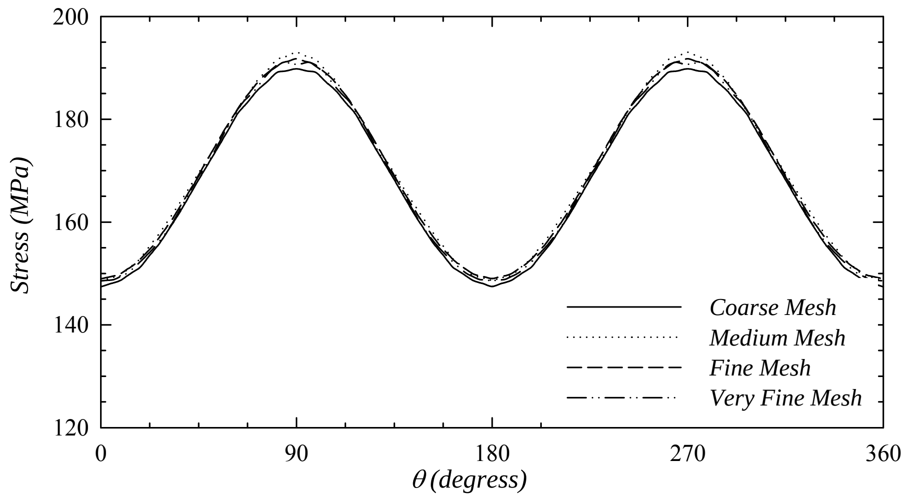

Figure 3.11 Equivalent stress under riveting loading along circular path, *r*= 2.5 z=1

Stress values for different mesh densities show similar behavior with slight difference along the selected paths. Stress values are much more dependent on mesh densities at the contact surfaces than the interior locations. This is due to the frictional contact condition at the contacting surfaces. Fine mesh is required for the contact modeling. Also the stress values from the external tensile loading phase are more dependent on the mesh density than stresses from the riveting simulation. Maximum differences in stress values occurs for tensile loading phase along circular path r=2.6 and z=0. For this case, comparisons were done within coarse-medium, medium-fine, and fine-very fine mesh densities. Table 3.3 summarizes the average and maximum differences in stress values for different mesh densities. Changing mesh density from coarse to medium results in 4.45 MPa average and 11.49 MPa maximum difference in von Mises equivalent stress. Medium to fine mesh density shifting results in 3.19 MPa average and 10.34 MPa maximum difference. Fine to very fine mesh density transition results in 1.81 MPa average and 4.32 MPa maximum difference. 1.81 MPa corresponds to less than about 1% of the average stress. The differences in fine to very fine mesh density transition are relatively small compared to the others. Therefore it is needless to use very fine mesh densities keeping in mind the computation time needed for the analysis. Thus fine mesh density is utilized throughout the study.

Table 3.3 Comparisons for different mesh densities

Difference (*MPa*)	Coarse to Medium	Medium to Fine	Fine to Very fine
Average	4.45	3.19	1.81
Maximum	11.49	10.34	4.32

3.6 Numerical Results and Conclusions

In this section stress state of the outer plate of the riveted joint was presented along the selected paths near the rivet hole and at the plane of probable crack. Stresses are calculated for sixteen different finite element models (as depicted in Table 3.1) for both riveting simulation and external loading conditions. For the path definition, angular locations and depth definitions for the joint model are obtained from Figure 3.1. First the residual stress state resulting from riveting process simulation was explored. Then the stress state under the external loading including the residual stress state was presented. Also the effects of interference and clamping on the residual stress state and the overall stress state under the external loading were investigated.

3.6.1 Residual Stress Analysis

Riveting simulation results in residual stress on the rivet and the plates. Tangential, radial and axial stress components distributions resulting from riveting simulation were obtained. Major concern for fatigue of riveted joint is the residual tangential stresses since they coincide with the direction of the applied external load along the net section of the riveted joint where cracks typically form.

Illustrative contours for the residual stress components for fixed interference and clamping values (*%D*=0.15 and *%L*=0.15) on the rivet and the plates at a plane perpendicular to the tensile loading are shown in Figure 3.12. The stress contours in these plots clearly illustrate the stress concentration locations where the maximum stress values are observed. These locations are mainly the chamfers of the rivet hole and matching places on the rivet.

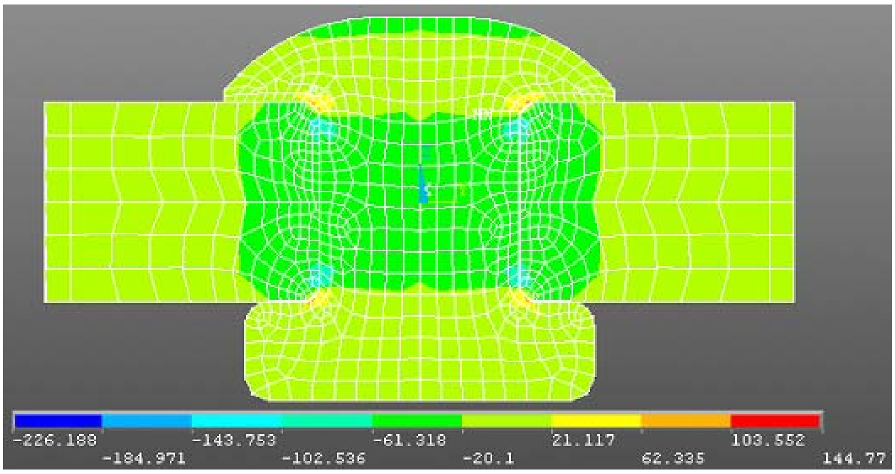

a)

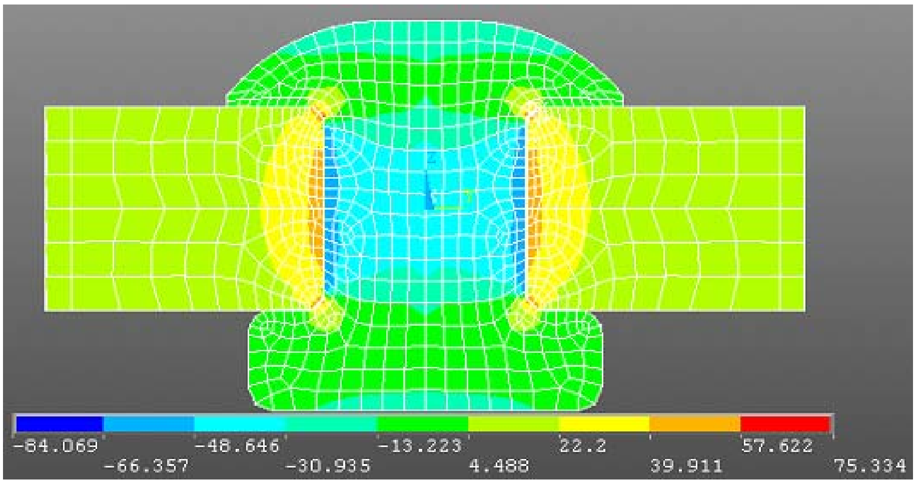

b)

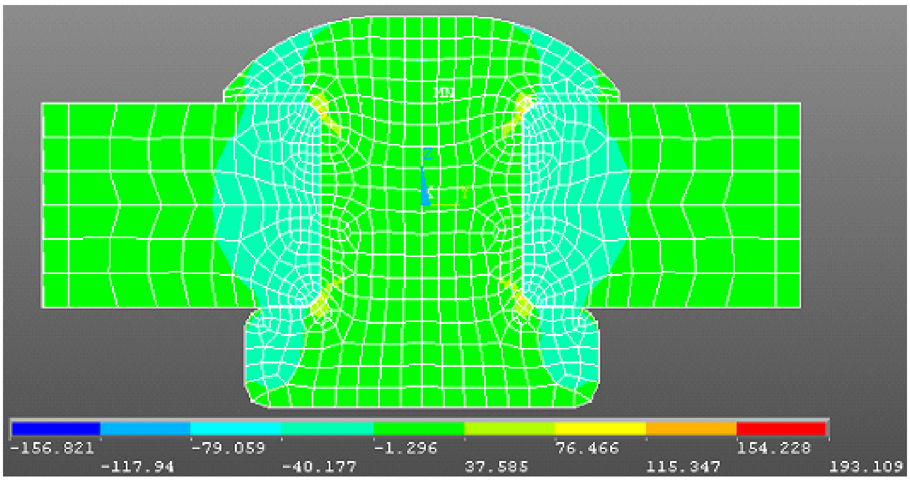

c)

Figure 3.12 Residual stress contours **a)** radial, **b)** tangential, **c)** axial stress components [in MPa]

Also tangential, radial, and equivalent von Mises stress components were compared along the selected paths (Figure 3.13) through the thickness of the outer plate. Thus, stress variation along the thickness could be investigated. These analyses were carried out for fixed values of clamping and interference (*%L*=0.30 and *%D*=0.30).

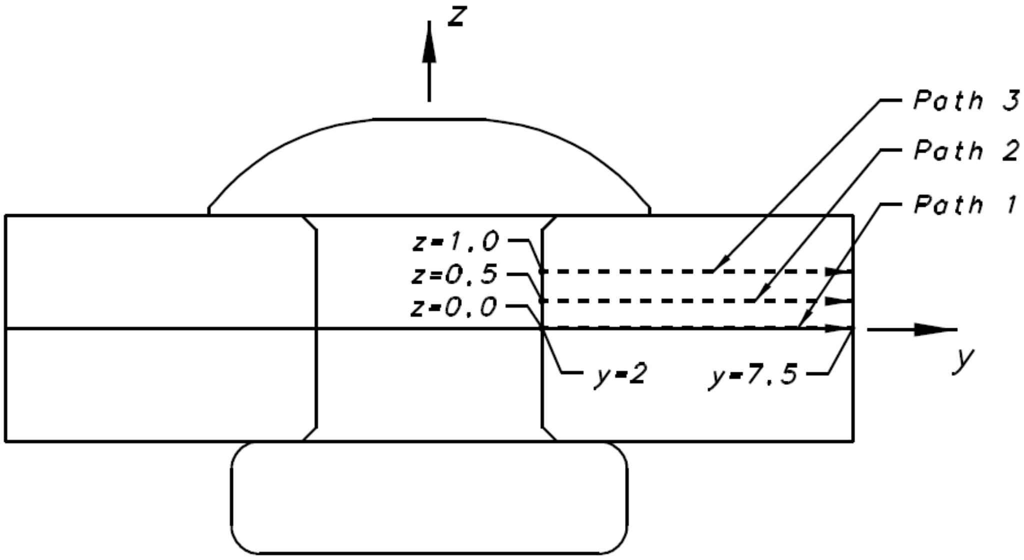

Figure 3.13 Definitions of paths at the plane illustrated in Figure 3.1.b

As shown in Figure 3.14.a, near the rivet hole, the magnitudes of the radial stress component increase as going away from the contacting surface side of the plate. As going away from the rivet hole, this trends change behavior. Values of the tangential stress component decrease going away from the faying surface side of the plate. Behavior of von Mises stress components is shown in Figure 3.14.c. It can be concluded that, variation of stress components are not significant through the thickness of the plate. For all parametric studies, values of the stress components along path 3 will be utilized, which is the center location of the outer plate.

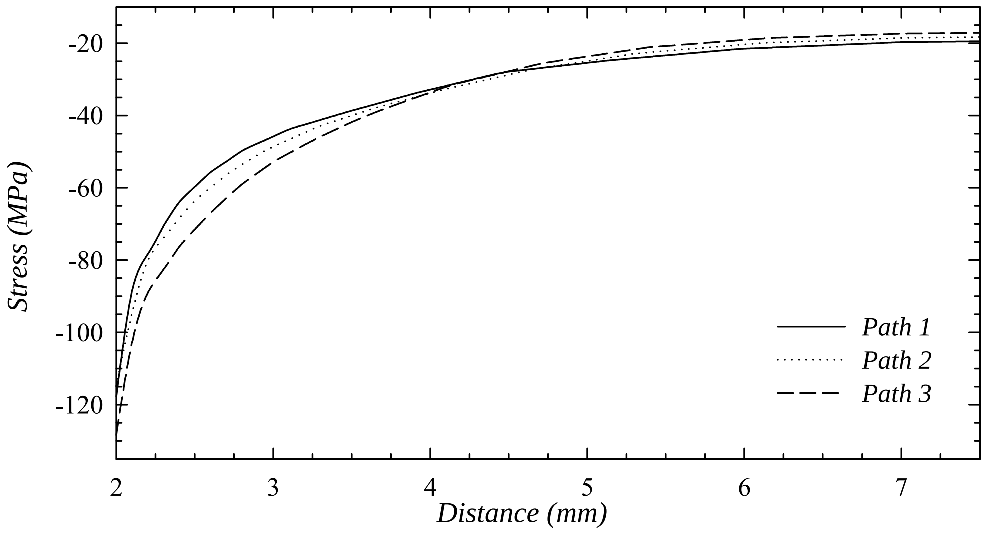
Stress (MPa)
Distance (mm)
Path 1
Path 2
Path 3

a)

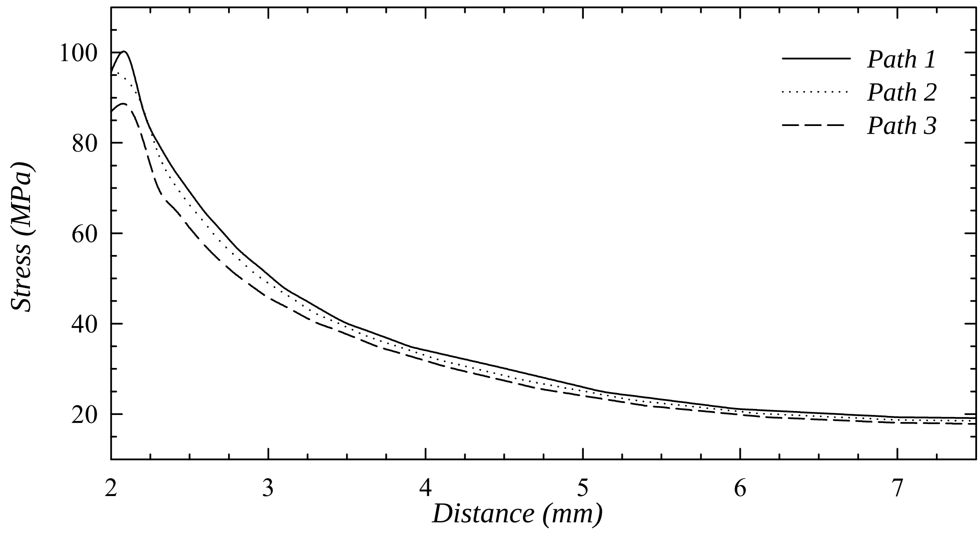
Stress (MPa)
Distance (mm)
Path 1
Path 2
Path 3

b)

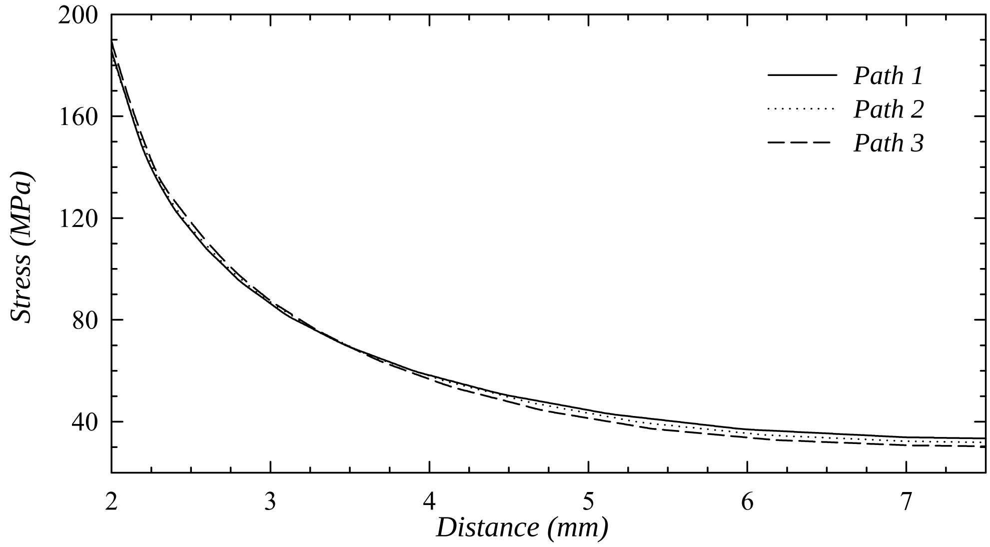

c)

Figure 3.14 Stress variation through plate thickness under riveting simulation **a)** Radial, **b)** Tangential, **c)** von Mises stress components

Also tangential, radial, and equivalent von Mises stress component distributions along circular path around the rivet hole are presented to see the radial variation of the stresses. Circular path is selected to be r=2.6 and z=1 by using the coordinate systems defined in Figure 3.1. As shown in the Figure 3.15, at $\theta = 90$ and $\theta = 270$ there are increases in radial and tangential stress components resulting in increase in equivalent von Mises stress. This is due to the multiple rivet symmetry conditions at the long edge of the riveted lap joint. Another important point is that riveting introduces tensile tangential and compressive radial stresses. Tensile tangential stress is known to be one of the causes of the crack initiation in riveted joint. And it has its maximum values at a plane perpendicular to the loading where cracks are located in fracture analysis of the riveted joint section.

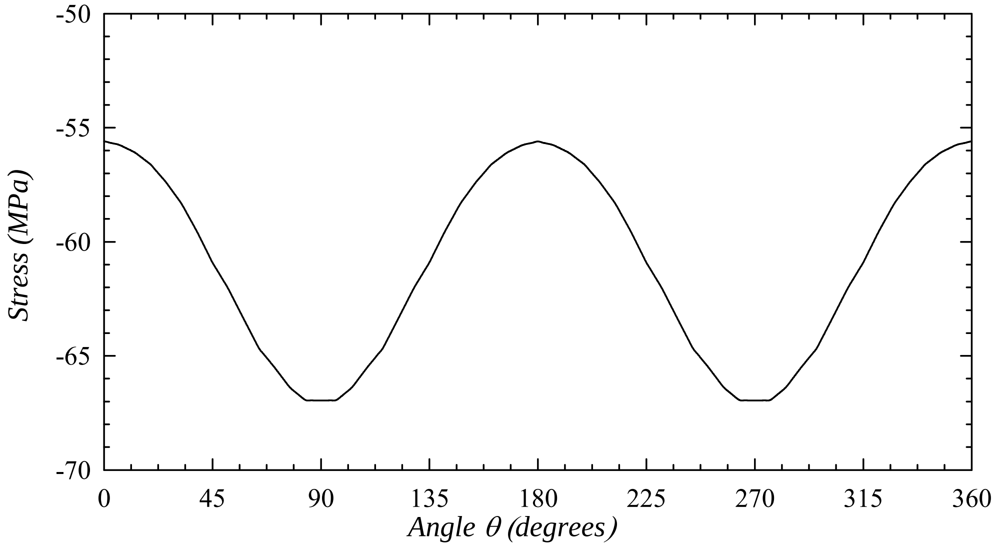
-50
-55
-60
-65
-70
Stress (MPa)
0
45
90
135
180
225
270
315
360
Angle θ (degrees)

a)

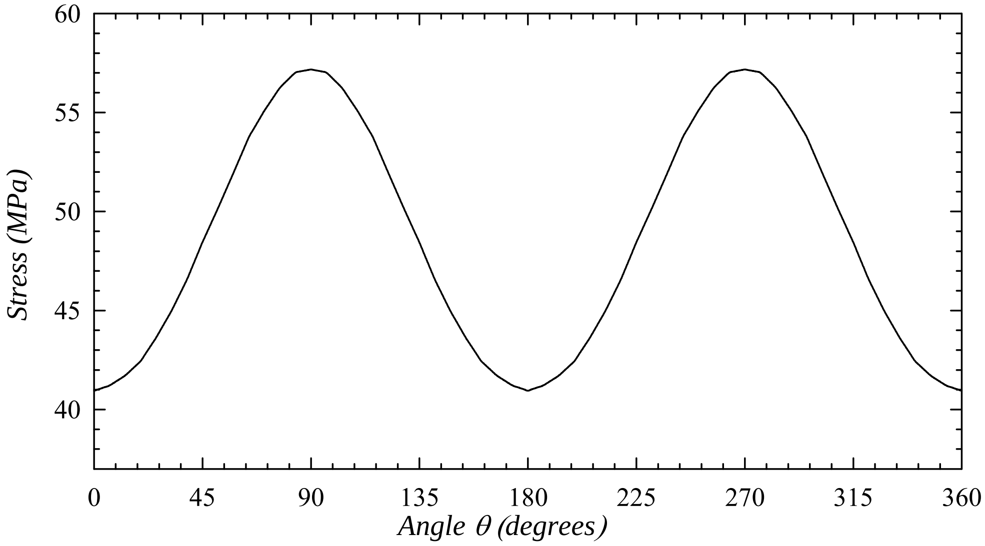
60
55
50
45
40
Stress (MPa)
0
45
90
135
180
225
270
315
360
Angle θ (degrees)

b)

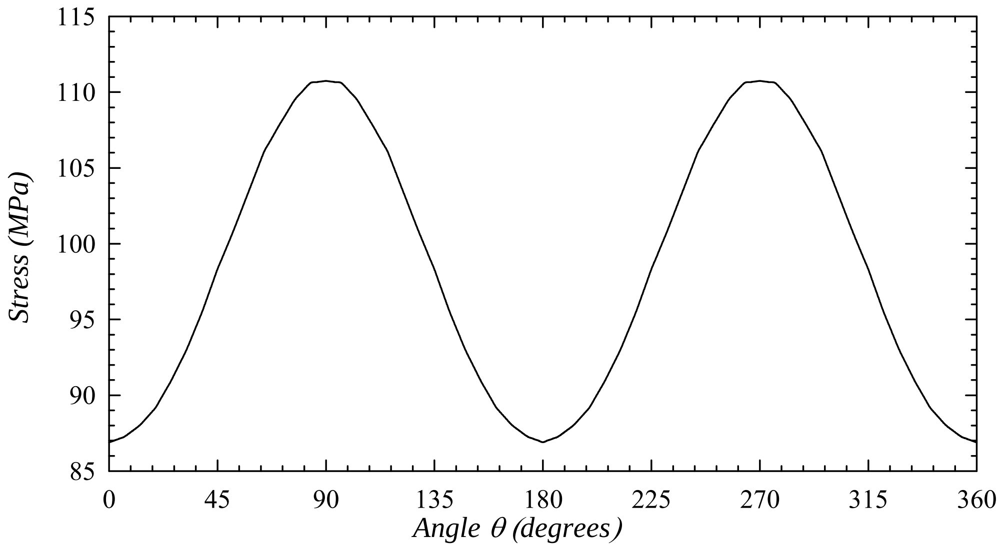

c)

Figure 3.15 Stress variation around rivet hole **a)** Radial, **b)** Tangential, **c)** von Mises stress components

3.6.1.1 Effects of Interference on Residual Stress

In order to investigate the effects of interference on the residual stress state, the radial and the tangential stress variations along selected path 3 in Figure 3.13 were compared for different interference values. Keeping the values of clamping ratios fixed, stress variations were observed for varying interference ratios. All comparisons were carried out for each fixed values of clamping ratios.

Figure 3.16 illustrates the effects of interference on residual radial stress component along path 3, for four fixed values of clamping. As shown in the figure, riveting simulation introduces compressive radial stress for the plates. For all clamping values, magnitudes of the radial stress are increasing as the values of interference are increasing. Also note that stress values are maximum at the rivet hole side and getting smaller as going away from the rivet hole. Stress values are much more sensitive to change in the interference values near the rivet hole and this sensitivity gets smaller as going away from the rivet hole.

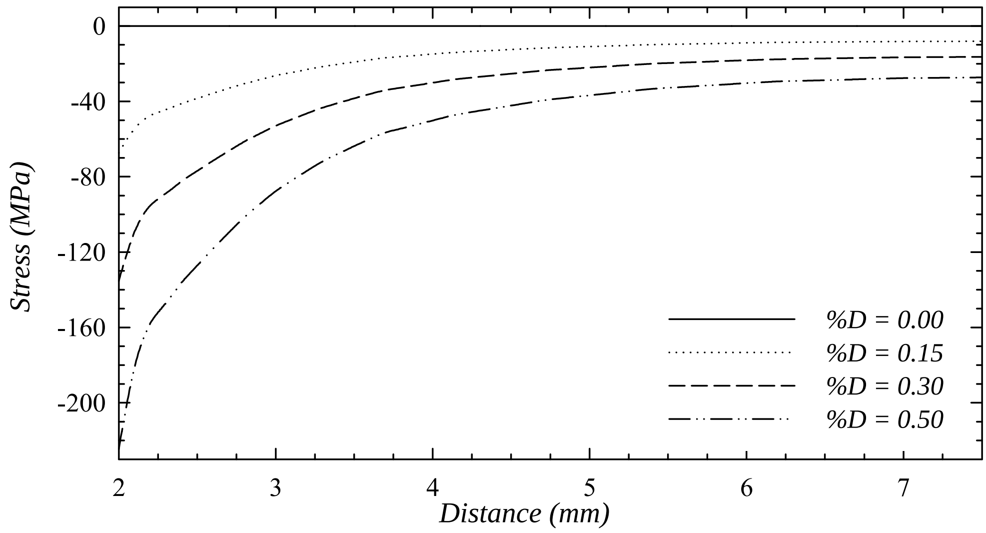
0
-40
-80
-120
-160
-200
Stress (MPa)
2
3
4
5
6
7
Distance (mm)
%D = 0.00
%D = 0.15
%D = 0.30
%D = 0.50

a)

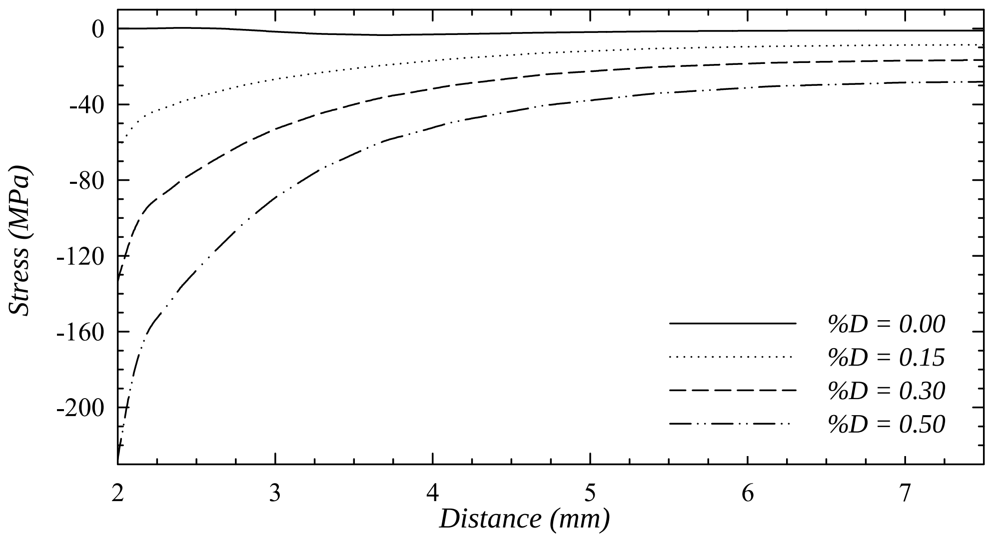
0
-40
-80
-120
-160
-200
Stress (MPa)
2
3
4
5
6
7
Distance (mm)
%D = 0.00
%D = 0.15
%D = 0.30
%D = 0.50

b)

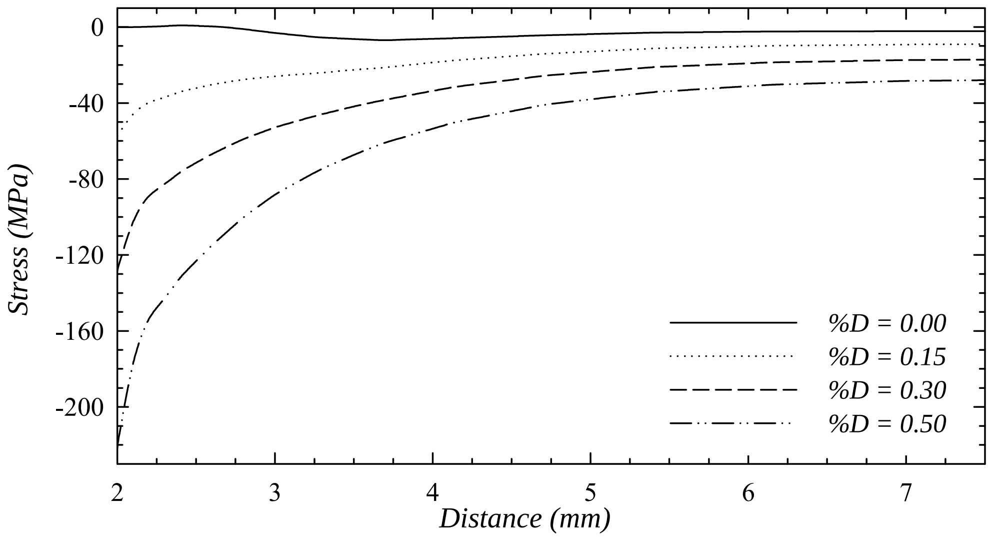

c)

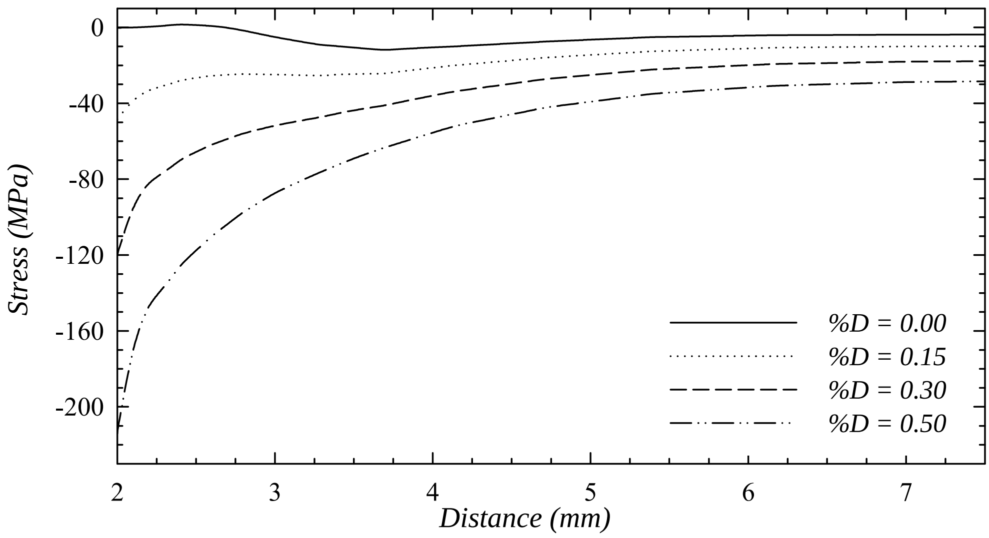

d)

Figure 3.16 Effects of interference on residual radial stress component along path 3, for the clamping: **a)** *%L=0.00,* **b)** *%L=0.15,* **c)** *%L=0.30,* **d)** *%L=0.50*

The effects of interference on residual tangential stress component along path 3 are shown in Figure 3.17. As shown in the figure, riveting simulation introduces tensile tangential stress for the plates. For all clamping values, magnitudes of the tangential stress are increasing as the values of interference are increasing. Also note that stress values are maximum near the rivet hole and getting smaller as going away from the rivet hole. Near the rivet hole stress values are much more sensitive to change in the interference values and this sensitivity gets smaller as going away from the rivet hole.

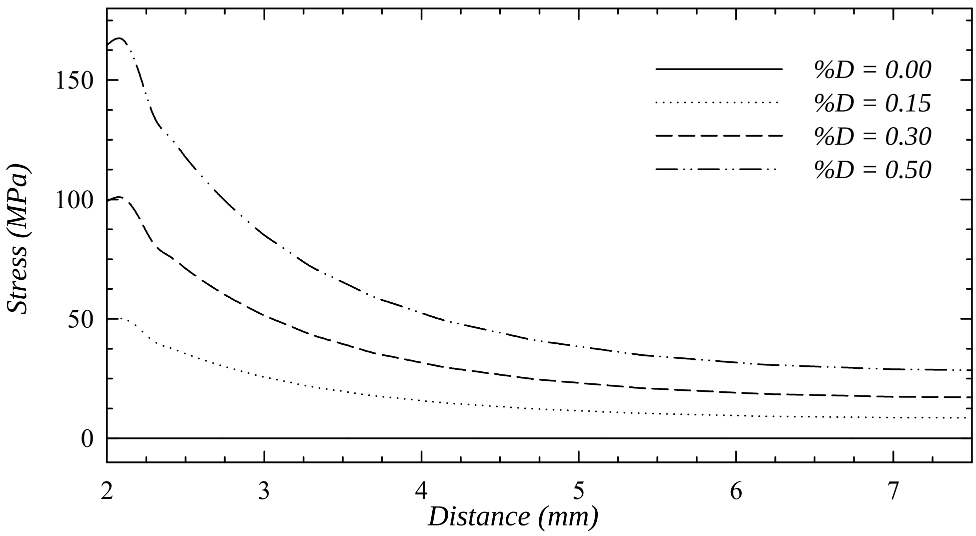

a)

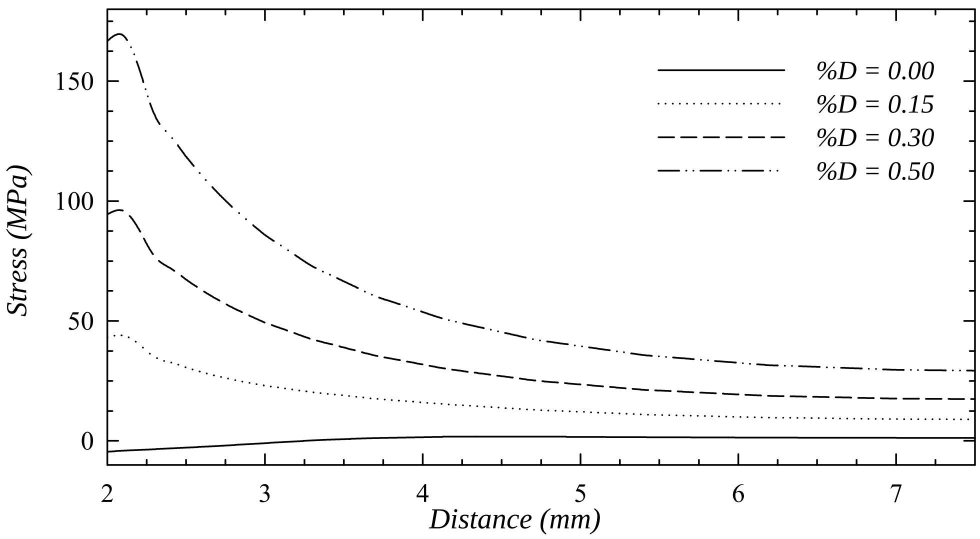

b)

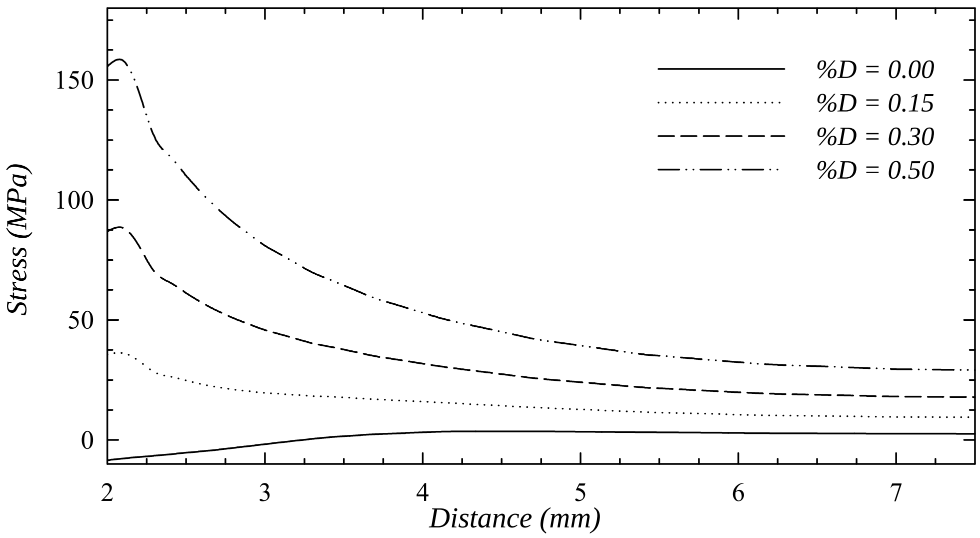

c)

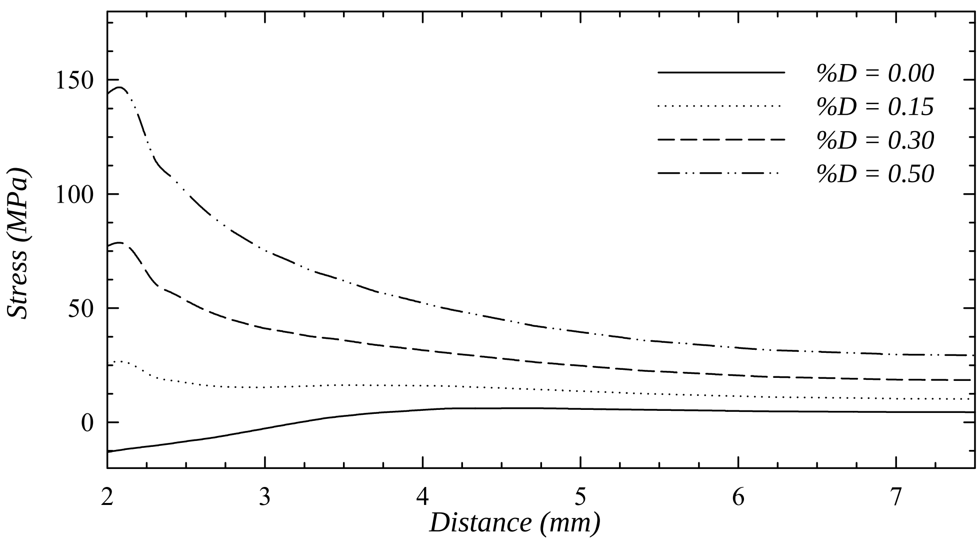

d)

Figure 3.17 Effects of interference on residual tangential stress component along path 3, for the clamping: **a)** *%L=0.00*, **b)** *%L=0.15*, **c)** *%L=0.30*, **d)** *%L=0.50*

In comparing the result for different interference values, it can be concluded that the changes in the interference affects the residual stress field considerably. Magnitudes of the compressive radial stress and tensile tangential stress increase as the interference values are increased. Stress values are decreasing as going away from the rivet. Also note that zero stress values for zero interference and clamping ratios.

3.6.1.2 Effects of Clamping on Residual Stress

In order to investigate the effects of clamping on the residual stress state, the radial, the tangential and the axial stress variations along path 3 were compared for varying clamping values.

Figure 3.18 illustrates the effects of clamping on residual radial stress component along path 3, for four fixed values of interference. As shown in Figure 3.18.a, for 0 interference values, magnitudes of the radial stress are extremely small and are generally increasing as the values of interference are increasing. For larger interference values, variation of stress change trends. Near the rivet hole, increasing clamping values decrease the stress values but increase the stress values far from the rivet hole. However, since the stress values near the rivet hole are highest, it can be concluded that increasing clamping generally decrease residual radial stress values. As the interference values are increasing, effect of clamping on stress values is getting insignificant.

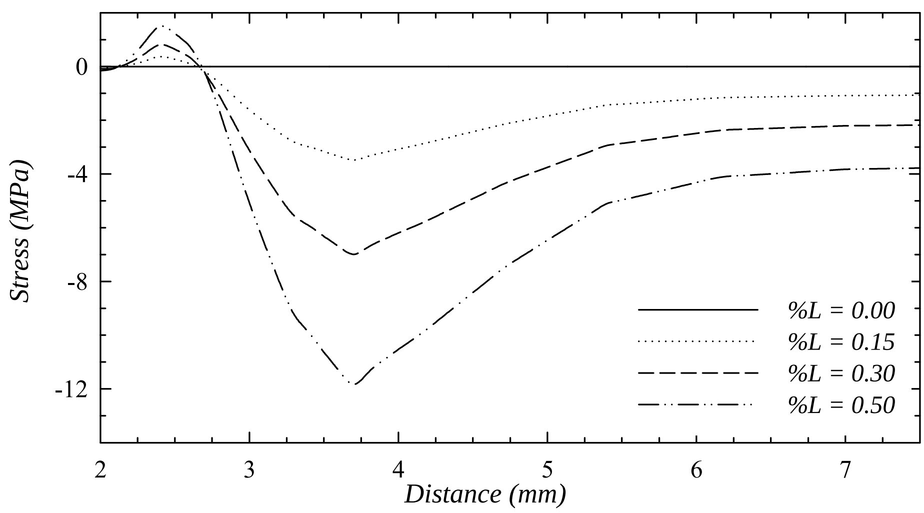
0
-4
-8
-12
Stress (MPa)
2
3
4
5
6
7
Distance (mm)
%L = 0.00
%L = 0.15
%L = 0.30
%L = 0.50

a)

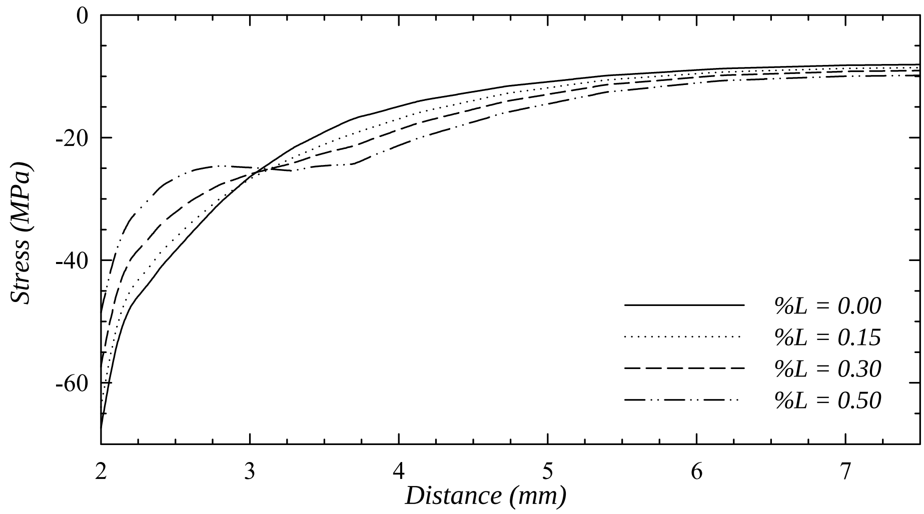
0
-20
-40
-60
Stress (MPa)
2
3
4
5
6
7
Distance (mm)
%L = 0.00
%L = 0.15
%L = 0.30
%L = 0.50

b)

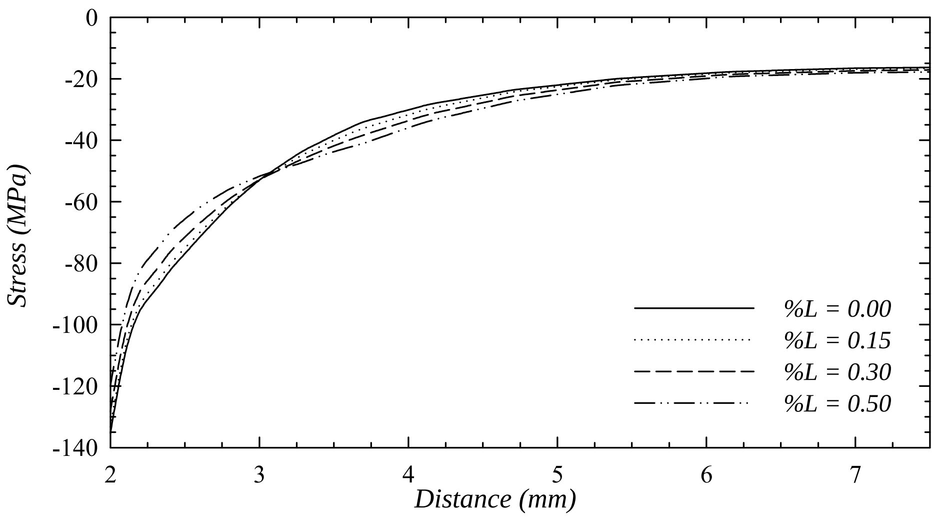

c)

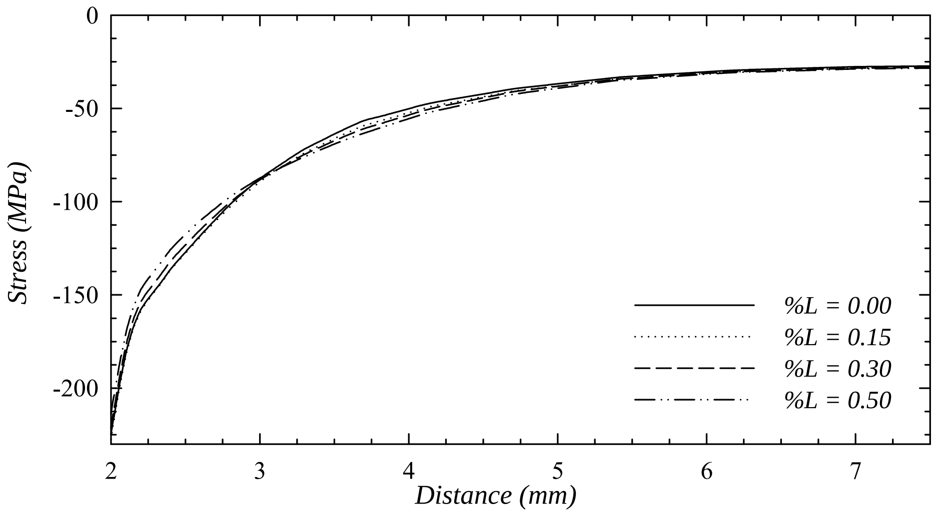

d)

Figure 3.18 Effects of clamping on residual radial stress component along path 3, for the interference: **a)** *%D=0.00,* **b)** *%D=0.15,* **c)** *%D=0.30,* **d)** *%D=0.50*

The effects of clamping on residual tangential stress component along path 3, for four fixed values of interference are illustrated in Figure 3.19. For 0 interference value, tangential stress component shows different behavior and has relatively small values. Near the rivet hole compressive, far from the rivet hole tensile tangential stress form. At about a distance of 3.2 mm from rivet hole center, all values become zero. For 0 interference values, magnitudes of the tangential stress are increasing as the values of interference are increasing. For larger interference values, increasing clamping values generally decrease the stress values near the rivet hole but increase the stress values far from the rivet hole. As the interference values are increasing, effect of clamping on stress values is getting insignificant.

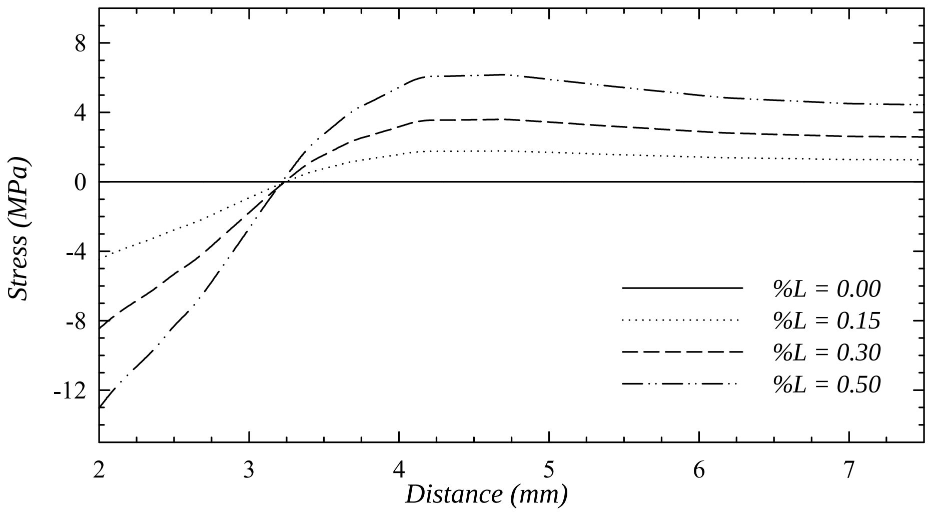

a)

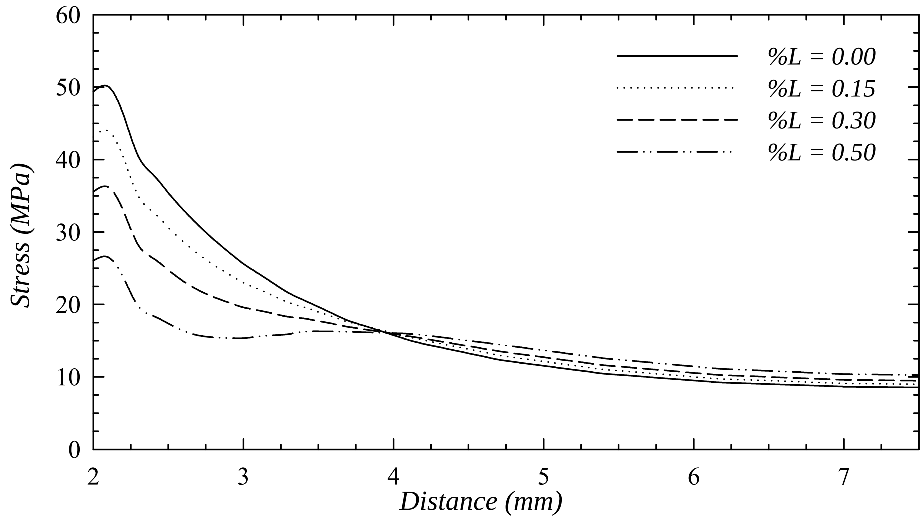

b)

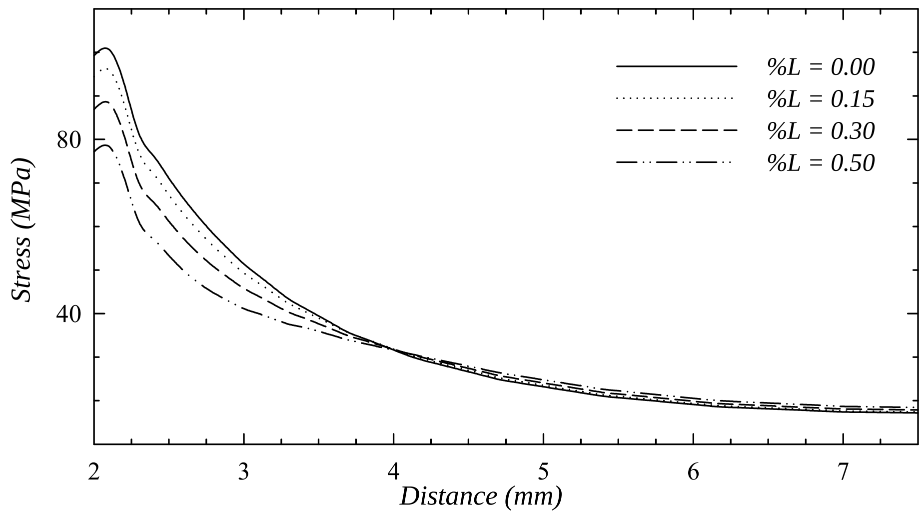

c)

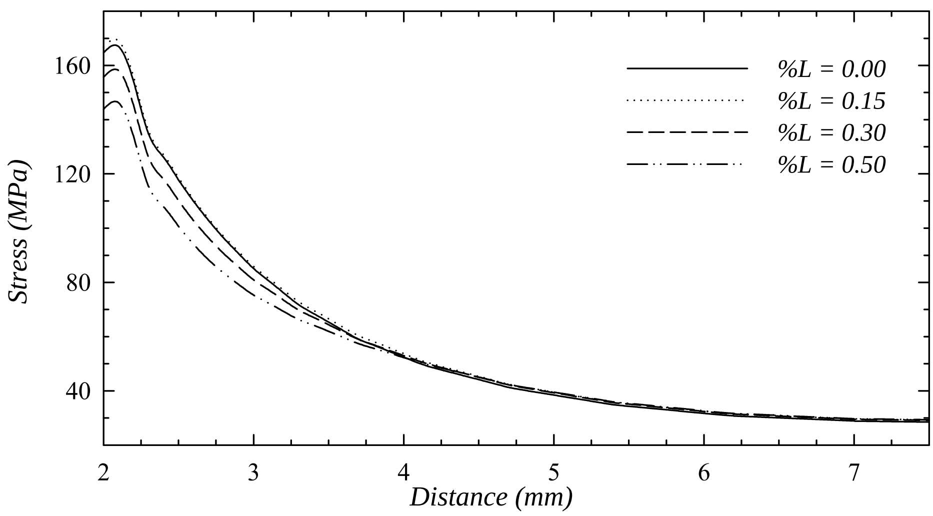

d)

Figure 3.19 Effects of clamping on residual tangential stress component along path 3, for the interference: **a)** *%D=0.00,* **b)** *%D=0.15,* **c)** *%D=0.30,* **d)***%D=0.50*

Figure 3.20 illustrates the effects of clamping on residual axial stress component. Clamping is the main source of axial stress. For all interference values magnitudes of the compressive axial stress are increasing as the values of clamping are increasing. For fixed values of interference, axial stress values get smaller as going away from the rivet hole and diminish at a distance of 4 mm from the rivet hole center.

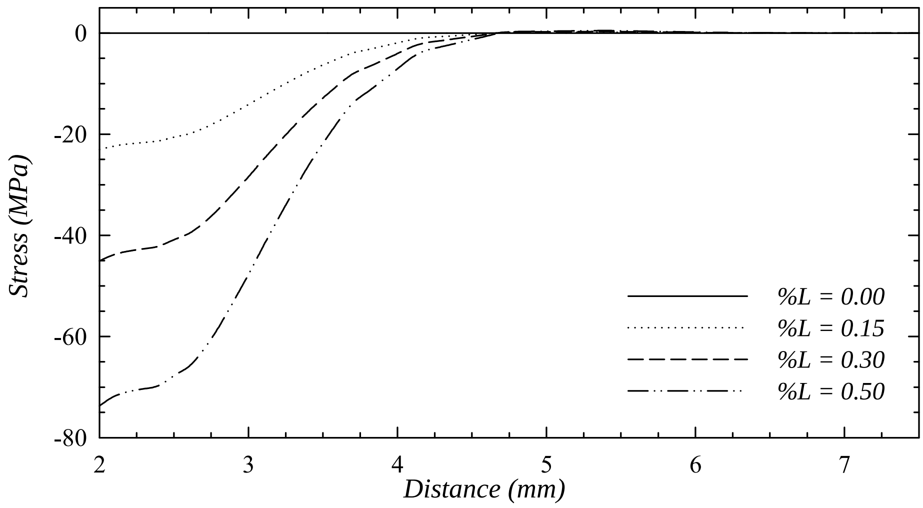
0
-20
-40
-60
-80
Stress (MPa)
2
3
4
5
6
7
Distance (mm)
%L = 0.00
%L = 0.15
%L = 0.30
%L = 0.50

a)

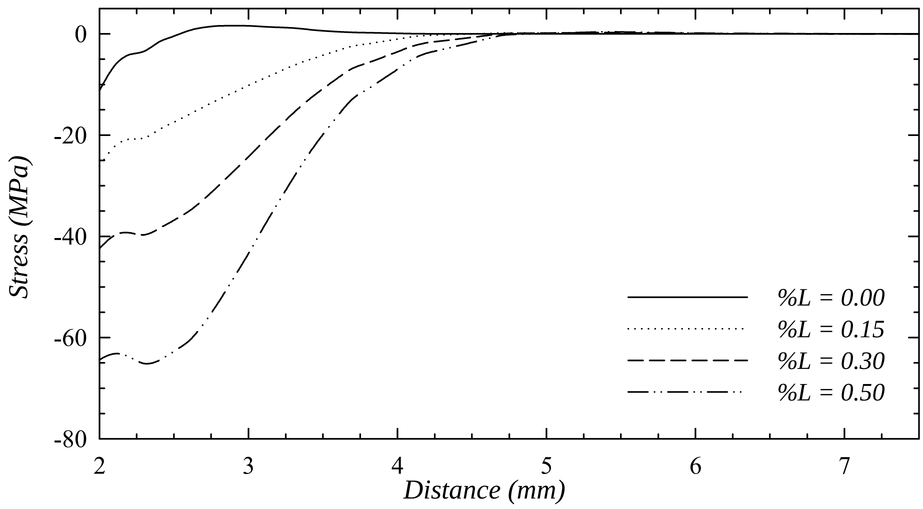
0
-20
-40
-60
-80
Stress (MPa)
2
3
4
5
6
7
Distance (mm)
%L = 0.00
%L = 0.15
%L = 0.30
%L = 0.50

b)

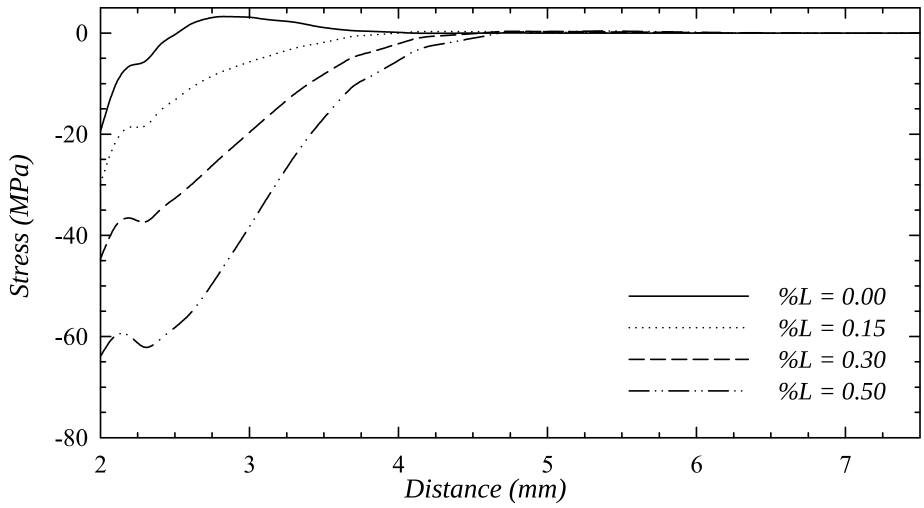

c)

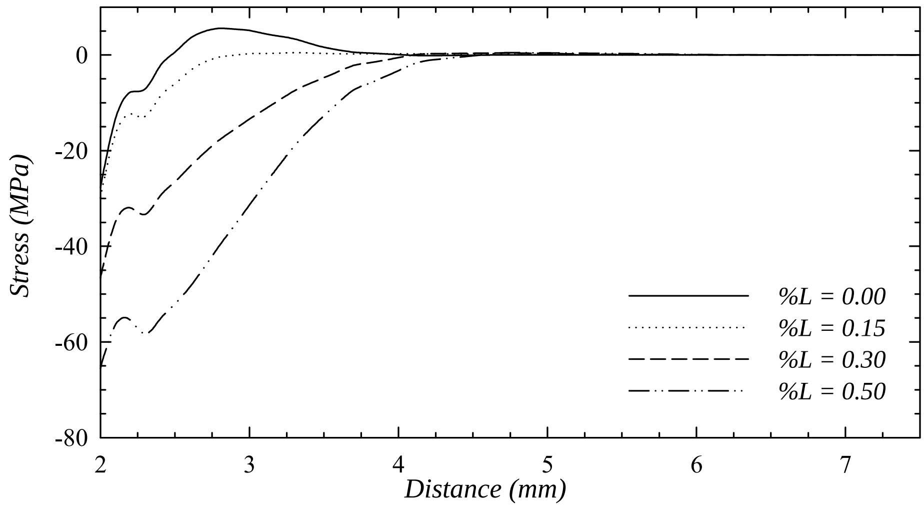

d)

Figure 3.20 Effects of clamping on residual axial stress component along path 3, for the interference: **a)** *%D=0.00*, **b)** *%D=0.15*, **c)** *%D=0.30*, **d)** *%D=0.50*

To sum up, increasing clamping generally increases the compressive radial, tensile tangential and compressive axial stress components. Effect of clamping on the radial stress is not much as the interference. Especially for high interference values effect of clamping is getting diminished. Clamping, which is the main cause of axial stress, has a deep effect on axial stress. All stress components change behavior at about a distance of 4 mm from the rivet hole center. 4 mm distance corresponds to the diameter of the rivet head which clamps plates together. It means clamping effect diminishes at a circular path having a radius of about 4 mm.

3.6.2 Stress Analysis under External Load

After obtaining residual stress state, now the overall stress state under external loading is investigated. Then effects of interference and clamping on the overall stress state are investigated. Overall stress state under external loading includes the residual stress due to the riveting simulation.

Tangential, radial, and axial stress components were compared along the selected paths (Figure 3.13) through the thickness of the outer plate under the external loading. Thus, stress variation along the thickness could be investigated. These analyses were carried out for fixed values of clamping and interference (*%L*=0.30 and *%D*=0.30). Radial, tangential and axial stress variations through plate thickness under external loading are shown in Figure 3.21. As shown in this figure overall stress variation along plate thickness is more significant than the residual stress variation. Near the rivet hole, values of the radial stress component are compressive and maximum and they increase as going away from the faying surface side of the plate. As going away from the rivet hole, compressive radial stress becomes tensile and values decrease as going away from the faying surface side of the plate. Values of the tangential stress component decrease going away from the faying surface side of the plate. Behavior of axial stress components is shown in Figure 3.21.c. Near the rivet hole, values of the axial stress component are compressive and maximum and they decrease as going away from the faying surface side of the plate.

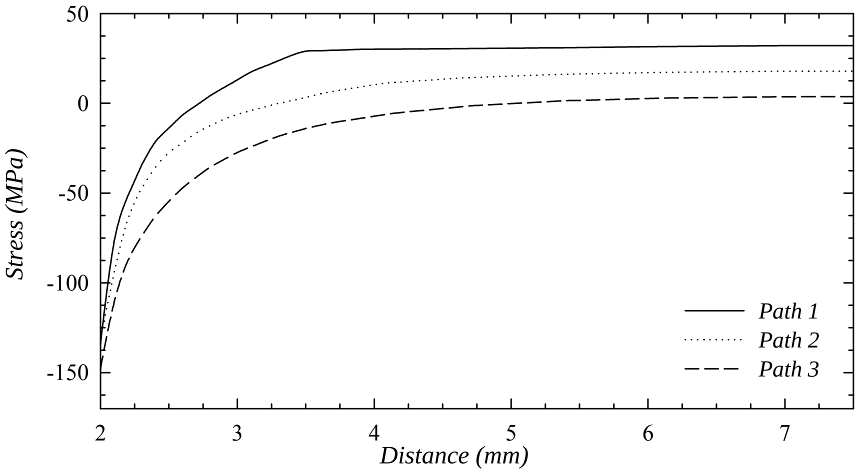
50
0
-50
-100
-150
Stress (MPa)
2
3
4
5
6
7
Distance (mm)
Path 1
Path 2
Path 3

a)

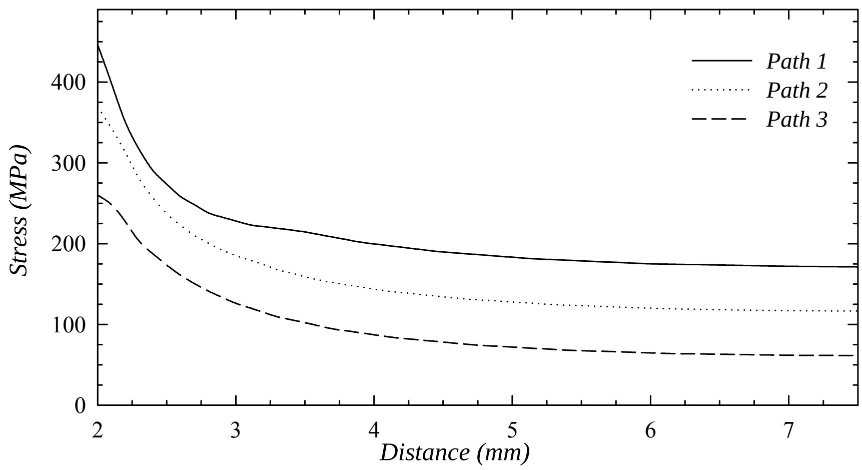
400
300
200
100
0
Stress (MPa)
2
3
4
5
6
7
Distance (mm)
Path 1
Path 2
Path 3

b)

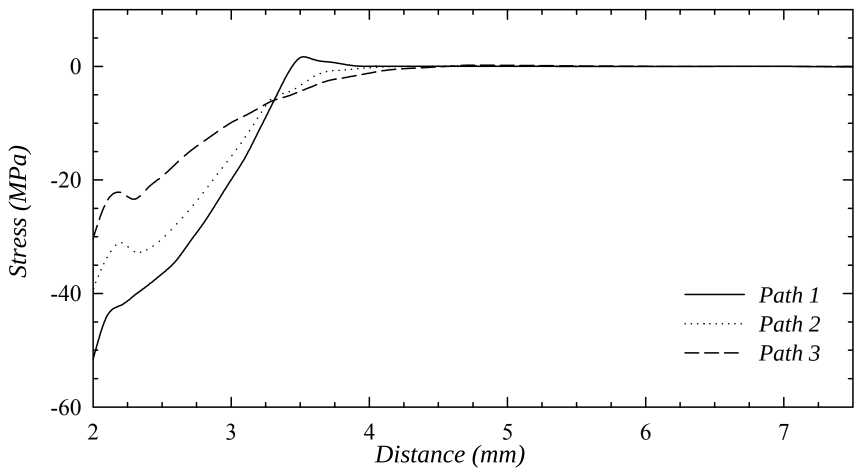

c)

Figure 3.21 Stress variation through plate thickness under external loading **a)** Radial, **b)** Tangential, **c)** Axial stress components (*%D=0.50* and *%L=0.50)*

In addition tangential, radial, and axial stress component distributions along circular path around the rivet hole are presented to see the radial variation of the stresses under external loading. Circular path is selected to be r=2.6 and z=1 by using the coordinate systems defined in Figure 3.1. External loading is applied to the model which is already in residual stress state due to the riveting simulation. As shown in Figure 3.22 compressive residual radial stress shifts to the tensile upon external loading between about 100 to 260 degrees. Magnitude of the compressive residual radial stresses at the plane perpendicular to loading ($\theta = 90^0$ and $\theta = 270^0$) remains nearly unchanged as compared to riveting simulation. Tensile tangential stress is known to be one of the causes of the crack initiation in riveted joint. And it has its maximum values at a plane perpendicular to the loading where cracks are located in fracture analysis of the riveted joint section. The maximum value of the tangential stress is approximately doubled and its location does not change much as in riveting simulation. Approximately uniform axial stress distribution around rivet hole is changed as in Figure 3.22.c due to the rivet tilting.

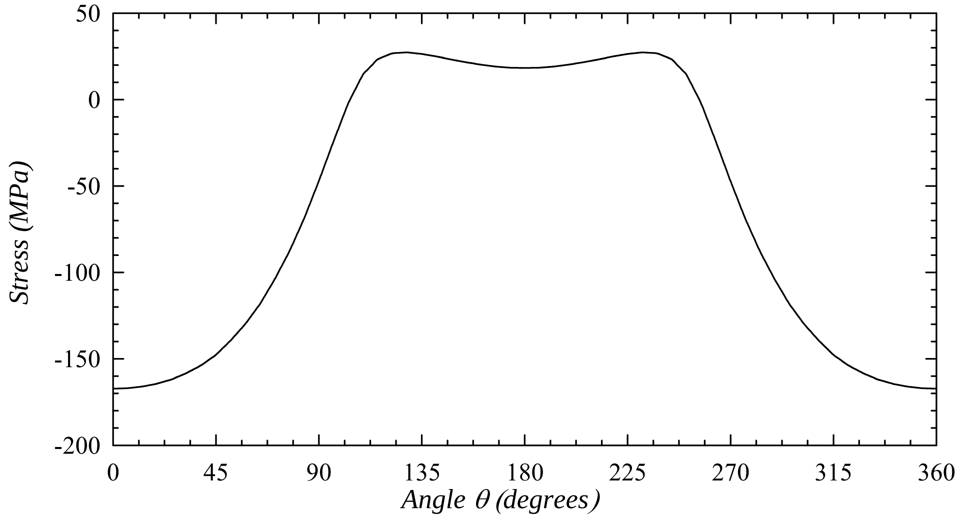
Stress (MPa)
Angle θ (degrees)
50
0
-50
-100
-150
-200
0
45
90
135
180
225
270
315
360
a)

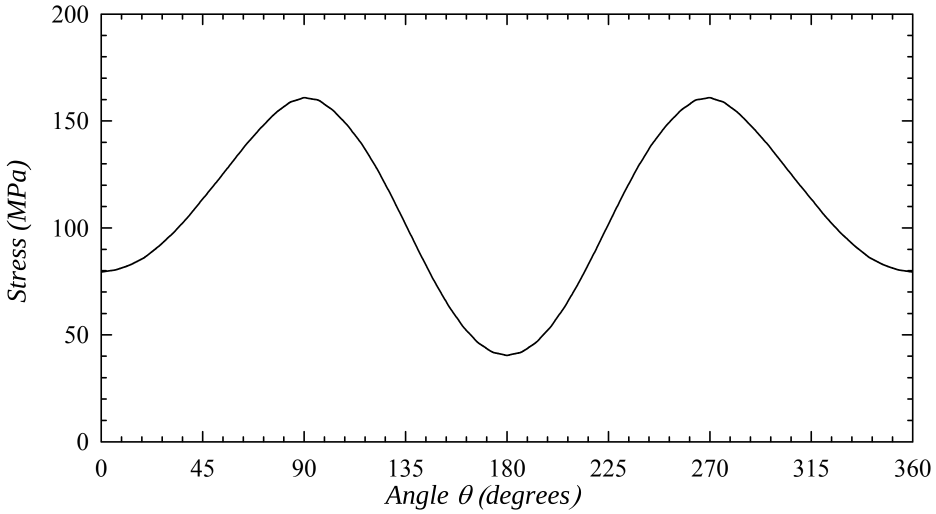
Stress (MPa)
Angle θ (degrees)
200
150
100
50
0
0
45
90
135
180
225
270
315
360
b)

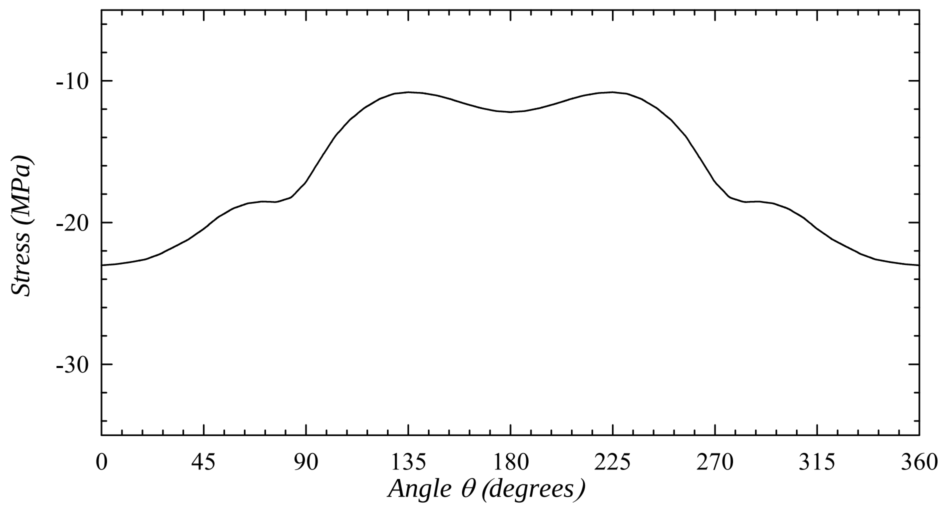

c)

Figure 3.22 Stress variation around rivet hole **a)** Radial, **b)** Tangential, **c)** Axial stress components

3.6.2.1 Effects of Interference on Overall Stress

Effects of interference on radial stress component along path 3 under the external load, for four fixed values of clamping are illustrated in Figure 3.23. As shown in the figure, for all clamping values radial stress components show very similar tendencies. For small interference values, tensile radial stress develops and magnitudes of the radial stress are generally decreasing as the values of interference are increasing. For high interference values, compressive radial stress develops and magnitudes of the radial stress are generally increasing as the values of interference are increasing. Also note that stress values are generally maximum at the rivet hole and getting diminished going away from the rivet hole. Stress values are much more sensitive to change in the interference values near the rivet hole and this sensitivity gets smaller as going away from the rivet hole.

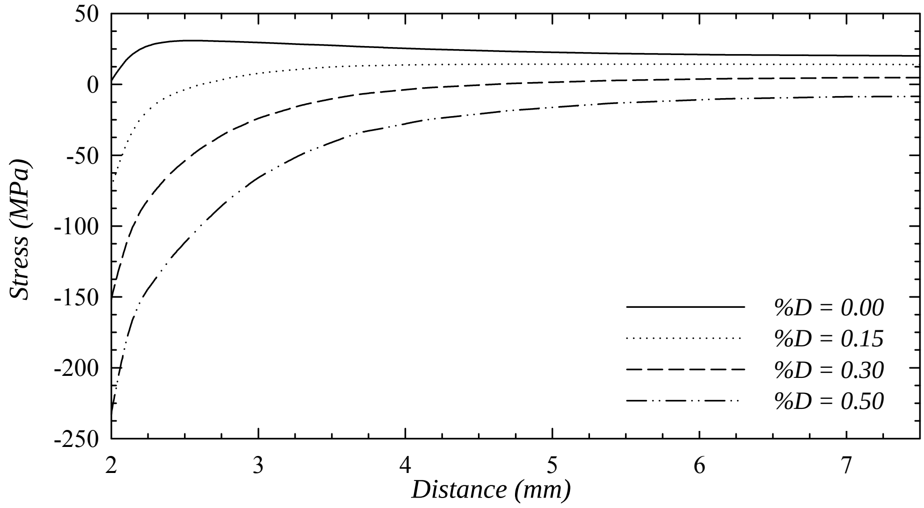
Stress (MPa)
Distance (mm)
%D = 0.00
%D = 0.15
%D = 0.30
%D = 0.50

a)

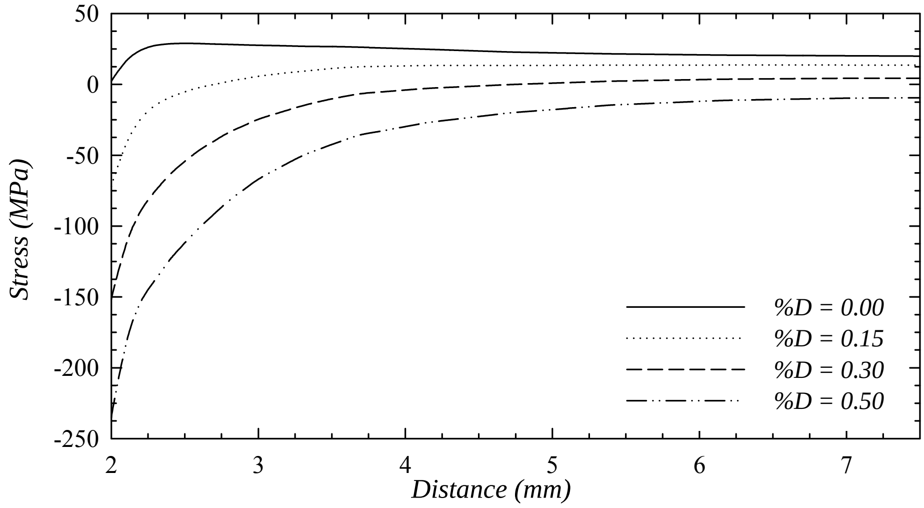
Stress (MPa)
Distance (mm)
%D = 0.00
%D = 0.15
%D = 0.30
%D = 0.50

b)

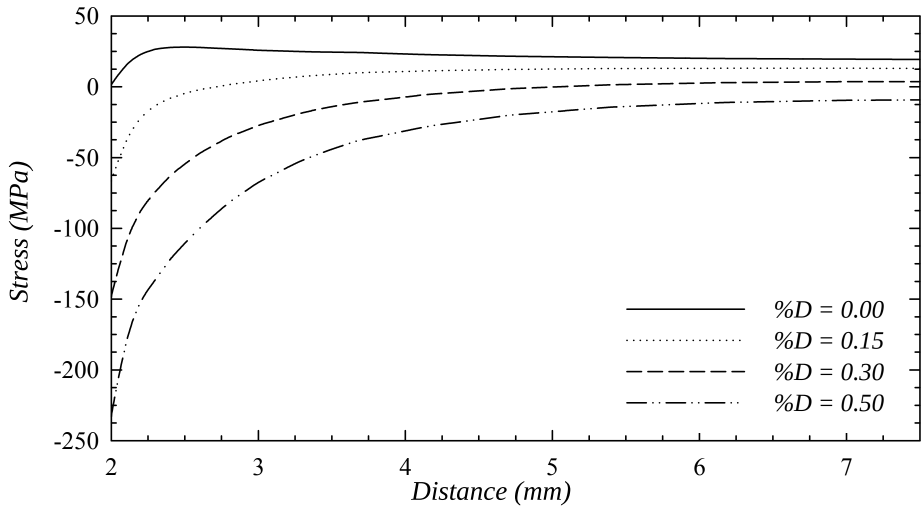

c)

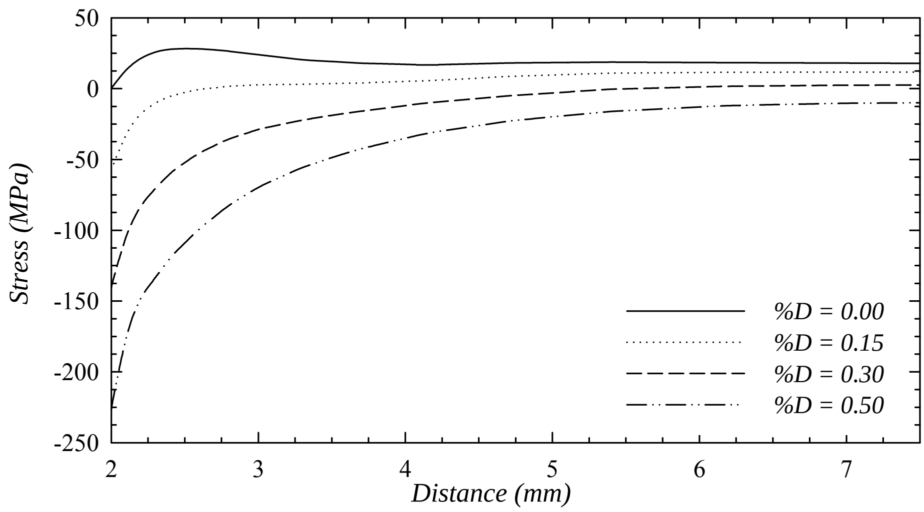

d)

Figure 3.23 Effects of interference on radial stress component along path 3, for the clamping: **a)** *%L=0.00,* **b)** *%L=0.15,* **c)** *%L=0.30,* **d)** *%L=0.50*

The effects of interference on tangential stress component along path 3 under external loading, for four fixed values of clamping are shown in Figure 3.24. For all clamping values, magnitudes of the tangential stress are increasing as the values of interference are increasing. Also note that stress values are maximum at the rivet hole and getting smaller going away from the rivet hole. Stress values are much more sensitive to change in the interference values and this sensitivity gets smaller as going away from the rivet hole.

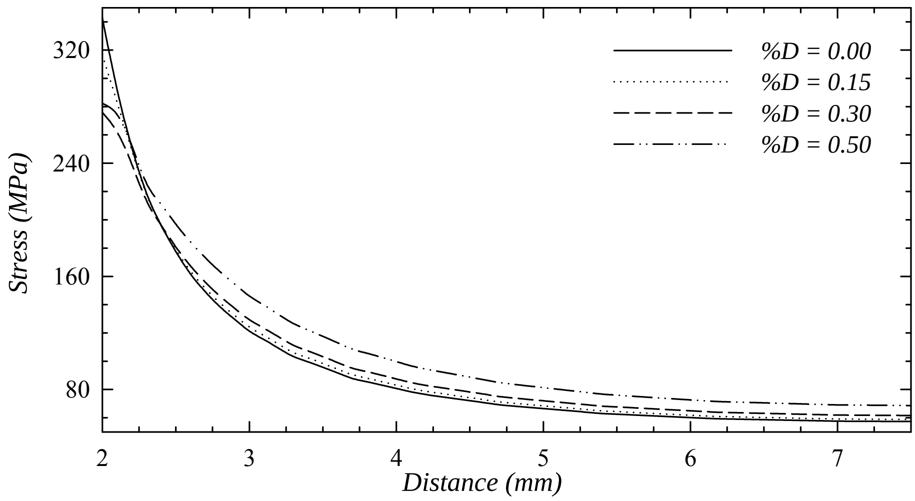

a)

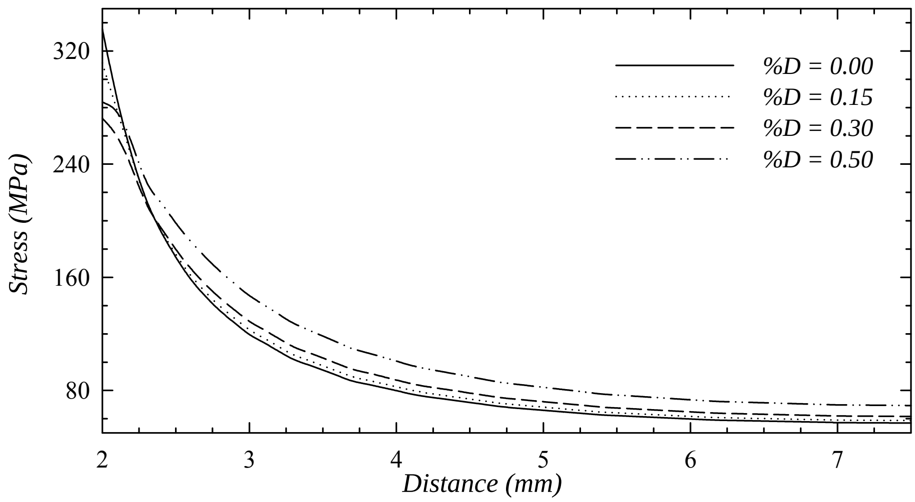

b)

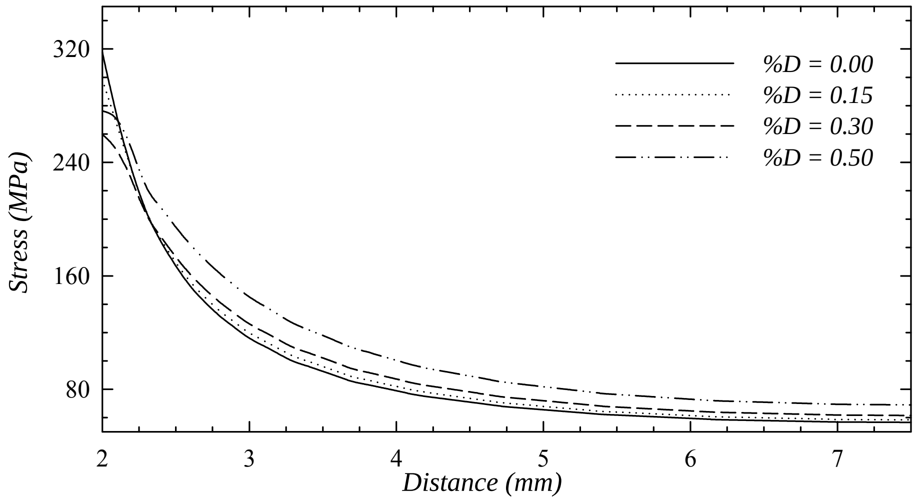

c)

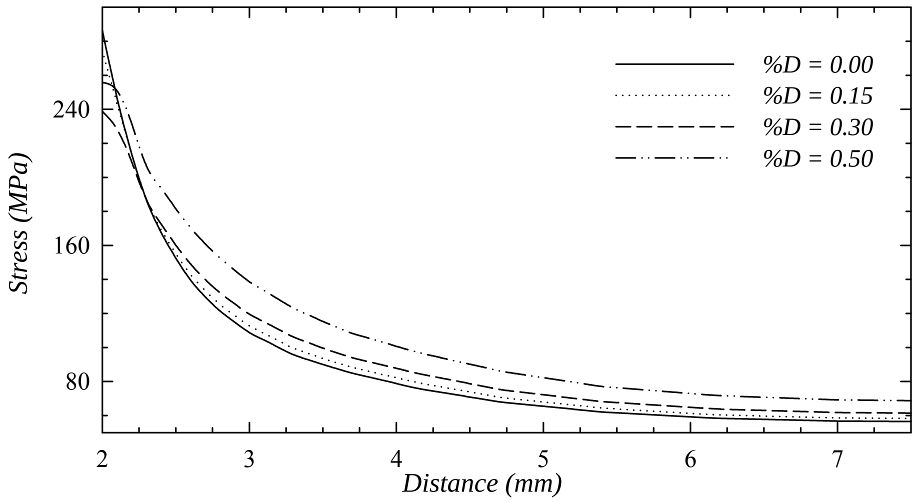

d)

Figure 3.24 Effects of interference on residual tangential stress component along path 3, for the clamping: **a)** *%L=0.00,* **b)** *%L=0.15,* **c)** *%L=0.30,* **d)** *%L=0.50*

In comparing the result for different interference values, it can be concluded that the changes in the interference affects the overall stress field considerably. Magnitudes of the compressive radial stress for high interference values and tensile tangential stress increase as the interference values are increased. Stress values are decreasing as going away from the rivet. Radial stress is much more sensitive to change in the interference values than tangential stress component.

3.6.2.2 Effects of Clamping on Overall Stress

In order to investigate the effects of clamping on the overall stress state, the radial, the tangential and the axial stress variations along the selected path were compared for different clamping values.

Figure 3.25 illustrates the effects of clamping on radial stress component along path 3, for four fixed values of interference. For 0 interference value, magnitudes of the tensile radial stress are decreasing as the values of interference are increasing. For larger interference values, increasing clamping values decrease the magnitudes of compressive radial stress. As the interference values are increasing, effect of clamping on stress values is getting insignificant.

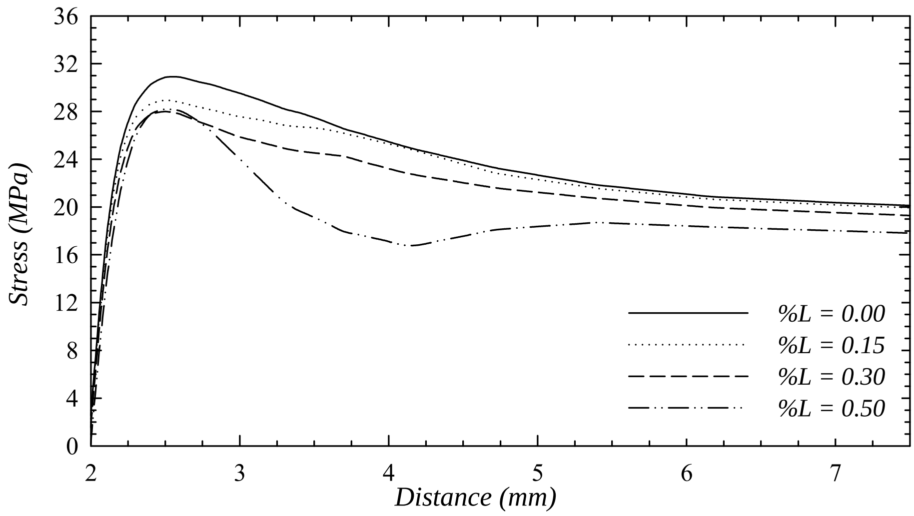

a)

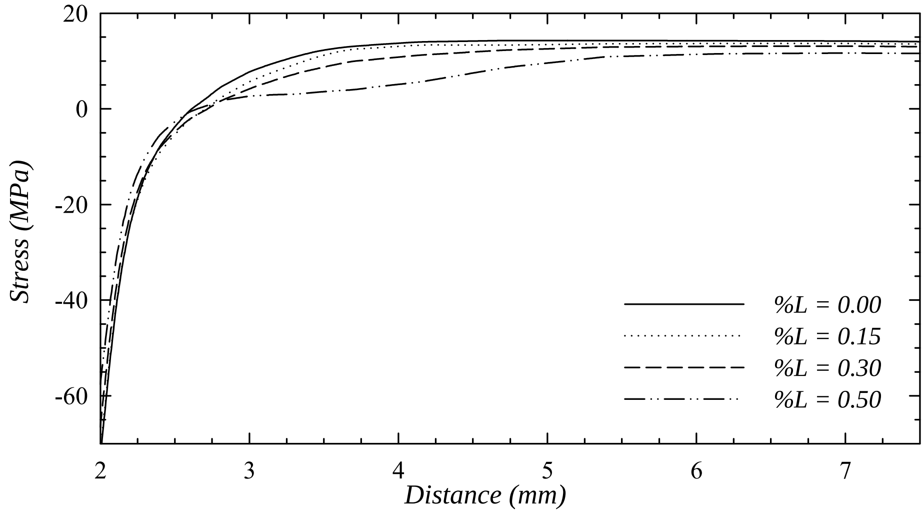
20
0
-20
-40
-60
Stress (MPa)
2
3
4
5
6
7
Distance (mm)
%L = 0.00
%L = 0.15
%L = 0.30
%L = 0.50

b)

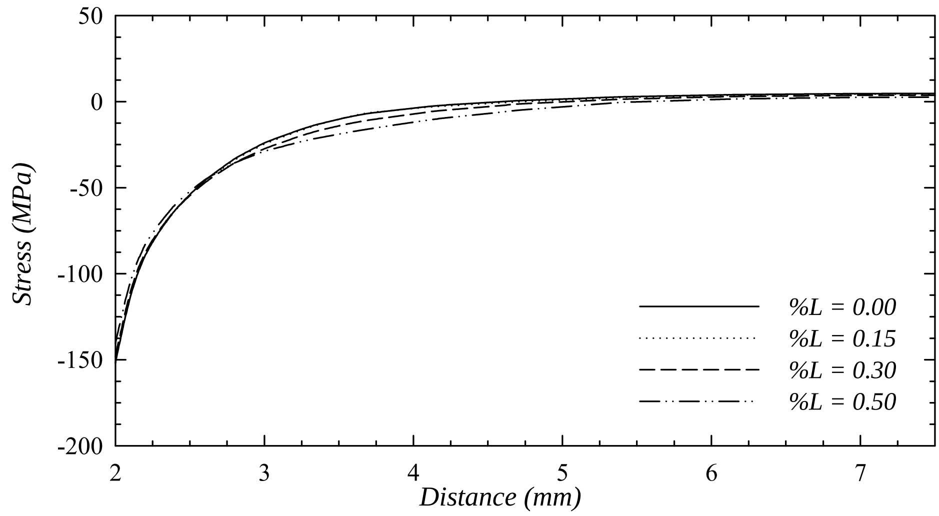
50
0
-50
-100
-150
-200
Stress (MPa)
2
3
4
5
6
7
Distance (mm)
%L = 0.00
%L = 0.15
%L = 0.30
%L = 0.50

c)

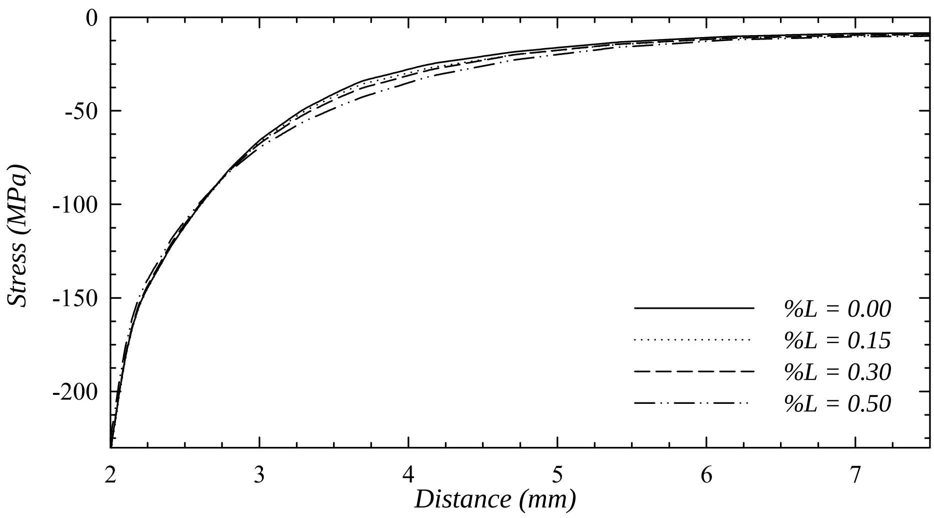

d)

Figure 3.25 Effects of clamping on residual radial stress component along path 3, for the interference: **a)** *%D=0.00,* **b)** *%D=0.15,* **c)** *%D=0.30,* **d)** *%D=0.50*

The effects of clamping on tangential stress component along path 3, for four fixed values of interference are illustrated in Figure 3.26. Magnitudes of the tensile tangential stress are decreasing as the values of clamping are increasing. Effect of clamping is significant near the rivet hole and diminishes as going away from the rivet hole. Also note that, as the interference values are increasing, effect of clamping on stress values is getting insignificant.

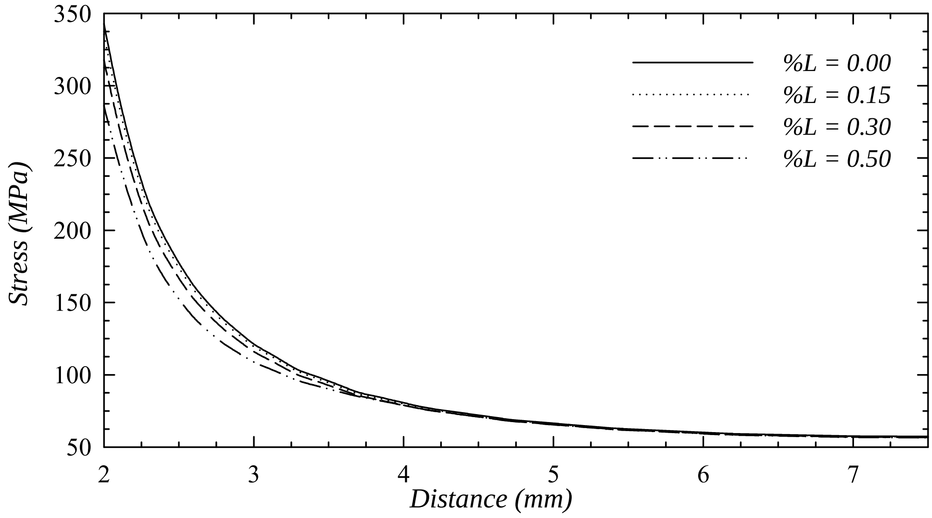

%L = 0.00
%L = 0.15
%L = 0.30
%L = 0.50
Stress (MPa)
Distance (mm)

a)

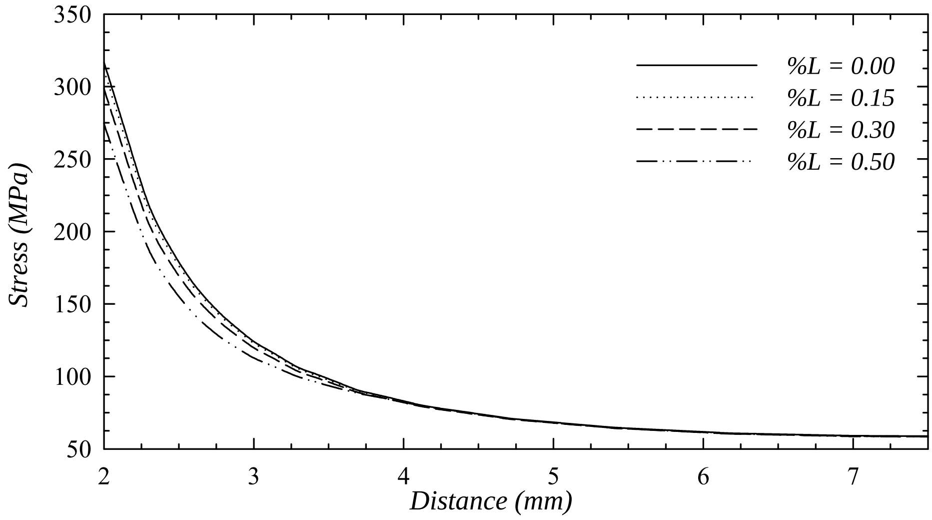

%L = 0.00
%L = 0.15
%L = 0.30
%L = 0.50
Stress (MPa)
Distance (mm)

b)

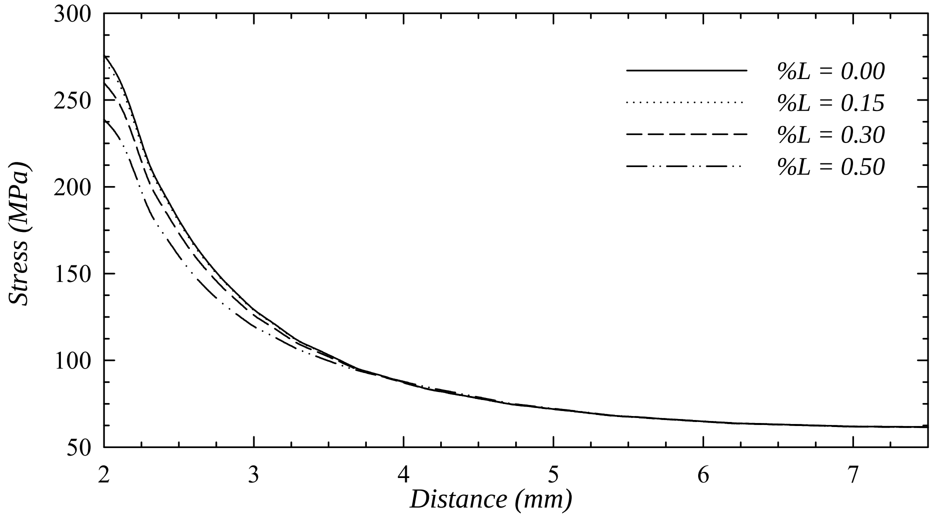

c)

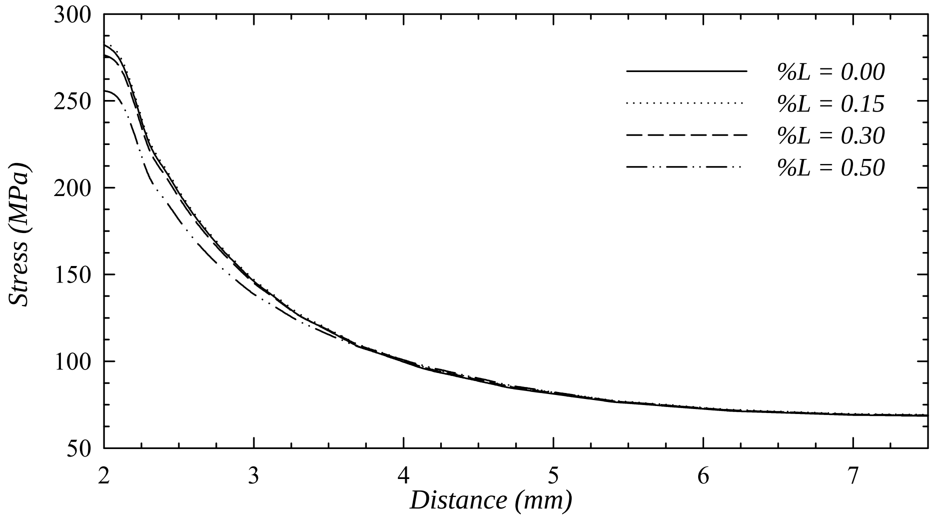

d)

Figure 3.26 Effects of clamping on residual tangential stress component along path 3, for the interference: **a)** *%D=0.00,* **b)** *%D=0.15,* **c)** *%D=0.30,* **d)***%D=0.50*

Figure 3.27 illustrates the effects of clamping on axial stress component along path 3, for four fixed values of interference. For all interference values magnitudes of the compressive axial stress are increasing as the values of clamping are increasing. For fixed values of interference, axial stress values get smaller and diminish at a distance of 4 mm from the rivet hole center as in the case of riveting simulation.

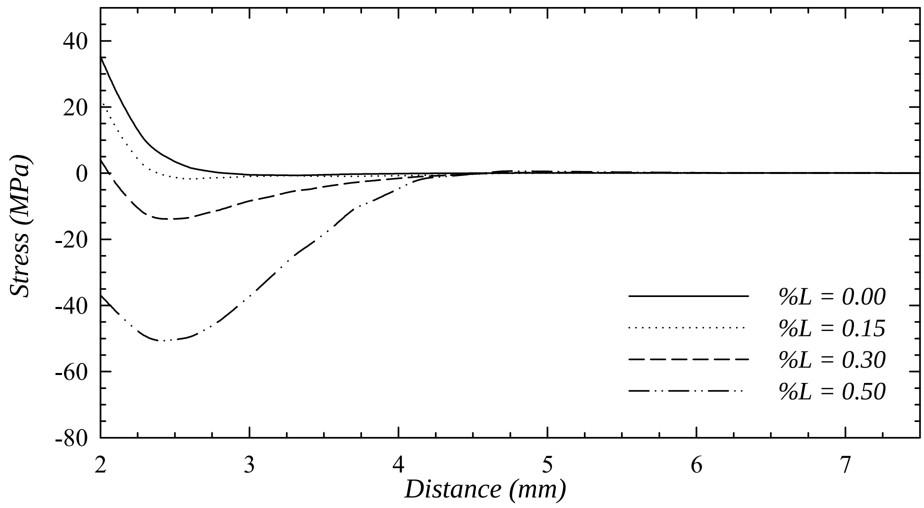

40
20
0
-20
-40
-60
-80
Stress (MPa)
2
3
4
5
6
7
Distance (mm)
%L = 0.00
%L = 0.15
%L = 0.30
%L = 0.50

a)

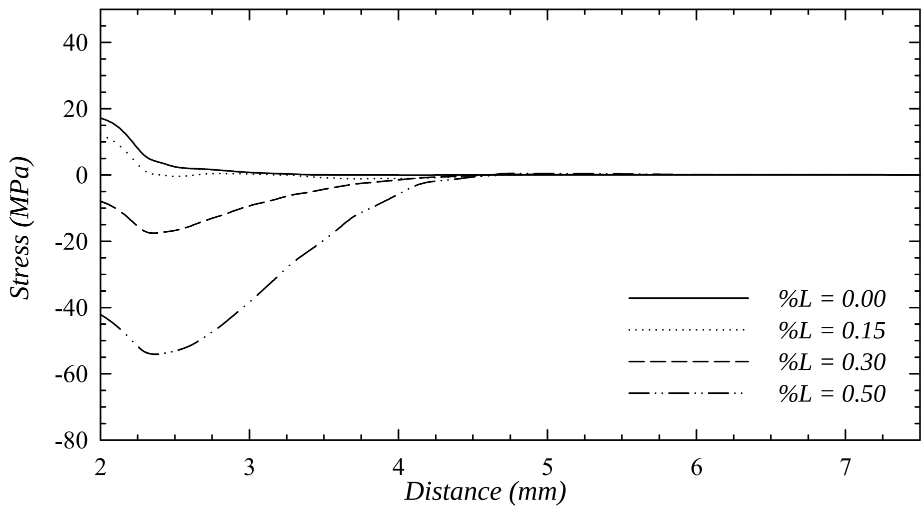

40
20
0
-20
-40
-60
-80
Stress (MPa)
2
3
4
5
6
7
Distance (mm)
%L = 0.00
%L = 0.15
%L = 0.30
%L = 0.50

b)

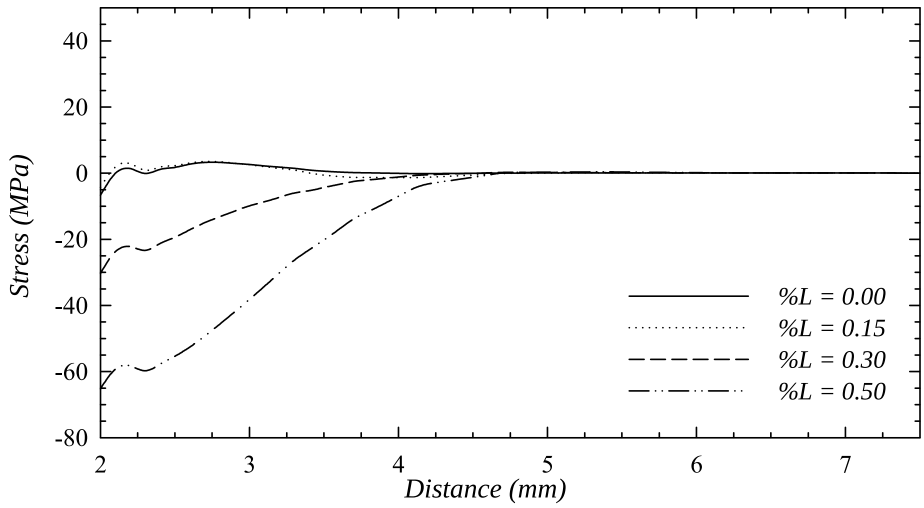

c)

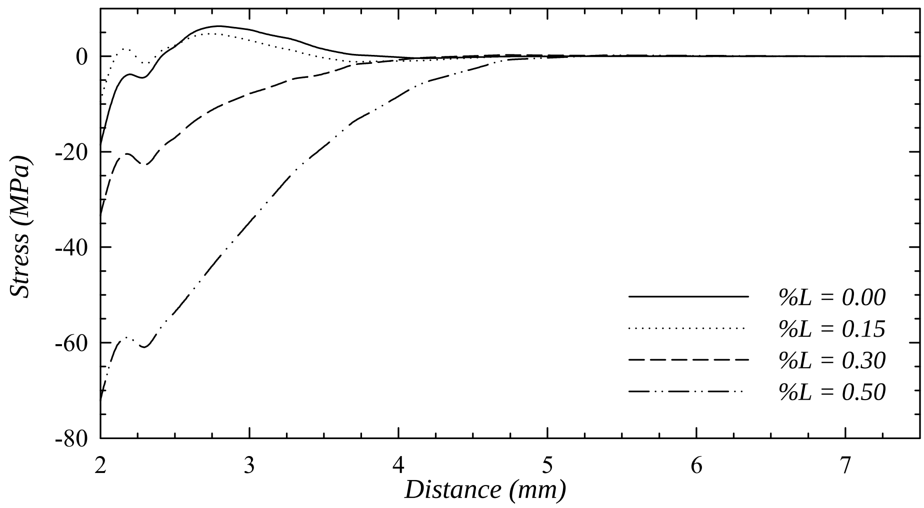

d)

Figure 3.27 Effects of clamping on residual axial stress component along path 1, for the interference: **a)** *%D=0.00,* **b)** *%D=0.15*, **c)** *%D=0.30,* **d)** *%D=0.50*

To sum up, increasing clamping generally increases the radial and axial stress; and decreases the tangential stress components. Effect of clamping on the radial and tangential stress is not much as the interference. Especially for high interference values effect of clamping is getting diminished. Clamping, which is the main cause of axial stress, has a profound effect on axial stress. Axial stress becomes zero at about a distance of 4 mm from the rivet hole center and stay zero beyond this point.

CHAPTER 4

CRACK MODELING AND STRESS INTENSITY FACTOR CALCULATION

4.1 Introduction

In this chapter, stress intensity factor calculations are carried out for semi elliptical surface cracks in a homogenous aluminum alloy plate under tensile loading. Since the crack model obtained in this section will be embedded in the riveted lap joint, crack dimensions and loading are selected accordingly.

A three dimensional finite element model containing a semi elliptical surface crack is generated using ANSYS, and calculated stress intensity factors are compared with those given by Newman and Raju [27] for various crack dimensions under tension load in order to examine the accuracy of the crack model. DCT is utilized to predict the SIF solutions.

This chapter is dedicated to demonstrate the validity and accuracy of the computational method used to evaluate SIFs.

4.2 Geometry of the Problem and Material Model

The geometry of the semi elliptical surface crack in a finite plate is shown at Figure 4.1. The semi elliptical surface crack has a length of $2c$ and a depth of a. The schematic of the crack front is shown at Figure 4.2. This figure illustrates a point P on the crack front that is located by the parametric angle ϕ.

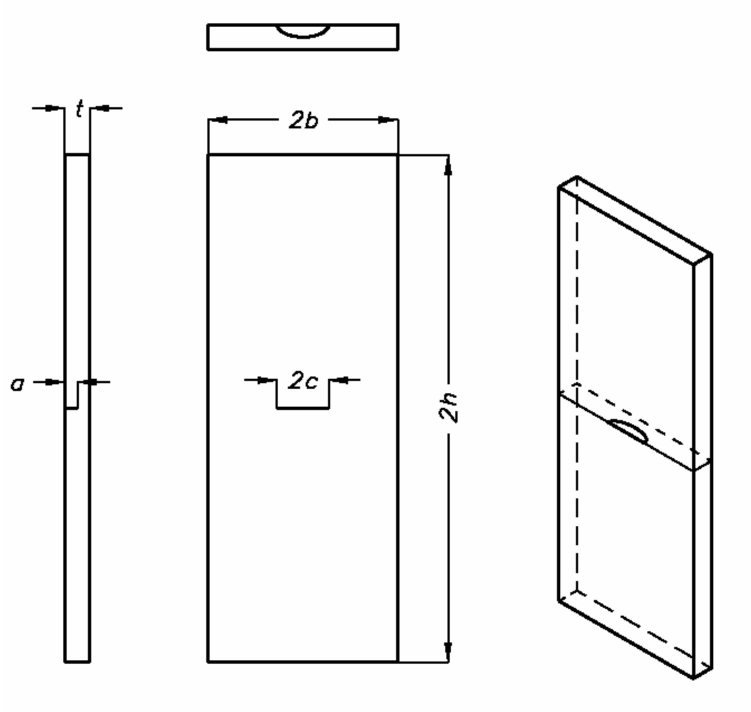

Figure 4.1 The geometry of the cracked plate

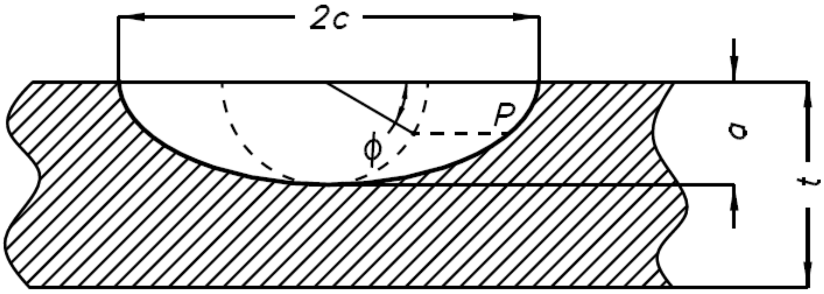

Figure 4.2 The schematic of the crack front for semi elliptical surface crack

Three different crack shapes and five different crack sizes for each crack shapes were modeled. Different crack shapes were obtained by varying the crack depth / half crack length (*a*/*c*) ratio (also known as aspect ratio). Also, different crack sizes were obtained by varying different crack depth / thickness (*a*/*t*) ratios. Sixteen finite element models and corresponding crack geometries are shown in Table 4.1

Table 4.1 Parametric finite element models for different crack shape and size

FE Models	Crack Size	Crack Shape	Crack Depth	Crack Length
#	*a/t*	*a/c*	*a*	*c*
1	0.2	0.6	0.4	2/3
2	0.3	0.6	0.6	1.0
3	0.4	0.6	0.8	4/3
4	0.5	0.6	1.0	5/3
5	0.6	0.6	1.2	2.0
6	0.2	0.8	0.4	0.5
7	0.3	0.8	0.6	0.75
8	0.4	0.8	0.8	1.0
9	0.5	0.8	1.0	1.25
10	0.6	0.8	1.2	1.5
11	0.1	1.0	0.2	0.2
12	0.2	1.0	0.4	0.4
13	0.3	1.0	0.6	0.6
14	0.4	1.0	0.8	0.8
15	0.5	1.0	1.0	1.0
16	0.6	1.0	1.2	1.2

Thickness of the plate (t) is kept constant as *2 mm* since it corresponds to the thickness of the cracked plate in riveted lap joint. Width of the plate ($2b$) is also kept constant as *15 mm* corresponding to the width of the riveted lap joint. Length of the plate ($2h$) is taken as *30 mm.*

The material of the plate is 2024-T3 aluminum alloy, which is the plate material in riveted lap joint. Elastic properties of the material are taken from Table 2.1. In order to make results comparable to the study of Newman and Raju [27], aluminum alloy 2014-T651 is also used in the comparison analysis. The elastic modulus and the Poisson’s ratio of the aluminum alloy 2014-T651 are given as 73.1 GPa and 0.33, respectively.

4.3 The Finite Element Model

Three dimensional finite element model of the cracked specimen obtained by ANSYS is shown in Figure 4.3. ANSYS Parametric Design Language (APDL) subroutines are highly utilized for generating the finite element model. Even though a quarter of the model is sufficient because of the symmetry, a full of the model is chosen in this study. Because this crack model will be used in the riveted lap joint analysis, and the crack in the lap joint analysis should be full in nature.

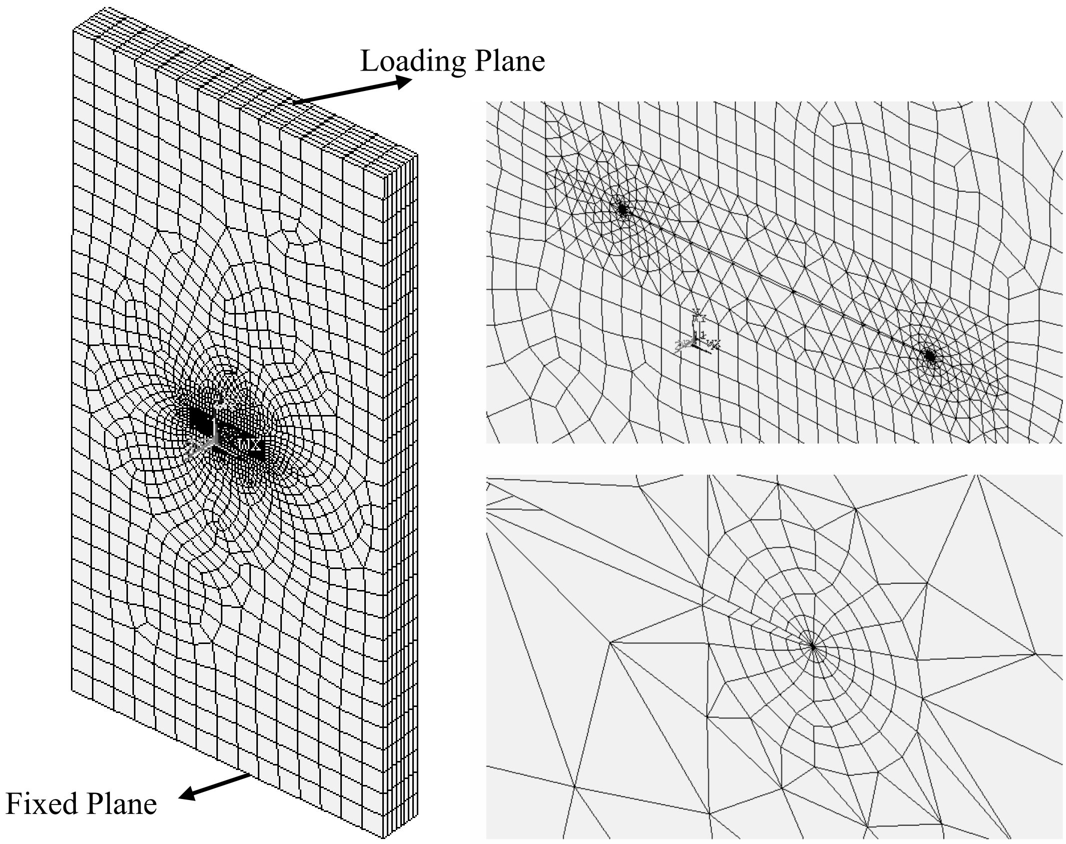

Figure 4.3 Finite element model of specimen and close-up view of the crack

Meshing facet elements (MESH200) and three dimensional 20-node structural solid elements (SOLID186) are used for the mesh generation. MESH200 is a mesh-only element which contributes nothing to the solution. This element type is employed to produce mesh area around crack tip with singular elements. The SOLID186 type element is used to produce three dimensional mesh around the crack front by sweeping mesh area around crack tip. This element type is also used to produce mesh for the remaining part of the plate. The characteristics of this type of element are given in part 3.2.

Due to the sharp crack tip, stress and deformation fields around the crack tip normally have high gradients. In order to capture this effect, a refined mesh in the region around the crack tip should be used. For linear elastic problems, the displacements near the crack tip (or crack front) vary as $1/\sqrt{r}$, where r is the radial distance from the crack tip. The stresses and strains are singular at the crack tip, varying as $1/\sqrt{r}$, which is known as square-root strain singularity. To simulate this singularity in finite element model, the crack tip mesh should have certain characteristics: the crack faces should be coincident and singular elements should be used around the crack tip (or crack front). In this analysis, in order to simulate the square-root strain singularity around the crack front, collapsed 20-node isoparametric brick elements are used. For this 20 node isoparametric three dimensional brick element is collapsed by moving the mid points nodes to the quarter points (Figure 4.4) [31].

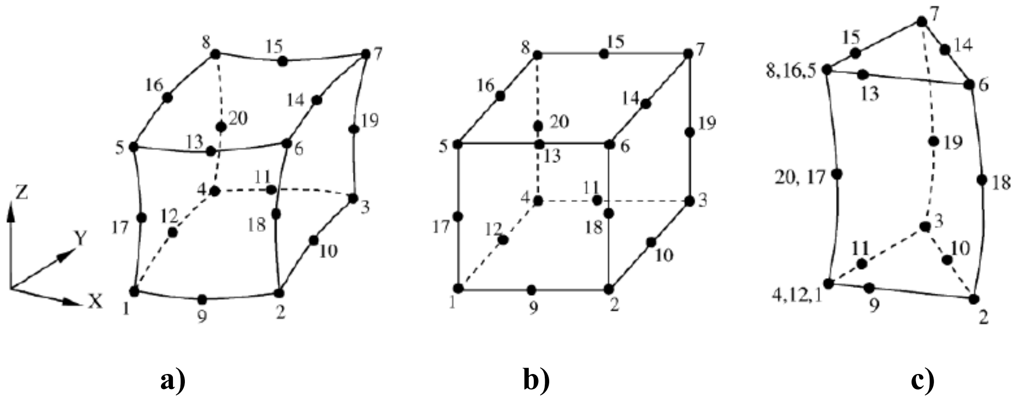

Figure 4.4 20 node isoparametric brick element **a)** in physical space **b)** in isoparametric space **c)** collapsed form

In order to create three-dimensional crack elements, first the area mesh is generated with MESH200 element. After obtaining two-dimensional singular area elements (Figure 4.5), the volume mesh is generated by extruding the area elements along the crack front. Thus three-dimensional volume mesh including singular elements around crack front is obtained (Figure 4.6). The radius of the singular elements is taken as 0.003 mm. Moreover, sixteen singular elements are used around the crack front. After iterating various number and radius of the singular elements, this combination is found to give more accurate results.

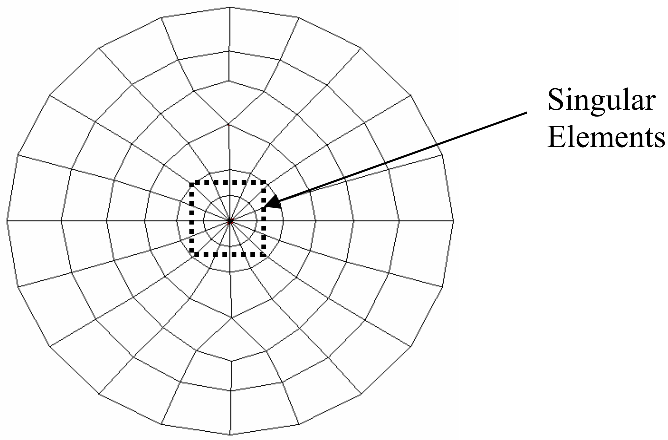

Figure 4.5 Two dimensional mesh area around crack tip with singular elements

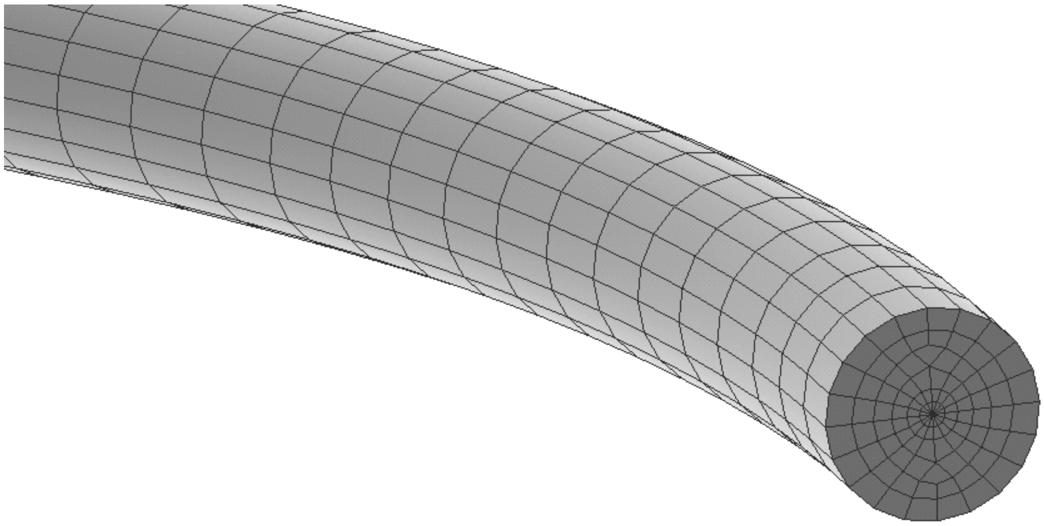

Figure 4.6 Mesh around crack front obtained by sweeping mesh area around crack tip

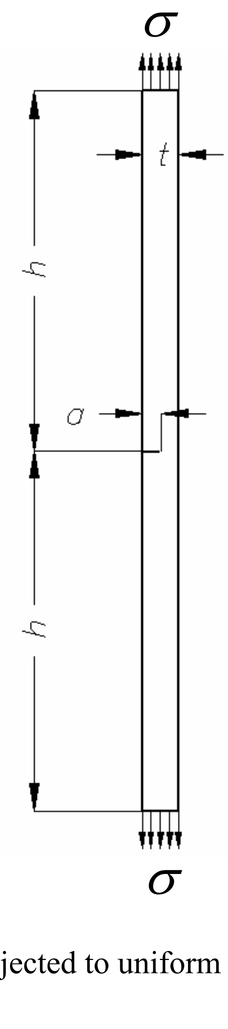

Figure 4.7 Plate subjected to uniform tension load at the ends

The specimen is subjected to uniform tensile stress σ, at the upper and lower ends. Figure 4.7 illustrates the loading on the specimen. Applied load σ is taken as 68.6 MPa which is the loading applied on the riveted lap joint.

4.5 Model Validation

In order to validate the numerical method, results of the present study were compared to the results found by analytical expressions of Newman and Raju [27] for various crack dimensions. These comparisons were carried out to check the accuracy of the crack modeling and SIF calculation procedures.

For the comparison aim, stress intensity factors were normalized as follows:

$$F = \frac{K}{\sigma \cdot \sqrt{\frac{\pi \cdot a}{Q}}} \tag{4.1}$$

where σ is the applied stress, a is the crack depth and Q is the shape factor for an elliptical crack. Empirical expression of the shape factor, Q, for an ellipse is given by Newman and Raju [27] as:

$$Q = 1 + 1.464 \cdot \left(\frac{a}{c}\right)^{1.65}, \quad \text{for} \left(\frac{a}{c}\right) \leq 1 \tag{4.2}$$

Normalized stress intensity factors were obtained for different crack shapes and sizes. Comparisons were carried out for polar angle from 0 to 90 degrees (for half of the crack) due to the symmetry condition of the model. Normalized mode I stress intensity factors were tabulated in Table 4.2 through Table 4.4. Normalized stress intensity factors are tabulated with respect to normalized polar angle along the crack front ($2\phi / \pi$).

Table 4.2 Comparisons of the normalized mode I stress intensity factors F_I for a plate subjected to uniform tension, $a/c = 0.6$

Normalized Parametric Angle	$a/t = 0.2$			$a/t = 0.3$		
$2\phi/\pi$	Ref [27]	Present Study	% Diff.	Ref [27]	Present Study	% Diff.
1.0000	1.0995	1.1048	0.4864	1.1288	1.1369	2.9016
0.8622	1.0914	1.0977	0.5803	1.1205	1.1307	3.0059
0.7244	1.0682	1.0761	0.7429	1.0968	1.1084	3.0033
0.5867	1.0335	1.0427	0.8956	1.0618	1.0749	3.0846
0.4489	0.9929	1.0005	0.7623	1.0216	1.0343	3.3791
0.3111	0.9547	0.9587	0.4168	0.9849	0.9936	3.6423
0.1733	0.9313	0.9350	0.3977	0.9646	0.9709	3.8448
0.0356	0.9395	0.9619	2.3833	0.9782	1.0023	4.1959
0.0000	0.9488	0.9150	3.5585	0.9894	0.9445	3.2303

Normalized Parametric Angle	$a/t = 0.4$			$a/t = 0.5$		
$2\phi/\pi$	Ref [27]	Present Study	% Diff.	Ref [27]	Present Study	% Diff.
1.0000	1.1690	1.1767	0.6532	1.2190	1.2190	0.0030
0.8622	1.1604	1.1698	0.8065	1.2100	1.2139	0.3236
0.7244	1.1362	1.1492	1.1518	1.1850	1.1986	1.1443
0.5867	1.1008	1.1192	1.6749	1.1493	1.1716	1.9397
0.4489	1.0611	1.0805	1.8206	1.1107	1.1366	2.3283
0.3111	1.0268	1.0431	1.5947	1.0797	1.1053	2.3726
0.1733	1.0112	1.0243	1.2946	1.0707	1.0930	2.0770
0.0356	1.0329	1.0638	2.9870	1.1036	1.1458	3.8294
0.0000	1.0468	0.9960	4.8573	1.1213	1.0701	4.5617

(continued)

Table 4.2 Continued

Normalized Parametric Angle	$a/t = 0.6$		
$2\phi/\pi$	Ref [27]	Present Study	% Diff.
1.0000	1.2770	1.2577	1.5081
0.8622	1.2676	1.2559	0.9254
0.7244	1.2418	1.2502	0.6748
0.5867	1.2059	1.2266	1.7214
0.4489	1.1690	1.2029	2.9035
0.3111	1.1427	1.1792	3.1962
0.1733	1.1427	1.1761	2.9227
0.0356	1.1901	1.2486	4.9143
0.0000	1.2127	1.1582	4.4957

Table 4.3 Comparisons of the normalized mode I stress intensity factors F_I for a plate subjected to uniform tension, $a/c = 0.8$

Normalized Parametric Angle	$a/t = 0.2$			$a/t = 0.3$		
$2\phi/\pi$	Ref [27]	Present Study	% Diff.	Ref [27]	Present Study	% Diff.
1.0000	1.0723	1.0801	0.7294	1.0900	1.1016	1.0638
0.8622	1.0679	1.0768	0.8401	1.0855	1.0983	1.1779
0.7244	1.0559	1.0679	1.1359	1.0735	1.0898	1.5175
0.5867	1.0400	1.0542	1.3659	1.0579	1.0780	1.9012
0.4489	1.0256	1.0405	1.4581	1.0447	1.0638	1.8202
0.3111	1.0192	1.0331	1.3632	1.0410	1.0589	1.7224
0.1733	1.0277	1.0431	1.4960	1.0539	1.0716	1.6859
0.0356	1.0570	1.0924	3.3495	1.0897	1.1273	3.4542
0.0000	1.0684	1.0281	3.7777	1.1031	1.0492	4.8856

(continued)

Table 4.3 Continued

Normalized Parametric Angle	$a/t = 0.4$			$a/t = 0.5$		
$2\phi/\pi$	Ref [27]	Present Study	% Diff.	Ref [27]	Present Study	% Diff.
1.0000	1.1140	1.1269	1.1525	1.1435	1.1518	0.7255
0.8622	1.1095	1.1241	1.3139	1.1388	1.1501	0.9967
0.7244	1.0974	1.1164	1.7325	1.1267	1.1445	1.5773
0.5867	1.0824	1.1060	2.1865	1.1124	1.1394	2.4289
0.4489	1.0710	1.0974	2.4640	1.1035	1.1372	3.0606
0.3111	1.0710	1.0952	2.2567	1.1086	1.1399	2.8206
0.1733	1.0903	1.1138	2.1548	1.1365	1.1661	2.6074
0.0356	1.1355	1.1752	3.4986	1.1942	1.2398	3.8188
0.0000	1.1519	1.0875	5.5908	1.2145	1.1322	6.7726

Normalized Parametric Angle	$a/t = 0.6$		
$2\phi/\pi$	Ref [27]	Present Study	% Diff.
1.0000	1.1769	1.1724	0.3803
0.8622	1.1721	1.1726	0.0402
0.7244	1.1600	1.1743	1.2298
0.5867	1.1467	1.1724	2.2364
0.4489	1.1410	1.1760	3.0677
0.3111	1.1528	1.1911	3.3226
0.1733	1.1916	1.2293	3.1663
0.0356	1.2653	1.3187	4.2193
0.0000	1.2905	1.2019	6.8658

Table 4.4 Comparisons of the normalized mode I stress intensity factors F_I for a plate subjected to uniform tension, $a/c = 1.0$

Normalized Parametric Angle	$a/t = 0.1$			$a/t = 0.2$		
$2\phi/\pi$	Ref [27]	Present Study	% Diff.	Ref [27]	Present Study	% Diff.
1.0000	1.0421	1.0482	0.5882	1.0483	1.0611	1.2198
0.8622	1.0421	1.0492	0.6846	1.0483	1.0623	1.3334
0.7244	1.0430	1.0534	0.9970	1.0493	1.0665	1.6414
0.5867	1.0465	1.0603	1.3212	1.0532	1.0732	1.9001
0.4489	1.0554	1.0720	1.5704	1.0631	1.0856	2.1159
0.3111	1.0724	1.0915	1.7834	1.0819	1.1060	2.2299
0.1733	1.0997	1.1257	2.3618	1.1121	1.1405	2.5493
0.0356	1.1382	1.1876	4.3380	1.1548	1.2057	4.4088
0.0000	1.1499	1.1382	1.0175	1.1678	1.1258	3.5920

Normalized Parametric Angle	$a/t = 0.3$			$a/t = 0.4$		
$2\phi/\pi$	Ref [27]	Present Study	% Diff.	Ref [27]	Present Study	% Diff.
1.0000	1.0585	1.0756	1.6095	1.0726	1.0927	1.8810
0.8622	1.0586	1.0774	1.7699	1.0727	1.0946	2.0428
0.7244	1.0597	1.0819	2.0945	1.0740	1.1004	2.4611
0.5867	1.0643	1.0906	2.4695	1.0795	1.1114	2.9528
0.4489	1.0758	1.1042	2.6441	1.0933	1.1277	3.1481
0.3111	1.0977	1.1265	2.6239	1.1197	1.1548	3.1429
0.1733	1.1329	1.1638	2.7258	1.1620	1.1983	3.1279
0.0356	1.1826	1.2331	4.2653	1.2217	1.2729	4.1898
0.0000	1.1977	1.1411	4.7304	1.2399	1.1688	5.7321

(continued)

Table 4.4 Continued

Normalized Parametric Angle	$a/t=0.5$			$a/t=0.6$		
$2\phi/\pi$	Ref [27]	Present Study	% Diff.	Ref [27]	Present Study	% Diff.
1.0000	1.0898	1.1090	1.7688	1.1094	1.1216	1.0969
0.8622	1.0899	1.1115	1.9882	1.1095	1.1245	1.3514
0.7244	1.0915	1.1198	2.5877	1.1115	1.1385	2.4237
0.5867	1.0982	1.1343	3.2869	1.1198	1.1578	3.3930
0.4489	1.1151	1.1561	3.6777	1.1404	1.1859	3.9845
0.3111	1.1473	1.1880	3.5504	1.1800	1.2268	3.9668
0.1733	1.1990	1.2396	3.3911	1.2434	1.2883	3.6151
0.0356	1.2719	1.3264	4.2840	1.3329	1.3935	4.5472
0.0000	1.2941	1.2095	6.5356	1.3601	1.2529	7.8843

Trends and difference between the reference and the results of the present study can be seen more clearly in plots. Therefore the variation of the normalized stress intensity factors are plotted with respect to normalized polar angle ($2\phi/\pi$) in Figures 4.8 through 4.10.

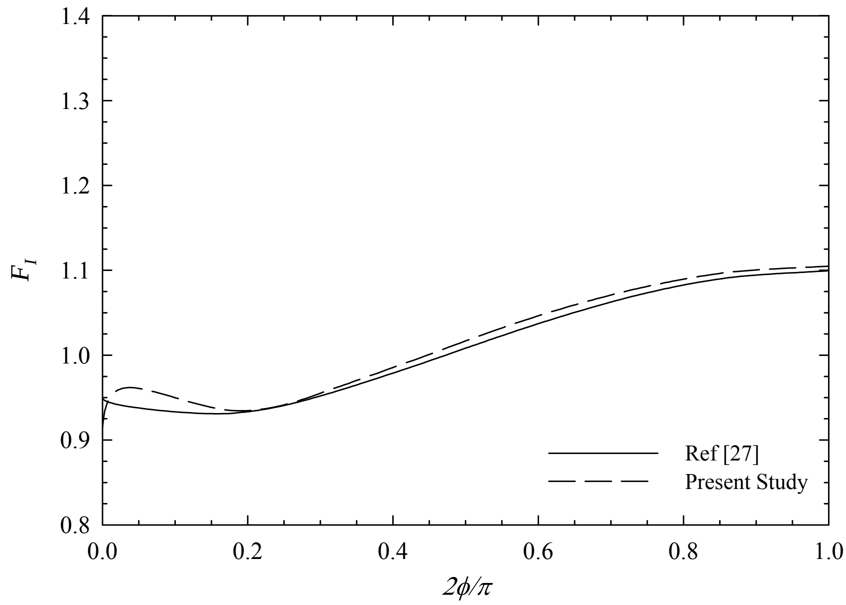

a)

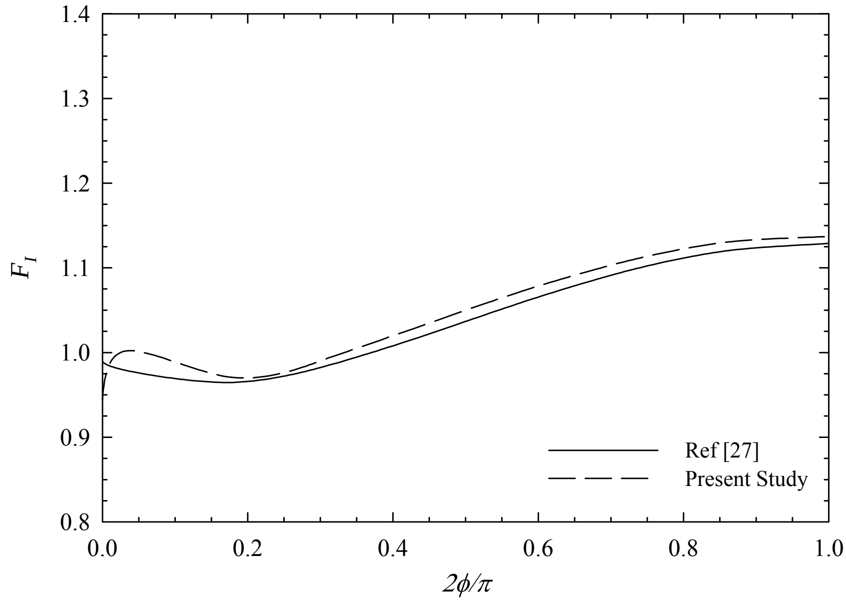
1.4
1.3
1.2
1.1
1.0
0.9
0.8
F_I
0.0
0.2
0.4
0.6
0.8
1.0
$2\phi/\pi$
Ref [27]
Present Study

b)

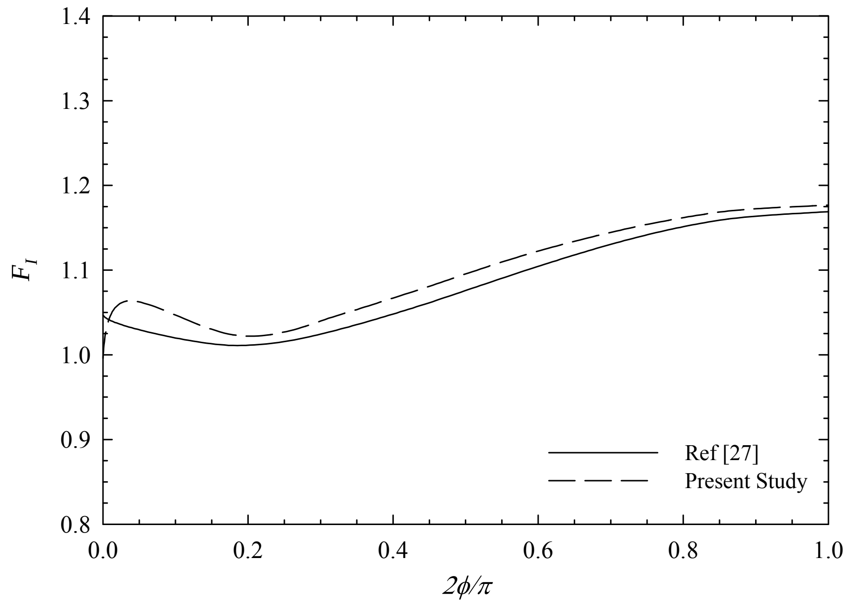
1.4
1.3
1.2
1.1
1.0
0.9
0.8
F_I
0.0
0.2
0.4
0.6
0.8
1.0
$2\phi/\pi$
Ref [27]
Present Study

c)

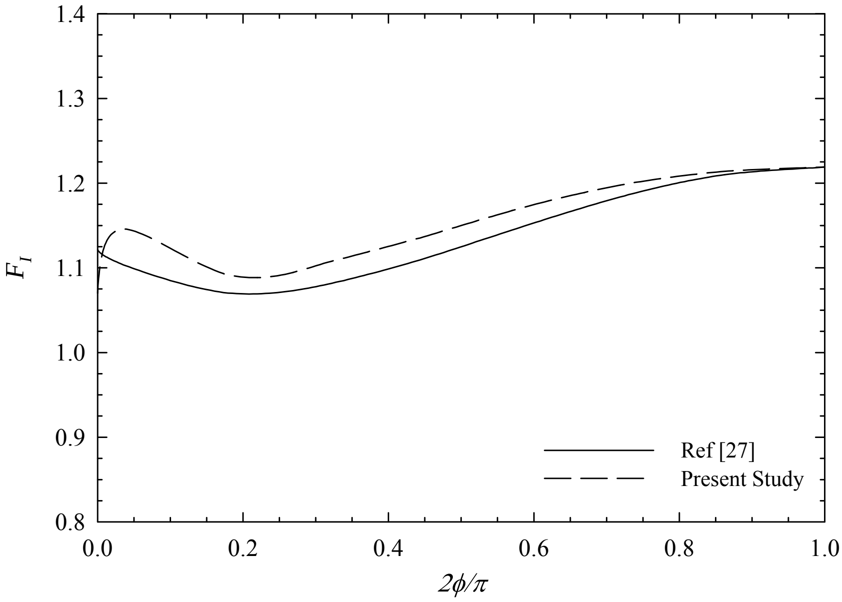

d)

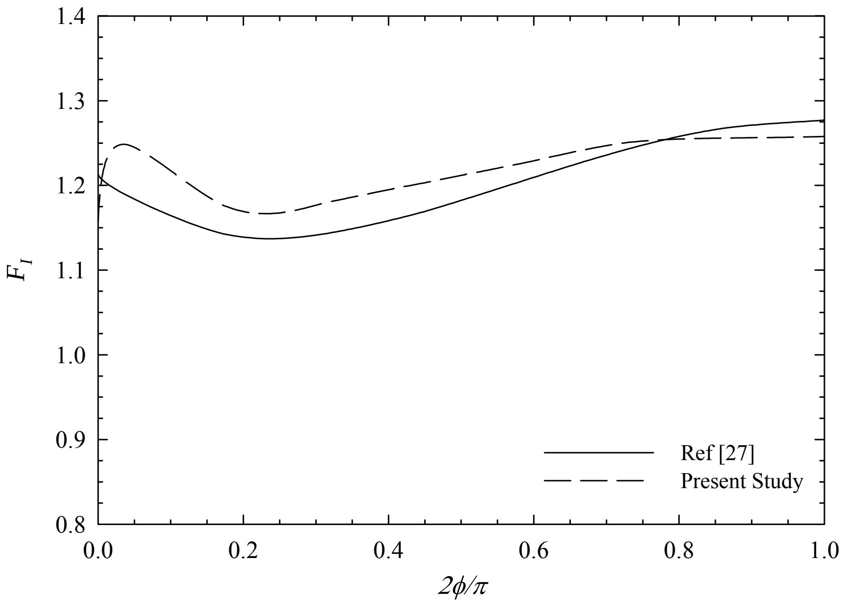

e)

Figure 4.8 Comparisons of the normalized mode I stress intensity factors F_I for crack shape *a/c=0.6,* **a)** *a/t=0.2,* **b)** *a/t=0.3,* **c)** *a/t=0.4,* **d)** *a/t=0.5,* **e)** *a/t=0.6*

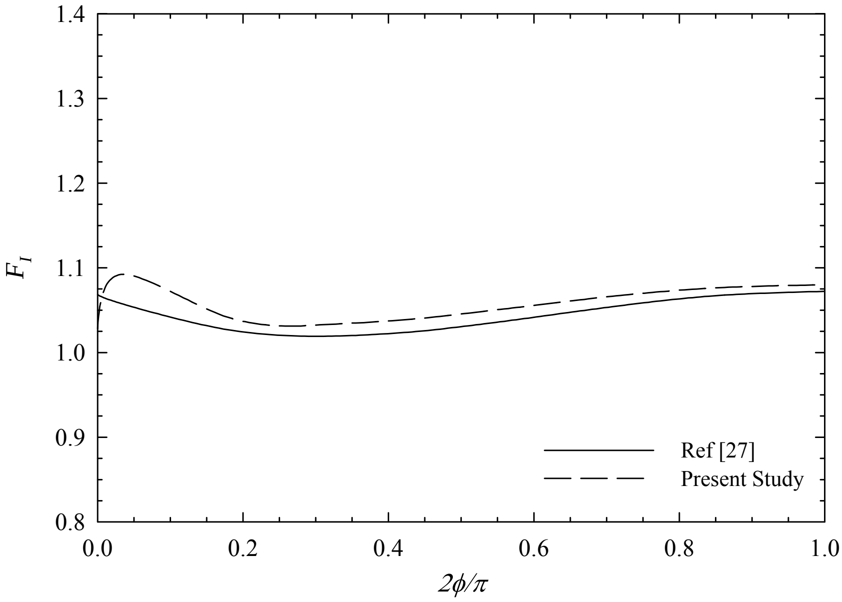
1.4
1.3
1.2
1.1
1.0
0.9
0.8
F_I
0.0
0.2
0.4
0.6
0.8
1.0
$2\phi/\pi$
Ref [27]
Present Study

a)

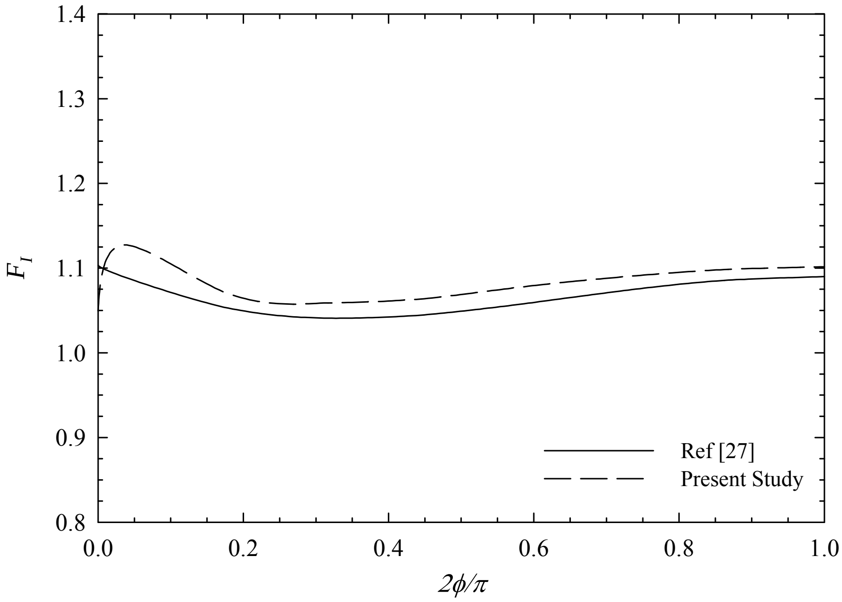
1.4
1.3
1.2
1.1
1.0
0.9
0.8
F_I
0.0
0.2
0.4
0.6
0.8
1.0
$2\phi/\pi$
Ref [27]
Present Study

b)

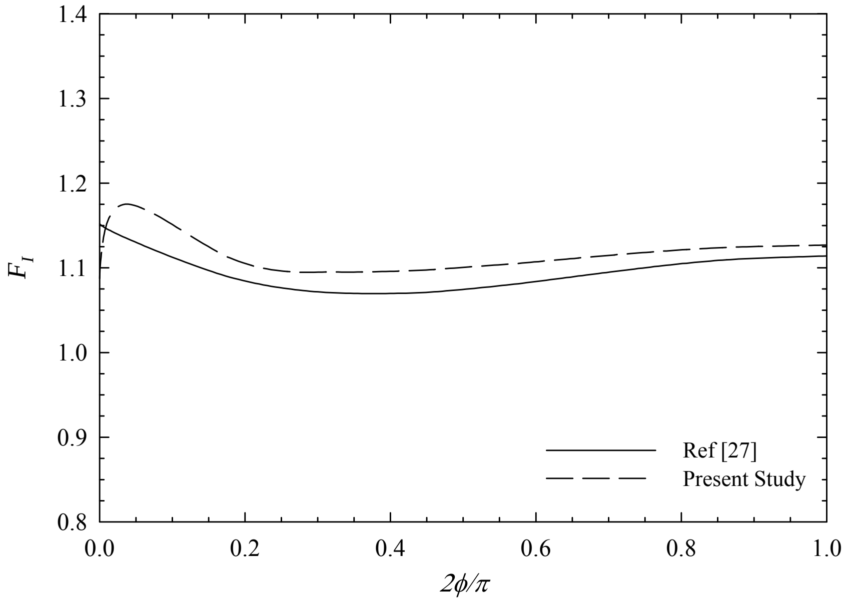
1.4
1.3
1.2
1.1
1.0
0.9
0.8
F_I
0.0
0.2
0.4
0.6
0.8
1.0
$2\phi/\pi$
Ref [27]
Present Study

c)

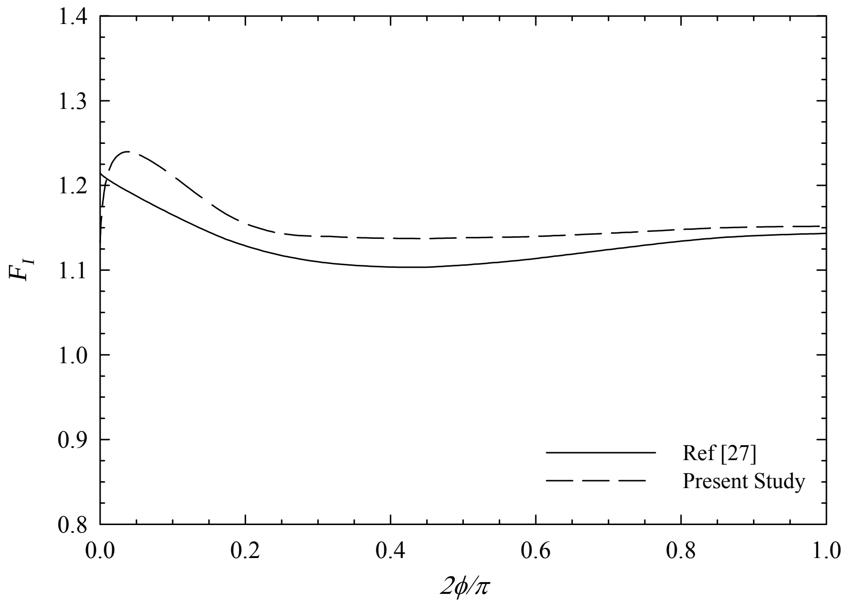
1.4
1.3
1.2
1.1
1.0
0.9
0.8
F_I
0.0
0.2
0.4
0.6
0.8
1.0
$2\phi/\pi$
Ref [27]
Present Study

d)

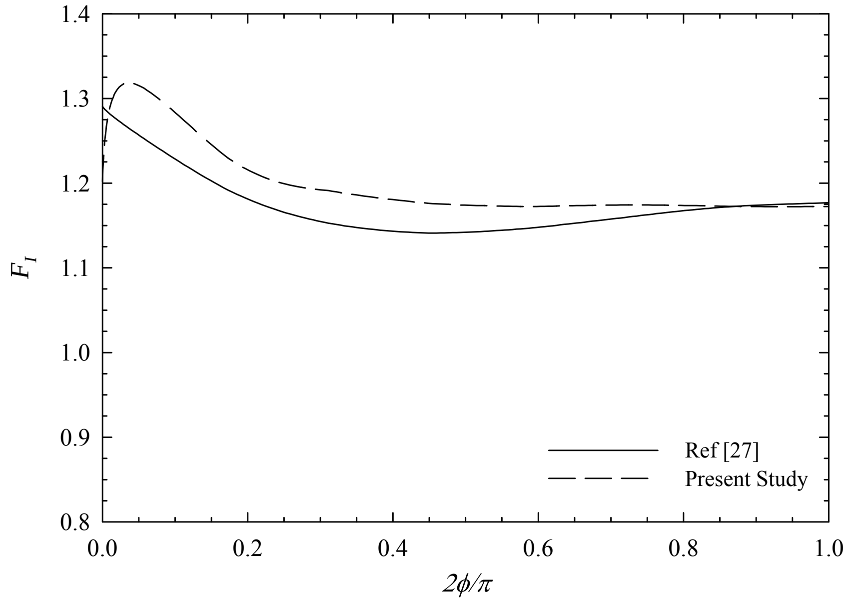

e)

Figure 4.9 Comparisons of the normalized mode I stress intensity factors F_I for crack shape *a/c=0.8,* **a)** *a/t=0.2,* **b)** *a/t=0.3,* **c)** *a/t=0.4,* **d)** *a/t=0.5,* **e)** *a/t=0.6*

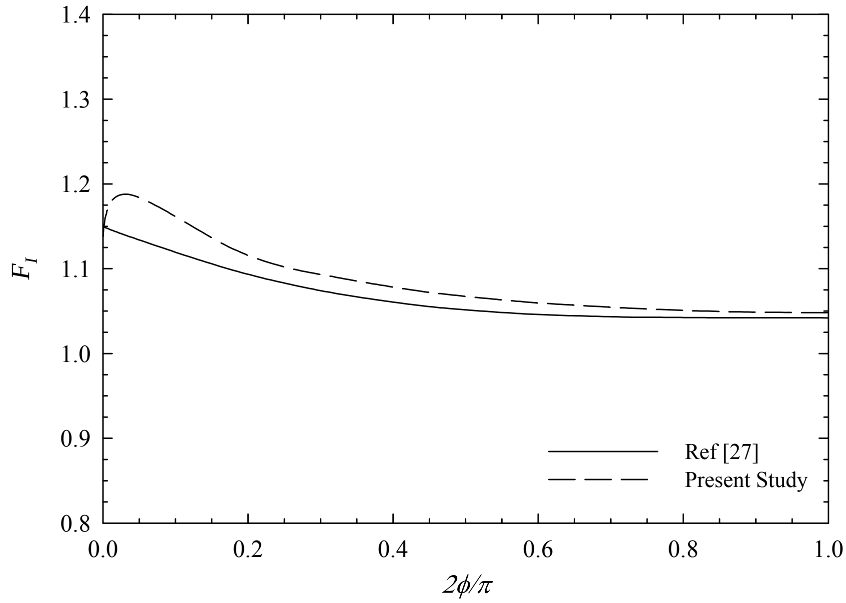

a)

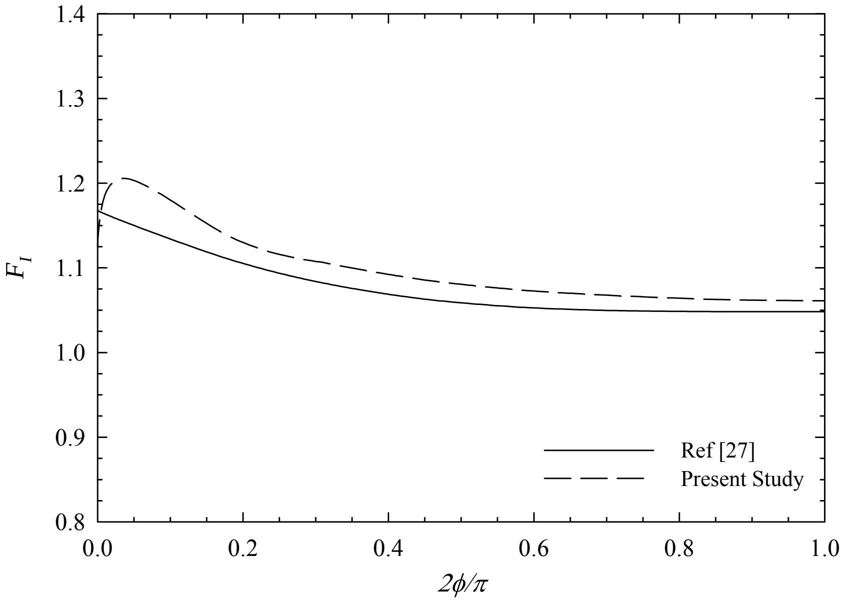
1.4
1.3
1.2
1.1
1.0
0.9
0.8
F_I
0.0
0.2
0.4
0.6
0.8
1.0
$2\phi/\pi$
Ref [27]
Present Study

b)

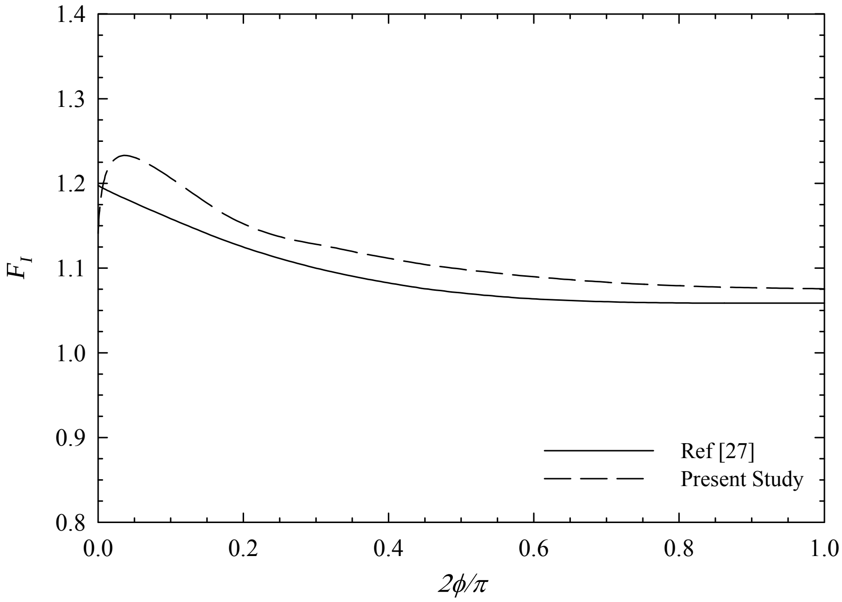
1.4
1.3
1.2
1.1
1.0
0.9
0.8
F_I
0.0
0.2
0.4
0.6
0.8
1.0
$2\phi/\pi$
Ref [27]
Present Study

c)

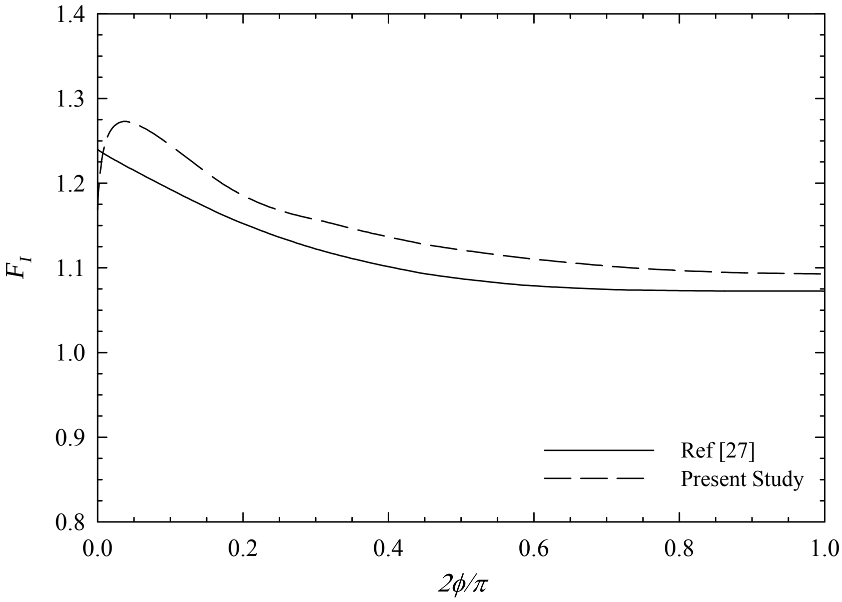
1.4
1.3
1.2
1.1
1.0
0.9
0.8
F_I
0.0
0.2
0.4
0.6
0.8
1.0
$2\phi/\pi$
Ref [27]
Present Study

d)

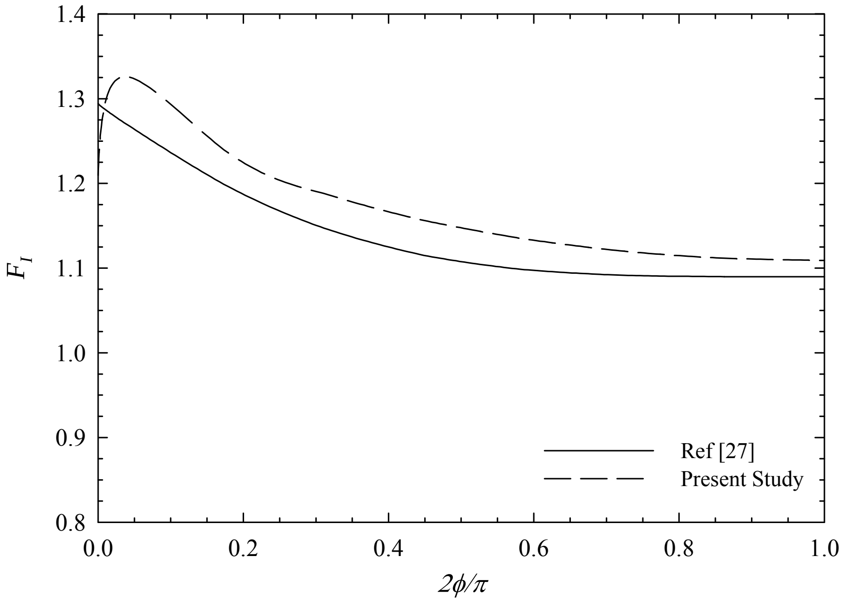
1.4
1.3
1.2
1.1
1.0
0.9
0.8
F_I
0.0
0.2
0.4
0.6
0.8
1.0
$2\phi/\pi$
Ref [27]
Present Study

e)

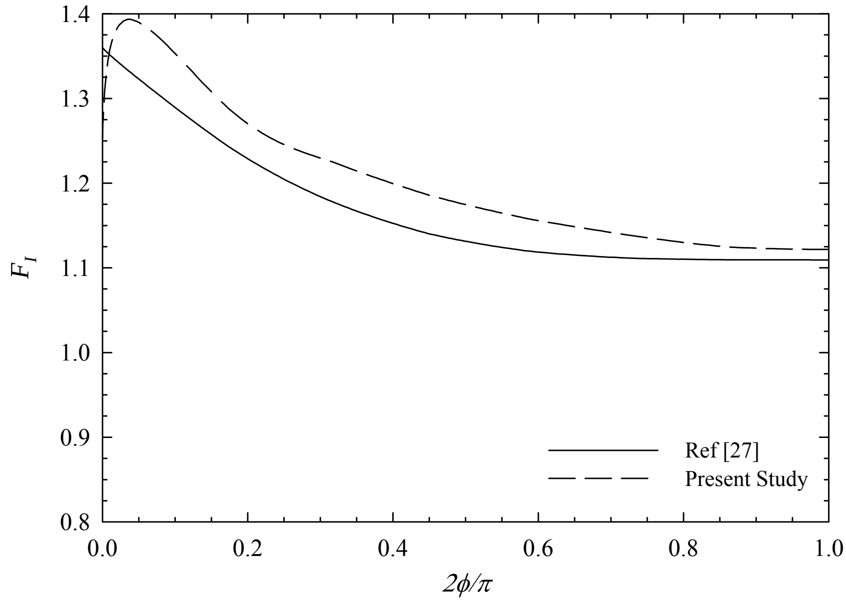

f)

Figure 4.10 Comparisons of the normalized mode I stress intensity factors F_I for crack the shape *a/c=1.0,* **a)** *a/t=0.1,* **b)** *a/t=0.2,* **c)** *a/t=0.3,* **d)** *a/t=0.4,* **e)** *a/t=0.5,* **f)** *a/t=0.6*

From the Figures 4.8 through 4.10, similar trends in SIF variation along the crack front are observed for each crack dimension. For all crack geometries, differences between the reference and the current study get diminished towards the deep point on the crack front ($2\phi/\pi \rightarrow 1$). The largest differences are observed near the free surface ($2\phi/\pi \rightarrow 0$). Except from a few free surfaces all differences are less than 5%. Maximum values of percent differences above 5% at the free surface are about 5.59%, 6.77%, and 6.87% for *a/c* = 0.8 and *a/t* = 0.4, 0.5, and 0.6 respectively. For *a/c* = 1.0; 5.73%, 6.54%, and 7.88% differences are observed for *a/t* = 0.4, 0.5, and 0.6, respectively.

The empirical SIF equations used for the comparison aim were obtained from a previous three dimensional finite element analysis. Newman and Raju [27] stated that for all calculations for which ratios of crack depth to plate thickness do not exceed 0.8 ($a/t \leq 0.8$), the equation is within ±5 % of the finite element results. For sixteen models, each model contains seventeen points; 272 SIF values are calculated. Six of them exceed 5% differences, which means about 98% of the calculated values are within the desired range. Therefore it can be said that the accuracy of the finite element model is acceptable.

As stated before, the largest differences between the present study and the Reference [27] are obtained at the free surfaces. It is known to be due to the free surface effects at the boundary zone [34]. Ayhan and Nied [34] have showed that, free surface effect is confined to a very small region near the free surface. As a result, the free surface effect is not considered in this study. Stress intensity factors calculated in this study can be employed as approximate stress intensity factors at the free surface.

4.5 Numerical Results and Conclusions

For the finite element models described above, mode I stress intensity factor distributions along the crack front were obtained for different crack shapes and sizes. Stress intensity factors were plotted with respect to normalized polar angle along the crack front (ϕ/π). Stress intensity factors are calculated at seventeen points on crack front (Figure 4.11). Near the free surfaces, two points close to the each other are selected to calculate SIFs at the free surface and very near to the free surface.

Figure 4.12 shows the variations of SIFs with changing crack size for fixed crack shape. From these figures, it can be observed that stress intensity factors are increasing with increase in a/t ratios (i.e. the increase in crack size) for all crack shapes. Maximum values of the stress intensity factors are observed near the deepest point on the crack front ($\phi/\pi \rightarrow 0.5$) for the crack shape *a/c*=0.6, and near the free surface on the crack front ($\phi/\pi \rightarrow 0$ and $\phi/\pi \rightarrow 1$) for the crack shape *a/c*=1.0. For the crack shape (*a/c*=0.8), relatively uniform variation along the crack front is observed. For all models, symmetry condition of the results is clearly seen on these figures.

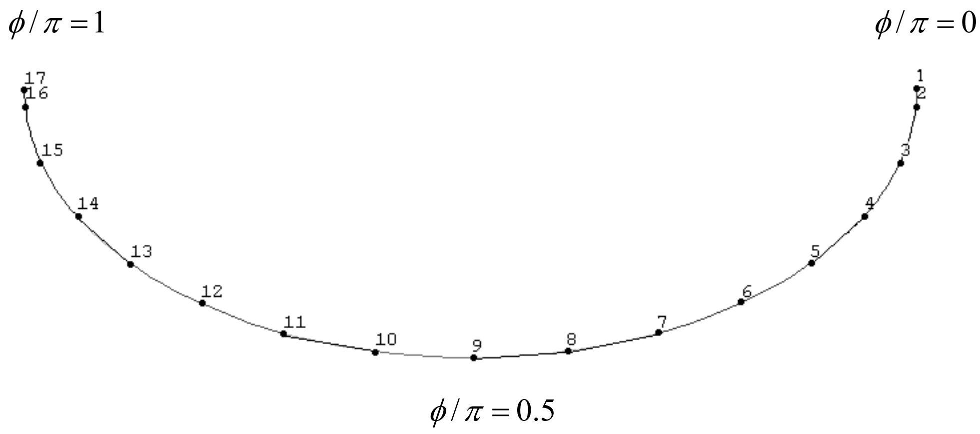

Figure 4.11 Points on crack front at which SIFs are calculated

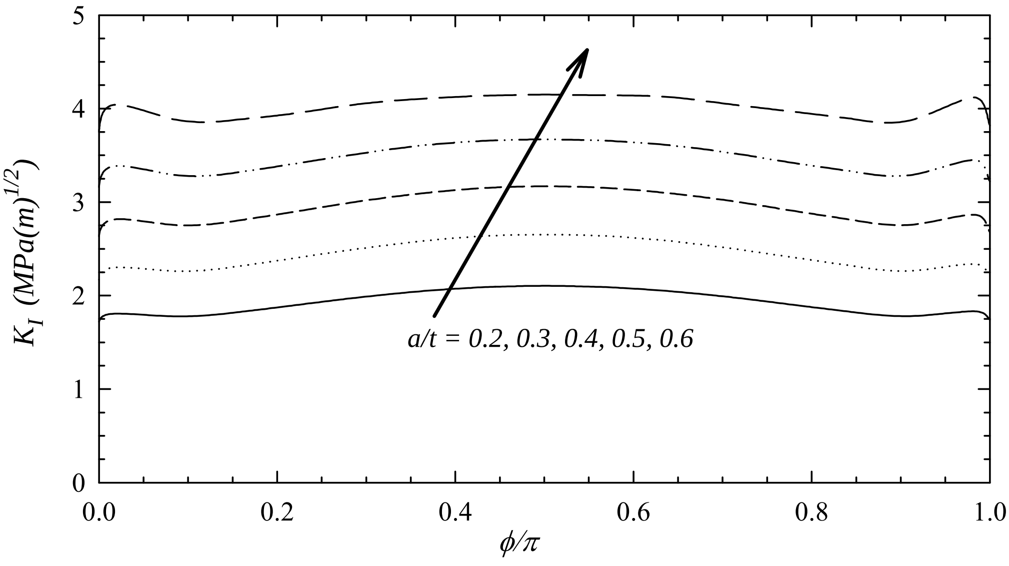

a)

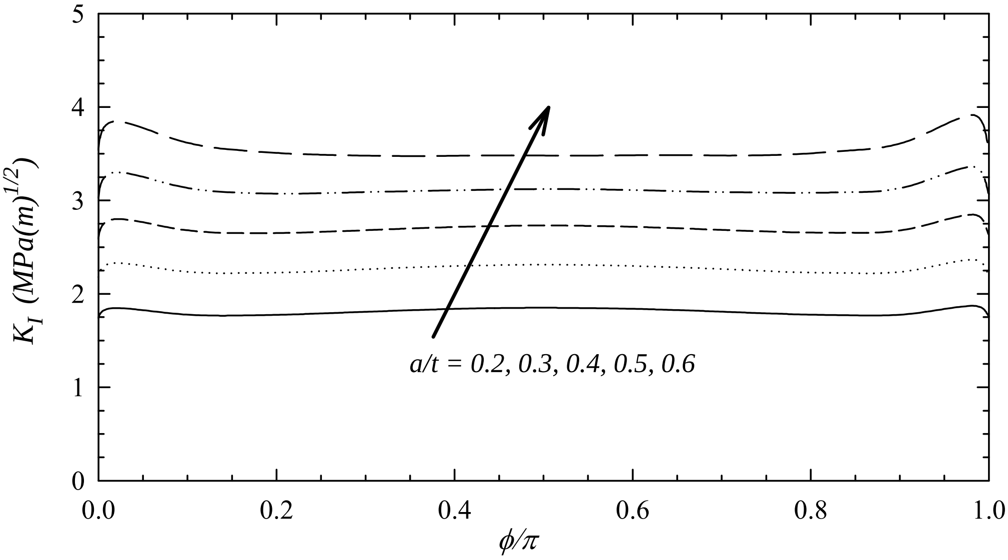

b)

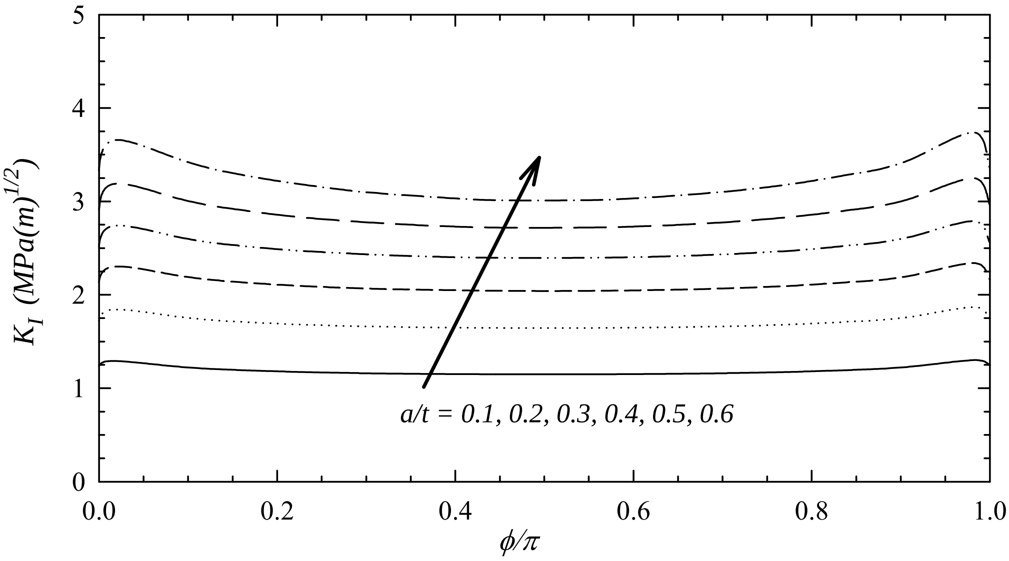

c)

Figure 4.12 Calculated stress intensity factor along crack front, for the crack shapes **a)** *a/c=0.6,* **b)** *a/c=0.8,* **c)** *a/c=1.0*

This chapter is dedicated to ensure the validity of the crack model in riveted joint. In this part validity of the model was achieved and mode I SIF distribution along semi elliptical surface crack front having various crack shapes and sizes were presented in this part of the study.

CHAPTER 5

FRACTURE ANALYSIS OF CRACKED RIVETED JOINT

5.1 Introduction

Until now, finite element models of the riveted lap joint and semi elliptical surface crack have been obtained separately. Accuracies of these models were observed to be reasonable. Based on these models, now the finite element models of the riveted lap joint containing semi elliptical surface or quarter elliptical corner cracks were obtained. Both types of cracks were placed at a plane perpendicular to the tensile loading (Figure 5.1). Mixed mode stress intensity factors and energy release rates distribution along the crack front were presented for both semi elliptical surface and quarter elliptical corner cracks. Fracture parameters were calculated both under the effect of riveting simulation and the external loading. Parametric studies were carried out by employing various crack shapes and sizes. Also, in order to capture the effects of residual stresses induced by the riveting simulation on fracture parameters, various finite element models were created by varying interference and clamping misfit ratios.

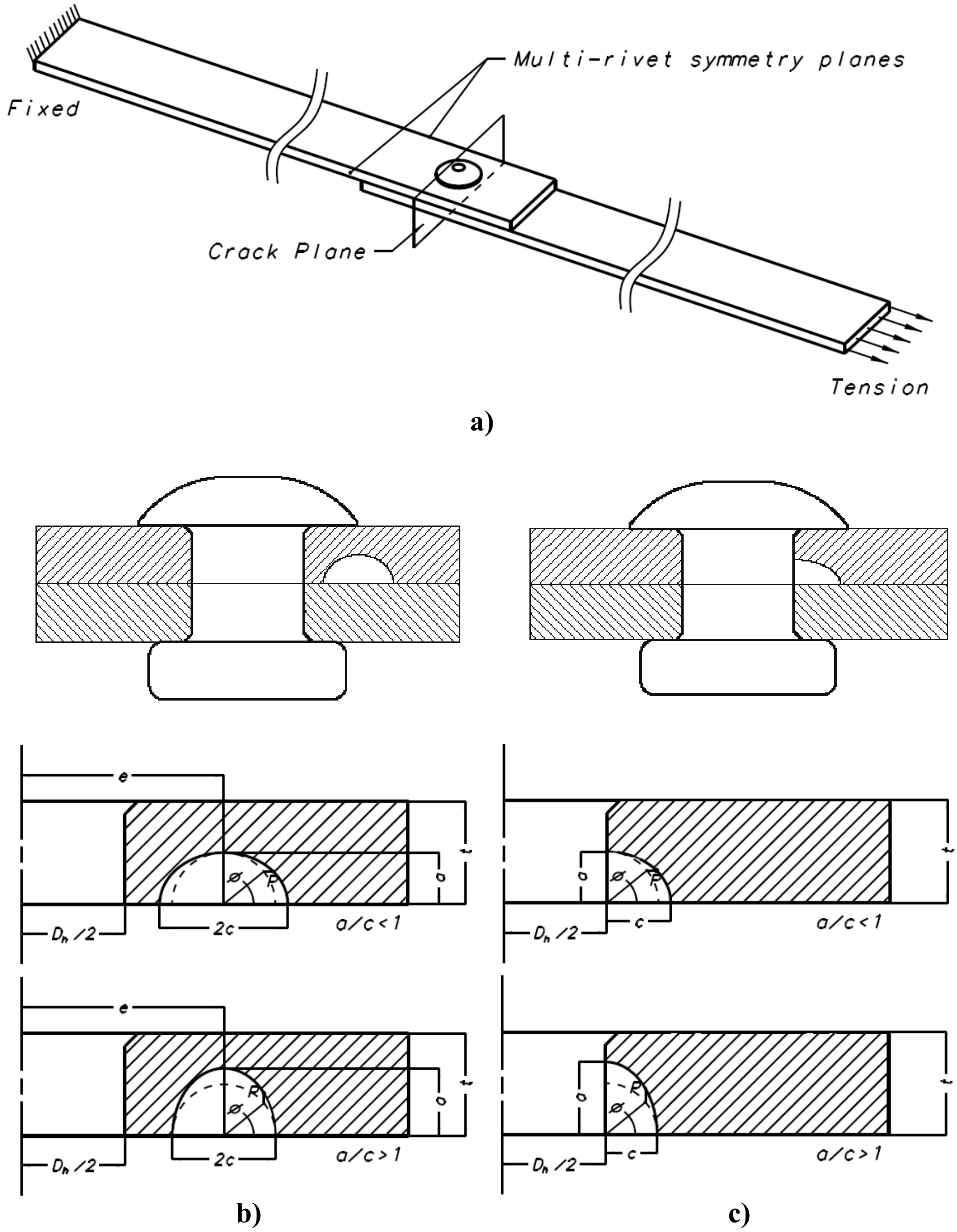

Figure 5.1 Cracked riveted joint showing **a)** general view, boundary conditions and crack plane **b)** schematics of semi elliptical surface crack **c)** schematics of quarter elliptical corner

5.2 The Finite Element Modeling of Cracked Riveted Lap Joint

Finite element models of the riveted lap joint containing quarter elliptical corner or semi elliptical surface cracks are illustrated in Figure 5.2 and 5.3, respectively. For the riveted joint model, same element types and sizes are utilized as in the stress analysis stage. For the crack modeling, again the same crack parameters, element types and sizes are utilized as in the stress intensity factor calculation chapter. Therefore the validity of the finite element models of the cracked riveted joints could be guaranteed. Also the material model, boundary conditions, contact conditions at touching surfaces, and loading conditions are exactly same as the section of stress analysis of riveted joint.

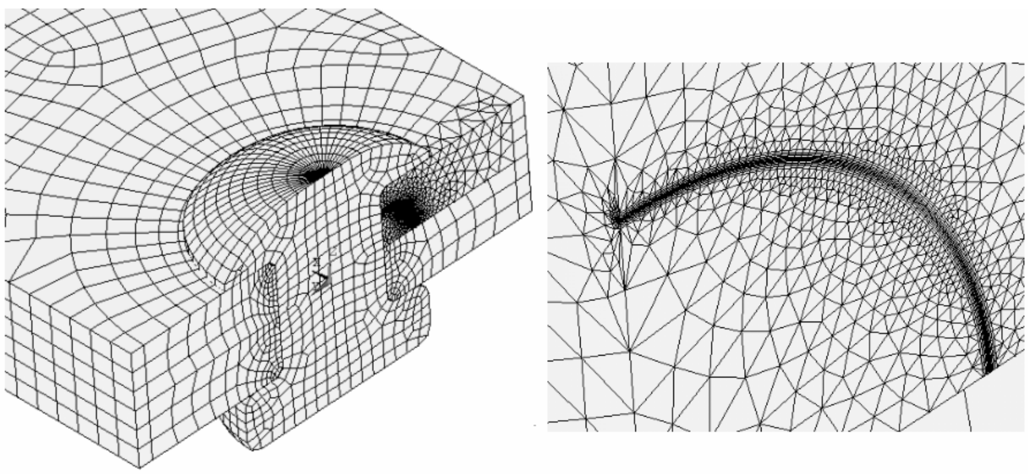

Figure 5.2 Close up views of finite element mesh of riveted joint having a quarter elliptical corner crack

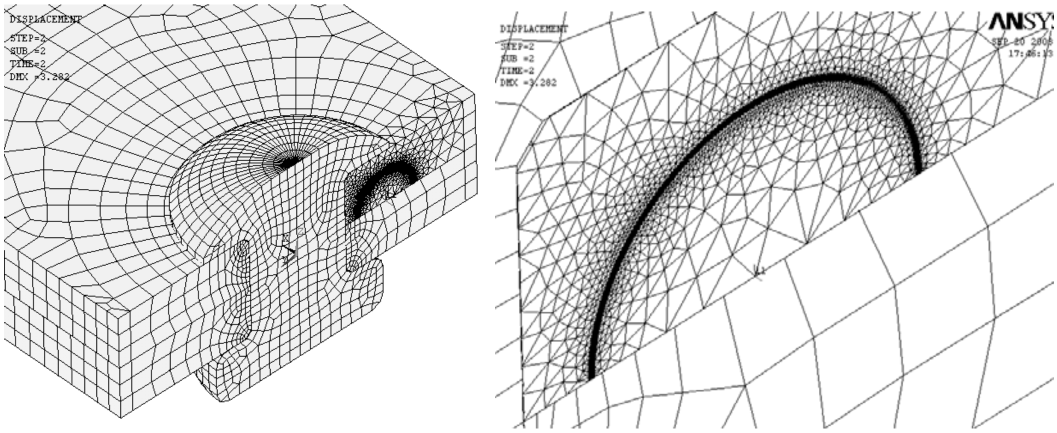

Figure 5.3 Close up views of finite element mesh of riveted joint having a semi elliptical surface crack

Sixteen finite element models for quarter elliptical corner crack and twelve finite element models for semi elliptical surface cracks were generated by employing four different crack shapes and corresponding four different crack sizes. Different crack sizes were obtained by varying crack depth / half crack length (a/c) ratios (also known as aspect ratio). For each crack shape different crack sizes were obtained by varying crack depth / thickness (a/t) ratios. For $a/c=0.6$ semi elliptical crack could not be modeled due to the lack of place. Table 5.1 summarizes the finite element models and corresponding a/c and a/t ratios. All models were obtained for fixed average values of interference and clamping ratios ($\%D$=0.30 and $\%L$=0.30).

Table 5.1 Parametric finite element models for different crack shape and size

FE Models	Crack Size	Crack Shape	Quarter Elliptical Corner Crack	Semi Elliptical Surface Crack
	a/t	*a/c*		
1	0.2	0.6	√	-
2	0.4	0.6	√	-
3	0.6	0.6	√	-
4	0.8	0.6	√	-
5	0.2	0.8	√	√
6	0.4	0.8	√	√
7	0.6	0.8	√	√
8	0.8	0.8	√	√
9	0.2	1	√	√
10	0.4	1	√	√
11	0.6	1	√	√
12	0.8	1	√	√
13	0.2	1.2	√	√
14	0.4	1.2	√	√
15	0.6	1.2	√	√
16	0.8	1.2	√	√

Since the residual stresses induced by the riveting simulation alters the overall stress distributions, stress intensity factors and energy release rates along the crack front are also influenced. Therefore parametric models that include different riveting simulation parameters (different interference and clamping ratios) have been produced. For both quarter elliptical corner and semi elliptical surface crack, sixteen FE models were generated. Table 5.2 summarizes the finite element models and corresponding interference and clamping ratios. All models were obtained for fixed values of crack dimensions (a/c=1.0 and a/t=0.6).

Table 5.2 Parametric finite element models for different interference and clamping ratios

FE Models	% Shank Radial Interference	% Shank Height Interference (Clamping)	Quarter Elliptical Corner Crack	Semi Elliptical Surface Crack
	%D	*%L*		
1	0.00	0.00	√	√
2	0.00	0.15	√	√
3	0.00	0.30	√	√
4	0.00	0.50	√	√
5	0.15	0.00	√	√
6	0.15	0.15	√	√
7	0.15	0.30	√	√
8	0.15	0.50	√	√
9	0.30	0.00	√	√
10	0.30	0.15	√	√
11	0.30	0.30	√	√
12	0.30	0.50	√	√
13	0.50	0.00	√	√
14	0.50	0.15	√	√
15	0.50	0.30	√	√
16	0.50	0.50	√	√

Deformed shape of the quarter elliptical corner crack and semi elliptical surfaces crack under loading are shown in Figure 5.4 and Figure 5.5, respectively. Deformations were exaggerated to observe the crack opening clearly. Loading on conditions in riveted joints are very complex including external tensile loading, residual stress induced by the riveting simulation, rivet tilting and out of bending of plate, and frictional contact conditions at contacting surfaces. Thus loading on the crack was thought to be mixed mode. In order to examine the mixed mode deformation of the crack, a portion of the finite element models around the crack front was observed. Ten times magnified view illustrated the mixed mode deformation of the crack clearly (Figure 5.6).

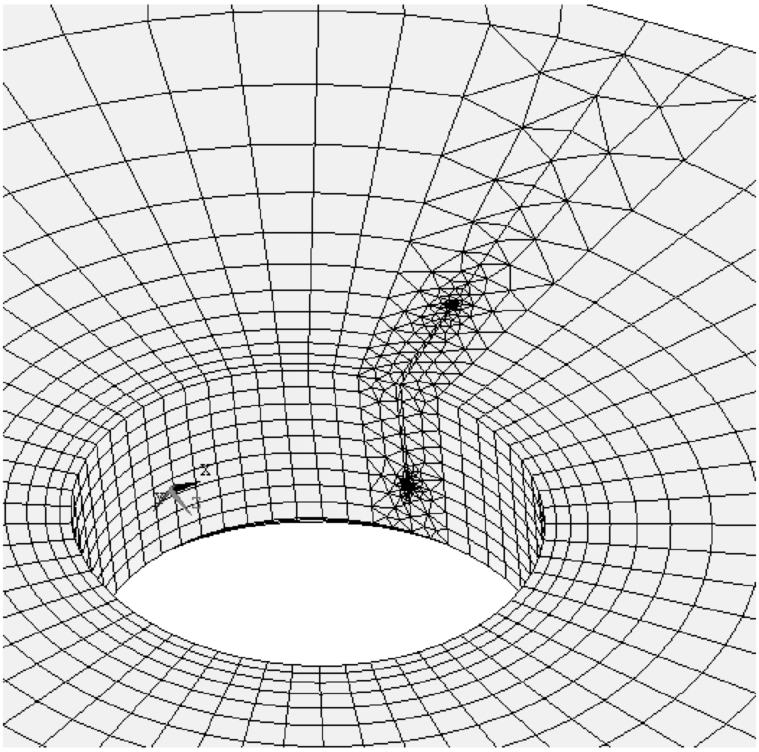

Figure 5.4 Deformed shaped of quarter elliptical corner crack (5 times magnified)

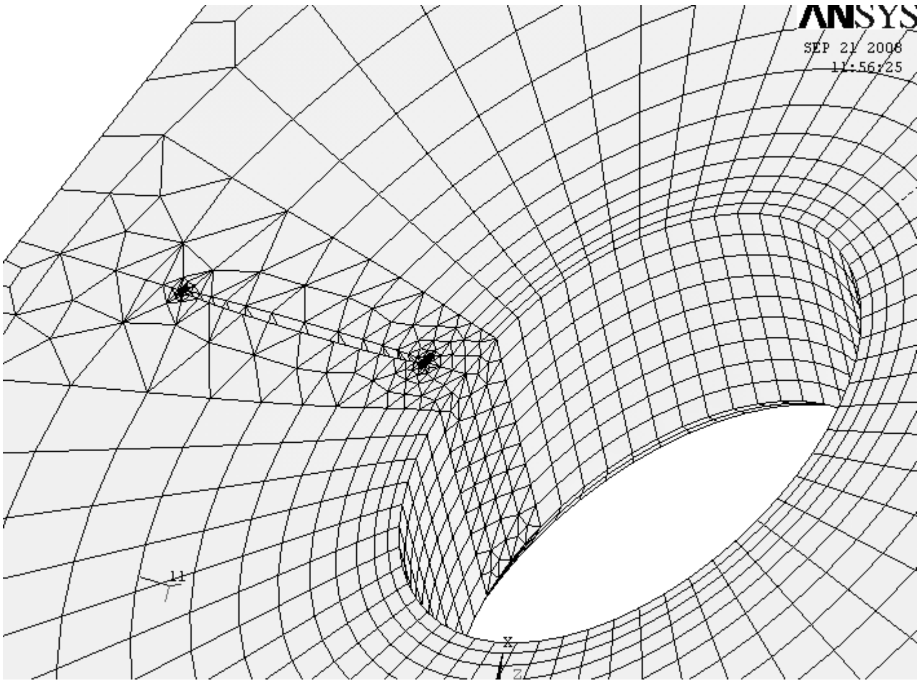

Figure 5.5 Deformed shaped of semi elliptical surface crack (10 times magnified)

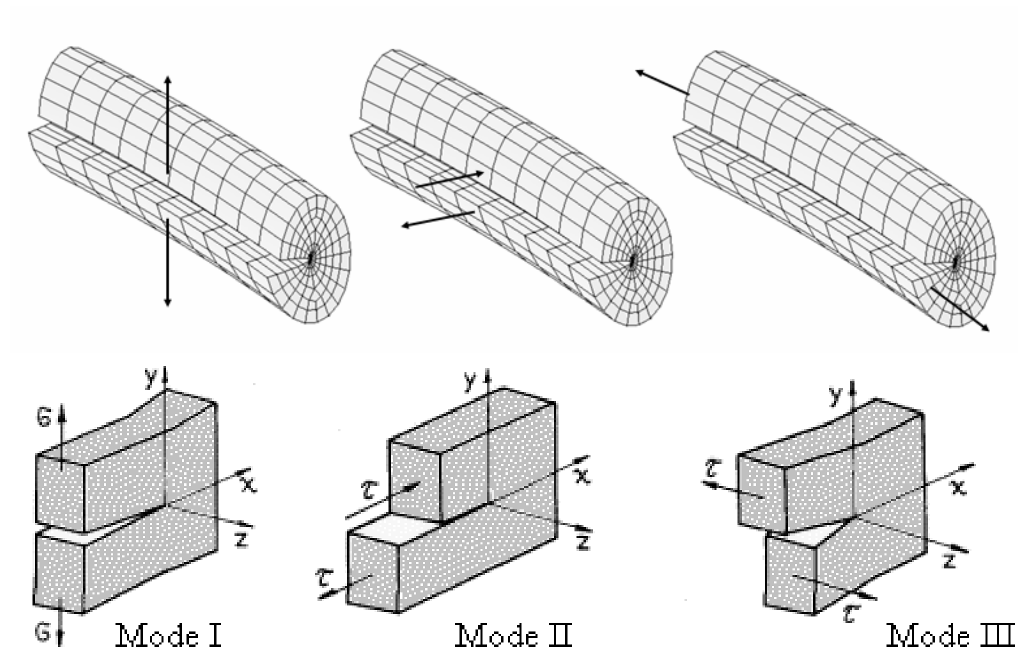

Figure 5.6 Mixed mode deformation of crack in riveted joint (10 times magnified)

After creating all finite element models, during the inspection inter penetration of crack faces thus negative mode I stress intensity factor values were observed at some locations of crack front for certain models (Figure 5.7). This is not a physically meaningful phenomenon. Therefore additional contact areas were defined at the contacting crack faces to prevent the penetration of crack faces. These were observed only under riveting simulation phases of models with quarter elliptical corner crack and for 0% shank radial interference values. This is due to the fact that radial interference results in tensile tangential stress around rivet hole which is the opening load for the crack at the rivet hole. This is not observed for the semi elliptical surface crack which is relatively far away from the rivet hole compared to the quarter elliptical crack. Mode I SIFs for these models before and after contact definition at crack faces are shown in Figure 5.8. Negative values of K_I before contact definition were shifted to zero by defining contact. Relatively small negative values after defining contact are due to the contact algorithm which permits initial penetration and then set the conformity of the contacting surfaces. The reason of the cut of the variation of stress intensity factors at a normalized angle of 0.9644 is explained in part 5.3.

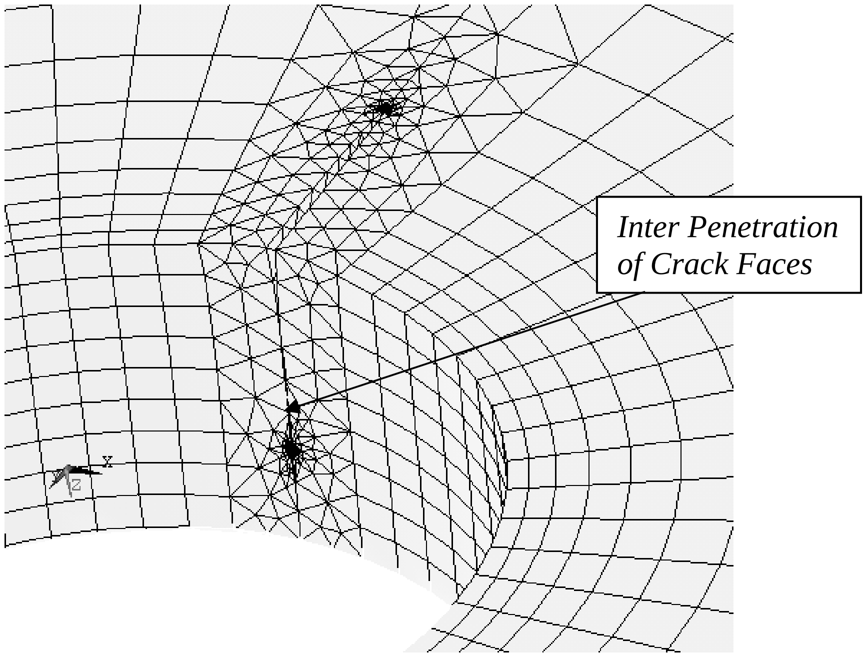

Figure 5.7 Inter penetration of crack faces during riveting simulation

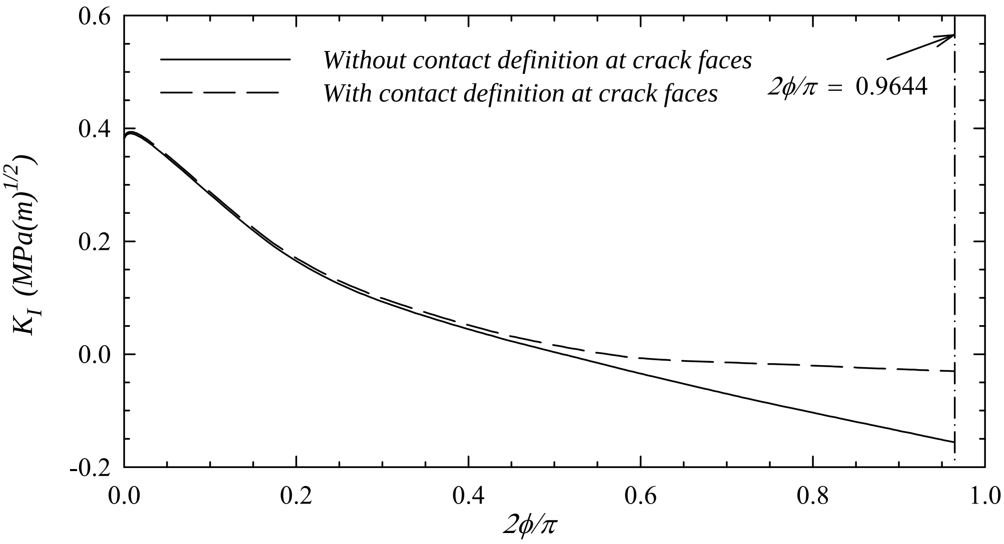

a)

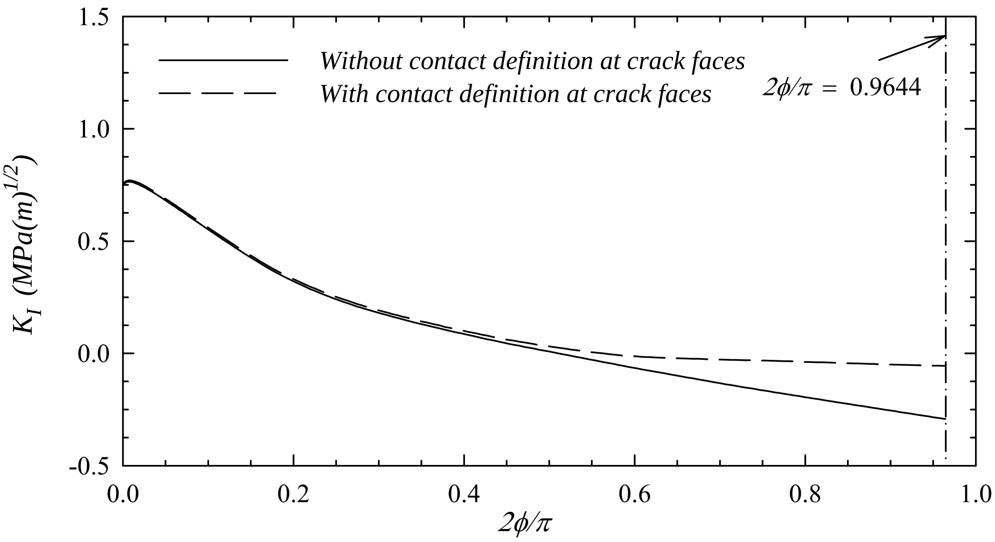

b)

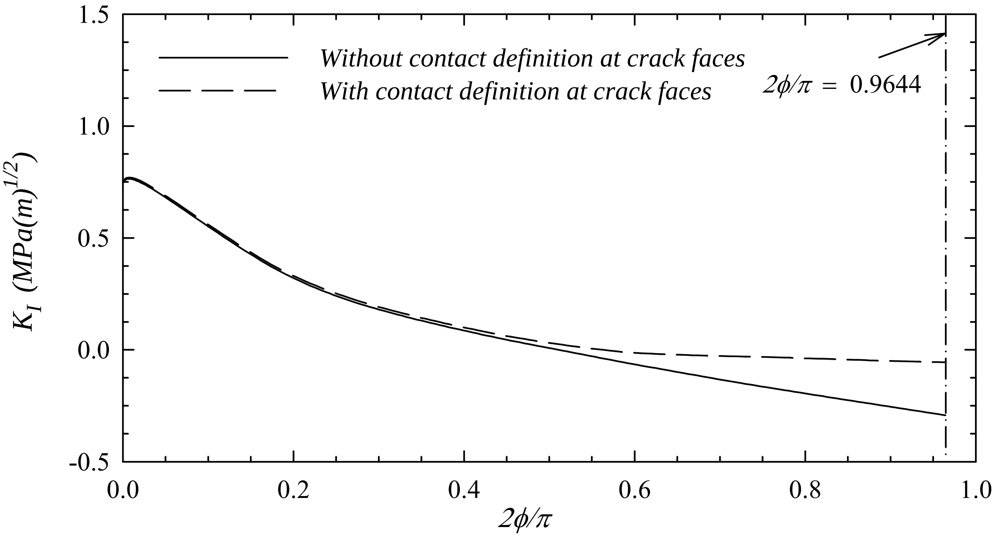

c)

Figure 5.8 Distribution of mode I SIF for quarter elliptical corner crack along crack front, under residual stress, *a/c=1.0, a/t=0.6, %D=0.00* **a)** *%L=0.15,* **b)** *%L=0.30,* **c)** *%L=0.50*

5.3 Numerical Results and Discussions

In this part of the study, fracture parameters (mode I, mode II and mode III stress intensity factors and energy release rates) were calculated along the crack fronts for both crack types. For all conditions fracture parameters were calculated under both riveting simulation and external tensile loading conditions. Results showed that mode II and mode III SIFs were negligible compared to the mode I SIF under residual stress condition. Therefore only mode I SIFs were presented for riveting simulation condition. Under external tensile loading condition, again mode I is dominating over the other modes. However other modes were not negligible compared to the mode I SIF. Therefore all three fracture modes SIFs and energy release rates were presented for external loading condition.

First fracture parameters were calculated for different crack shapes and sizes to observe the effects of crack shape and size on the fracture parameters (finite element models in Table 5.1). Then the fracture parameters were calculated for different interference and clamping ratios to capture the effect of rivet installation parameters on fracture parameters (finite element models in Table 5.2).

Mixed mode stress intensity factors (K_I, K_{II} and K_{III}) and energy release rates (G) are plotted with respect to normalized polar angle along the crack front ($2\phi / \pi$ for quarter elliptical crack and ϕ / π for semi elliptical crack). In order to calculate fracture parameters at a point at the crack front, a local Cartesian coordinate system at this point should be created. For the quarter elliptical crack, crack tip at $\phi = 90^o$ coincides with the free surface of the rivet hole. At this point it is not possible to create a local Cartesian coordinate system. Therefore fracture parameters were calculated along the crack front from the parametric angle $\phi = 0^o$ to $\phi = 86.8^o$ which is very close to the free surface at the rivet hole. $\phi = 86.8^o$ angle corresponds to $2\phi / \pi = 0.9644$ normalized angle as shown in the plots.

5.3.1 Fracture Parameters as Functions of Crack Geometry

Mixed mode stress intensity factors and energy release rates distributions along the crack front for different crack shapes and sizes were calculated for fixed values of radial and height interference ratios. Average values of interference and clamping (*%D*=0.30 and *%L*=0.30) were selected. Effects of crack shape and size were investigated for both quarter and semi elliptical crack types separately.

5.3.1.1 Effects of Crack Geometry for Quarter Elliptical Corner Crack

Mode I stress intensity factor under riveting simulation, and mixed mode stress intensity factors and energy release rates distributions along the crack front under external loading were plotted for cracks of four different crack shapes (*a/c*=0.6, 0.8, 1.0 and 1.2), and corresponding four different crack sizes (*a/t*=0.2, 0.4, 0.6 and 0.8.). These are plotted in Figure 5.9 to 5.13.

In order to study the effect of residual stress due to riveting simulation, first the fracture parameters were calculated under the residual stress only. As stated before, mode I SIF is very dominant and other modes of SIFs are negligible for the riveting simulation. Therefore only mode I SIFs are presented for residual stress state. Figure 5.9 show the distribution of mode I SIF around crack front for quarter elliptical corner crack under residual stress due to the riveting simulation. For all crack sizes, values of K_I are generally increasing with increase in *a/c* ratios. There are junction points on the crack front near the rivet hole at which K_I values match and change trends. However, these portions are relatively small compared to the rest of the crack front and they diminish with increasing in *a/t* ratios. Another important point is that for all crack geometries magnitudes of K_I are maximum at the rivet hole side of the crack front ($2\phi/\pi \to 1$) and minimum at the faying surface of the plates ($2\phi/\pi \to 0$).

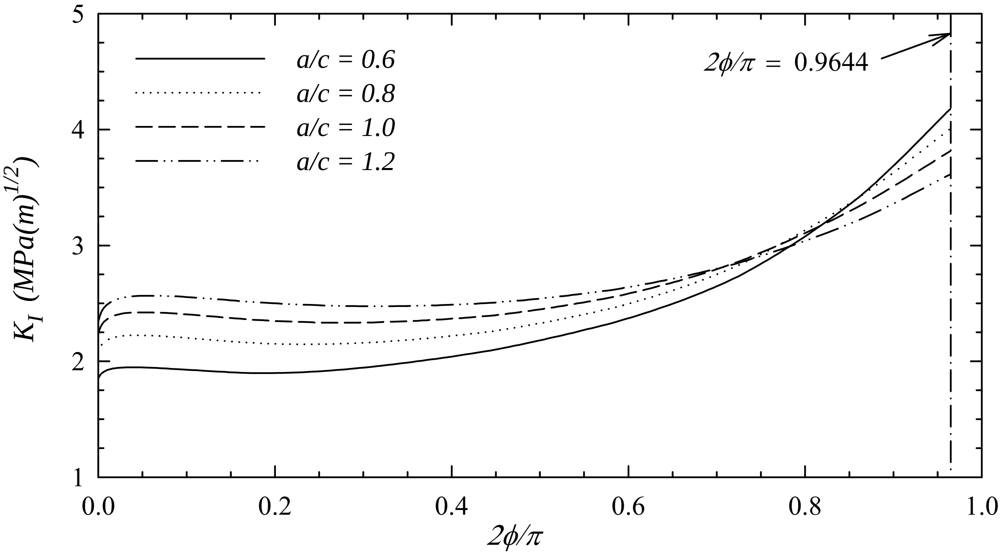

a/c = 0.6
a/c = 0.8
a/c = 1.0
a/c = 1.2
2ϕ/π = 0.9644
K_I (MPa(m)$^{1/2}$)
2ϕ/π

a)

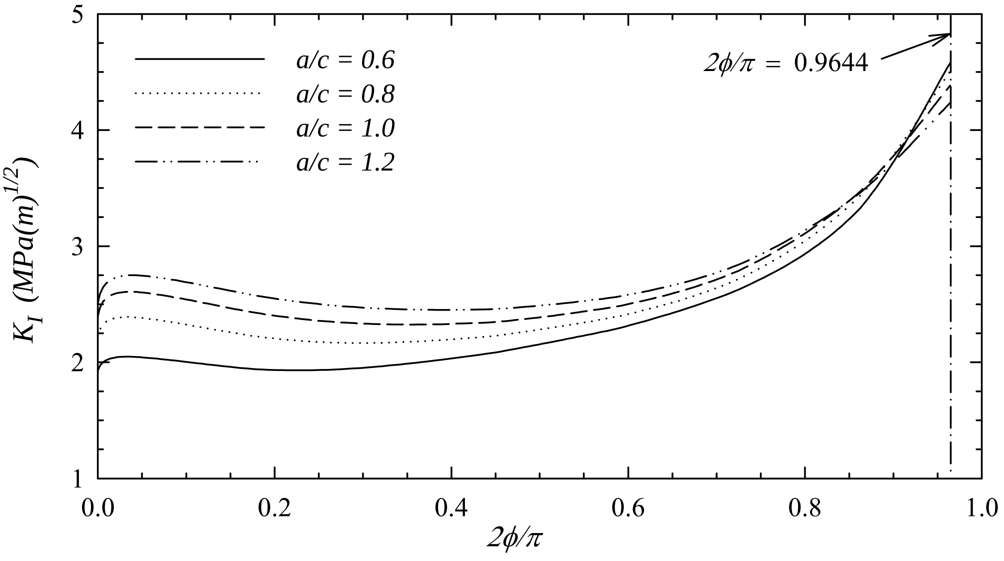

a/c = 0.6
a/c = 0.8
a/c = 1.0
a/c = 1.2
2ϕ/π = 0.9644
K_I (MPa(m)$^{1/2}$)
2ϕ/π

b)

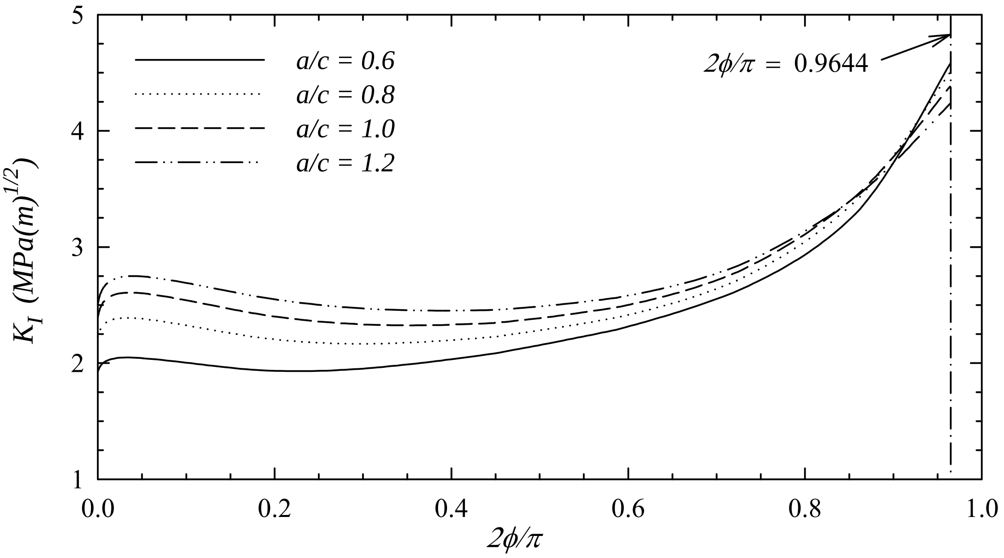

c)

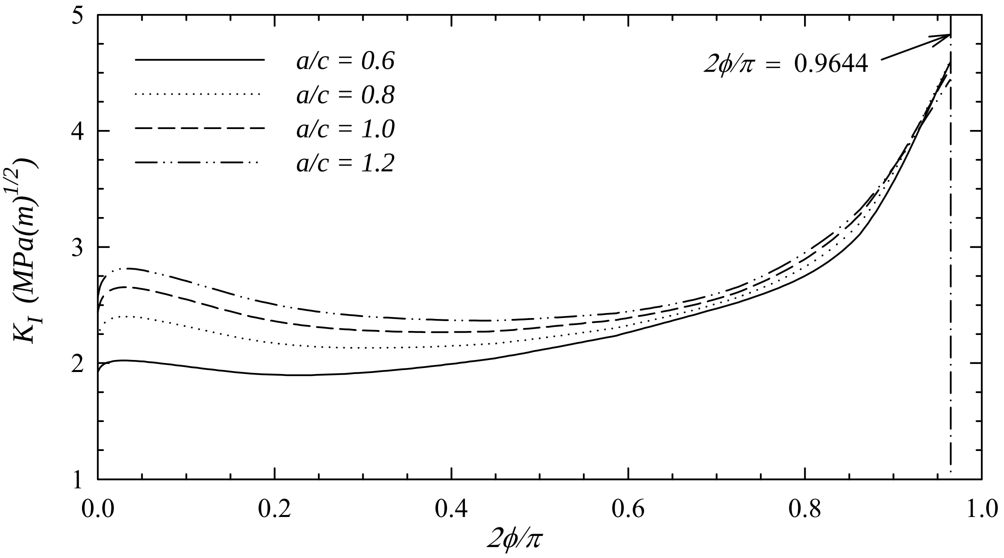

d)

Figure 5.9 Effects of crack geometry on the distribution of mode I SIF along crack front for quarter elliptical corner crack, under residual stress, **a)** *a/t=0.2* **b)** *a/t=0.4* **c)** *a/t=0.6* **d)** *a/t=0.8*

The distributions of mode I SIF around crack front for quarter elliptical corner crack under tensile loading are plotted in Figure 5.10. There are junction points on the crack at which K_I values match and change trends. Before these junction points, values of K_I are increasing with increase in *a/c* ratios, after these points vice versa is valid. For the same crack geometry, magnitudes of K_I under external loading are approximately four times larger than the residual stress state.

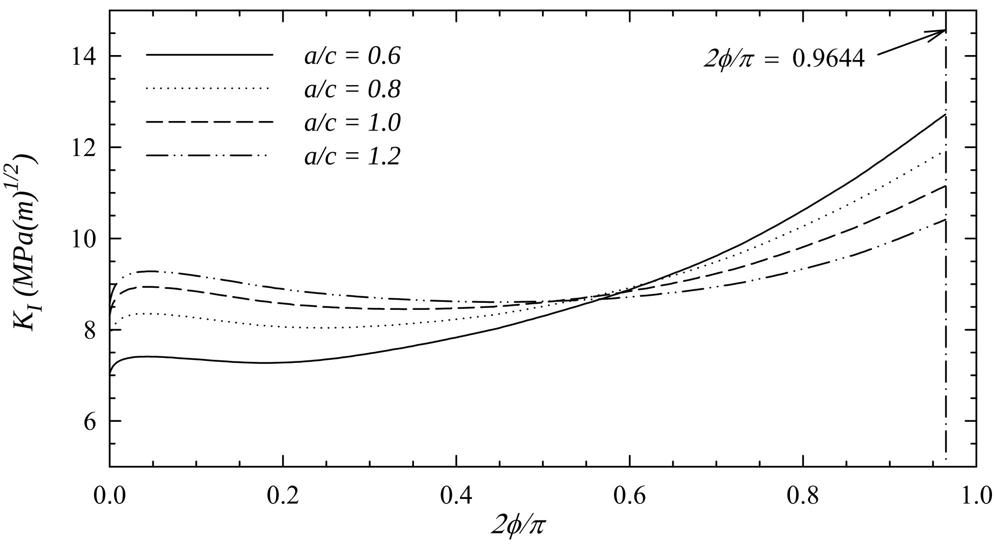

a)

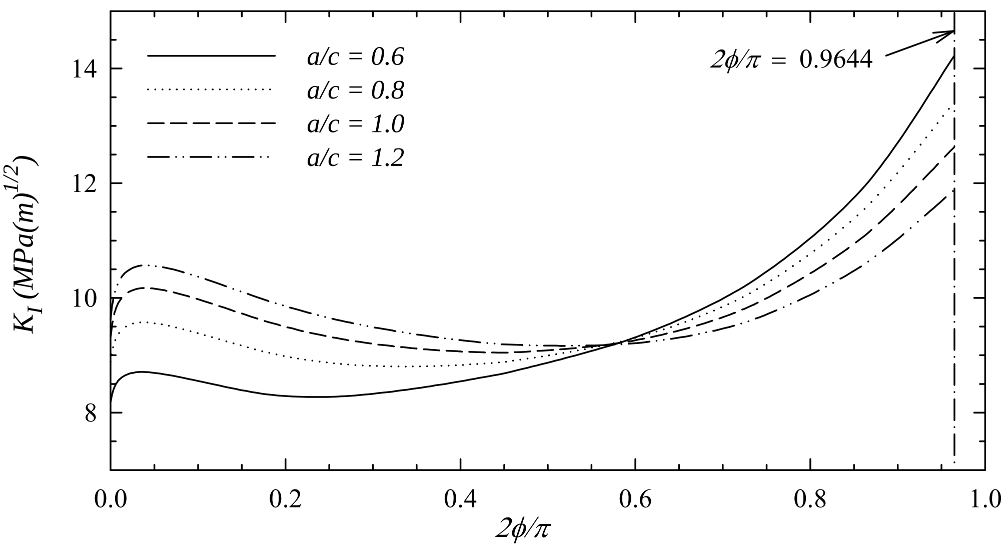

b)

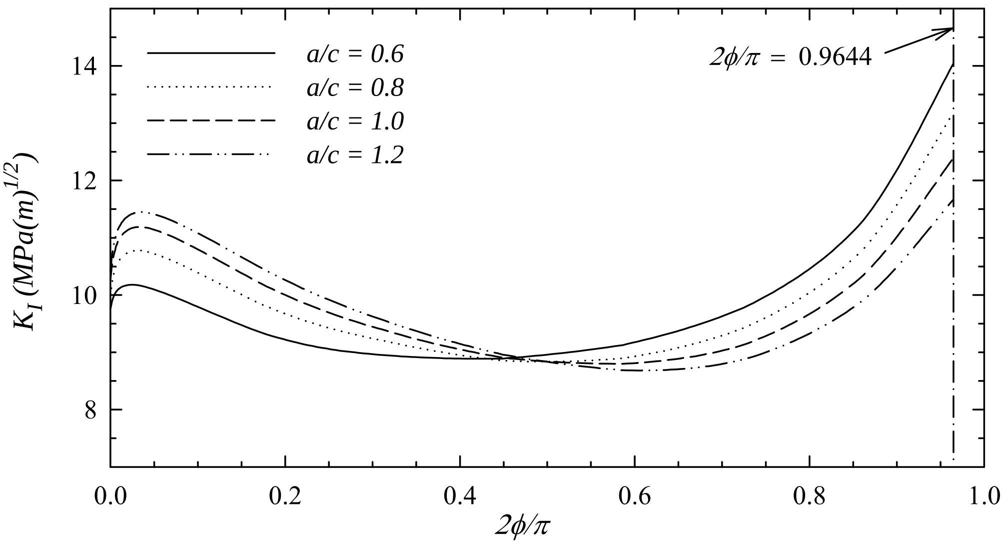

c)

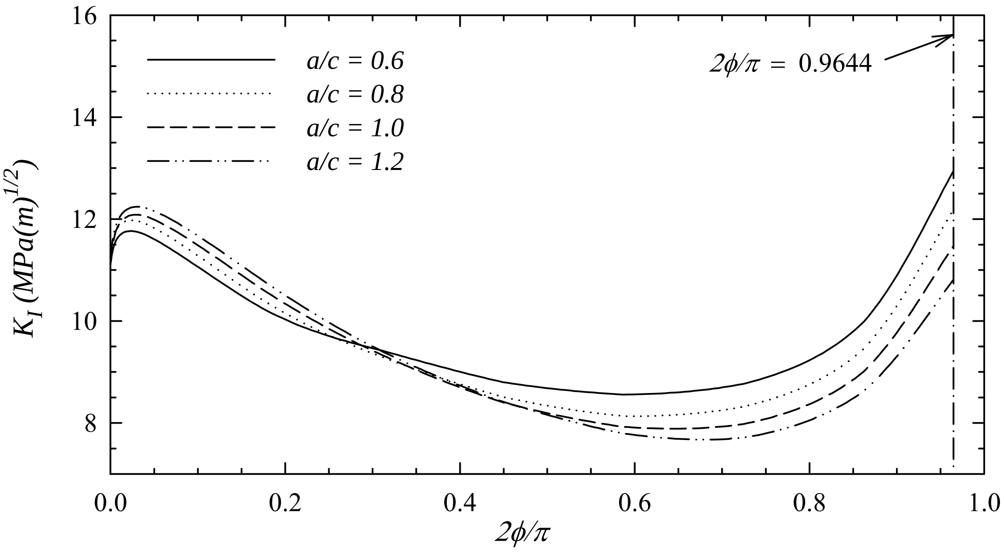

d)

Figure 5.10 Effects of crack geometry on the distribution of mode I SIF along crack front for quarter elliptical corner crack, under external loading, **a)** *a/t=0.2* **b)** *a/t=0.4* **c)** *a/t=0.6* **d)** *a/t=0.8*

Figure 5.11 show the distribution of mode II SIF along crack front for quarter elliptical corner crack under external loading. As shown in the figure, there are junction points on the crack front near the faying surface at which K_{II} values match, change signs and trends. Magnitudes of K_{II} are generally increasing with increase in crack size (*a/t* ratios).

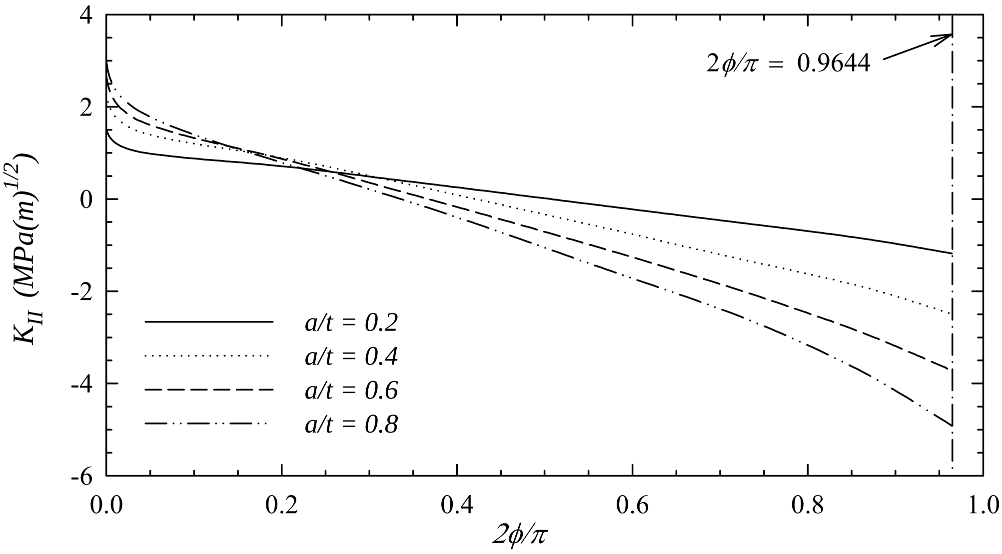

a)

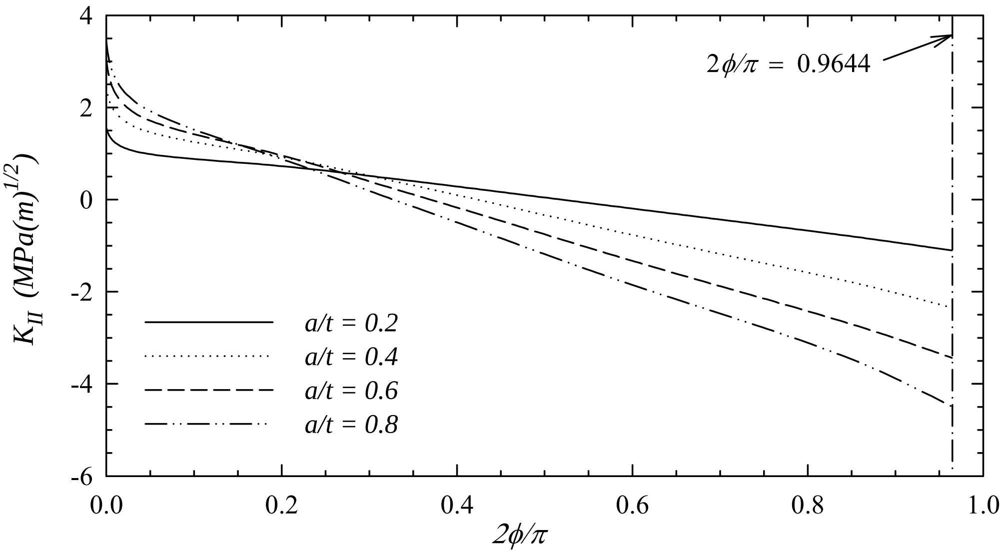

b)

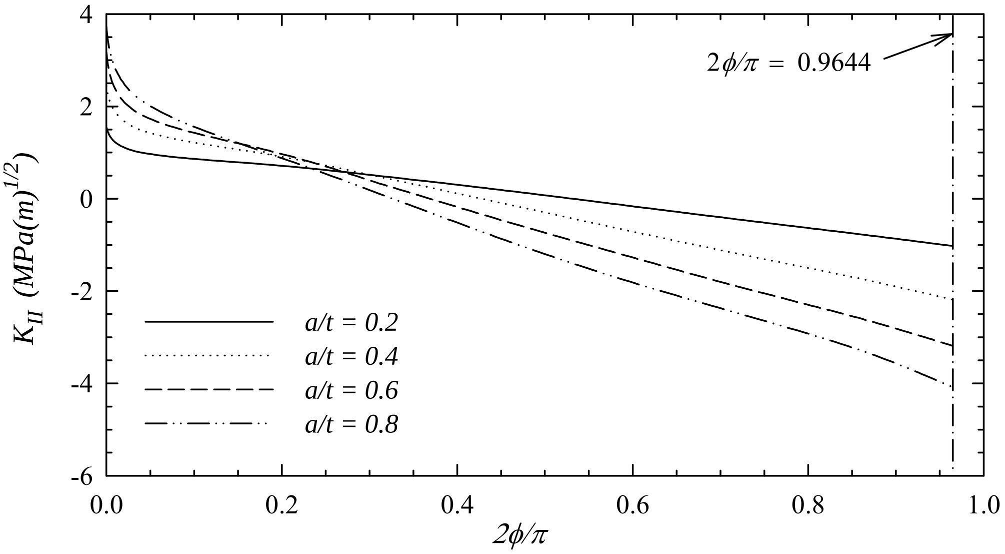

c)

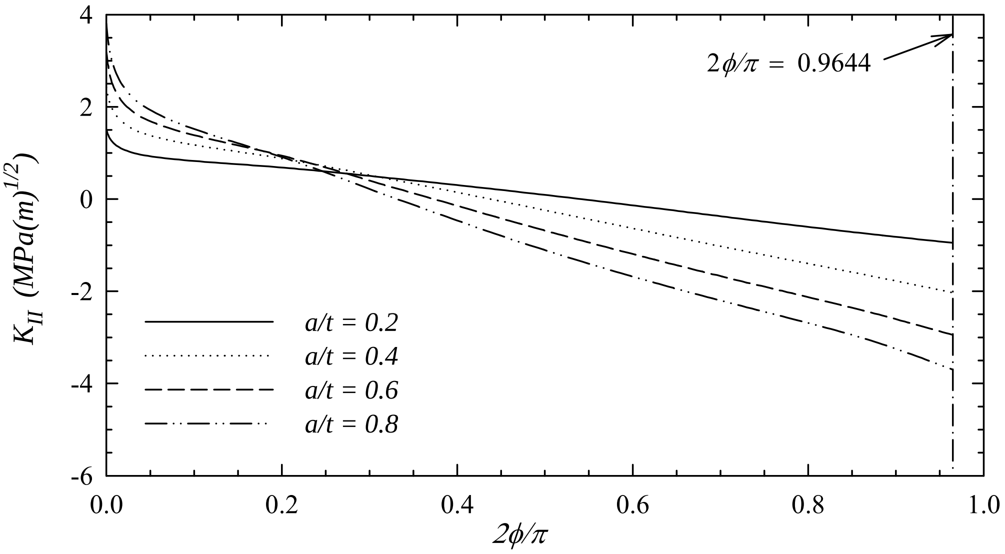

d)

Figure 5.11 Effects of crack geometry on the distribution of mode II SIF along crack front for quarter elliptical corner crack, under external load, **a)** *a/c=0.6,* **b)** *a/c=0.8,* **c)** *a/c=1.0,* **d)** *a/c=1.2*

Figure 5.12 show the distribution of mode III SIF around crack front for quarter elliptical corner crack under external loading. All K_{III} values are negative and small in magnitudes (0 to -1.5 $MPa\sqrt{m}$). For *a/t*=0.2, K_{III} values increase with increase in *a/c* values. For *a/t*=0.4, K_{III} values are nearly insensitive to change in *a/c* values. For *a/t*=0.6 and 0.8, K_{III} values decrease with increase in *a/c* values.

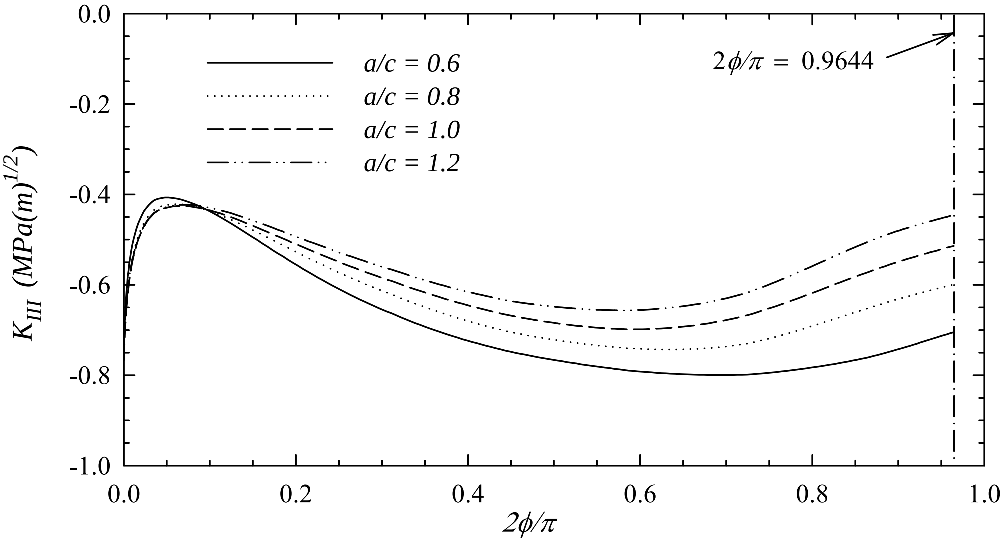

a)

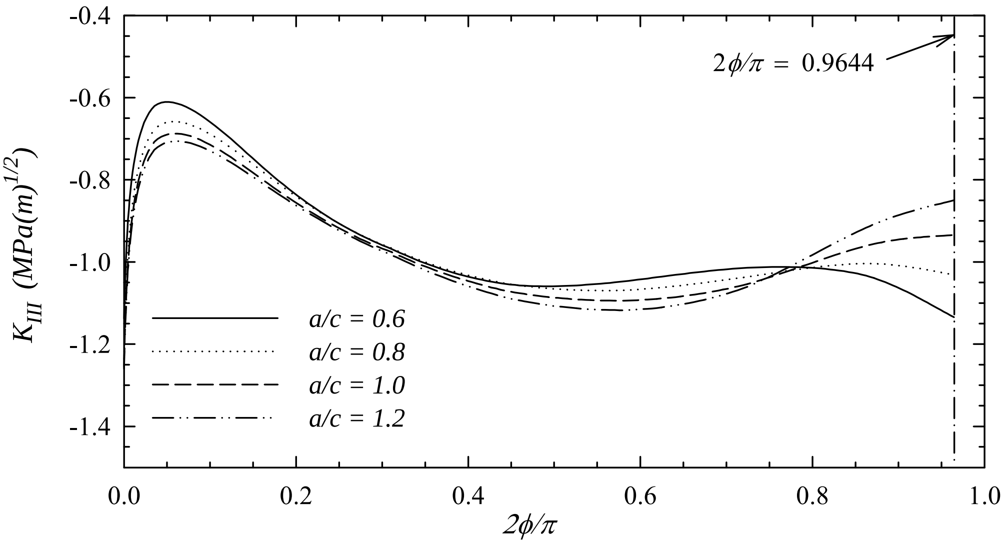

b)

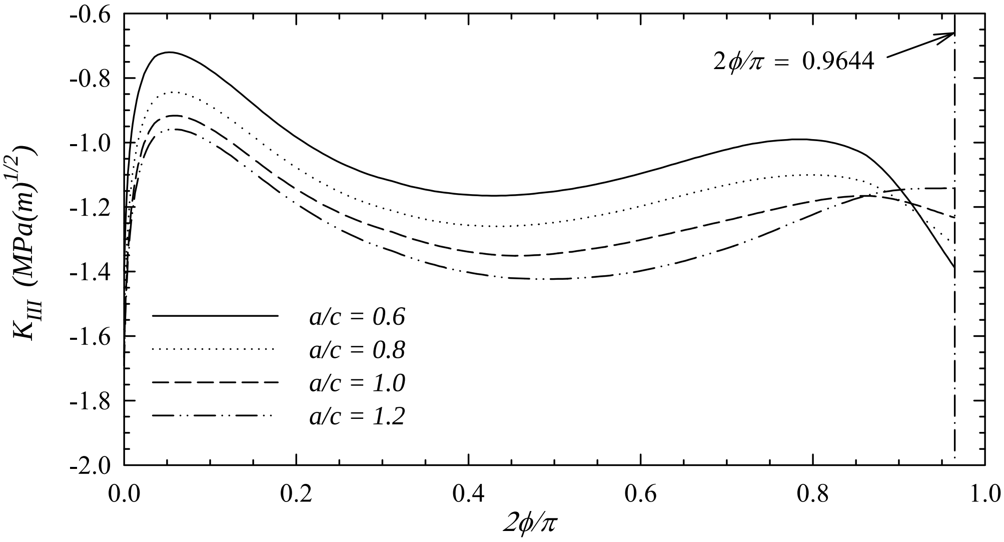

c)

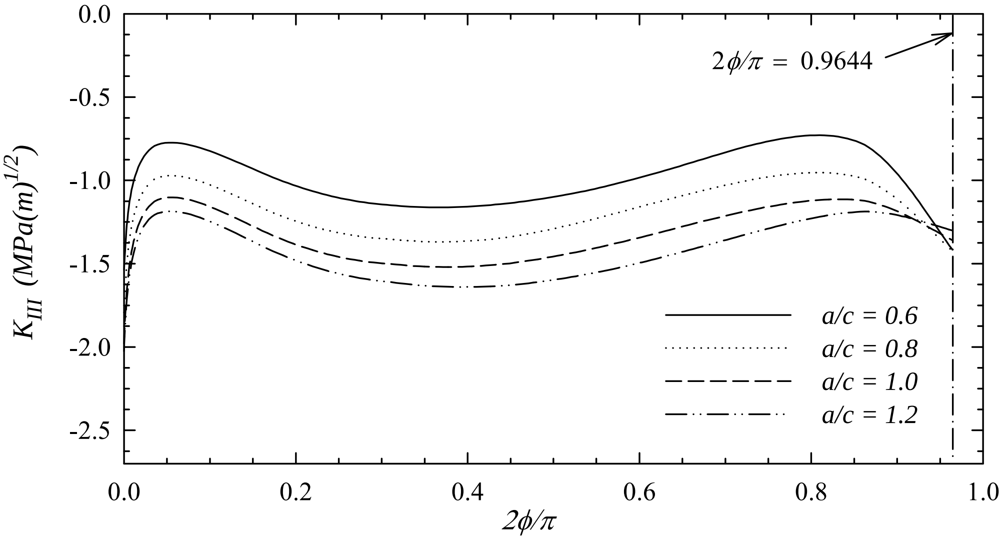

d)

Figure 5.12 Effects of crack geometry on the distribution of mode III SIF along crack front for quarter elliptical corner crack, under external loading, **a)** *a/t=0.2* **b)** *a/t=0.4* **c)** *a/t=0.6* **d)** *a/t=0.8*

Figure 5.13 show the distribution of energy release rate (G) along crack front for quarter elliptical corner crack under external load. Distribution of G is very similar to K_I. The energy release rate can be treated as an equivalent stress intensity factor which includes the combined effects of three modes of SIFs. This is clearly seen in equation 2.36, which gives the energy release rate as a function of stress intensity factors. Since mode II and mode III SIF values are small compared to the values of mode I SIF, contribution of mode I SIF on energy release rate is much higher than the other modes. Therefore trends of the distribution of G are very similar to that of K_I .

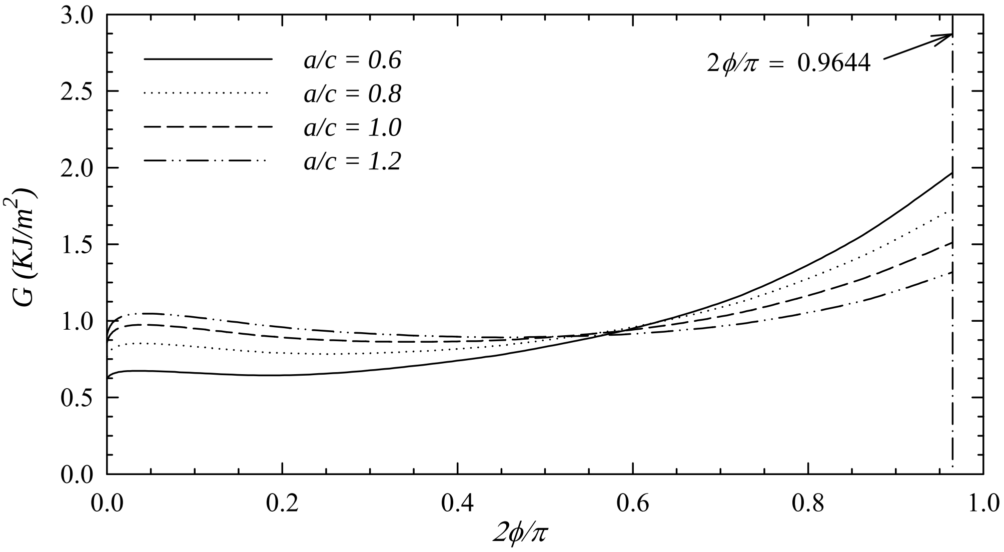

a)

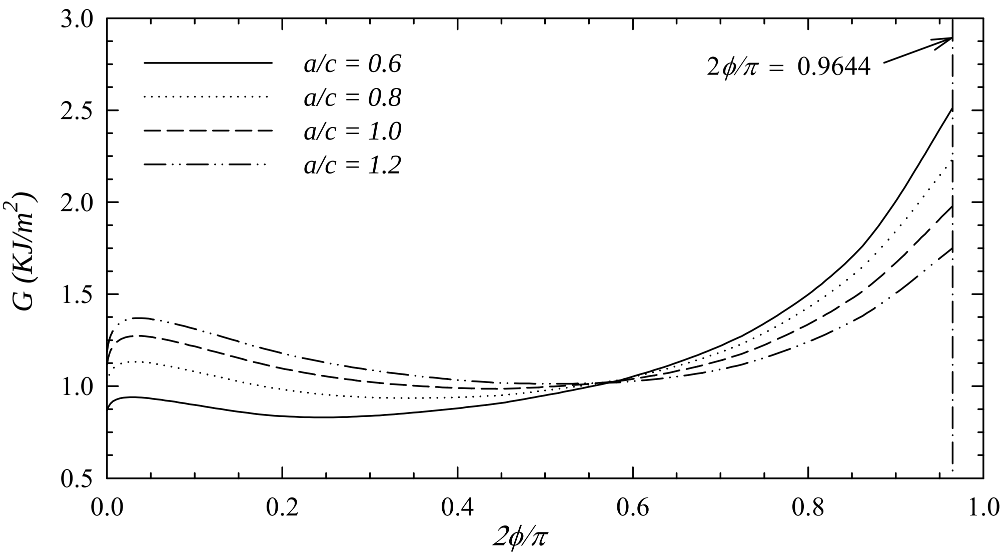

b)

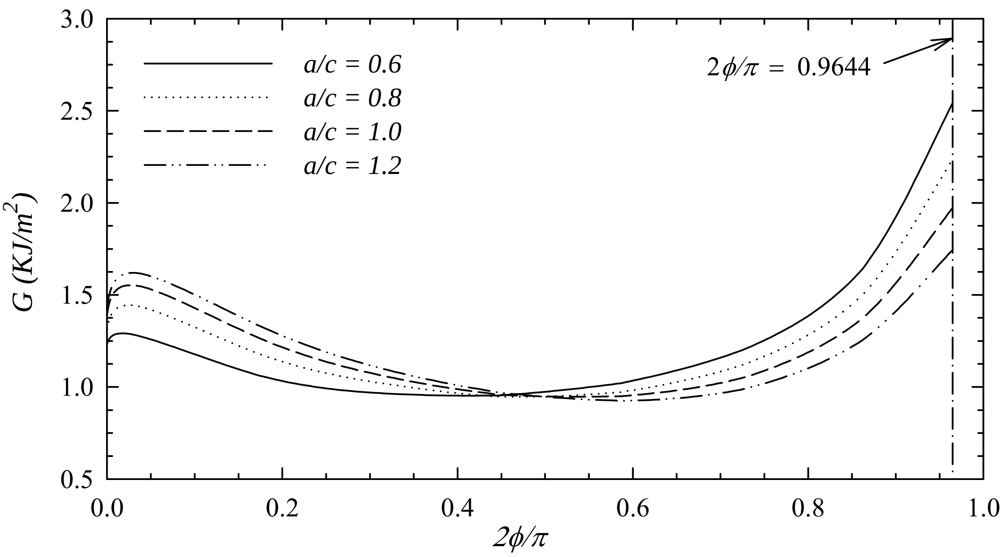

c)

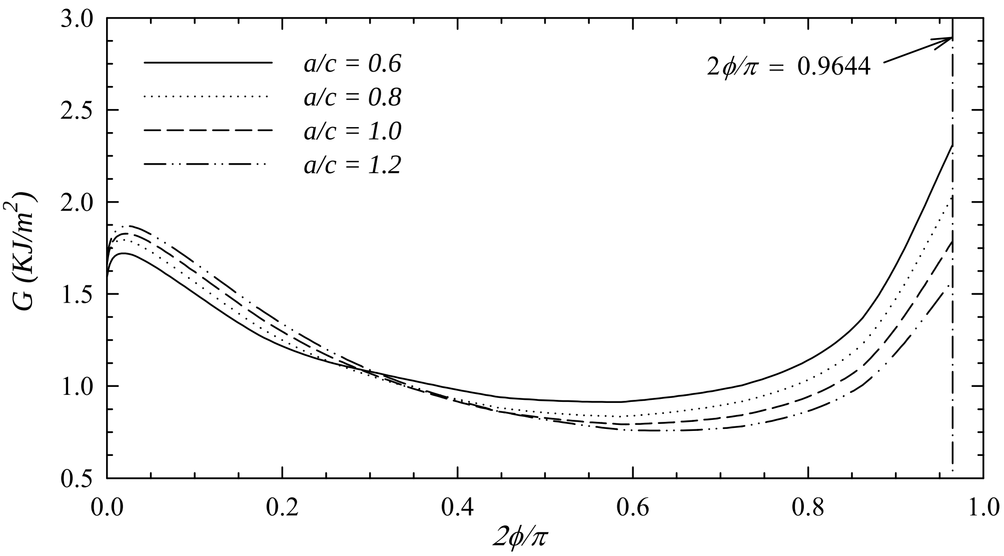

d)

Figure 5.13 Effects of crack geometry on the distribution of energy release rate along crack front for quarter elliptical corner crack, under external loading, **a)** *a/t=0.2* **b)** *a/t=0.4* **c)** *a/t=0.6* **d)** *a/t=0.8*

5.3.1.2 Effects of Crack Geometry for Semi Elliptical Surface Crack

Similar to the quarter elliptical crack case, for the semi elliptical crack, mode I stress intensity factor under riveting simulation, and mixed mode stress intensity factors and energy release rates distributions along the crack front under external loading were plotted for cracks of three different crack shapes (*a/c*= 0.8, 1.0 and 1.2), and corresponding four different crack sizes (*a/t*=0.2, 0.4, 0.6 and 0.8.). These are plotted in Figure 5.14 to 5.18 for fixed values of crack size and residual stress state due to the riveting simulation.

Mode I SIF distributions along the crack front for various crack shapes and sizes under residual stress state are plotted in Figure 5.14. For all crack sizes, values of K_I are increasing with increase in *a/t* ratios. Because the effects of residual stress field decrease going away from the rivet hole, for all crack geometries magnitudes of K_I along crack front are maximum at the crack tip which is close to the rivet hole edge ($2\phi/\pi \to 1$) and minimum at the opposite side far from the rivet hole ($2\phi/\pi \to 0$). Also it is important to note that average magnitudes of K_I values for semi elliptical crack are smaller than the quarter elliptical crack due to the same fact.

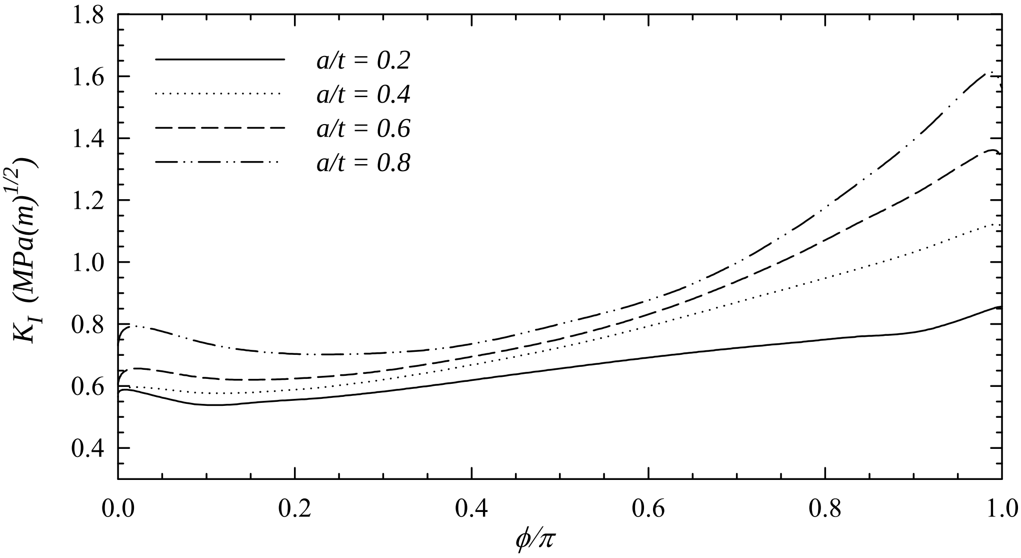

1.8
1.6
1.4
1.2
1.0
0.8
0.6
0.4
K_I $(MPa(m)^{1/2})$
a/t = 0.2
a/t = 0.4
a/t = 0.6
a/t = 0.8
0.0
0.2
0.4
0.6
0.8
1.0
ϕ/π

a)

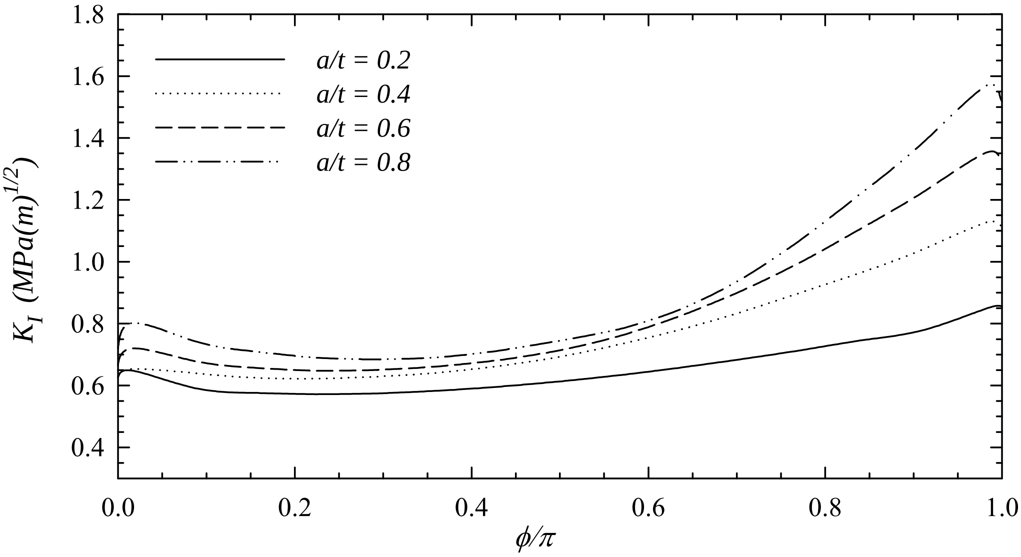

1.8
1.6
1.4
1.2
1.0
0.8
0.6
0.4
K_I $(MPa(m)^{1/2})$
a/t = 0.2
a/t = 0.4
a/t = 0.6
a/t = 0.8
0.0
0.2
0.4
0.6
0.8
1.0
ϕ/π

b)

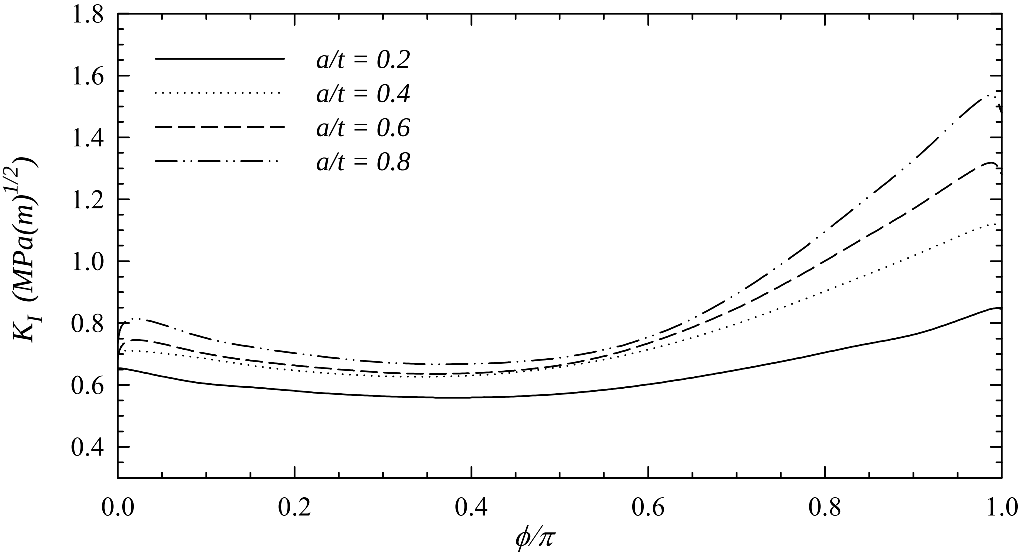

c)

Figure 5.14 Effects of crack geometry on the distribution of mode I SIF along crack front for semi elliptical surface crack, under residual stress, **a)** *a/c=0.8,* **b)** *a/c=1.0,* **c)** *a/c=1.2*

Mode I SIF distributions along the crack front for various crack shapes and sizes under external loading are plotted in Figure 5.15.

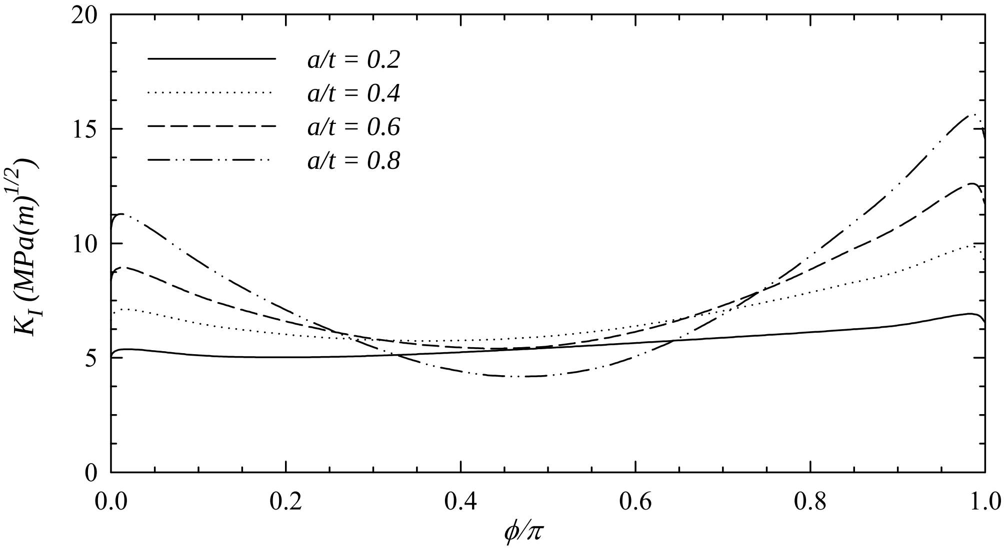

a)

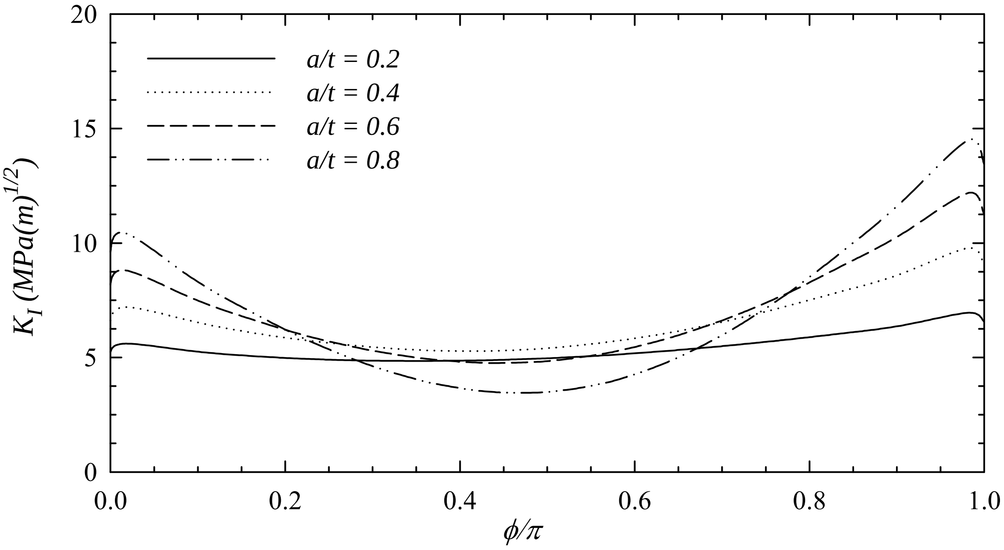

b)

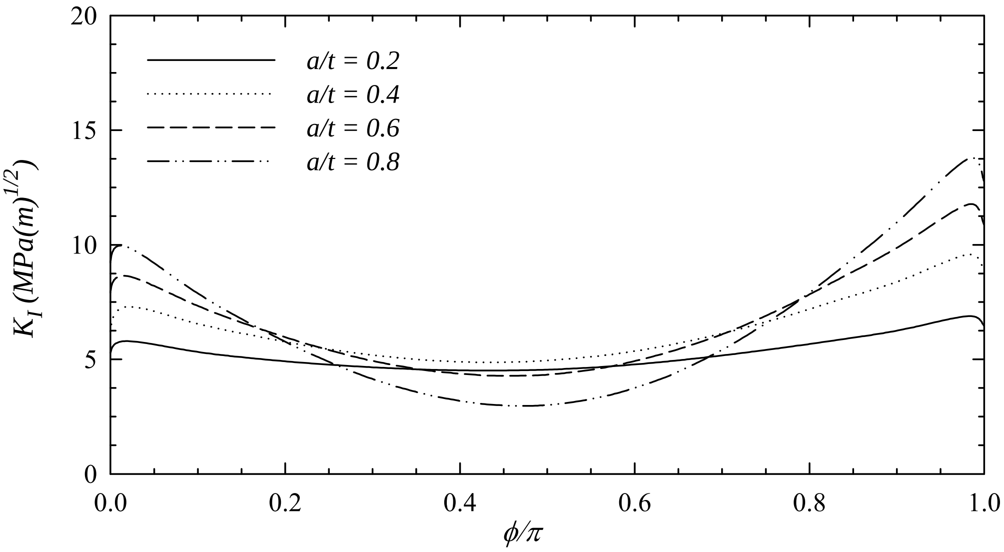

c)

Figure 5.15 Effects of crack geometry on the distribution of mode I SIF along crack front for semi elliptical surface crack, under external load, **a)** *a/c=0.8,* **b)** *a/c=1.0,* **c)** *a/c=1.2*

Figure 5.16 show the distribution of mode II SIF around crack front for semi elliptical surface crack under tensile loading.

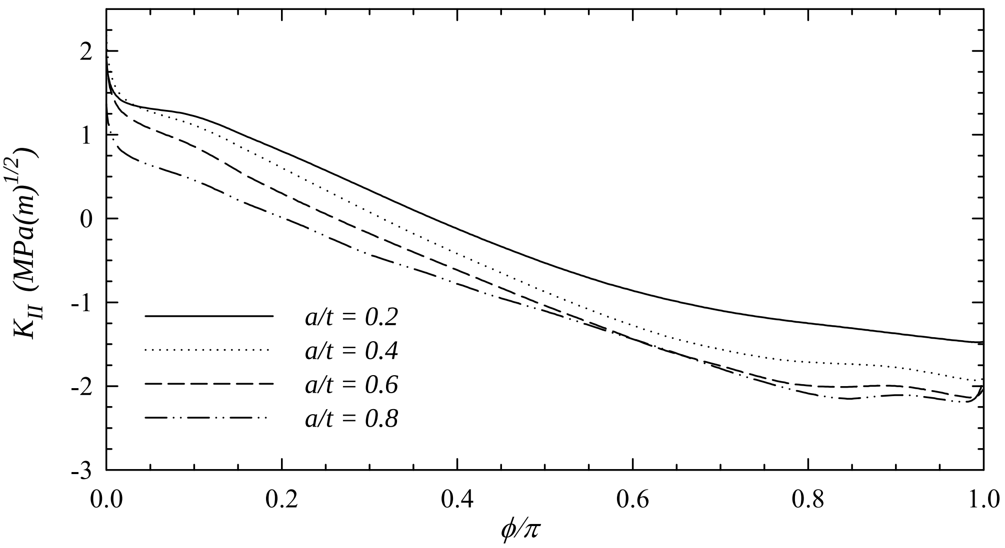
K_{II} $(MPa(m)^{1/2})$
2
1
0
-1
-2
-3
0.0
0.2
0.4
0.6
0.8
1.0
ϕ/π
a/t = 0.2
a/t = 0.4
a/t = 0.6
a/t = 0.8

a)

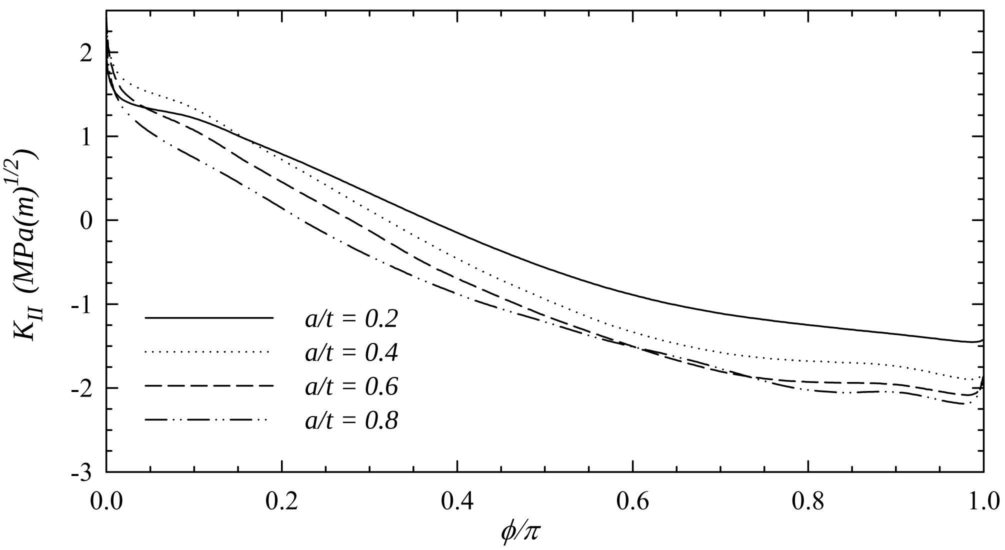
K_{II} $(MPa(m)^{1/2})$
2
1
0
-1
-2
-3
0.0
0.2
0.4
0.6
0.8
1.0
ϕ/π
a/t = 0.2
a/t = 0.4
a/t = 0.6
a/t = 0.8

b)

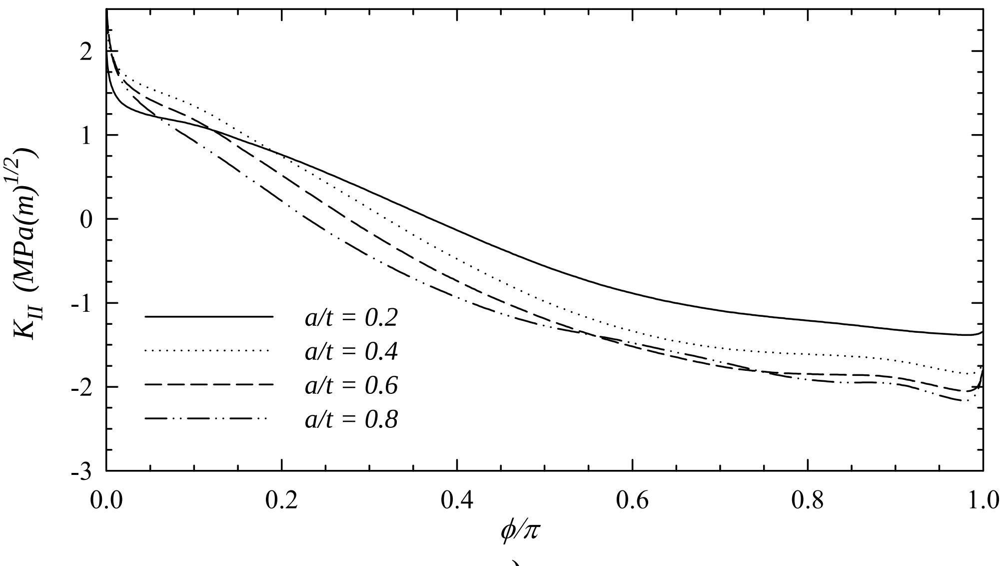

c)

Figure 5.16 Effects of crack shape and size on the distribution of mode II SIF along crack front for semi elliptical surface crack, under external load, **a)** *a/c=0.8,* **b)** *a/c=1.0,* **c)** *a/c=1.2*

Figure 5.17 show the distribution of mode III SIF around crack front for semi elliptical surface crack under tensile loading.

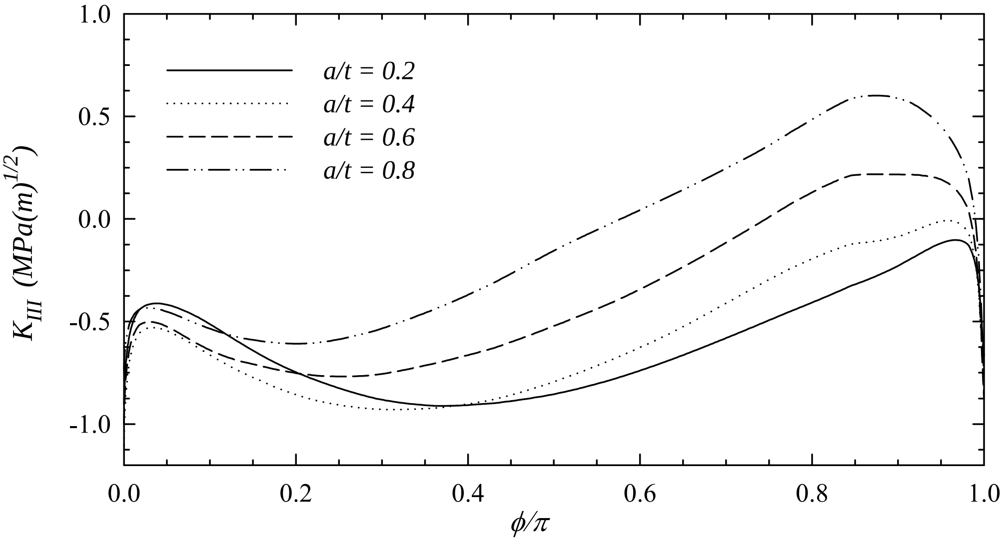

a)

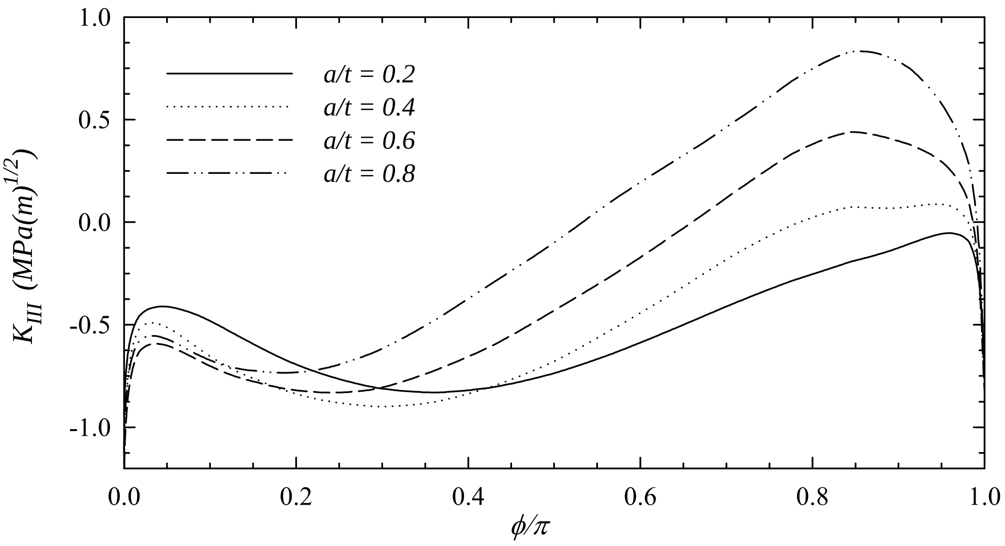

b)

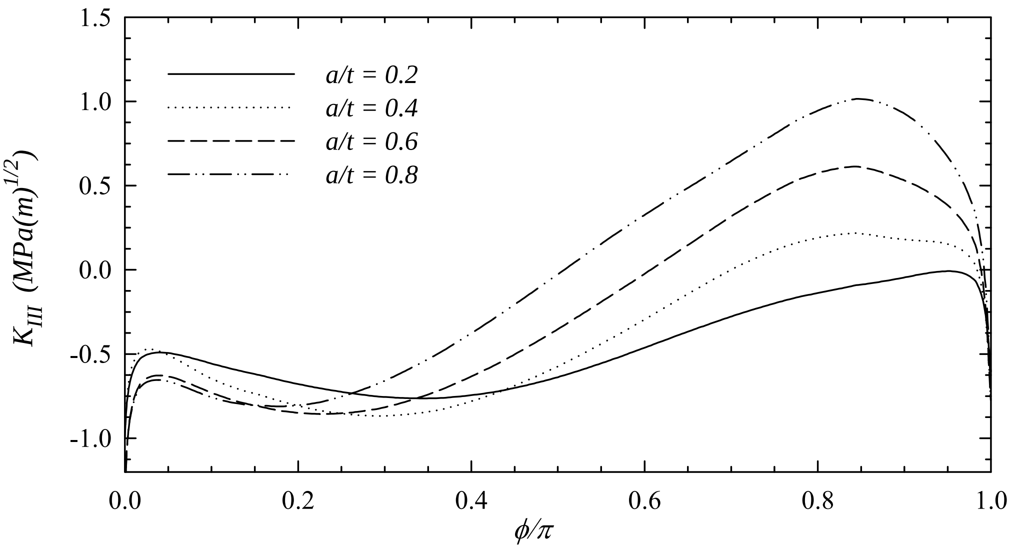

c)

Figure 5.17 Effects of crack geometry on the distribution of mode III SIF along crack front for semi elliptical surface crack, under external load, **a)** *a/c=0.8,* **b)** *a/c=1.0,* **c)** *a/c=1.2*

Figure 5.18 show the distribution of energy release rate along crack front for semi elliptical surface crack under tensile loading.

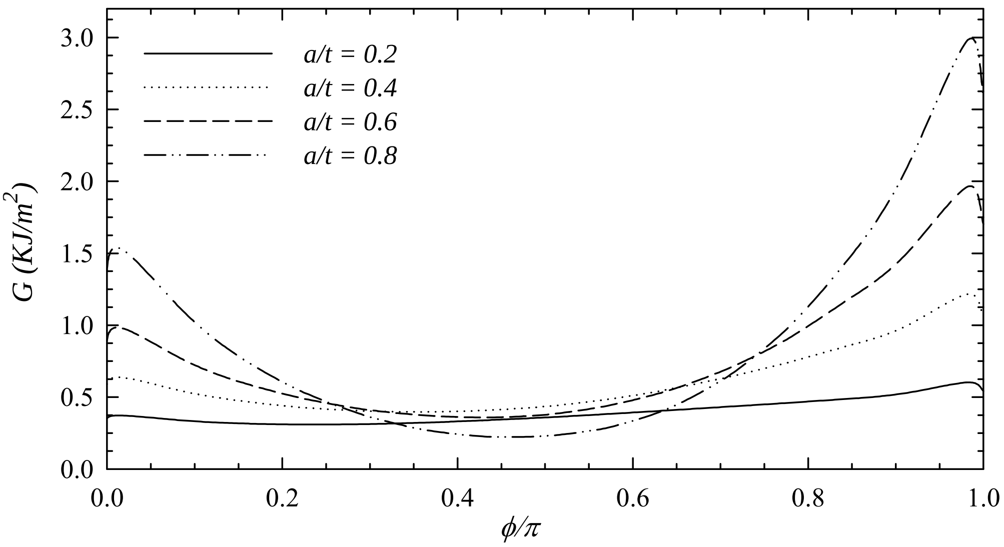
a/t = 0.2
a/t = 0.4
a/t = 0.6
a/t = 0.8
G (KJ/m2)
ϕ/π
0.0
0.5
1.0
1.5
2.0
2.5
3.0
0.2
0.4
0.6
0.8
1.0

a)

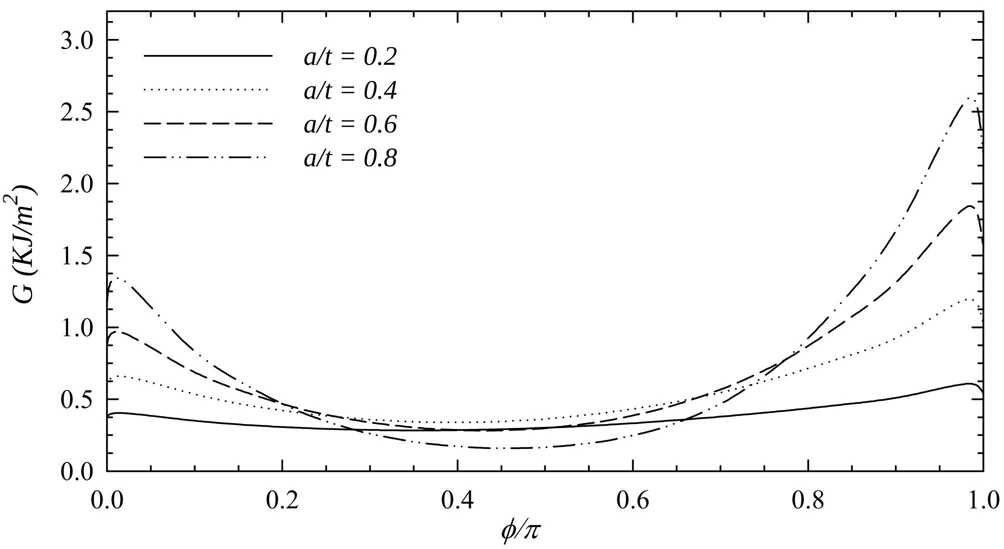
a/t = 0.2
a/t = 0.4
a/t = 0.6
a/t = 0.8
G (KJ/m2)
ϕ/π
0.0
0.5
1.0
1.5
2.0
2.5
3.0
0.2
0.4
0.6
0.8
1.0

b)

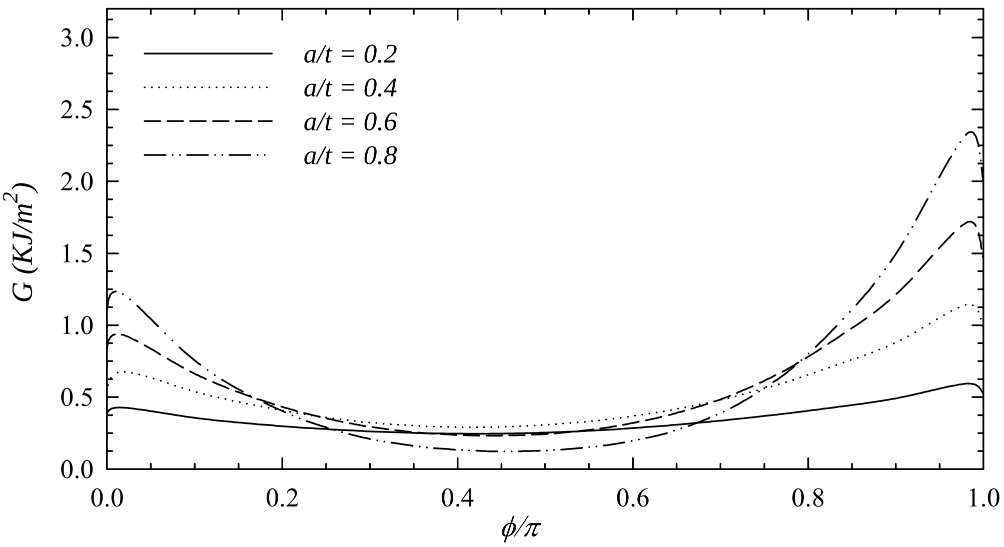

c)

Figure 5.18 Effects of crack geometry on the distribution of energy release rate along crack front for semi elliptical surface crack, under external load, **a)** *a/c=0.8,* **b)** *a/c=1.0,* **c)** *a/c=1.2*

5.3.2 Effects of Residual Stress on Fracture Parameters

It is observed that stress state for the riveted joint is dependent on the riveting process parameters (interference and clamping). Once the stress state is changed, fracture parameters are expected to be changed accordingly. In this part of the study, effects of riveting parameters on the fracture parameters are investigated.

5.3.2.1 Effects of Interference for Quarter Elliptical Corner Crack

Mode I stress intensity factor under riveting simulation, and mixed mode stress intensity factors and energy release rates distributions along the crack front under external loading were plotted for the fixed crack geometry (*a/c*=1.0 and *a/t*=0.6) and varying values of interference (*%D*) and clamping (*%L*). Four different interference and clamping values (%0.00, %015, %0.30 and %0.50) were applied. These are plotted in Figure 5.19 to 5.22.

In order to study the effect of residual stress due to riveting simulation, first the fracture parameters were calculated under the residual stress only. As stated before, mode I SIF is very dominant and other modes of SIFs are negligible for the riveting simulation. Therefore only mode I SIFs are presented for residual stress loading. Mode I SIF distributions along the crack front for various interference and clamping values under residual stress state are plotted in Figure 5.18. From this figure, it is observed that for all clamping values (*%L*), values of K_I are increasing with increase in interference values (*%D*). Generally the magnitudes of K_I are maximum at the rivet hole side of the crack front ($2\phi/\pi \to 1$) and minimum at the faying surface of the plates ($2\phi/\pi \to 0$).

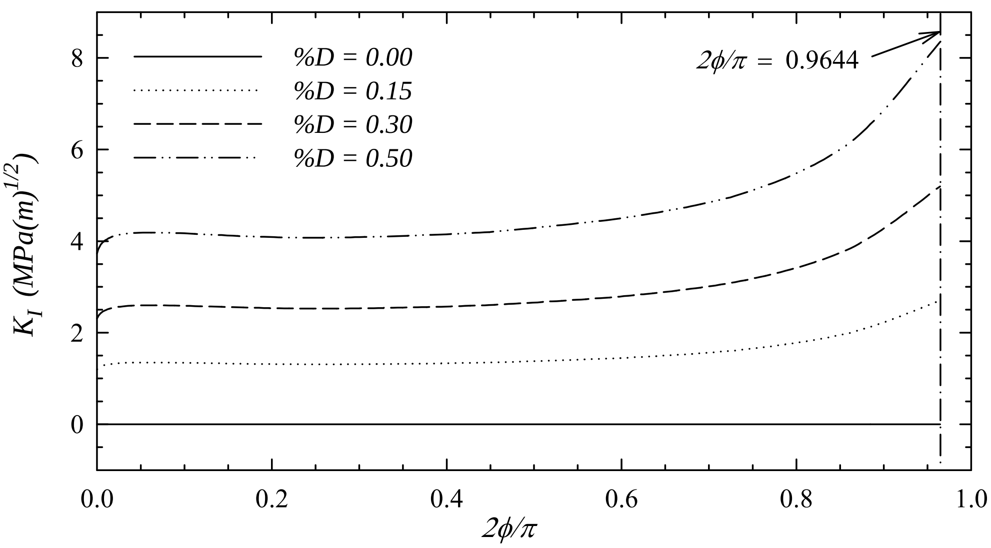

a)

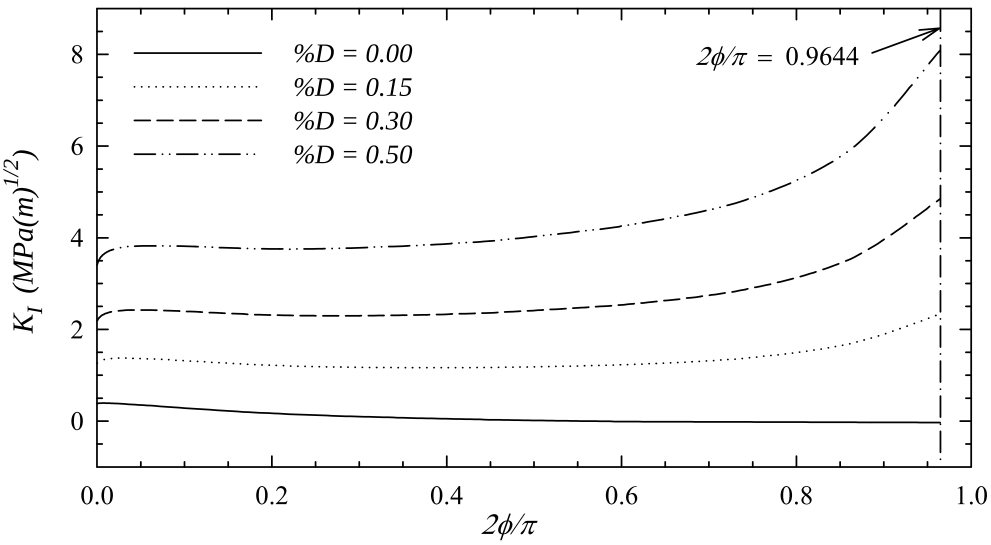
%D = 0.00
%D = 0.15
%D = 0.30
%D = 0.50
2φ/π = 0.9644
K_I (MPa(m)$^{1/2}$)
2φ/π

b)

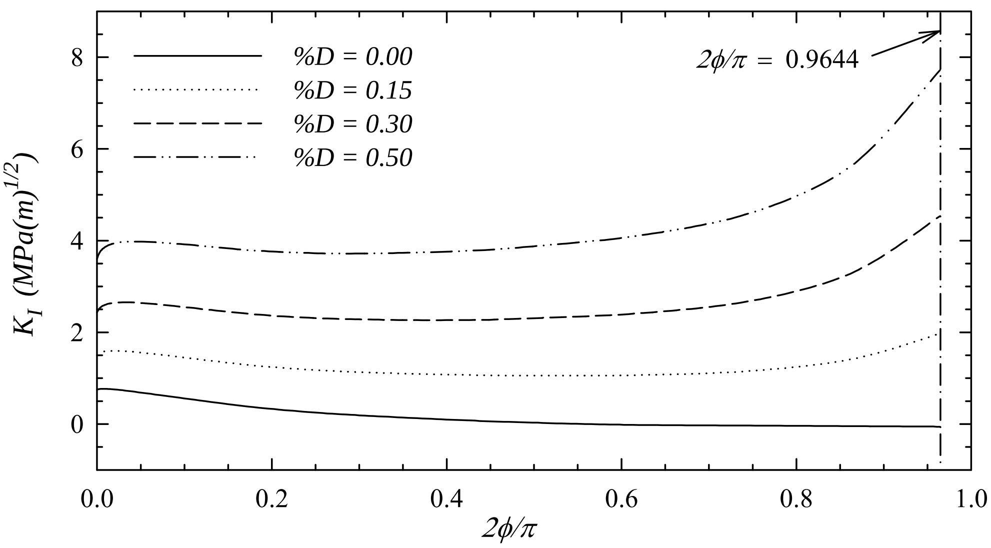
%D = 0.00
%D = 0.15
%D = 0.30
%D = 0.50
2φ/π = 0.9644
K_I (MPa(m)$^{1/2}$)
2φ/π

c)

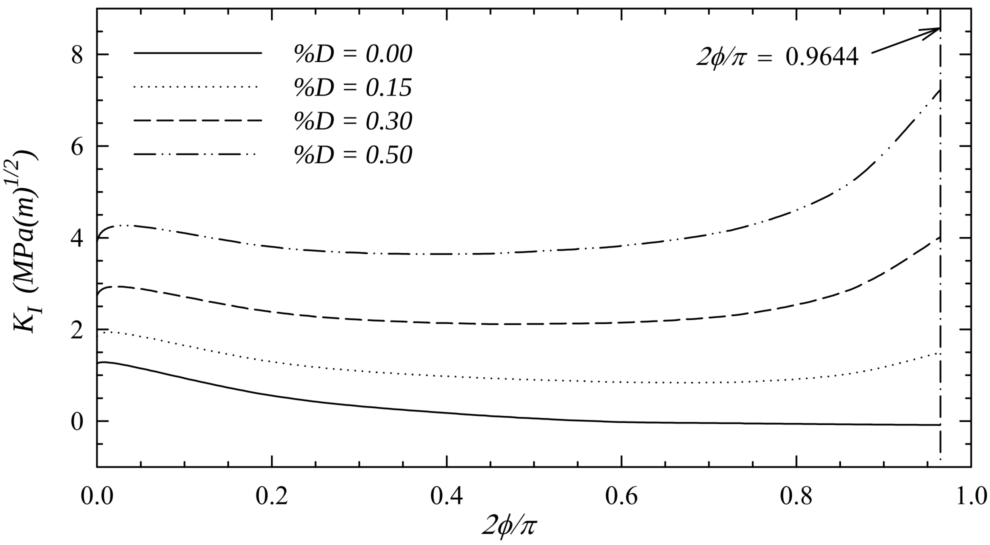

d)

Figure 5.19 Effects of interference on the distribution of mode I SIF along crack front for quarter elliptical corner crack, under residual stress, **a)** *%L=0.00,* **b)** *%L=0.15,* **c)** *%L=0.30,* **d)** *%L=0.50*

Figure 5.20 show the distribution of mode I SIF around crack front for quarter elliptical corner crack under external load. For all clamping values (*%L*), values of K_I are increasing with increase in interference values (*%D*). Generally the magnitudes of K_I are maximum at the rivet hole side of the crack front ($2\phi/\pi \rightarrow 1$) and minimum at the faying surface of the plates ($2\phi/\pi \rightarrow 0$). For the same interference and clamping values, magnitudes of K_I under external loading are approximately five times larger than that of residual stress state.

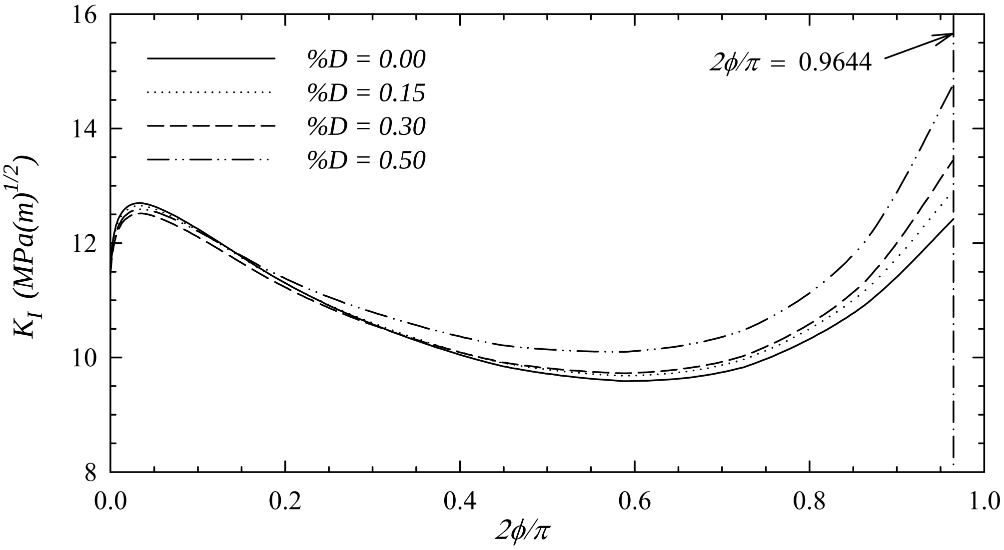
%D = 0.00
%D = 0.15
%D = 0.30
%D = 0.50
2ϕ/π = 0.9644
K_I (MPa(m)^1/2)
2ϕ/π

a)

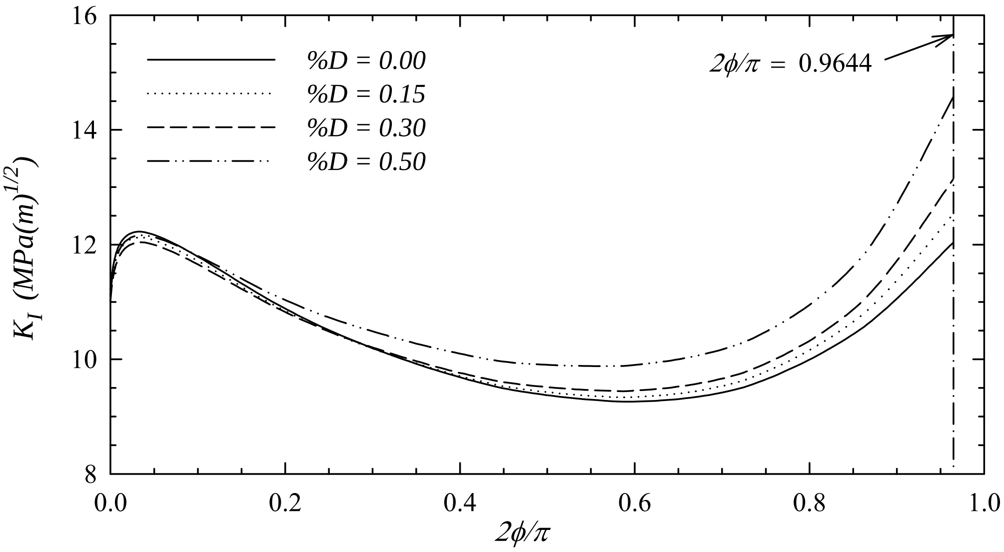
%D = 0.00
%D = 0.15
%D = 0.30
%D = 0.50
2ϕ/π = 0.9644
K_I (MPa(m)^1/2)
2ϕ/π

b)

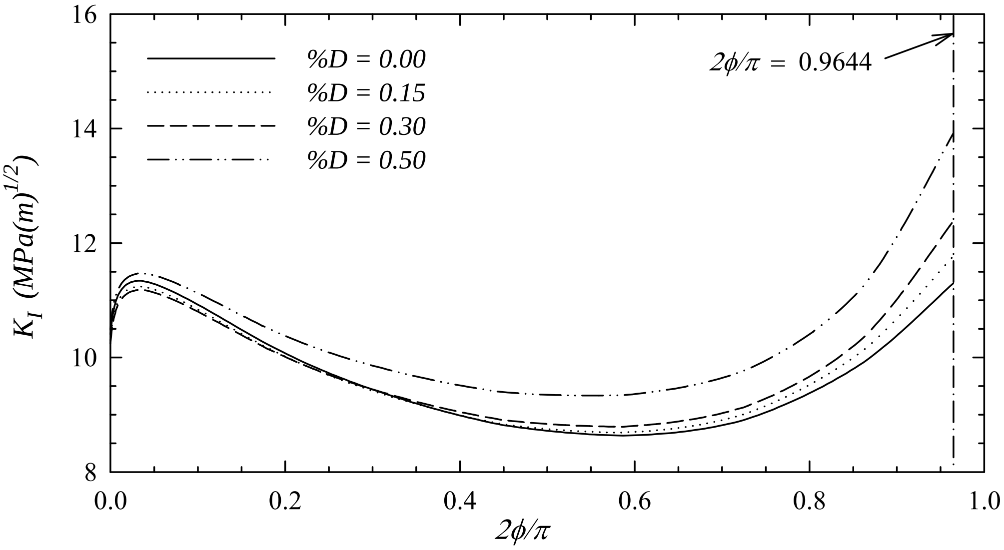

c)

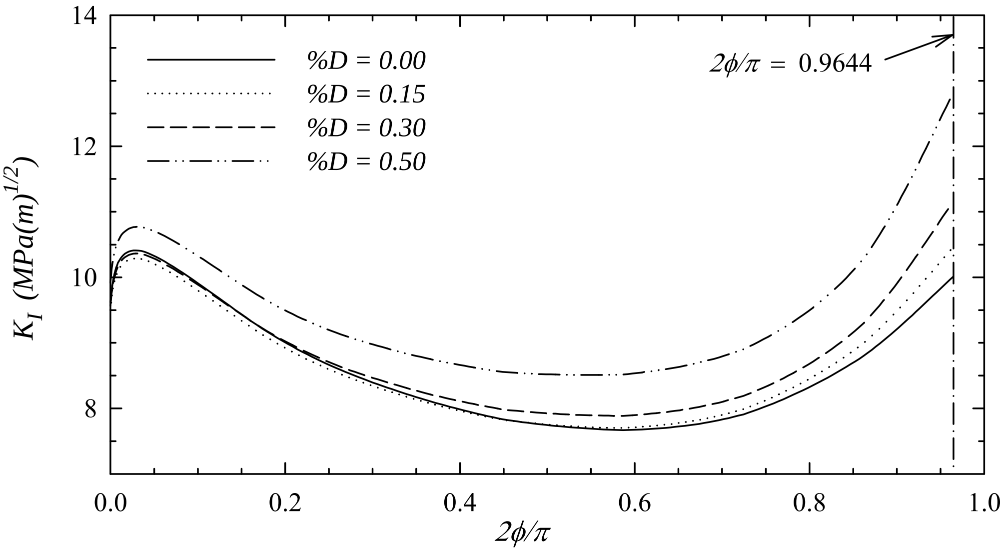

d)

Figure 5.20 Effects of interference on the distribution of mode I SIF along crack front for quarter elliptical corner crack, under external load, **a)** *%L=0.00,* **b)** *%L=0.15,* **c)** *%L=0.30,* **d)** *%L=0.50*

Magnitudes of mode II and III SIFs are small compared to mode I SIF values. Also effects of interference on the distributions of mode II and mode III SIFs are small compared to the mode I SIF. Illustrative plots for these modes are shown in Figure 5.21. Therefore, instead of presenting all mode II and mode III results, energy release rate which contains the contribution of all fracture modes of SIFs are presented.

Figure 5.21.a and 5.21.b show the distribution of mode II and mode III SIF around crack front for quarter elliptical corner crack under tensile loading for the clamping value of %0.50, respectively. Distributions show similar trends for all clamping values. For the distribution of mode II SIF along crack front, there are junction points on the crack front at which K_{II} values match, change signs and trends. Magnitudes of K_{II} are generally decreasing with increase in interference values. For all cases, magnitudes of K_{II} are approximately the same at the faying surface side of the crack front ($2\phi/\pi \rightarrow 0$) and faying surface of the plates ($2\phi/\pi \rightarrow 1$). For the distribution of mode III SIF along crack front, magnitudes of K_{III} are generally decreasing with increase in interference values.

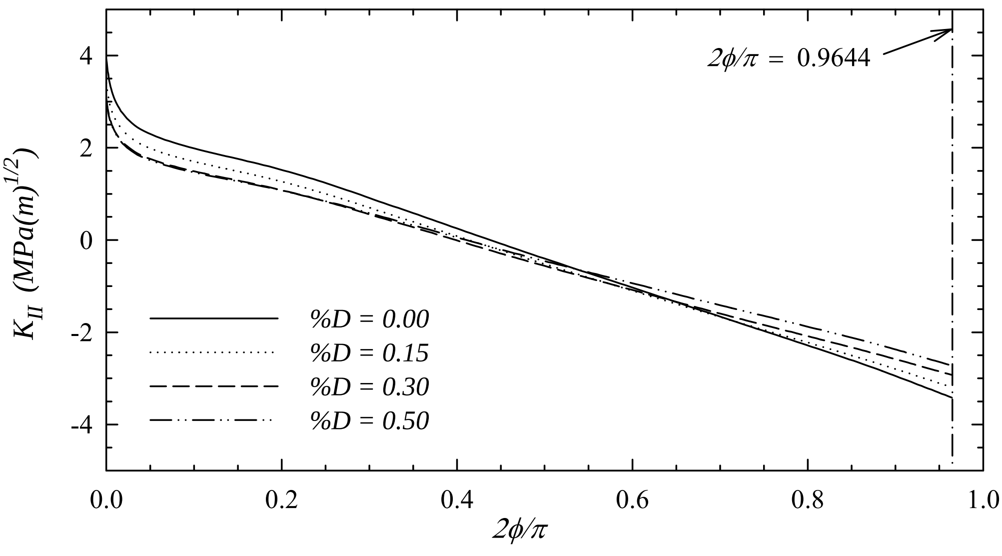

a)

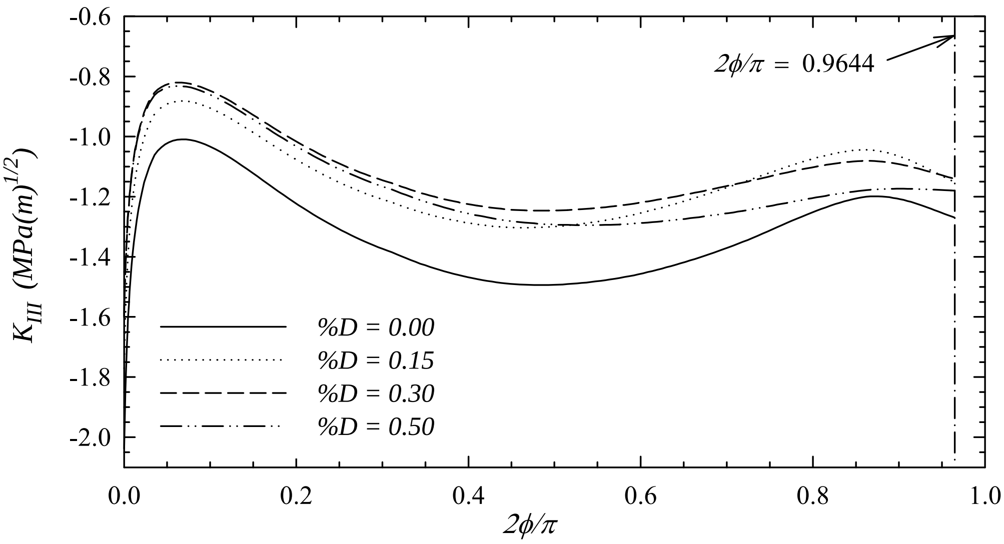

b)

Figure 5.21 Effects of interference on the distribution of **a)** mode II SIF, **b)** mode III SIF along crack front for quarter elliptical corner crack, under external loading, *%L=0.50*

Figure 5.22 show the distribution of energy release rate along crack front for quarter elliptical corner crack under external load. Distribution of G is very similar to K_I. As stated before the energy release rate can be treated as an equivalent stress intensity factor which includes the effects of three modes of SIFs. Since mode II and mode III SIF values are small compared to the values of mode I SIF, contribution of mode I SIF on energy release rate is much higher than the other modes.

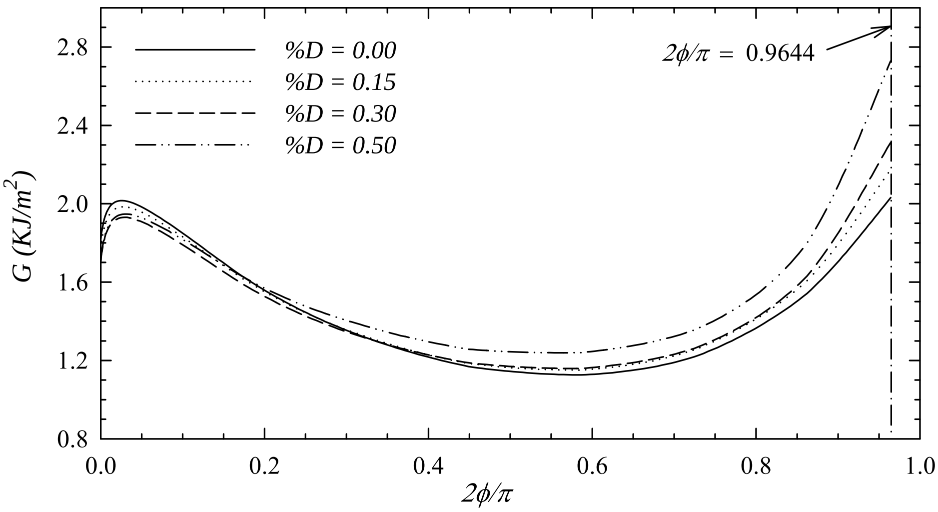
%D = 0.00
%D = 0.15
%D = 0.30
%D = 0.50
2ϕ/π = 0.9644
G (KJ/m²)
2ϕ/π
0.0
0.2
0.4
0.6
0.8
1.0
0.8
1.2
1.6
2.0
2.4
2.8

a)

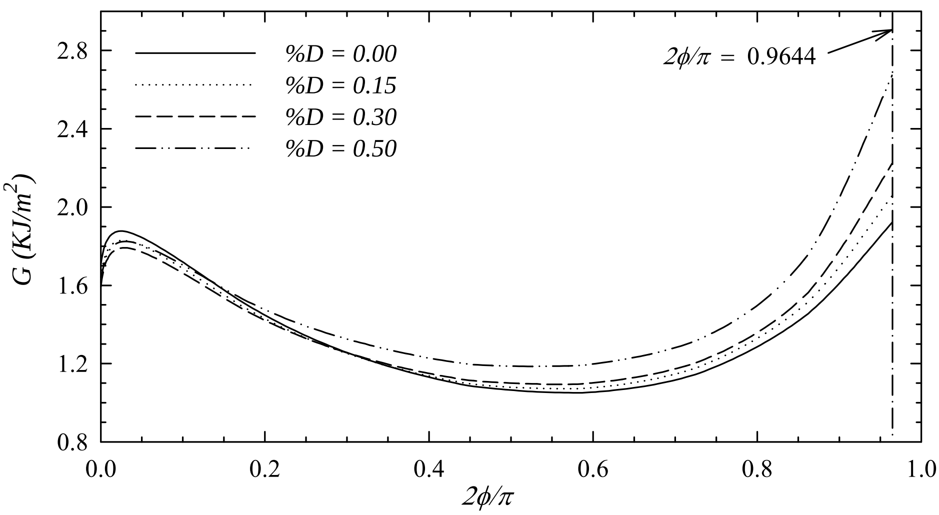
%D = 0.00
%D = 0.15
%D = 0.30
%D = 0.50
2ϕ/π = 0.9644
G (KJ/m²)
2ϕ/π
0.0
0.2
0.4
0.6
0.8
1.0
0.8
1.2
1.6
2.0
2.4
2.8

b)

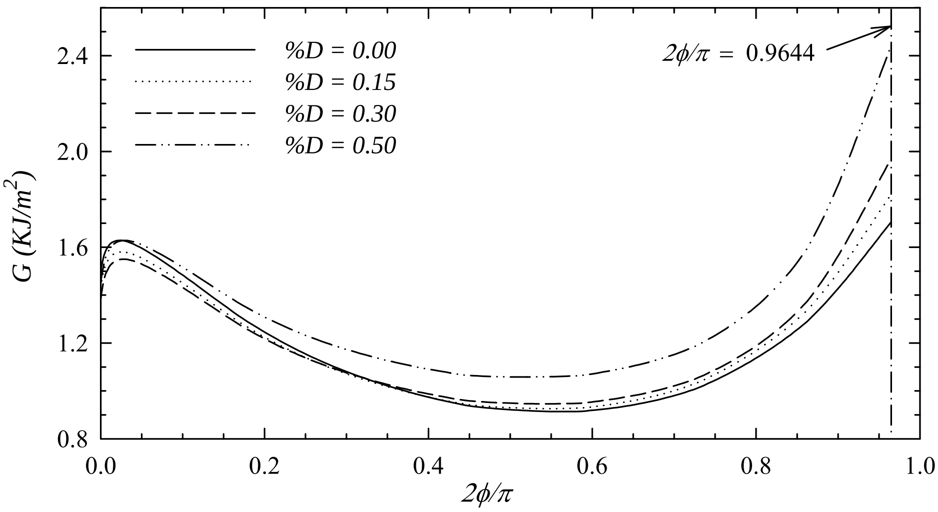

c)

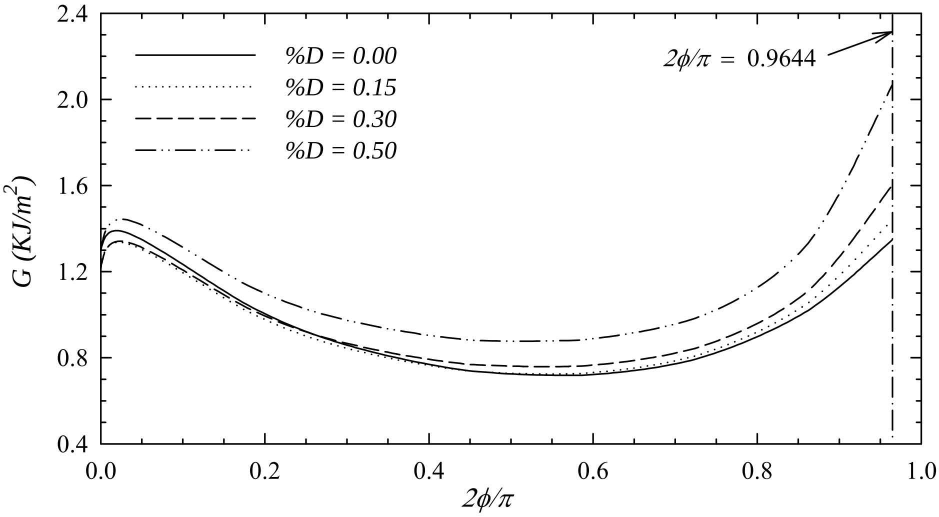

d)

Figure 5.22 Effects of interference on the distribution of energy release rate along crack front for quarter elliptical corner crack, under external load, **a)** *%L=0.00*, **b)** *%L=0.15*, **c)** *%L=0.30*, **d)** *%L=0.50*

5.3.2.2 Effects of Interference for Semi Elliptical Surface Crack

For the riveting simulation, effects of interference on the distribution of mode I SIF along crack front for semi elliptical surface crack are plotted in Figure 5.23. As shown in this figure, for all clamping values (*%L*), values of K_I are increasing with increase in interference values (*%D*). Generally the magnitudes of K_I are maximum at the rivet hole side of the crack front ($\phi/\pi \rightarrow 1$) and minimum at the opposite side of the crack ($\phi/\pi \rightarrow 0$). Note that the 0 values for SIF for 0 interference and clamping values, as expected.

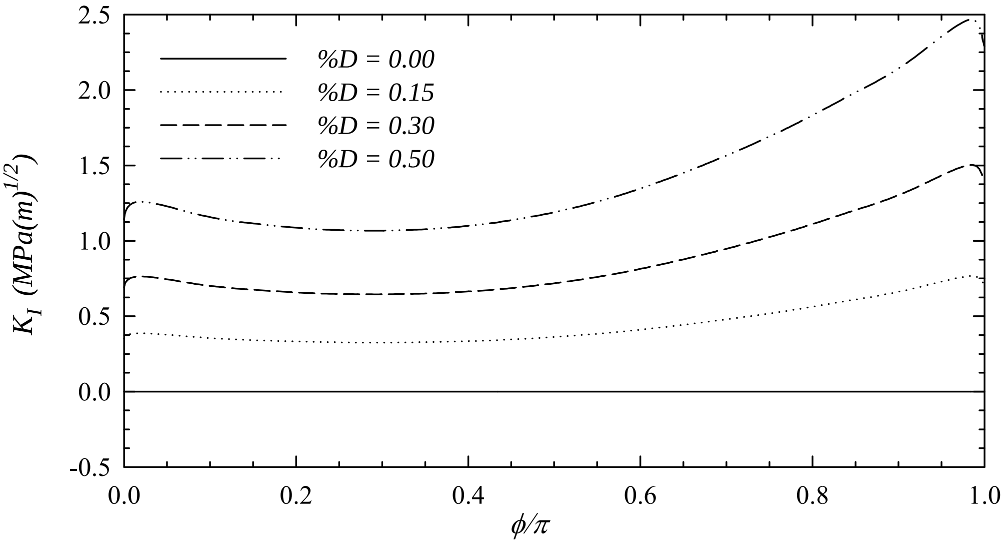

a)

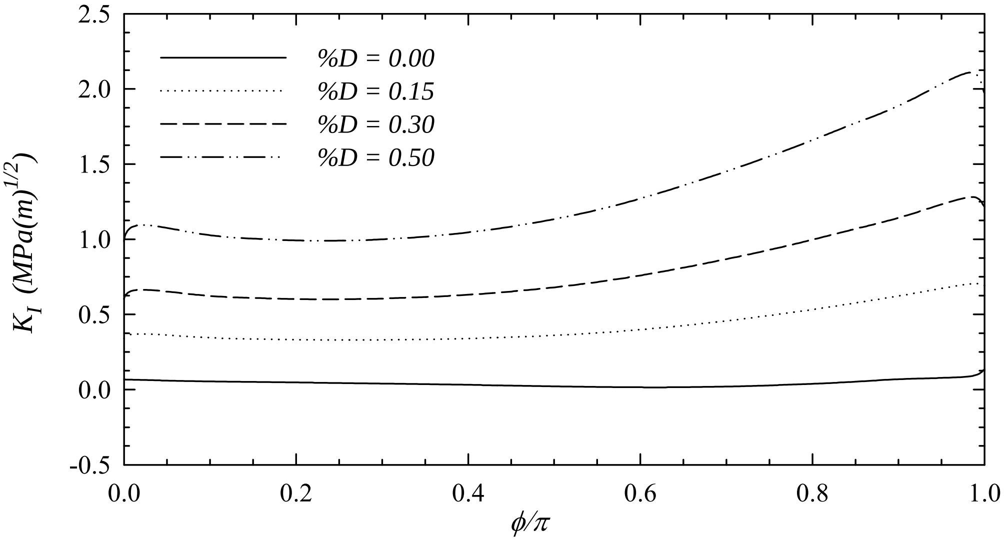
%D = 0.00
%D = 0.15
%D = 0.30
%D = 0.50
K_I $(MPa(m)^{1/2})$
ϕ/π

b)

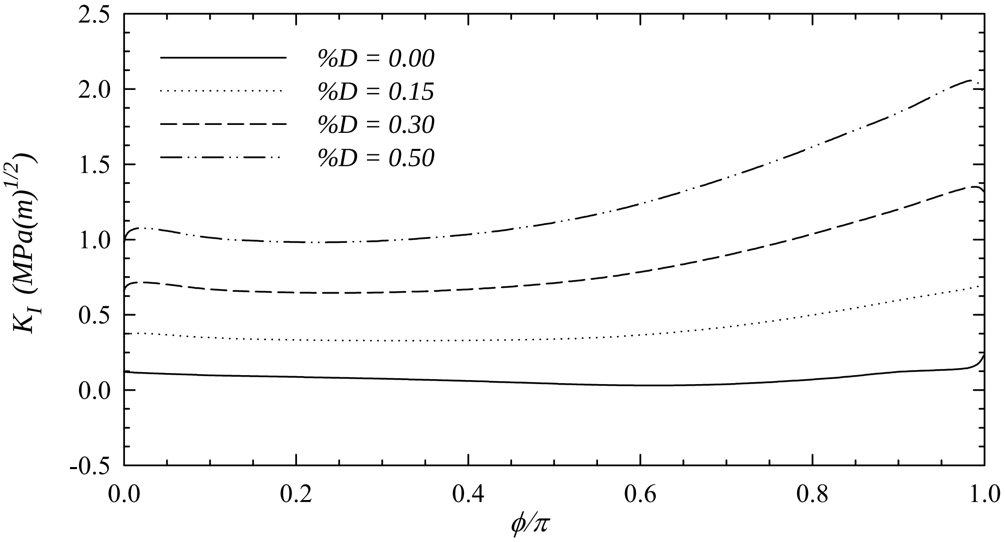
%D = 0.00
%D = 0.15
%D = 0.30
%D = 0.50
K_I $(MPa(m)^{1/2})$
ϕ/π

c)

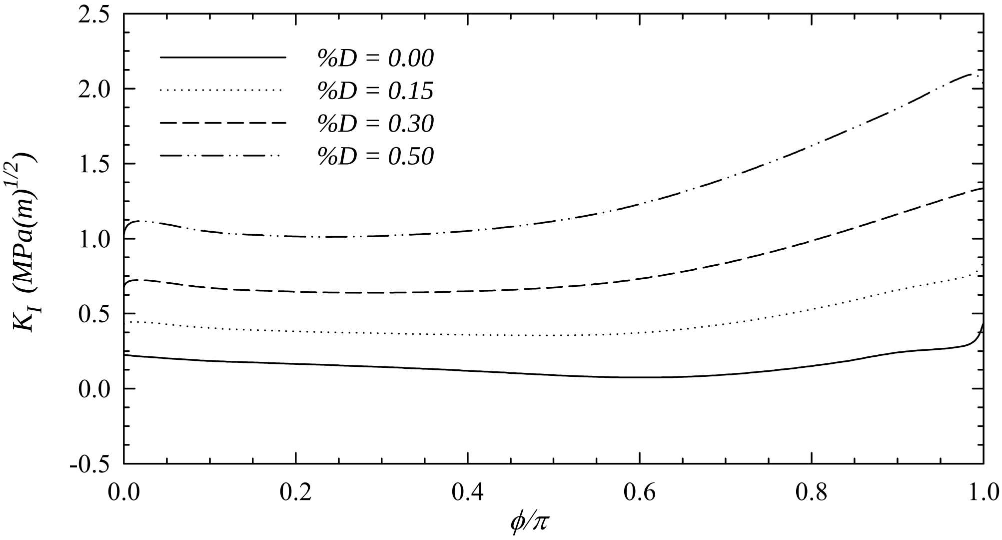

d)

Figure 5.23 Effects of interference on the distribution of mode I SIF along crack front for semi elliptical surface crack, under residual stress, **a)** *%L=0.00,* **b)** *%L=0.15,* **c)** *%L=0.30,* **d)** *%L=0.50*

Figure 5.24 show the effects of interference on the distribution of mode I SIF along crack front for semi elliptical surface crack under tensile loading. As shown in the figure effects of interference on the distribution of mode I SIF are not significant especially for high clamping values. For low clamping values, magnitude of the mode I SIF generally decreases with increase in interference values.

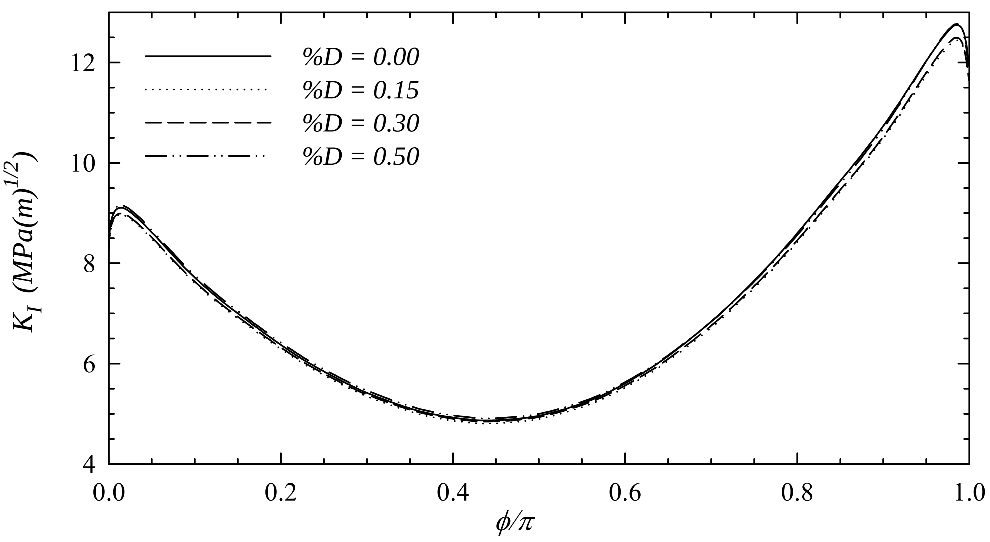
%D = 0.00
%D = 0.15
%D = 0.30
%D = 0.50
K_I $(MPa(m)^{1/2})$
ϕ/π

a)

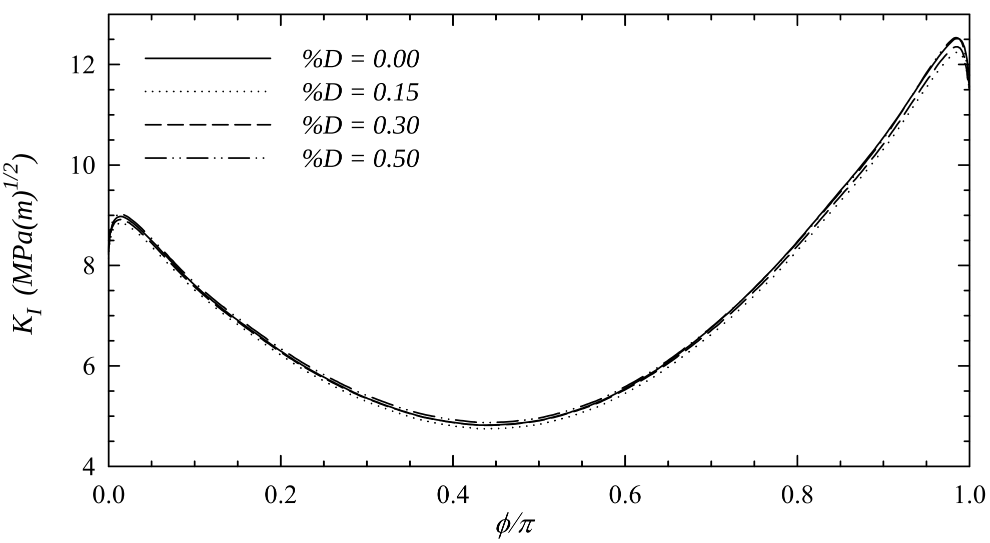
%D = 0.00
%D = 0.15
%D = 0.30
%D = 0.50
K_I $(MPa(m)^{1/2})$
ϕ/π

b)

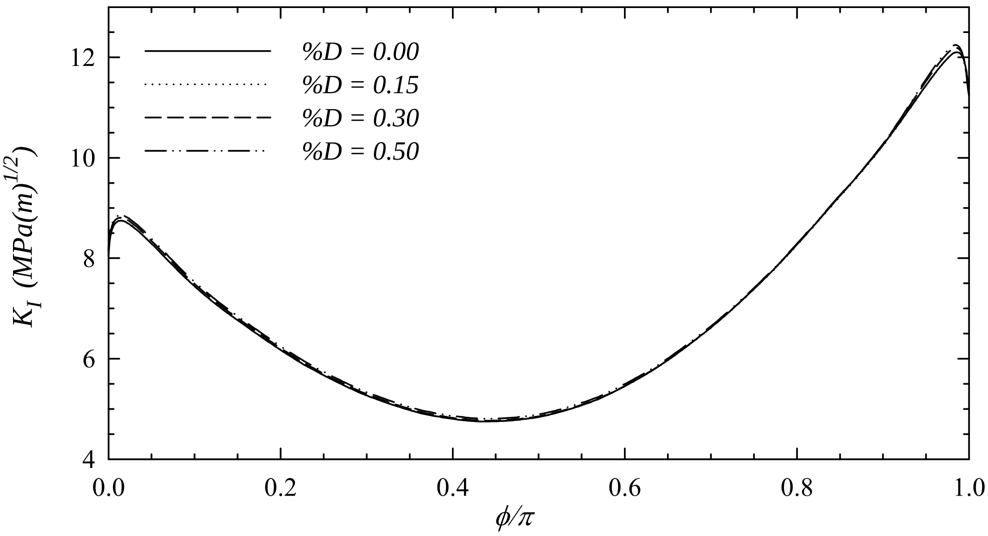

c)

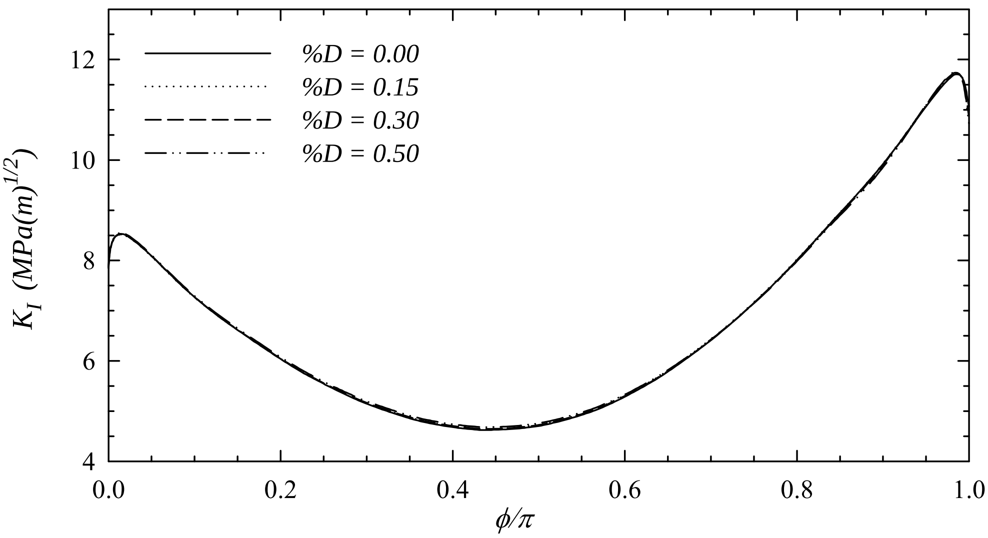

d)

Figure 5.24 Effects of interference on the distribution of mode I SIF along crack front for semi elliptical surface crack, under external load, **a)** *%L=0.00,* **b)** *%L=0.15,* **c)** *%L=0.30,* **d)** *%L=0.50*

For mode II and mode III SIFs, effects of interference are not significant as in the case of mode I SIF. Consequently no significant effect on the distribution of energy release rate is observed. Therefore only illustrative results are presented for mode II SIF, mode III SIF and energy release distribution for clamping values of %0.50. Figure 5.25.a illustrates the effects of interference on mode II SIF. Except from a portion of crack front near the rivet hole side, effect is not significant. At the crack front near the rivet hole side ($\phi / \pi \rightarrow 0$), magnitudes of mode II SIF is decreasing with increase in interference values. Figure 5.25.b illustrates the effects of interference on mode III SIF. Being not significant, magnitudes of mode III SIF is generally decreasing with increase in interference values. Figure 5.25.c illustrates the effects of interference on energy release rate. Again it is observed that effect of interference is not significant.

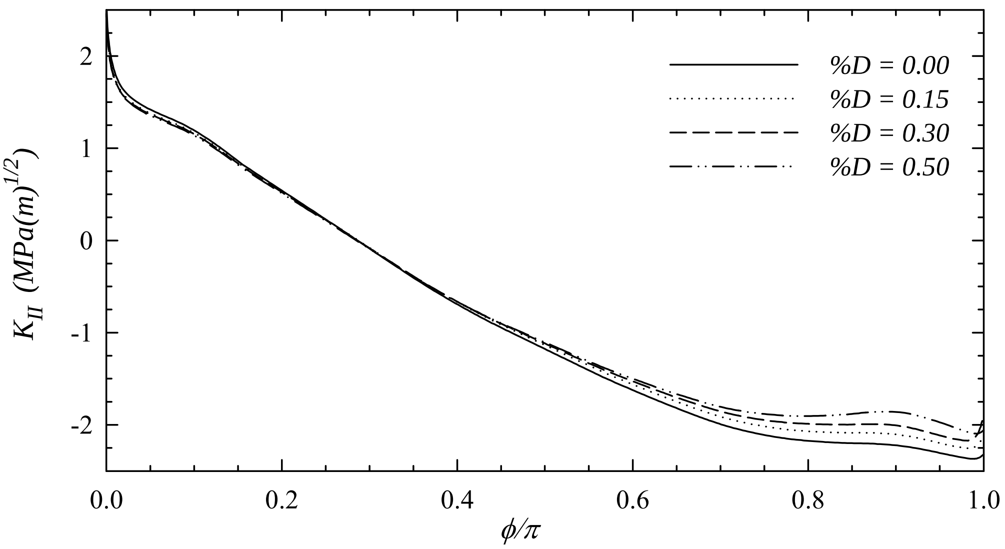

a)

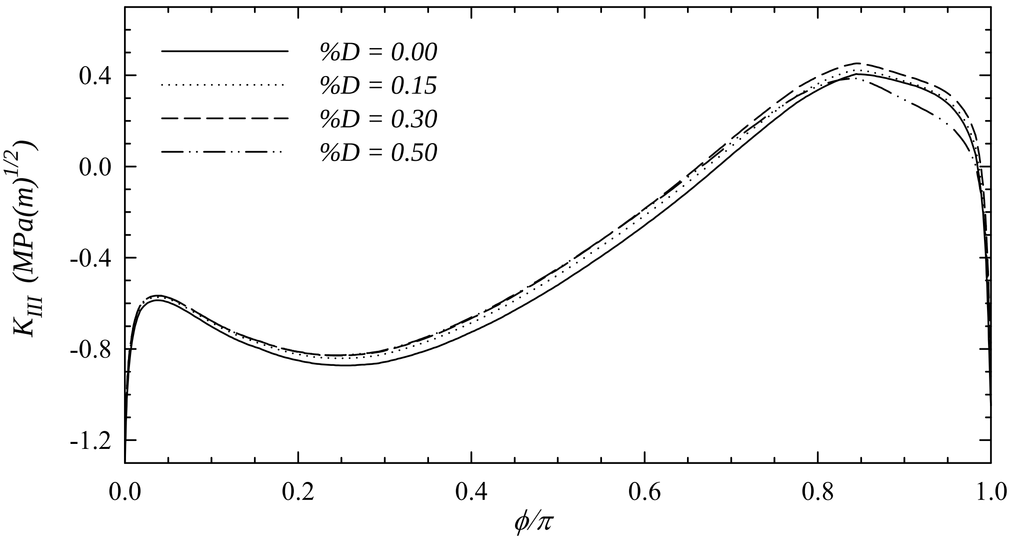

b)

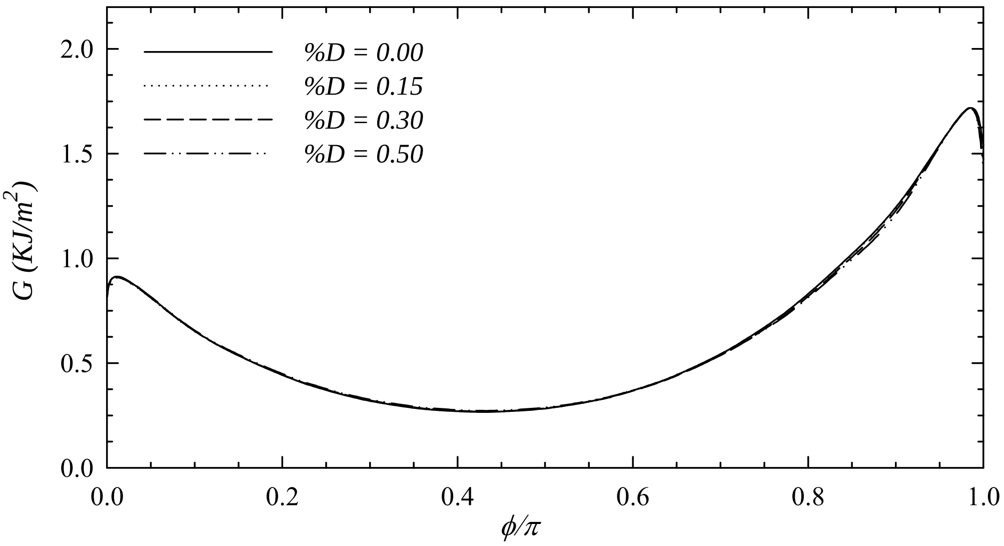

c)

Figure 5.25 Effects of interference on the distribution of **a)** mode II SIF, **b)** mode III SIF, **c)** energy release rate , along crack front for semi elliptical surface crack, under external loading, *%L=0.50*

5.3.2.3 Effects of Clamping for Quarter Elliptical Corner Crack

Mode I stress intensity factor under riveting simulation, and mixed mode stress intensity factors and energy release rates distributions along the crack front under external loading were plotted for the fixed crack geometry (*a/c*=1.0 and *a/t*=0.6) and varying values of interference (*%D*) and clamping (*%L*). Four different interference and clamping values (%0.00, %015, %0.30 and %0.50) were applied. These are plotted in Figure 5.26 to 5.28.

In order to study the effect of residual stress due to riveting simulation, first the fracture parameters were calculated under the residual stress only. Mode I SIF distributions along the crack front for various interference and clamping values under residual stress state are plotted in Figure 5.26. For zero interference (*%D*=0), values of K_I are generally increasing with increase in clamping values (*%L*). For higher interference values, values of K_I are generally decreasing with increase in clamping values (*%L*). Note that zero interference and clamping results in 0 values for SIF along the crack front.

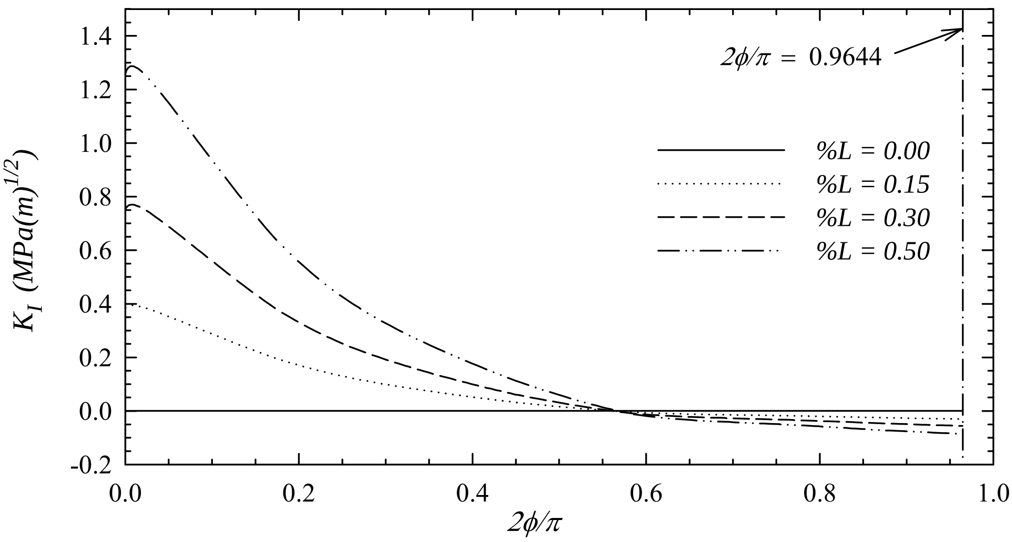

a)

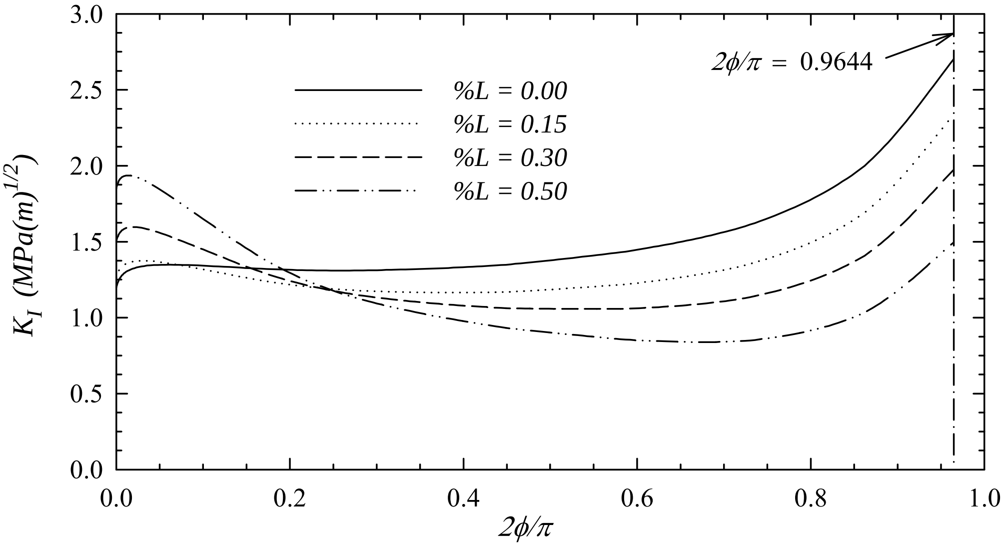
3.0
2.5
2.0
1.5
1.0
0.5
0.0
K_I $(MPa(m)^{1/2})$
%L = 0.00
%L = 0.15
%L = 0.30
%L = 0.50
$2\phi/\pi$ = 0.9644
0.0
0.2
0.4
0.6
0.8
1.0
$2\phi/\pi$

b)

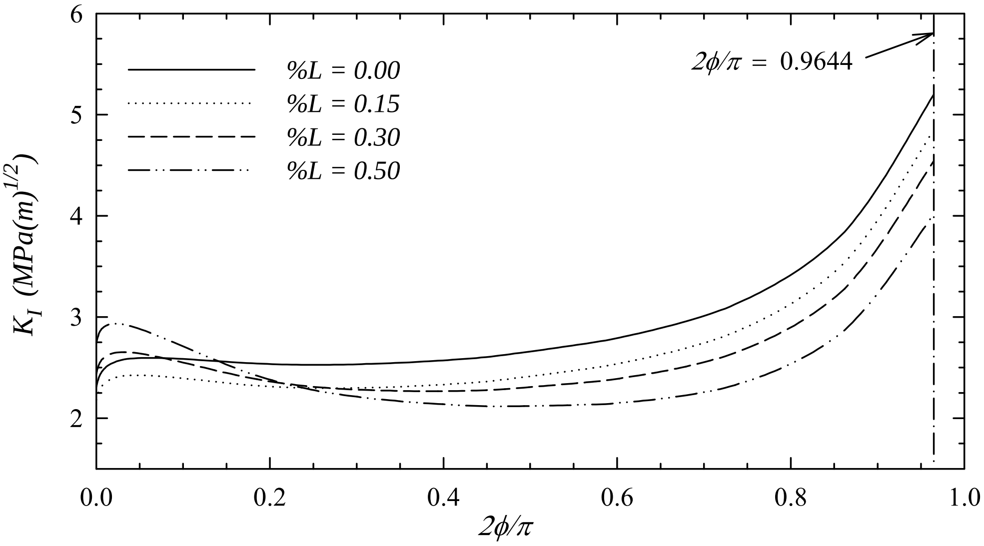
6
5
4
3
2
K_I $(MPa(m)^{1/2})$
%L = 0.00
%L = 0.15
%L = 0.30
%L = 0.50
$2\phi/\pi$ = 0.9644
0.0
0.2
0.4
0.6
0.8
1.0
$2\phi/\pi$

c)

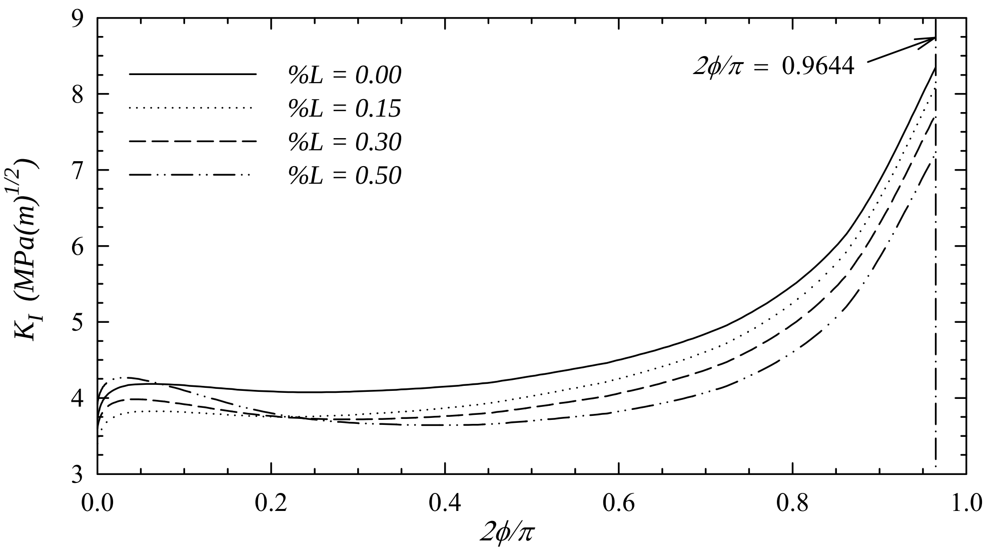

d)

Figure 5.26 Effects of clamping on the distribution of mode I SIF along crack front for quarter elliptical corner crack, under residual stress, **a)** *%D=0.00,* **b)** *%D=0.15,* **c)** *%D=0.30,* **d)** *%D=0.50*

Figure 5.27 show the distribution of mode I SIF along crack front for quarter elliptical corner crack under external load. From the figures it is observed that clamping has a deep effect on mode I SIF. For all interference values (*%D*), values of K_I are decreasing with increase in clamping values (*%L*). Generally the magnitudes of K_I are maximum at two ends of the crack front ($2\phi/\pi \to 0$ and $2\phi/\pi \to 1$) and minimum at a middle point on the crack front ($2\phi/\pi \to 0.6$).

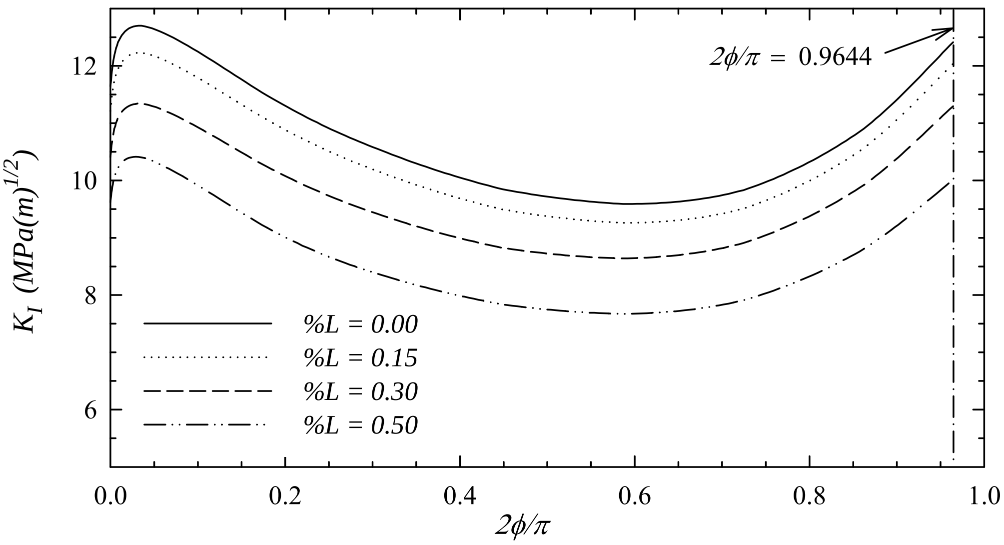

$2\phi/\pi = 0.9644$
12
10
8
6
K_I $(MPa(m)^{1/2})$
%L = 0.00
%L = 0.15
%L = 0.30
%L = 0.50
0.0
0.2
0.4
0.6
0.8
1.0
$2\phi/\pi$

a)

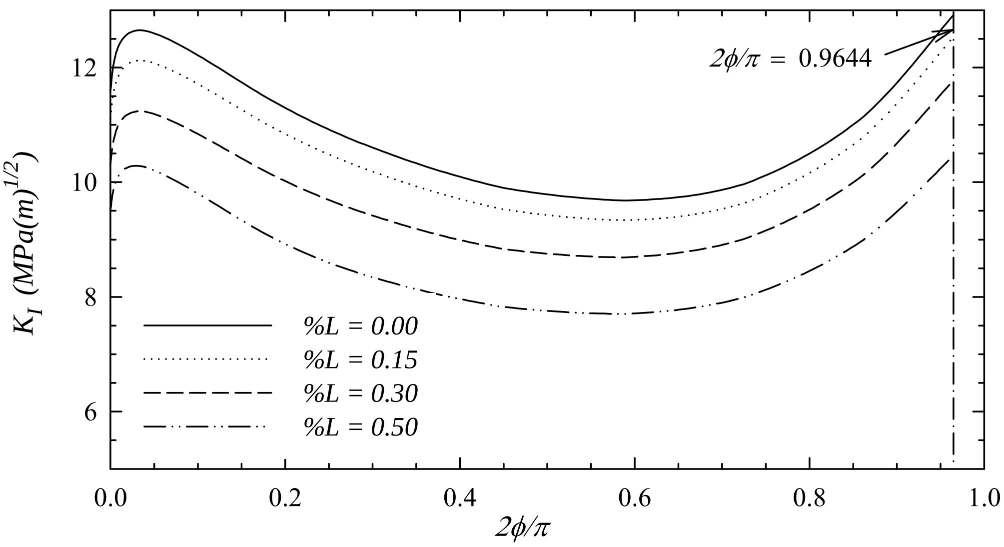

$2\phi/\pi = 0.9644$
12
10
8
6
K_I $(MPa(m)^{1/2})$
%L = 0.00
%L = 0.15
%L = 0.30
%L = 0.50
0.0
0.2
0.4
0.6
0.8
1.0
$2\phi/\pi$

b)

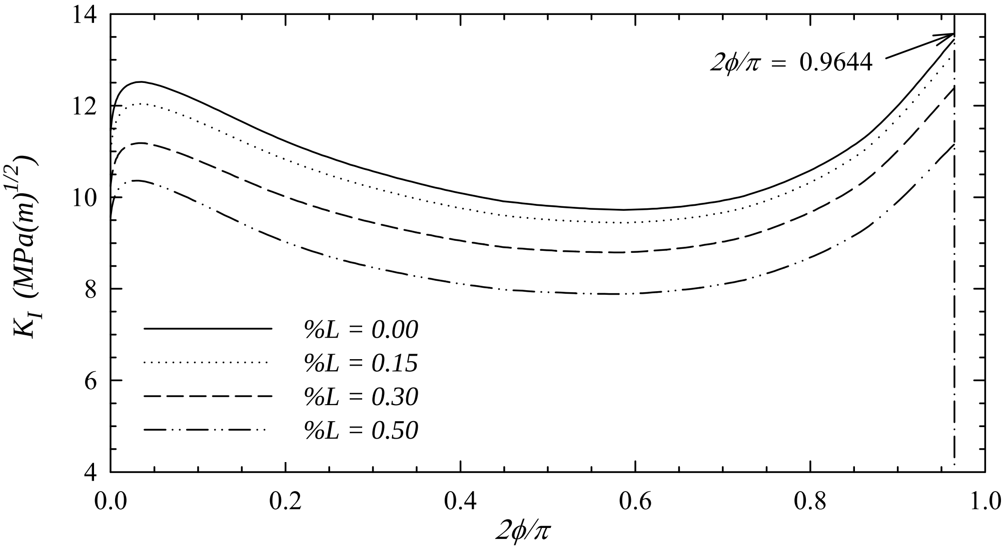

c)

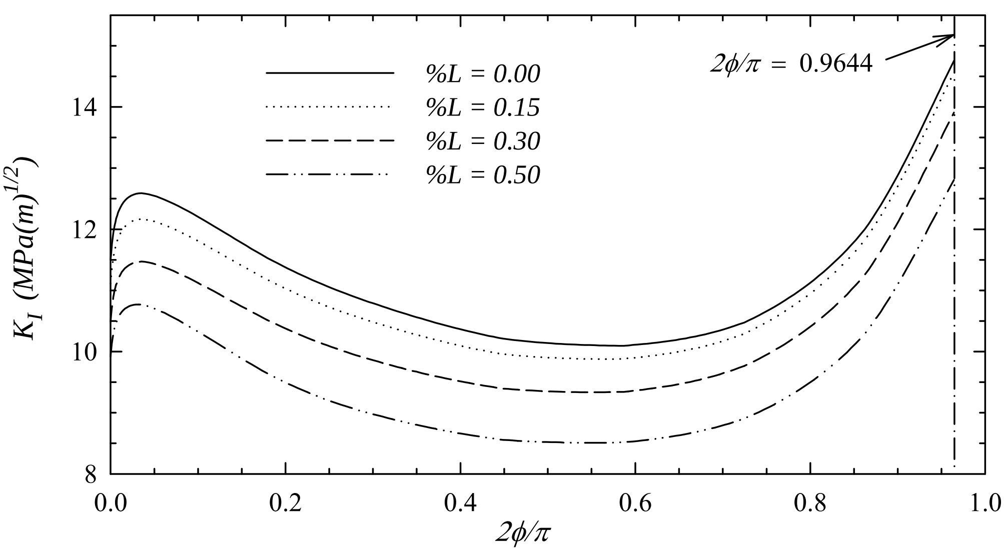

d)

Figure 5.27 Effects of clamping on the distribution of mode I SIF along crack front for quarter elliptical corner crack, under external load, **a)** *%D=0.00,* **b)** *%D=0.15,* **c)** *%D=0.30,* **d)** *%D=0.50*

For mode II and mode III SIFs, magnitudes are small compared to mode I SIF, and effects of clamping are not significant. Therefore only illustrative results are presented for mode II SIF, mode III SIF and energy release distribution for interference value of %0.15. Figure 5.28.a illustrates the effects of clamping on mode II SIF. It is observed that effect is not significant. Figure 5.28.b illustrates the effects of clamping on mode III SIF. Being not significant, magnitudes of mode III SIF is generally decreasing with increase in interference values. Figure 5.28.c illustrates the effects of clamping on energy release rate. Since mode I SIF is dominating over the other modes, trends of energy release rate is very similar to mode I SIF distribution.

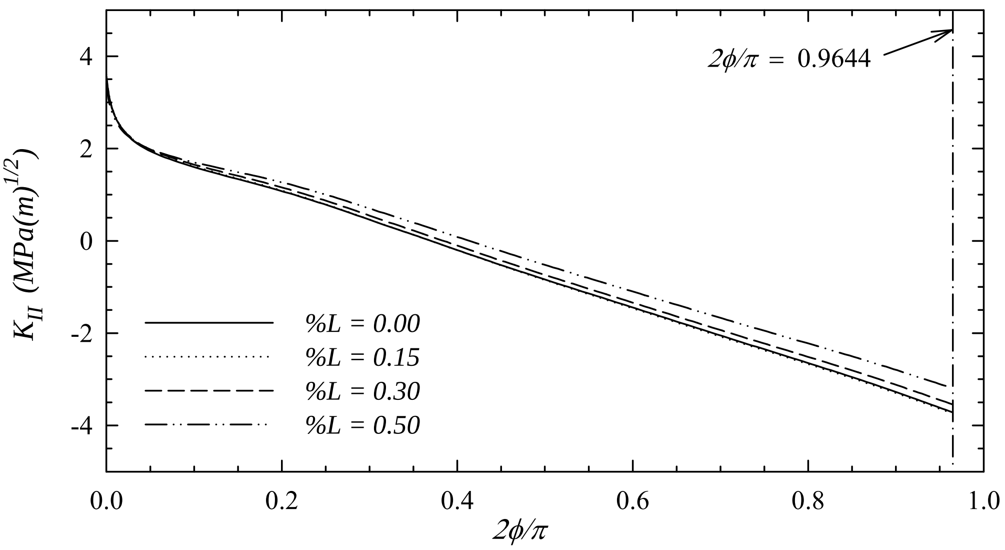

a)

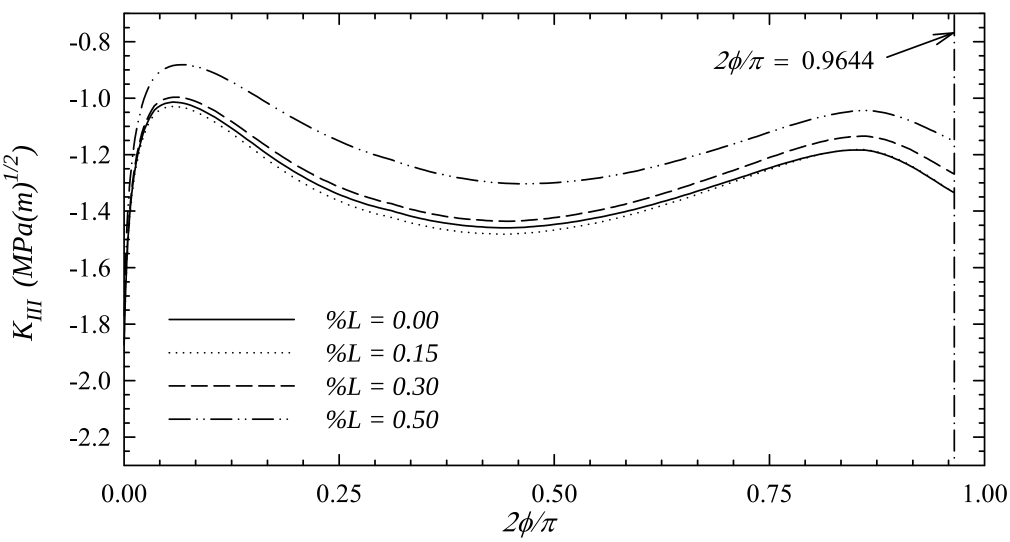

b)

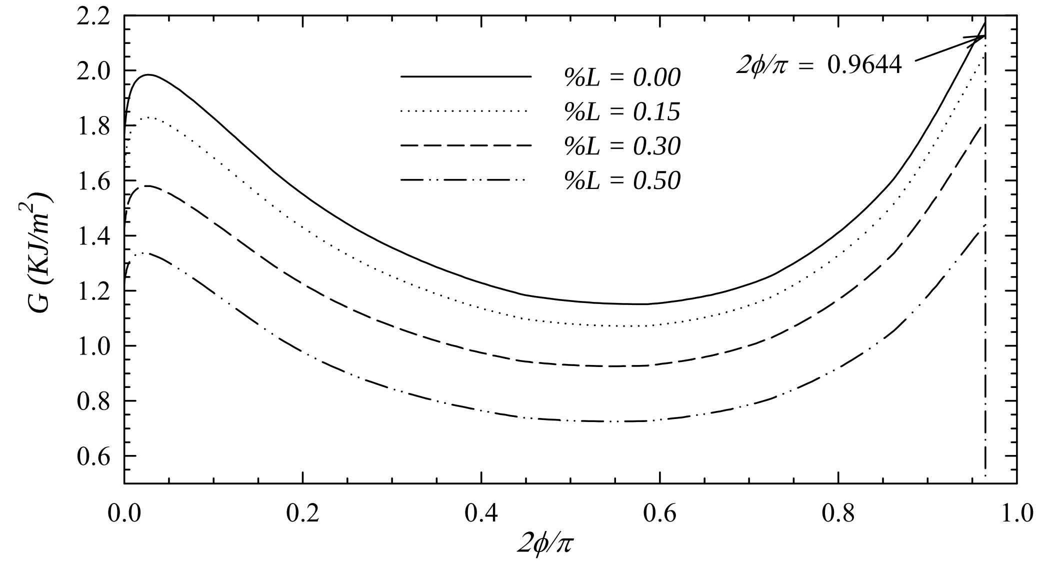

c)

Figure 5.28 Effects of clamping on the distribution of **a)** mode II SIF, **b)** mode III SIF, **c)** energy release rate , along crack front for quarter elliptical corner crack, under external loading, *%D=0.15*

5.3.2.4 Effects of Clamping for Semi Elliptical Surface Crack

Mode I stress intensity factor under riveting simulation, and mixed mode stress intensity factors and energy release rates distributions along the crack front under external loading were plotted for the fixed crack geometry (*a/c*=1.0 and *a/t*=0.6) and varying values of interference (*%D*) and clamping (*%L*). Four different interference and clamping values (%0.00, %015, %0.30 and %0.50) were applied. These are plotted in Figure 5.29 to 5.31.

In order to study the effect of residual stress due to riveting simulation, first the fracture parameters were calculated under the residual stress only. As stated before, mode I SIF is very dominant and other modes of SIFs are negligible for the riveting simulation. Therefore only mode I SIFs are presented for residual stress loading. Mode I SIF distributions along the crack front for various interference and clamping values under residual stress state are plotted in Figure 5.29. For zero interference (*%D*=0), values of K_I are generally increasing with increase in clamping values (*%L*). For higher interference values, values of K_I are generally decreasing with increase in clamping values (*%L*). Note that zero interference and clamping results in 0 values for SIF along the crack front.

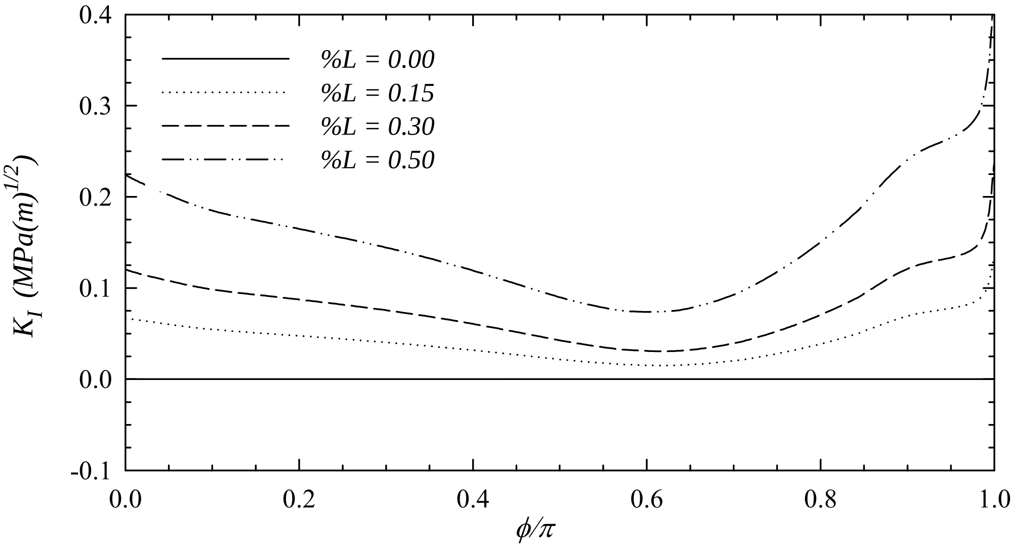

a)

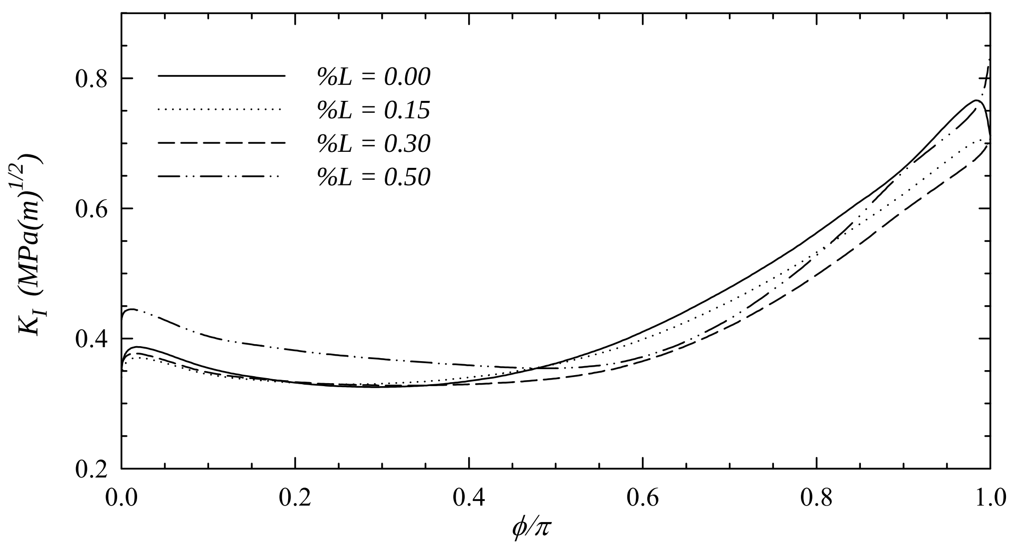

b)

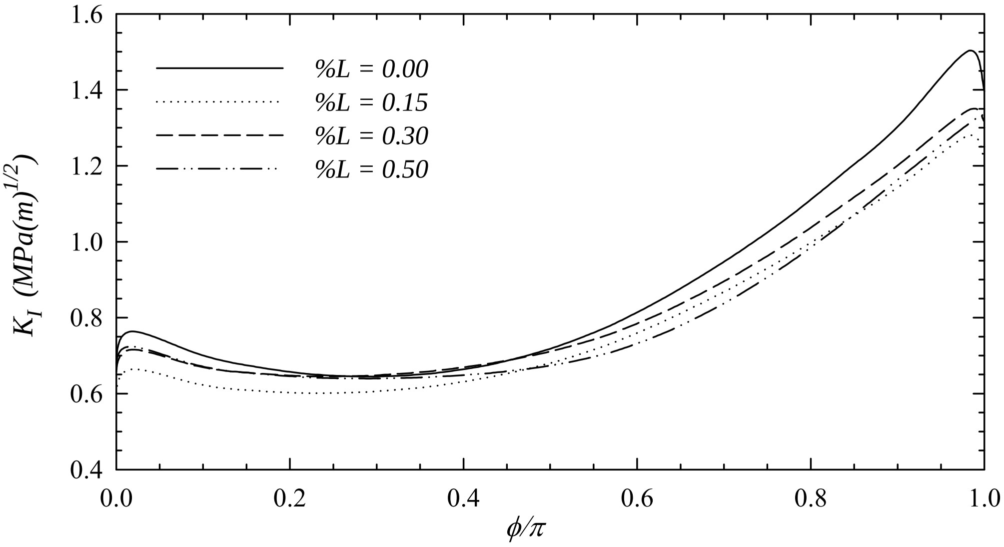

c)

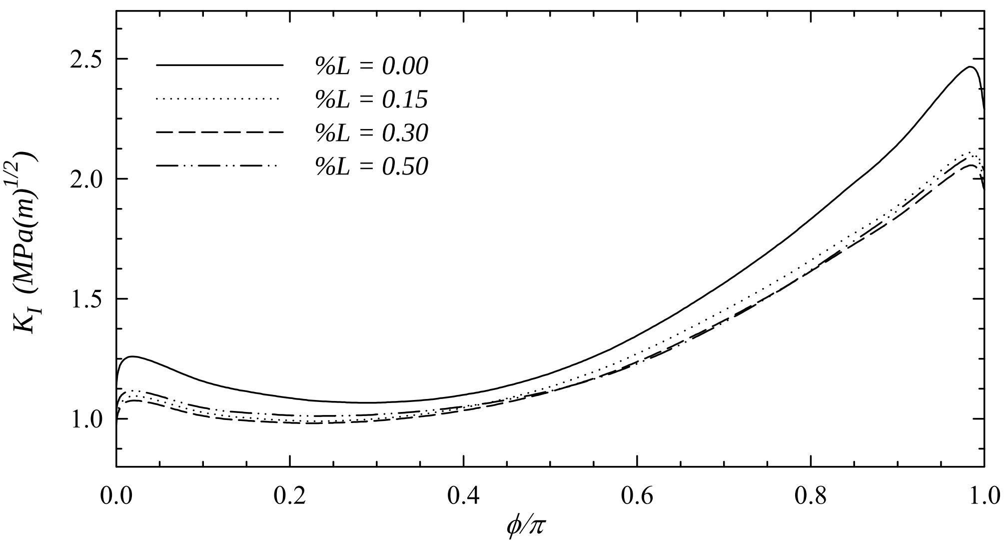

d)

Figure 5.29 Effects of clamping on the distribution of mode I SIF along crack front for semi elliptical surface crack, under residual stress, **a)** *%D=0.00,* **b)** *%D=0.15,* **c)** *%D=0.30,* **d)** *%D=0.50*

Figure 5.30 show the distribution of mode I SIF along crack front for semi elliptical surface crack under external load. For all interference values (*%D*), values of K_I are decreasing with increase in clamping values (*%L*). Generally the magnitudes of K_I are maximum at the crack tip near the rivet hole ($2\phi/\pi \to 1$) and minimum at a middle point on the crack front ($2\phi/\pi \to 0.45$).

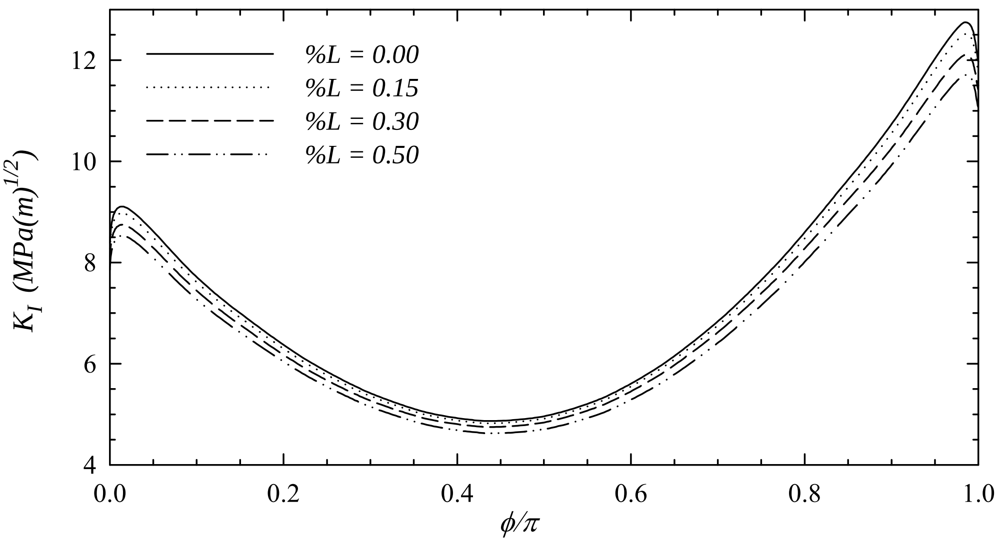

a)

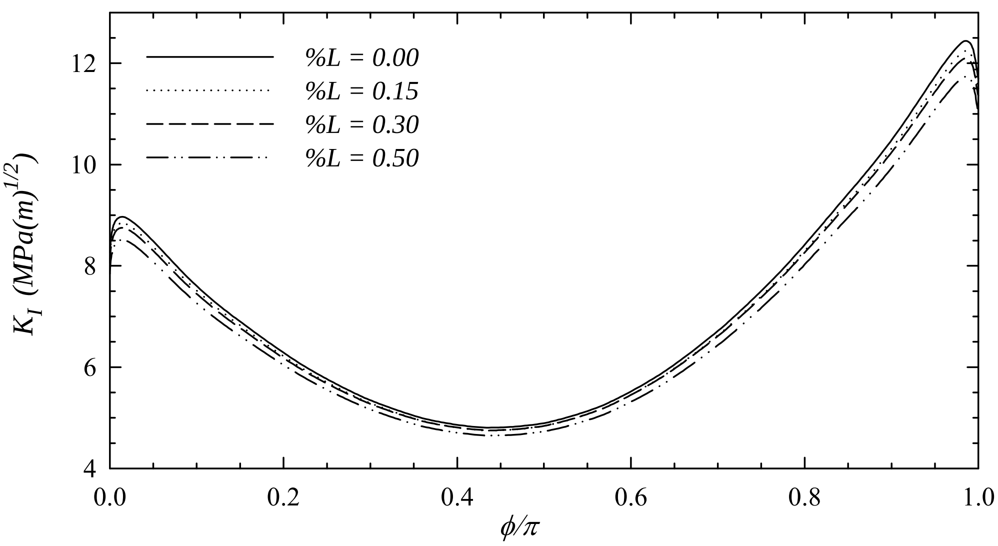

b)

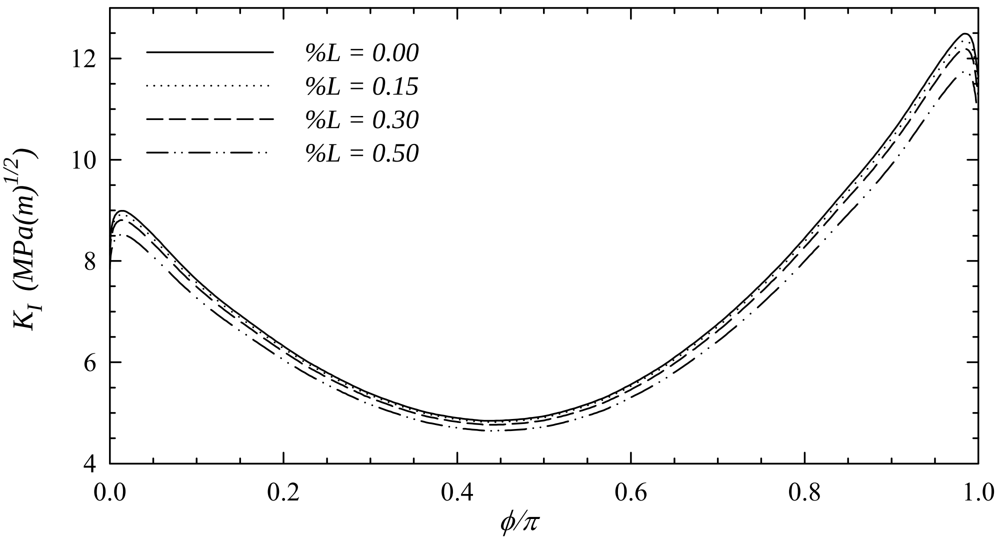

c)

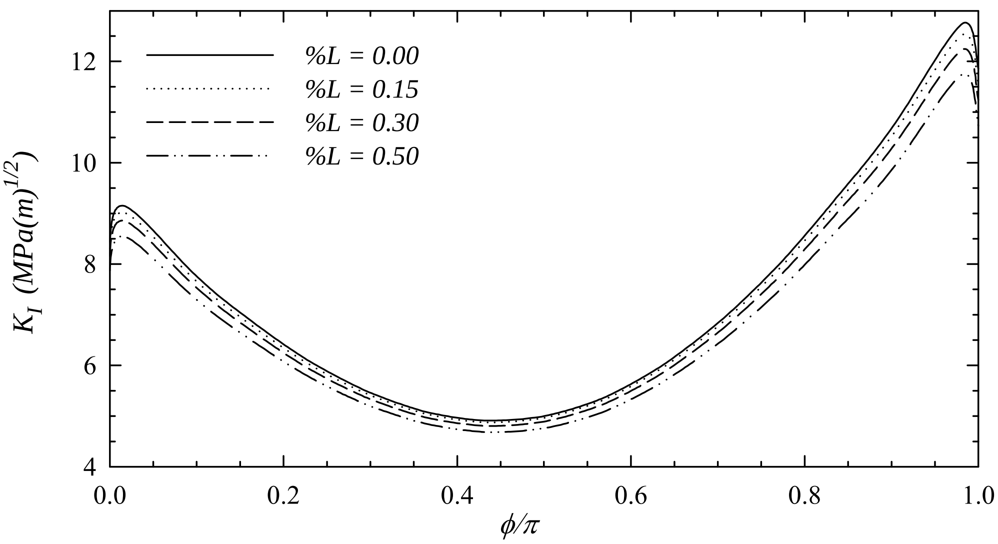

d)

Figure 5.30 Effects of clamping on the distribution of mode I SIF along crack front for semi elliptical surface crack, under external load, **a)** *%D=0.00,* **b)** *%D=0.15,* **c)** *%D=0.30,* **d)** *%D=0.50*

For mode II and mode III SIFs, magnitudes are small compared to mode I SIF, and effects of clamping are not significant. Therefore only illustrative results are presented for mode II SIF, mode III SIF and energy release distribution for interference value of %0.15. Figure 5.31.a illustrates the effects of clamping on mode II SIF. It is observed that effect is not significant. Figure 5.31.b illustrates the effects of clamping on mode III SIF. Figure 5.31.c illustrates the effects of clamping on energy release rate. Since mode I SIF is dominating over the other modes, trends of energy release rate is very similar to mode I SIF distribution.

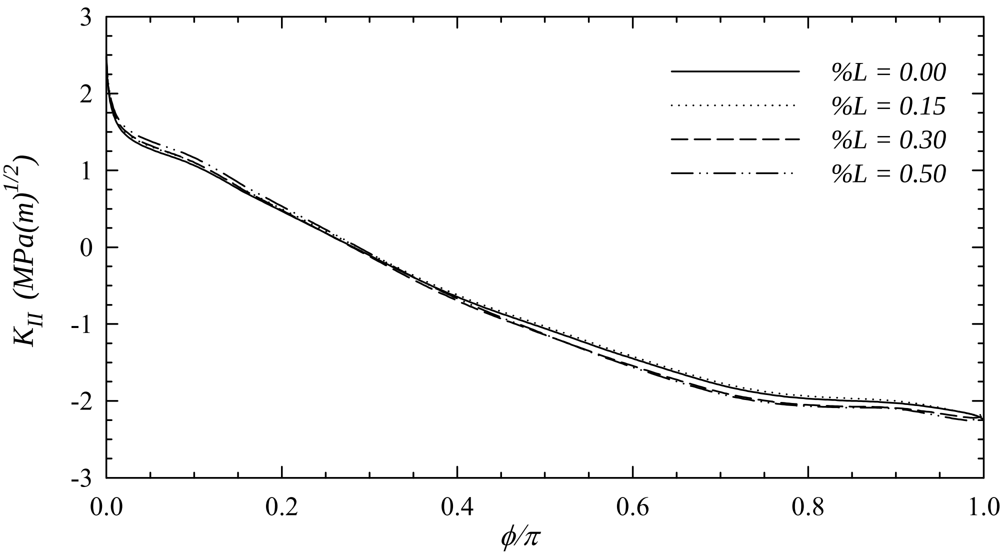

a)

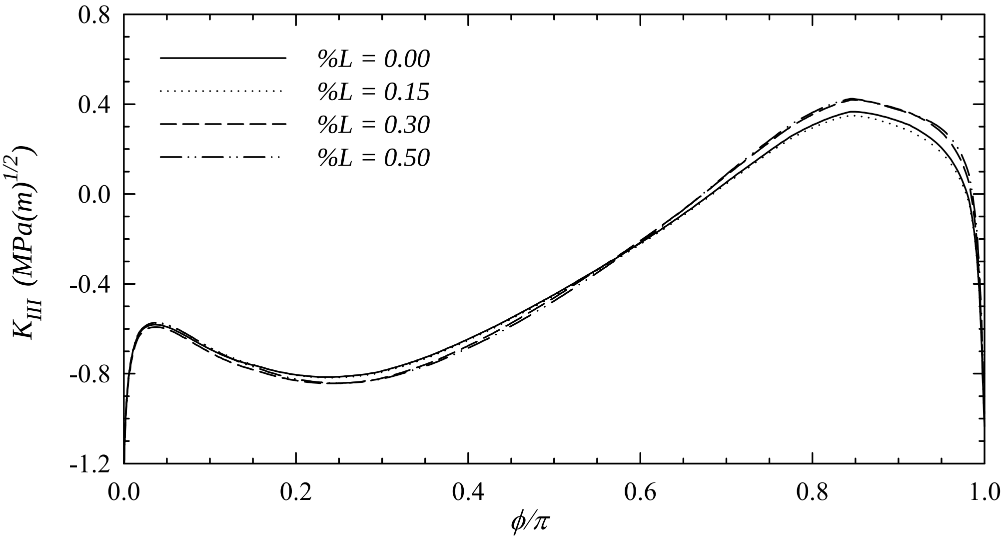

b)

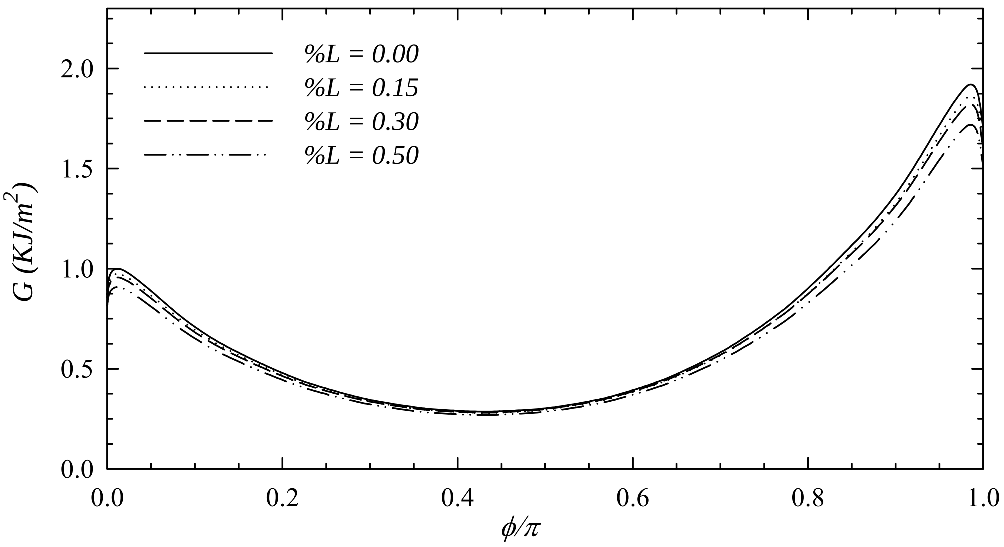

c)

Figure 5.31 Effects of clamping on the distribution of **a)** mode II SIF, **b)** mode III SIF, **c)** energy release rate , along crack front for semi elliptical surface crack, under external loading, *%D=0.15*

CHAPTER 6

DISCUSSION AND CONCLUSION

In this thesis, finite element analysis of single riveted lap joint with and without a crack was carried out. Stress state of the riveted lap joint was determined under the riveting simulation and external tensile loading. For the parametric stress analysis, interference and clamping, which are two important riveting process parameters, were selected as the parameters to be inspected. Before analyzing riveted lap joint having a crack, a plate with semi elliptical surface cracks subjected to uniform tension is analyzed. Then the fracture analysis was carried out for the cracked riveted lap joint having semi elliptical surface of quarter elliptical corner crack. For the parametric fracture analysis, crack geometry (crack shape and size), interference and clamping were selected as the parameters to be inspected.

First, three-dimensional stress field solutions in the panels of realistic riveted lap joints under both the residual stress field and external tensile loading were obtained. Three-dimensional finite element models of riveted lap joints have been developed using the commercial finite element program ANSYS. Two load steps were applied to the model. First, the riveting simulation was carried out and then an external tensile load was applied to the deformed and residual stress loaded riveted joint. Riveting process is simulated by a simplified method, namely the interference and clamping misfit method. In order to validate the model, a convergence check study was carried out by altering the overall mesh density of the numerical model. Results of the models with different mesh densities were compared and check whether results are converging certain values.

For the residual stress analysis, first illustrative contours for the residual stress components for fixed interference and clamping values on the rivet and the plates at a plane perpendicular to the tensile loading were presented to illustrate the stress concentration locations where the maximum stress values are observed. These locations are mainly the chamfers of the rivet hole and matching places on the rivet. Then stress components were compared through the thickness of the outer plate to see the variation along thickness. It was observed that variations of stress components are not significant through the thickness of the plate. Also stress distributions along circular path around the rivet hole were presented to see the radial variation of the stresses. Due to the multiple rivet symmetry conditions at the long edge of the riveted lap joint, tensile tangential and compressive radial stress values were observed to be maximum at a plane perpendicular to the loading, which is the probable crack plane.

Different values of misfit between rivet hole and rivet shank were modeled to capture the effects of riveting process parameters like interference and clamping on the residual stress state. Sixteen FE models were created by applying four different interference and clamping values. In comparing the stress results for different interference values, it can be concluded that the changes in the interference affects the residual stress field considerably. Magnitudes of the compressive radial stress and tensile tangential stress increase as the interference values are increased. Increasing clamping generally increases the compressive radial, tensile tangential and compressive axial stress components. Effect of clamping on the radial stress is not much as the interference. Especially for high interference values, effect of clamping is getting diminished. Clamping, which is the main cause of axial stress, has a deep effect on axial stress. All stress components change behavior at about a distance of 4 mm from the rivet hole center. 4 mm distance corresponds to the diameter of the rivet head which clamps plates together. Stress values are maximum near the rivet hole and decreasing as going away from the rivet.

After obtaining residual stress state, then the overall stress state under external loading was investigated. First overall stress variation along plate thickness is observed to be more significant than the residual stress variation. Also applying external load alters the stress distribution around the rivet hole. The maximum value of the tangential stress was approximately doubled and its location did not change much as in riveting simulation. Then effects of interference and clamping on the overall stress state were investigated. Magnitudes of the compressive radial stress for high interference values and tensile tangential stress increase as the interference values are increased. Stress values are decreasing as going away from the rivet. Radial stress is much more sensitive to change in the interference values than tangential stress component. Increasing clamping generally increases the compressive radial stress and axial stress; and decreases the tensile tangential stress components. Effect of clamping on the radial and tangential stress is not much as the interference. Especially for high interference values effect of clamping is getting diminished. As in the case of riveting simulation, axial stress becomes zero at about a distance of 4 mm from the rivet hole center and stay zero beyond this point.

Before analyzing riveted lap joint having a crack, a plate with semi elliptical surface cracks subjected to uniform tension was analyzed. By this, validity and accuracy of the computational method used to evaluate SIFs was demonstrated. Displacement correlation technique (DCT) was used to extract the mode I stress intensity factors for various crack shapes and sizes. APDL was utilized to carry out parametric analyses. Calculated stress intensity factors were compared with those given by Newman and Raju [27] for various crack geometries. The results were found consistent with the reference.

After developing the capability to carry out fracture mechanics analysis, cracks in riveted lap joints were examined. Semi elliptical surface crack at faying surfaces of plates and quarter elliptical corner crack at rivet hole were introduced at a plane perpendicular to the tensile loading. The mixed mode stress intensity factors (SIFs) and energy release rate distributions along crack fronts for these two types of cracks were obtained by using displacement correlation technique (DCT). Effect of residual stress state obtained by using different interference and clamping misfit values and crack geometrical parameters (crack shapes and sizes) on fracture parameters were studied. After creating all finite element models, during the inspection penetration of crack faces thus negative mode I stress intensity factor values were observed. By defining contact at the crack faces negative values of K_I before contact definition were shifted to zero.

Sixteen FE models for quarter elliptical corner crack and twelve FE models for semi elliptical crack were created by applying different crack shapes and sizes. Mode I SIF for riveting simulation and mixed modes SIFs and energy release rates distribution under external loading were presented along the crack front for all FE models. In order to study the effect of residual stress due to riveting simulation, first the fracture parameters were calculated under the residual stress only. Mode I SIF was shown to be very dominant and other modes of SIFs are negligible for the riveting simulation. Upon applying external load values of mode I SIF becomes approximately four times larger for the same crack geometry.

In order to study the effect of interference and clamping on fracture parameters, sixteen FE models for both types of cracks were generated by varying values of interference and clamping. Four different interference and clamping values (%0.00, %015, %0.30 and %0.50) were applied. In order to study the effect of residual stress due to riveting simulation, first the fracture parameters were calculated under the residual stress only. For all clamping values, values of K_I are increasing with increase in interference values. For interference values larger than 0, values of K_I are generally decreasing with increase in clamping values. The magnitudes of K_I for quarter elliptical crack are larger than the semi elliptical crack. It is due to the fact that quarter elliptical crack is in close proximity to residual stress. Also quarter elliptical crack is much more sensitive to riveting parameters than semi elliptical crack due to the same reason.

Under the external loading, for all clamping values, values of K_I are increasing with increase in interference values for quarter elliptical crack. For semi elliptical crack, effects of interference on the distribution of mode I SIF are not significant especially for high clamping values. For low clamping values, magnitude of the mode I SIF generally decreases with increase in interference values. Clamping has a deep effect on mode I SIF for both crack types. For all interference values, values of K_I are decreasing with increase in clamping values.

Magnitudes of mode II and III SIFs are small compared to mode I SIF values. Also effects of interference and clamping on the distributions of mode II and mode III SIFs are small compared to the mode I SIF. Therefore illustrative plots for these modes were presented and energy release rate which contains the contribution of all fracture modes of SIFs were presented.

Fracture parameters obtained here could be useful for correlating fatigue crack growth rates. Also they can be used to compute fracture toughness of riveted joints which have surface cracks at the plate and the quarter elliptical cracks at the plate hole. These SIF solutions can also be utilized in multiple site damage (MSD) analysis in aircraft fuselage.

Finally, this thesis study can be extended by the following subjects:

- In this thesis study, riveting process was simulated by a simplified method. In the future, actual riveting simulation can be utilized in order to obtain the residual stress state.
- A correlation between this simplified method and actual riveting process could be investigated. Correlations between interference and clamping misfit ratios in simplified method; and applied squeezing force and

clearance between rivet and rivet hole in actual riveting process to give equivalent residual stress state could be obtained.

- Elastic analysis was carried out throughout this study. Hardening of plates and rivet (i.e. plasticity) could be included in further study. Then elasto-plastic fracture mechanics should be considered for this case. Different procedures like J- Integral method should be applied rather than DCT method to calculate fracture parameters.
- Sealant usage between plates can be included in the analyses.
- High temperature variation in service life of the aircraft body can be included and effects of temperature variation on fracture parameters could be investigated.
- Different materials such as Fiber Metal Laminate (FML) and Functionally Graded Materials (FGM) can also be considered extension to the typical aluminum alloy fuselage material.
- This work can be extended for various dimensions of riveted joint and crack.

REFERENCES

[1] Aykan M., 2005, “Vibration Fatigue Analysis of Equipments Used in Aerospace”, M.S. Thesis, Middle East Technical University, Ankara

[2] Harris C. E., Piascik R. S., Newman C., 1999, “A practical engineering approach to predicting fatigue crack growth in riveted lap joints”, International Conference on Aeronautical Fatigue (ICAF), W.A.: Seattle.

[3] Pratt J.D., 2001, “Testing and Analysis of Mechanically-Fastened Joints”, University of California, Irvine, Dissertation.

[4] Fitzgerald T.J., Cohen J.B.,1994, “Residual stresses in and around rivets in clad aluminium alloy plates,” Materials Science and Engineering, A188, pp. 51-58

[5] Matos P.F.P., Moreira P.M.G.P., Nedbal I, Castro P.M.S.T., 2005, “Reconstitution of fatigue crack growth in Al-alloy 2024-T3 open-hole specimens using microfractographic techniques”, Engineering Fracture Mechanics,72, pp. 2232–2246

[6] Matos P.F.P., McEvily A.J., Moreira P.M.G.P., Castro P.M.S.T.,2007, “Analysis of the effect of cold-working of rivet holes on the fatigue life of an aluminum alloy”, International Journal of Fatigue, 29, pp. 575–586

[7] Langrand B., Patronelli L., Deletombe E., Markiewicz E., Drazetic P., 2002, “Full scale experimental characterization for riveted joint design”, Aerospace Science and Technology 6, pp. 333-342.

[8] Atre A., and Johnson W. S., “Analysis of the Effects of Riveting Process Parameters on the Fatigue of Aircraft Fuselage Lap Joints”, 9th Joint FAA/DoD/NASA Aging Aircraft Conference

[9] Szolwinski M. P., and Farris T. N., 2000, “Linking Riveting Process Parameters to the Fatigue Performance of Riveted Aircraft Structures”, Journal of Aircraft, Vol. 37, No. 1, pp. 130-137.

[10] Ryan L., and Monaghan J., 2000, “Failure Mechanism of Riveted Joint in Fibre Metal Laminants,” J. Mater. Process. Technol., 103, pp. 36–43.

[11] Karasan M.M., 2007, “Residual Stress Analysis of Riveting Process Using Finite Element Method”, M.S. Thesis, Middle East Technical University, Ankara

[12] Iyer K., Rubin C.A., Hahn, G.T., 2001, “Influence of interference and clamping on fretting fatigue in single rivet-row lap joints,” Journal of Tribology, Vol. 123, pp. 686-698.

[13] Fung C.P., and Smart, J., 1997, “Riveted Single-Lap-Joints. Part 1: A Numerical Parametric Study,” Proc. Instn. Mech. Engrs. –G- J. of Aerospace Engineering, 211 (1), pp. 13–27

[14] Bedair O.K, Eastaugh G.F, 2007, “A numerical model for analysis of riveted splice joints accounting for secondary bending and plates/rivet interaction”, Thin-Walled Structures 45, pp. 251–258

[15] Xiong Y., Bedair O.K., 1999, “Analytical and finite element modeling of riveted lap joints in aircraft structure,” AIAA Journal, Vol. 37, No.1, pp. 93-99.

[16] Harish G. and Farris T.N., 1999, “An Integrated Approach for Prediction of Fretting Crack Nucleation in Riveted Lap Joints,” American Institute of Aeronautics and Astronautics, pp. 1219-1226

[17] Moreira P.M.G.P., Matos P.F.P., Camanho P.P., Pastrama S.D., Castro P.M.S.T., 2007, ”Stress intensity factor and load transfer analysis of a cracked riveted lap joint,” Materials and Design 28, pp. 1263-1270.

[18] Szolwinski M.P., Harish G., Farris T.N., 1995, “Experimental Observation of the Effect of Contact Parameters on Fretting Fatigue Crack Nucleation”, Proceedings of the 1995 USAF Structural Integrity Program Conference, San Antonio.

[19] Szolwinski M.P., Farris T.N., 1998, “Observation, Analysis and Prediction of Fretting Fatigue in 2024-T352 Aluminum Alloy”, Wear, 221:24-36.

[20] Pitt S., Jones R., 1997, “Multiple-site and widespread fatigue damage in aging aircraft”, Engineering Failure Analysis, Vol. 4 No. 4, pp. 237-257.

[21] Silva L.F.M, Gonçalves J.P.M., Oliveira F.M.F., and de Castro P.M.S.T., 2000, “Multiple Site Damage in Riveted Lap-Joints: Experimental Simulation and Finite Element Prediction,” Int. J. Fatigue, 22, pp. 319–338.

[22] Ahmed A., Bakuckas J.G., Awerbuch J., Lau A.C., and Tan T.M., 2005, “Evolution of Multiple-Site Damage in the Riveted Lap Joint of a Fuselage Panel”, Proceedings of the 8th Joint NASA/FAA/DoD Conference on Aging Aircraft, Palm Springs, CA

[23] Heo S.P., Yang W.H, 2002, “Stress intensity factor analysis of elliptical corner cracks in mechanical joints by weight function method”, International Journal of Fracture 115: 377–399

[24] Liao M., Shi G., Y. Xiong, 2001 “Analytical methodology for predicting fatigue life distribution of fuselage splices” International Journal of Fatigue S177–S185

[25] Apicella A., Citarella R., Esposito R., 1999, “MSD residual strength assessment for a cracked joint” Fracture and Damage Mechanics Conference proceedings, London.

[26] Fung C-P., Smart J., 1997, “Riveted single lap joints Part 2: fatigue life prediction,” Proc. Instn Mech. Engrs, Part G, 211, pp. 123-128.

[27] Newman, J.C. and Raju, I.S., 1981, “An Empirical Stress – Intensity Factor Equation for the Surface Crack”, Engineering Fracture Mechanics, Vol. 15, pp. 185-192.

[28] Langrand B., Patronelli L., Deletombe E., Markiewicz E., Drazétic P., 2002, “An alternative numerical approach for full scale characterization for riveted joint design. Aerospace Sci Technol, 6(5):343–54.

[29] Military Standard NASM20470 “Rivet, Solid, Universal Head, Aluminum Alloy and Titanium Columbium Alloy, August 1998

[30] Davies D.P. et al., 2007, “Survey of Fatigue Failures in Helicopter Components and Lessons Learnt”, Technical Report

[31] ANSYS Release 11.0 Documentation for ANSYS.

[32] Qu J., Wang X., 2006, “Solutions of T-stresses for quarter-elliptical corner cracks in finite thickness plates subject to tension and bending”, International Journal of Pressure Vessels and Piping 83 593–606

[33] Kosker S., 2007, ”Three Dimensional Mixed Mode Fracture Analysis of Functionally Graded Material”, M.S. Thesis, Middle East Technical University, Ankara

[34] Ayhan, A.O. and Nied, H.F., 2002, “Stress Intensity Factors for Three-Dimensional Surface Cracks Using Enriched Finite Elements”, International Journal for Numerical Methods in Engineering, Vol. 54, pp.899-921.

[35] Lin XB, Smith RA., 1996, “Stress intensity factors for corner cracks emanating from fastener holes under tension.”, Engineering Fracture Mechanics 62 535–553

[36] Fawaz, S.A., 1999, “Stress intensity factor solutions for part-elliptical through cracks”, Engineering Fracture Mechanics 63, 209–226.